Journal of
Mechanics of
Materials and Structures

JOURNAL OF MECHANICS OF MATERIALS AND STRUCTURES

msp.org/jomms

Founded by Charles R. Steele and Marie-Louise Steele

msp

AN INTERFACIAL ARC CRACK IN
BONDED DISSIMILAR ISOTROPIC LAMINATED PLATES

Xu Wang, Cuiying Wang and Peter Schiavone

We consider an arc-shaped crack lying along the interface of a through-thickness circular elastic inhomogeneity in an infinite isotropic laminated thin plate subjected to bending and stretching within the context of classical Kirchhoff theory. A novel Stroh-type formalism is developed to reduce the original boundary value problem to a nonhomogeneous Riemann–Hilbert problem of vector form. The latter is solved analytically using a matrix diagonalization scheme. Elegant closed-form solutions are obtained for the stress resultants, in-plane displacements and slopes everywhere in the composite when the plate is subjected to remote uniform membrane stress resultants and bending moments. In particular, the surface stress resultants and surface bending moment along the bonded part of the interface, the jump in the generalized displacement vector across the debonded segment of the interface and the two complex intensity factors at each of the two crack tips are given in explicit form.

1. Introduction

Laminated composite plate structures have been widely used in the fields of aerospace, mechanical and civil engineering. The Kirchhoff plate theory is the most celebrated model for describing the bending deformations of a thin plate [Timoshenko and Woinowsky-Krieger 1959; Lekhnitskii 1968; Reddy 1997]. Problems involving cracks lying along the straight interface between two dissimilar plates under in-plane and bending loads have been studied extensively (see, for example, [Williams 1959; England 1965; Rice and Sih 1965; Erdogan 1965; Rice 1988; Suo 1989] for in-plane stretching, [Sih and Rice 1964; Sih 1966] for out-of-plane bending, and [Wang and Schiavone 2013] for coupled stretching and bending). The problem associated with interfacial arc-shaped cracks in bonded dissimilar homogeneous and isotropic elastic plates subjected to in-plane loads has also been considered by various authors (see, for example, [England 1966; Perlman and Sih 1967; Toya 1974; Herrmann 1991; 1994]).

Using the framework of Kirchhoff plate bending theory, we endeavour to study the coupled stretching and bending deformations of an infinite isotropic laminated plate (the matrix) containing a partially bonded isotropic laminated circular inhomogeneity when the matrix is subjected to remote uniform membrane stress resultants and bending moments. In order to solve the problem, we first propose an elegant Stroh-type formalism based on the complex variable formulation in [Wang and Zhou 2014b]. As a result, the original boundary value problem is reduced to a nonhomogeneous Riemann–Hilbert problem of vector form. Through simultaneous diagonalization of two positive definite Hermitian matrices, we arrive at four separate Riemann–Hilbert problems of scalar form which can be solved analytically by evaluating the corresponding Cauchy integrals. Consequently, we are able to determine the four analytic functions

---

defined in the inhomogeneity as well as the four analytic functions defined in the matrix. The resulting stress resultant and displacement fields can then be obtained from the corresponding analytic functions.

The original Stroh sextic formalism was developed for generalized plane strain deformations of an anisotropic elastic material [Stroh 1958; 1962; Ting 1996]. A new Stroh octet formalism was later developed for coupled stretching and bending deformations of an anisotropic elastic thin plate [Cheng and Reddy 2002; 2005]. Both formalisms become rather cumbersome for mathematically degenerate materials in which the 6×6 fundamental elasticity matrix or the 8×8 fundamental elastic plate matrix becomes nonsemisimple [Ting 1996; Cheng and Reddy 2002]. An isotropic laminated plate is degenerate in the sense that there are only two independent eigenvectors associated with the quadruple roots $p_1 = p_2 = p_3 = p_4 = \mathrm{i}$ [Cheng and Reddy 2002]. As part of our analysis, we develop an elegant Stroh-type formalism to tackle the problem at hand: that of an arc-shaped crack in bonded dissimilar isotropic laminated plates.

Finally, we mention that although laminated plates are typically elastically anisotropic, laminates composed of isotropic layers arise quite frequently in practice. In fact, only a simple modification of the aforementioned complex variable formulation developed by Wang and Zhou [2014b] for an isotropic laminated plate will accommodate the more general case of a transversely isotropic laminated plate with the x_3-axis as axis of symmetry [Cheng and Reddy 2002].

2. Basic formulation

2.1. *Complex variable formulation.* In this section, we undertake a brief review of the complex variable formulation for coupled stretching and bending deformations of an isotropic laminated plate.

We establish a Cartesian coordinate system $\{x_i\}$ $(i = 1, 2, 3)$ in which the reference plane of an undeformed plate of uniform thickness h is located at $x_3 = 0$. The plate is composed of an isotropic, linearly elastic material that can be inhomogeneous and laminated in the thickness direction. In what follows, Greek and Latin indices take the values $1, 2$ and $1, 2, 3$, respectively and we sum over repeated indices.

The displacement field in the Kirchhoff plate theory is assumed to take the form

$$\tilde{u}_\alpha(x_i) = u_\alpha + x_3 \vartheta_\alpha, \quad \tilde{u}_3(x_i) = w, \tag{1}$$

where the two in-plane displacements u_α, the deflection w and the slopes $\vartheta_\alpha = -w_{,\alpha}$ on the reference plane are all independent of x_3.

The coordinate system is judiciously chosen such that the two in-plane displacements and the deflection on the reference plane are *decoupled* in the equilibrium equations [Beom and Earmme 1998]. We introduce the integral operator $Q(\cdots) = \int_{-h_0}^{h-h_0} (\cdots) \, \mathrm{d}x_3$ in which h_0 is the distance between the reference plane and the lower surface of the plate. Accordingly, the membrane stress resultants and bending moments defined by $N_{\alpha\beta} = Q\sigma_{\alpha\beta}$ and $M_{\alpha\beta} = Qx_3\sigma_{\alpha\beta}$ (with $\sigma_{\alpha\beta}$ denoting the in-plane stress components), the transverse shearing forces $\Re_\beta = M_{\alpha\beta,\alpha}$, in-plane displacements, deflection and slopes on the reference plane of the plate as well as the four stress functions φ_α and η_α can be expressed concisely in terms of four complex potentials $\phi(z)$, $\psi(z)$, $\Phi(z)$ and $\Psi(z)$ of the complex variable $z = x_1 + \mathrm{i}x_2$ as [Wang and Zhou 2014b]

$$
\begin{aligned}
N_{11} + N_{22} &= 4\,\mathrm{Re}\{\phi'(z) + B\Phi'(z)\}, \\
N_{22} - N_{11} + 2\mathrm{i}N_{12} &= 2\big[\bar{z}\phi''(z) + \psi'(z) + B\bar{z}\Phi''(z) + B\Psi'(z)\big],
\end{aligned}
\tag{2}
$$

$$M_{11} + M_{22} = 4D(1 + v^D)\,\mathrm{Re}\{\Phi'(z)\} + \frac{B(\kappa^A - 1)}{\mu}\,\mathrm{Re}\{\phi'(z)\},$$

$$M_{22} - M_{11} + 2\mathrm{i}M_{12} = -2D(1 - v^D)[\bar{z}\Phi''(z) + \Psi'(z)] - \frac{B}{\mu}[\bar{z}\phi''(z) + \psi'(z)], \tag{3}$$

$$\mathfrak{R}_1 - \mathrm{i}\mathfrak{R}_2 = 4D\Phi''(z) + \frac{B(\kappa^A + 1)}{2\mu}\phi''(z),$$

$$2\mu(u_1 + \mathrm{i}u_2) = \kappa^A\phi(z) - z\overline{\phi'(z)} - \overline{\psi(z)},$$

$$\vartheta_1 + \mathrm{i}\vartheta_2 = \Phi(z) + z\overline{\Phi'(z)} + \overline{\Psi(z)}, \quad w = -\mathrm{Re}\{\bar{z}\Phi(z) + \gamma(z)\},$$

$$\varphi_1 + \mathrm{i}\varphi_2 = \mathrm{i}[\phi(z) + z\overline{\phi'(z)} + \overline{\psi(z)}] + \mathrm{i}B[\Phi(z) + z\overline{\Phi'(z)} + \overline{\Psi(z)}], \tag{4}$$

$$\eta_1 + \mathrm{i}\eta_2 = \mathrm{i}D(1 - v^D)[\kappa^D\Phi(z) - z\overline{\Phi'(z)} - \overline{\Psi(z)}] + \mathrm{i}\frac{B}{2\mu}[\kappa^A\phi(z) - z\overline{\phi'(z)} - \overline{\psi(z)}],$$

in which $\Psi(z) = \gamma'(z)$, and

$$\mu = \tfrac{1}{2}(A_{11} - A_{12}), \quad B = B_{12}, \quad D = D_{11}, \quad v^A = \frac{A_{12}}{A_{11}}, \quad v^D = \frac{D_{12}}{D_{11}},$$

$$\kappa^A = \frac{3A_{11} - A_{12}}{A_{11} + A_{12}} = \frac{3 - v^A}{1 + v^A}, \quad \kappa^D = \frac{3D_{11} + D_{12}}{D_{11} - D_{12}} = \frac{3 + v^D}{1 - v^D}, \tag{5}$$

with $A_{ij} = QC_{ij}$, $B_{ij} = Qx_3C_{ij}$ and $D_{ij} = Qx_3^2C_{ij}$ ($ij = 11, 12$). The parameters C_{11} and C_{12} can be expressed in terms of the Young's modulus $E = E(x_3)$ and Poisson's ratio $v = v(x_3)$ of the plate as $C_{11} = E/(1 - v^2)$ and $C_{12} = vE/(1 - v^2)$. The distance h_0 is determined as

$$h_0 = \frac{\int_0^h X_3C_{11}\,\mathrm{d}X_3}{\int_0^h C_{11}\,\mathrm{d}X_3}$$

with $X_3 = x_3 + h_0$ being the vertical coordinate of the given point from the lower surface of the plate. Detailed derivations of equations (2)–(5) can be found in [Wang and Zhou 2014b].

In addition, the membrane stress resultants, bending moments, transverse shearing forces, and modified Kirchhoff transverse shearing forces $V_1 = \mathfrak{R}_1 + M_{12,2}$ and $V_2 = \mathfrak{R}_2 + M_{21,1}$ (which apply exclusively to free edges), can be expressed in terms of the four stress functions φ_α and η_α [Cheng and Reddy 2002] as

$$N_{\alpha\beta} = -\epsilon_{\beta\omega}\varphi_{\alpha,\omega}, \quad M_{\alpha\beta} = -\epsilon_{\beta\omega}\eta_{\alpha,\omega} - \tfrac{1}{2}\epsilon_{\alpha\beta}\eta_{\omega,\omega}, \quad \mathfrak{R}_\alpha = -\tfrac{1}{2}\epsilon_{\alpha\beta}\eta_{\omega,\omega\beta}, \quad V_\alpha = -\epsilon_{\alpha\omega}\eta_{\omega,\omega\omega}. \tag{6}$$

Here $\epsilon_{\alpha\beta}$ are the components of the two-dimensional permutation tensor.

In a new coordinate system $\{\hat{x}_i\}$ ($i = 1, 2, 3$) in which $\hat{x}_3 = 0$ lies on an arbitrary plane parallel to the reference plane and $\hat{x}_\alpha = x_\alpha$, the in-plane displacements $\hat{u}_\alpha$ and slopes $\hat{\vartheta}_\alpha$ on $\hat{x}_3 = 0$ and the stress functions $\hat{\varphi}_\alpha$ and $\hat{\eta}_\alpha$ in the new coordinate system can be given quite simply as

$$\hat{\vartheta}_1 + \mathrm{i}\hat{\vartheta}_2 = \vartheta_1 + \mathrm{i}\vartheta_2, \quad \hat{u}_1 + \mathrm{i}\hat{u}_2 = u_1 + \mathrm{i}u_2 - \hat{h}(\vartheta_1 + \mathrm{i}\vartheta_2),$$

$$\hat{\varphi}_1 + \mathrm{i}\hat{\varphi}_2 = \varphi_1 + \mathrm{i}\varphi_2, \quad \hat{\eta}_1 + \mathrm{i}\hat{\eta}_2 = \eta_1 + \mathrm{i}\eta_2 + \hat{h}(\varphi_1 + \mathrm{i}\varphi_2). \tag{7}$$

Here,

$$\hat{h} = h_1 - h_0, \tag{8}$$

and h_1 is the distance between $\hat{x}_3 = 0$ and the lower surface of the plate (we note that h_1 is positive or negative, respectively, if $\hat{x}_3 = 0$ is above or below the lower surface of the plate). In the new coordinate system, the stress resultants $\hat{N}_{\alpha\beta} = \hat{Q}\sigma_{\alpha\beta}$ and $\hat{M}_{\alpha\beta} = \hat{Q}\hat{x}_3\sigma_{\alpha\beta}$ with

$$\hat{Q}(\cdots) = \int_{-h_1}^{h-h_1} (\cdots)\,\mathrm{d}\hat{x}_3,$$

the transverse shearing forces $\hat{\Re}_\beta = \hat{M}_{\alpha\beta,\alpha}$, and the modified Kirchhoff transverse shearing forces $\hat{V}_1 = \hat{\Re}_1 + \hat{M}_{12,2}$ and $\hat{V}_2 = \hat{\Re}_2 + \hat{M}_{21,1}$ can also be expressed in terms of the newly introduced stress functions $\hat{\varphi}_\alpha$ and $\hat{\eta}_\alpha$ as

$$\hat{N}_{\alpha\beta} = -\epsilon_{\beta\omega}\hat{\varphi}_{\alpha,\omega}, \quad \hat{M}_{\alpha\beta} = -\epsilon_{\beta\omega}\hat{\eta}_{\alpha,\omega} - \tfrac{1}{2}\epsilon_{\alpha\beta}\hat{\eta}_{\omega,\omega}, \quad \hat{\Re}_\alpha = -\tfrac{1}{2}\epsilon_{\alpha\beta}\hat{\eta}_{\omega,\omega\beta}, \quad \hat{V}_\alpha = -\epsilon_{\alpha\omega}\hat{\eta}_{\omega,\omega\omega}. \quad (9)$$

2.2. *Statement of the problem.* As shown in Figure 1, we consider the coupled stretching and bending deformations of an infinite isotropic laminated plate containing a partially bonded through-thickness isotropic laminated circular inhomogeneity of radius R. The centre of the circular inhomogeneity is located at the origin and an interface arc crack lies along the arc L_c of the interface. Along the remaining arc L_b of the interface, the inhomogeneity remains perfectly bonded to the surrounding matrix. The centre of the arc L_b lies on the positive x_1-axis and the central angle subtended by the arc L_b is given by $2\theta_0$. The two crack tips are located at $a = Re^{i\theta_0}$ and $\bar{a} = Re^{-i\theta_0}$. We represent the matrix by the domain S_2 and assume that the circular inhomogeneity occupies the region S_1. The matrix is subjected to remote uniform membrane stress resultants $(N_{11}^\infty, N_{12}^\infty, N_{22}^\infty)$ and bending moments $(M_{11}^\infty, M_{12}^\infty, M_{22}^\infty)$ measured on its reference plane. In what follows, the subscripts 1 and 2 (or the superscripts (1) and (2)) are used to identify the respective quantities in S_1 and S_2, respectively.
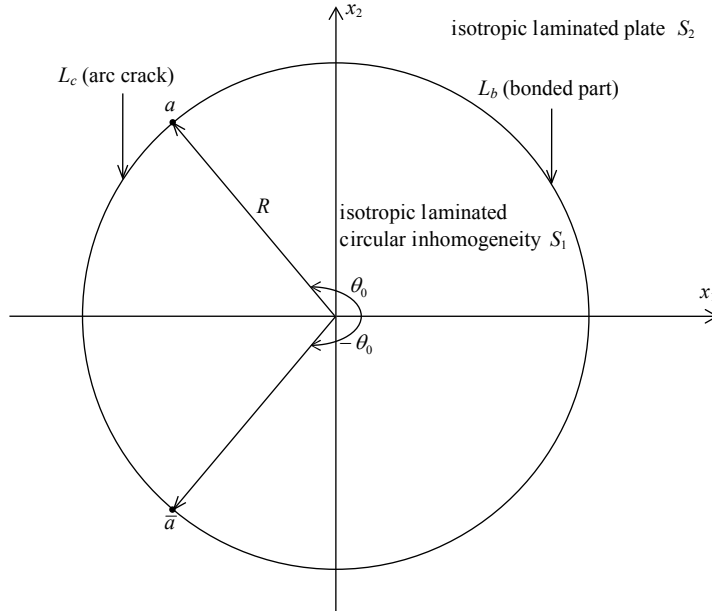

Figure 1. An isotropic laminated circular inhomogeneity partially bonded to an infinite isotropic laminated plate.

The boundary conditions on the circular interface are given specifically by

$$\hat{\varphi}_1^{(1)} = \hat{\varphi}_1^{(2)}, \qquad \hat{\varphi}_2^{(1)} = \hat{\varphi}_2^{(2)}, \qquad \hat{\eta}_1^{(1)} = \hat{\eta}_1^{(2)}, \qquad \hat{\eta}_2^{(1)} = \hat{\eta}_2^{(2)}, \qquad z \in L_b; \qquad (10\text{a})$$

$$\hat{u}_1^{(1)} = \hat{u}_1^{(2)}, \qquad \hat{u}_2^{(1)} = \hat{u}_2^{(2)}, \qquad \hat{\vartheta}_1^{(1)} = \hat{\vartheta}_1^{(2)}, \qquad \hat{\vartheta}_2^{(1)} = \hat{\vartheta}_2^{(2)}, \qquad z \in L_b; \qquad (10\text{b})$$

$$\hat{\varphi}_1^{(1)} = \hat{\varphi}_1^{(2)} = 0, \quad \hat{\varphi}_2^{(1)} = \hat{\varphi}_2^{(2)} = 0, \quad \hat{\eta}_1^{(1)} = \hat{\eta}_1^{(2)} = 0, \quad \hat{\eta}_2^{(1)} = \hat{\eta}_2^{(2)} = 0, \quad z \in L_c. \qquad (10\text{c})$$

The conditions in equations (10a)–(10b) imply that the stress resultants and displacements are continuous across L_b, whilst equation (10c) indicates that the free edge condition is satisfied on L_c.

3. The Stroh-type formalism

It is extremely problematic to apply the complex variable formulation in Section 2.1 directly to solve the boundary value problem associated with the arc-shaped interface crack described in Section 2.2 mainly because of the formidable number of elastic constants involved in the two phases of the composite as well as the expression of the interface conditions in the new coordinate system common to both the inhomogeneity and the matrix. As an alternative, in this section we propose an elegant Stroh-type formalism. We introduce the following analytic function vector $\boldsymbol{f}(z)$ for the circular inhomogeneity and the surrounding matrix

$$\boldsymbol{f}(z) = \begin{bmatrix} \phi(z) \\ \psi(z) + (R^2/z)\phi'(z) \\ \Phi(z) \\ \Psi(z) + (R^2/z)\Phi'(z) \end{bmatrix}. \qquad (11)$$

As a result, the generalized displacement vector and the stress function vector along the circular interface $|z| = R$ in the new coordinate system can be concisely and elegantly expressed in terms of $\boldsymbol{f}(z)$ as

$$\hat{\boldsymbol{u}} = \boldsymbol{A}\boldsymbol{f}(z) + \overline{\boldsymbol{A}}\,\overline{\boldsymbol{f}(z)}, \quad \hat{\boldsymbol{\varphi}} = \boldsymbol{B}\boldsymbol{f}(z) + \overline{\boldsymbol{B}}\,\overline{\boldsymbol{f}(z)}, \quad |z| = R, \qquad (12)$$

where

$$\hat{\boldsymbol{u}} = \begin{bmatrix} \hat{u}_1 & \hat{u}_2 & \hat{\vartheta}_1 & \hat{\vartheta}_2 \end{bmatrix}^T, \quad \hat{\boldsymbol{\varphi}} = \begin{bmatrix} \hat{\varphi}_1 & \hat{\varphi}_2 & \hat{\eta}_1 & \hat{\eta}_2 \end{bmatrix}^T, \qquad (13)$$

$$A = \frac{1}{2} \begin{bmatrix} \boldsymbol{I} & -\hat{h}\boldsymbol{I} \\ \boldsymbol{0} & \boldsymbol{I} \end{bmatrix} \begin{bmatrix} \kappa^A/(2\mu) & -1/(2\mu) & 0 & 0 \\ -\mathrm{i}\kappa^A/(2\mu) & -\mathrm{i}/(2\mu) & 0 & 0 \\ 0 & 0 & 1 & 1 \\ 0 & 0 & -\mathrm{i} & \mathrm{i} \end{bmatrix}, \qquad (14)$$

$$B = \frac{1}{2} \begin{bmatrix} \boldsymbol{I} & \boldsymbol{0} \\ \hat{h}\boldsymbol{I} & \boldsymbol{I} \end{bmatrix} \begin{bmatrix} \mathrm{i} & -\mathrm{i} & \mathrm{i}B & -\mathrm{i}B \\ 1 & 1 & B & B \\ \mathrm{i}B\kappa^A/(2\mu) & \mathrm{i}B/(2\mu) & \mathrm{i}D(3+v^D) & \mathrm{i}D(1-v^D) \\ B\kappa^A/(2\mu) & -B/(2\mu) & D(3+v^D) & -D(1-v^D) \end{bmatrix}. \qquad (15)$$

It can be deduced that

$$\mathrm{i}\boldsymbol{A}\boldsymbol{B}^{-1} = \boldsymbol{M}^{-1} = \boldsymbol{L}^{-1} - \mathrm{i}\boldsymbol{S}\boldsymbol{L}^{-1} = \begin{bmatrix} \hat{\alpha}_{11} & \mathrm{i}\hat{\alpha}_{12} & \hat{\alpha}_{13} & -\mathrm{i}\hat{\alpha}_{23} \\ -\mathrm{i}\hat{\alpha}_{12} & \hat{\alpha}_{11} & \mathrm{i}\hat{\alpha}_{23} & \hat{\alpha}_{13} \\ \hat{\alpha}_{13} & -\mathrm{i}\hat{\alpha}_{23} & \hat{\alpha}_{33} & -\mathrm{i}\hat{\alpha}_{43} \\ \mathrm{i}\hat{\alpha}_{23} & \hat{\alpha}_{13} & \mathrm{i}\hat{\alpha}_{43} & \hat{\alpha}_{33} \end{bmatrix}, \tag{16}$$

where

$$\hat{\alpha}_{11} = \alpha_{11} - 2\hat{h}\alpha_{13} + \hat{h}^2\alpha_{33}, \quad \hat{\alpha}_{12} = \alpha_{12} + 2\hat{h}\alpha_{23} - \hat{h}^2\alpha_{43},$$
$$\hat{\alpha}_{13} = \alpha_{13} - \hat{h}\alpha_{33}, \quad \hat{\alpha}_{23} = \alpha_{23} - \hat{h}\alpha_{43}, \quad \hat{\alpha}_{33} = \alpha_{33}, \quad \hat{\alpha}_{43} = \alpha_{43}, \tag{17}$$

with α_{ij} given by [Wang and Zhou 2014a] as

$$\alpha_{11} = \frac{2D[2\mu D(1-\nu^D)(3+\nu^D) - B^2(3-\nu^A)]}{[2\mu D(1-\nu^D) - B^2][2\mu D(3+\nu^D)(1+\nu^A) - B^2(3-\nu^A)]},$$

$$\alpha_{12} = \frac{D[2\mu D(1-\nu^D)(3+\nu^D)(1-\nu^A) - B^2(1+\nu^D)(3-\nu^A)]}{[2\mu D(1-\nu^D) - B^2][2\mu D(3+\nu^D)(1+\nu^A) - B^2(3-\nu^A)]},$$

$$\alpha_{13} = \frac{4B\mu D(\nu^D + \nu^A)}{[2\mu D(1-\nu^D) - B^2][2\mu D(3+\nu^D)(1+\nu^A) - B^2(3-\nu^A)]},$$

$$\alpha_{23} = \frac{B[2\mu D(3-\nu^D + \nu^A + \nu^D\nu^A) - B^2(3-\nu^A)]}{[2\mu D(1-\nu^D) - B^2][2\mu D(3+\nu^D)(1+\nu^A) - B^2(3-\nu^A)]}, \tag{18}$$

$$\alpha_{33} = \frac{4\mu[2\mu D(1+\nu^A) - B^2]}{[2\mu D(1-\nu^D) - B^2][2\mu D(3+\nu^D)(1+\nu^A) - B^2(3-\nu^A)]},$$

$$\alpha_{43} = \frac{2\mu[2\mu D(1+\nu^D)(1+\nu^A) - B^2(1-\nu^A)]}{[2\mu D(1-\nu^D) - B^2][2\mu D(3+\nu^D)(1+\nu^A) - B^2(3-\nu^A)]}.$$

Furthermore, $\boldsymbol{M}^{-1}$ is a positive definite Hermitian matrix. As a result $\boldsymbol{L}$ is real symmetric and positive definite, while $\boldsymbol{S}\boldsymbol{L}^{-1}$ is antisymmetric.

Remark 1. Equations (16) and (17) are obtained by utilizing the following relationship during coordinate translation

$$\boldsymbol{M}^{-1} = \begin{bmatrix} \boldsymbol{I} & -\hat{h}\boldsymbol{I} \\ \boldsymbol{0} & \boldsymbol{I} \end{bmatrix} \boldsymbol{M}_0^{-1} \begin{bmatrix} \boldsymbol{I} & \boldsymbol{0} \\ -\hat{h}\boldsymbol{I} & \boldsymbol{I} \end{bmatrix},$$

where

$$\boldsymbol{I} = \begin{bmatrix} 1 & 0 \\ 0 & 1 \end{bmatrix}, \quad \boldsymbol{M}_0^{-1} = \begin{bmatrix} \alpha_{11} & \mathrm{i}\alpha_{12} & \alpha_{13} & -\mathrm{i}\alpha_{23} \\ -\mathrm{i}\alpha_{12} & \alpha_{11} & \mathrm{i}\alpha_{23} & \alpha_{13} \\ \alpha_{13} & -\mathrm{i}\alpha_{23} & \alpha_{33} & -\mathrm{i}\alpha_{43} \\ \mathrm{i}\alpha_{23} & \alpha_{13} & \mathrm{i}\alpha_{43} & \alpha_{33} \end{bmatrix}.$$

4. Closed-form solution

The continuity condition of stress resultants across the circular interface $|z| = R$ can then be expressed in terms of $f_1(z)$ and $f_2(z)$ as

$$B_1 f_1^+(z) + \overline{B}_1 \overline{f}_1^-(R^2/z) = B_2 f_2^-(z) + \overline{B}_2 \overline{f}_2^+(R^2/z), \quad |z| = R. \tag{19}$$

By applying the generalized Liouville's theorem, we arrive at the relationship

$$\overline{B}_2 \overline{f}_2(R^2/z) - B_1 f_1(z) = \overline{B}_1 \overline{f}_1(R^2/z) - B_2 f_2(z) = g(z), \tag{20}$$

where $g(z)$ is given by

$$g(z) = \left[\overline{B}_1 (i_2 \overline{\phi_1'(0)} + i_4 \overline{\Phi_1'(0)}) - B_2 k \right] z + R^2 \left[\overline{B}_2 \overline{k} - B_1 (i_2 \phi_1'(0) + i_4 \Phi_1'(0)) \right] z^{-1}, \tag{21}$$

i_K is a unit 4-vector defined by $(i_K)_L = \delta_{KL}$ and the vector k is related to the remote uniform membrane stress resultants and bending moments through

$$k = \begin{bmatrix} \dfrac{\mu_2 D_2 (1+v_2^D)(N_{11}^\infty + N_{22}^\infty) - B_2 \mu_2 (M_{11}^\infty + M_{22}^\infty)}{4\mu_2 D_2 (1+v_2^D) - B_2^2 (\kappa_2^A - 1)} \\[2.5ex] \dfrac{\mu_2 D_2 (1-v_2^D)(N_{22}^\infty - N_{11}^\infty + 2iN_{12}^\infty) + B_2 \mu_2 (M_{22}^\infty - M_{11}^\infty + 2iM_{12}^\infty)}{2\mu_2 D_2 (1-v_2^D) - B_2^2} \\[2.5ex] \dfrac{4\mu_2 (M_{11}^\infty + M_{22}^\infty) - B_2 (\kappa_2^A - 1)(N_{11}^\infty + N_{22}^\infty)}{16\mu_2 D_2 (1+v_2^D) - 4B_2^2 (\kappa_2^A - 1)} \\[2.5ex] \dfrac{-2\mu_2 (M_{22}^\infty - M_{11}^\infty + 2iM_{12}^\infty) - B_2 (N_{22}^\infty - N_{11}^\infty + 2iN_{12}^\infty)}{4\mu_2 D_2 (1-v_2^D) - 2B_2^2} \end{bmatrix}. \tag{22}$$

Remark 2. Equation (20) can be obtained by noting that $f_1(z) \cong R^2 [i_2 \phi_1'(0) + i_4 \Phi_1'(0)] z^{-1} + O(1)$ as $z \to 0$ and $f_2(z) \cong kz + O(1)$ as $|z| \to \infty$.

The continuity condition for the generalized displacement vector across the bonded section of the interface can be expressed in terms of $f_1(z)$ and $f_2(z)$ by

$$A_1 f_1^+(z) + \overline{A}_1 \overline{f}_1^-(R^2/z) = A_2 f_2^-(z) + \overline{A}_2 \overline{f}_2^+(R^2/z), \quad z \in L_b. \tag{23}$$

Eliminating $\overline{f}_1^-(R^2/z)$ and $\overline{f}_2^+(R^2/z)$ from equation (23) using the relationship in equation (20) yields

$$M_* B_1 f_1'^+(z) - \overline{M}_* B_2 f_2'^-(z) = (\overline{M}_1^{-1} - \overline{M}_2^{-1}) g'(z), \quad z \in L_b, \tag{24}$$

where

$$M_* = M_1^{-1} + \overline{M}_2^{-1} = L_1^{-1} + L_2^{-1} - i(S_1 L_1^{-1} - S_2 L_2^{-1}). \tag{25}$$

For convenience, we write the positive definite Hermitian matrix M_* in the component form as

$$M_* = \begin{bmatrix} Y_{11} & -iY_{21} & Y_{13} & -iY_{23} \\ iY_{21} & Y_{11} & iY_{23} & Y_{13} \\ Y_{13} & -iY_{23} & Y_{33} & -iY_{43} \\ iY_{23} & Y_{13} & iY_{43} & Y_{33} \end{bmatrix}, \tag{26}$$

where

$$
\begin{aligned}
&Y_{11} = \hat{\alpha}_{11}^{(1)} + \hat{\alpha}_{11}^{(2)}, \quad Y_{13} = \hat{\alpha}_{13}^{(1)} + \hat{\alpha}_{13}^{(2)}, \quad Y_{33} = \hat{\alpha}_{33}^{(1)} + \hat{\alpha}_{33}^{(2)}, \\
&Y_{21} = \hat{\alpha}_{12}^{(2)} - \hat{\alpha}_{12}^{(1)}, \quad Y_{23} = \hat{\alpha}_{23}^{(1)} - \hat{\alpha}_{23}^{(2)}, \quad Y_{43} = \hat{\alpha}_{43}^{(1)} - \hat{\alpha}_{43}^{(2)}.
\end{aligned}
\tag{27}
$$

Considering equation (24), we introduce the sectionally holomorphic function vector $\boldsymbol{h}(z)$ as

$$
\boldsymbol{h}(z) = \boldsymbol{B}_1 \boldsymbol{f}_1'(z) - \boldsymbol{M}_*^{-1} \big[(\overline{\boldsymbol{M}}_1^{-1} - \overline{\boldsymbol{M}}_2^{-1}) \overline{\boldsymbol{B}}_1 (\boldsymbol{i}_2 \overline{\phi_1'(0)} + \boldsymbol{i}_4 \overline{\Phi_1'(0)}) + 2 \boldsymbol{L}_2^{-1} \boldsymbol{B}_2 \boldsymbol{k} \big]
$$
$$
+ R^2 \boldsymbol{B}_1 (\boldsymbol{i}_2 \phi_1'(0) + \boldsymbol{i}_4 \Phi_1'(0)) z^{-2}, \qquad |z| < R, \quad \text{(28a)}
$$
$$
\boldsymbol{h}(z) = \boldsymbol{M}_*^{-1} \overline{\boldsymbol{M}}_* \boldsymbol{B}_2 \boldsymbol{f}_2'(z) - \boldsymbol{M}_*^{-1} \overline{\boldsymbol{M}}_* \boldsymbol{B}_2 \boldsymbol{k}
$$
$$
- R^2 \boldsymbol{M}_*^{-1} \big[(\overline{\boldsymbol{M}}_1^{-1} - \overline{\boldsymbol{M}}_2^{-1}) \overline{\boldsymbol{B}}_2 \overline{\boldsymbol{k}} - 2 \boldsymbol{L}_1^{-1} \boldsymbol{B}_1 (\boldsymbol{i}_2 \phi_1'(0) + \boldsymbol{i}_4 \Phi_1'(0)) \big] z^{-2}, \qquad |z| > R. \quad \text{(28b)}
$$

It is not difficult to check that the newly introduced function $\boldsymbol{h}(z)$ is analytic in the regions $|z| < R$ and $|z| > R$ and is continuous across the bonded section of the interface. In addition, $\boldsymbol{h}(z) \cong O(z^{-2})$ as $|z| \to \infty$. The traction-free condition on the debonded portion of the interface will yield the nonhomogeneous Riemann–Hilbert problem of vector form as

$$
\begin{aligned}
\overline{\boldsymbol{M}}_* \boldsymbol{h}^+(z) + \boldsymbol{M}_* \boldsymbol{h}^-(z) &= \boldsymbol{v}(z), \quad z \in L_c, \\
\boldsymbol{h}^+(z) - \boldsymbol{h}^-(z) &= \boldsymbol{0}, \qquad z \in L_b.
\end{aligned}
\tag{29}
$$

Here, the superscripts "+" and "−" denote the limiting values as we approach the circular interface from S_1 and S_2 respectively, while the vector $\boldsymbol{v}(z)$ is defined by

$$
\boldsymbol{v}(z) = -2 \overline{\boldsymbol{M}}_* \boldsymbol{M}_*^{-1} \big[\boldsymbol{L}_2^{-1} \boldsymbol{B}_2 \boldsymbol{k} + \boldsymbol{L}_1^{-1} \overline{\boldsymbol{B}}_1 (\boldsymbol{i}_2 \overline{\phi_1'(0)} + \boldsymbol{i}_4 \overline{\Phi_1'(0)}) \big]
$$
$$
+ 2 R^2 \big[\boldsymbol{L}_2^{-1} \overline{\boldsymbol{B}}_2 \overline{\boldsymbol{k}} + \boldsymbol{L}_1^{-1} \boldsymbol{B}_1 (\boldsymbol{i}_2 \phi_1'(0) + \boldsymbol{i}_4 \Phi_1'(0)) \big] z^{-2}. \quad \text{(30)}
$$

In order to solve the nonhomogeneous Riemann–Hilbert problem in equation (29), we consider the eigenvalue problem

$$
\overline{\boldsymbol{M}}_* \boldsymbol{w} = \mathrm{e}^{2\pi\epsilon} \boldsymbol{M}_* \boldsymbol{w}.
\tag{31}
$$

In view of the fact that both Hermitian matrices $\boldsymbol{M}_*$ and $\overline{\boldsymbol{M}}_*$ are positive definite, we can identify four distinct eigenpairs $(\epsilon_1, \boldsymbol{w}_1)$, $(-\epsilon_1, \overline{\boldsymbol{w}}_1)$, $(\epsilon_3, \boldsymbol{w}_3)$, $(-\epsilon_3, \overline{\boldsymbol{w}}_3)$ with ϵ_1, ϵ_3 two real numbers and $\boldsymbol{w}_1$, $\boldsymbol{w}_3$ two complex vectors such that

$$
\overline{\boldsymbol{M}}_* \boldsymbol{w}_1 = \mathrm{e}^{2\pi\epsilon_1} \boldsymbol{M}_* \boldsymbol{w}_1, \quad \overline{\boldsymbol{M}}_* \boldsymbol{w}_3 = \mathrm{e}^{2\pi\epsilon_3} \boldsymbol{M}_* \boldsymbol{w}_3.
\tag{32}
$$

The four eigenvectors are orthogonal in the sense that

$$
\boldsymbol{w}_i^T \boldsymbol{M}_* \boldsymbol{w}_j = \overline{\boldsymbol{w}}_k^T \boldsymbol{M}_* \boldsymbol{w}_l = \boldsymbol{w}_k^T \boldsymbol{M}_* \overline{\boldsymbol{w}}_l = 0, \quad (i, j, k, l = 1, 3 \text{ and } k \neq l).
\tag{33}
$$

The two oscillatory indices ϵ_1 and ϵ_3 are given explicitly by [Wang and Schiavone 2013]:

$$
\epsilon_1 = \frac{1}{2\pi} \ln \frac{1 + \beta_1}{1 - \beta_1}, \quad \epsilon_3 = \frac{1}{2\pi} \ln \frac{1 + \beta_2}{1 - \beta_2},
\tag{34}
$$

where

$$
\beta_1, \beta_2 = \sqrt{\xi} \big(\big[\tfrac{1}{2}(\rho + 1) \big]^{\frac{1}{2}} \pm \big[\tfrac{1}{2}(\rho - 1) \big]^{\frac{1}{2}} \big) > 0,
\tag{35}
$$

with

$$\xi = \sqrt{|\check{\boldsymbol{S}}|} > 0, \quad \rho = -\frac{\operatorname{tr}(\check{\boldsymbol{S}}^2)}{4\sqrt{|\check{\boldsymbol{S}}|}} \geq 1, \tag{36}$$

and

$$\check{\boldsymbol{S}} = (\boldsymbol{L}_1^{-1} + \boldsymbol{L}_2^{-1})^{-1}(\boldsymbol{S}_1 \boldsymbol{L}_1^{-1} - \boldsymbol{S}_2 \boldsymbol{L}_2^{-1}). \tag{37}$$

Furthermore, the two parameters ξ and ρ are found explicitly as

$$\xi = \frac{|Y_{21}Y_{43} - Y_{23}^2|}{Y_{11}Y_{33} - Y_{13}^2}, \quad \rho = \frac{(Y_{11}Y_{43} + Y_{33}Y_{21} - 2Y_{13}Y_{23})^2 - 2(Y_{11}Y_{33} - Y_{13}^2)(Y_{21}Y_{43} - Y_{23}^2)}{2(Y_{11}Y_{33} - Y_{13}^2)|Y_{21}Y_{43} - Y_{23}^2|}. \tag{38}$$

Now $\boldsymbol{h}(z)$ can be represented as a linear combination of the four eigenvectors as

$$\boldsymbol{h}(z) = h_1(z)\boldsymbol{w}_1 + h_2(z)\overline{\boldsymbol{w}}_1 + h_3(z)\boldsymbol{w}_3 + h_4(z)\overline{\boldsymbol{w}}_3. \tag{39}$$

Premultiplying equation $(29)_1$ by $[\overline{\boldsymbol{w}}_1 \ \boldsymbol{w}_1 \ \overline{\boldsymbol{w}}_3 \ \boldsymbol{w}_3]^T$ and using the representation in equation (39) with the orthogonal relations in equation (33), we obtain the decoupled form of the equations as

$$\left.\begin{aligned}
h_1^+(z) + \mathrm{e}^{-2\pi\epsilon_1} h_1^-(z) &= \frac{\overline{\boldsymbol{w}}_1^T \boldsymbol{v}(z)}{\overline{\boldsymbol{w}}_1^T \overline{\boldsymbol{M}}_* \boldsymbol{w}_1}, \\[2mm]
h_2^+(z) + \mathrm{e}^{2\pi\epsilon_1} h_2^-(z) &= \frac{\boldsymbol{w}_1^T \boldsymbol{v}(z)}{\boldsymbol{w}_1^T \overline{\boldsymbol{M}}_* \overline{\boldsymbol{w}}_1}, \\[2mm]
h_3^+(z) + \mathrm{e}^{-2\pi\epsilon_3} h_3^-(z) &= \frac{\overline{\boldsymbol{w}}_3^T \boldsymbol{v}(z)}{\overline{\boldsymbol{w}}_3^T \overline{\boldsymbol{M}}_* \boldsymbol{w}_3}, \\[2mm]
h_4^+(z) + \mathrm{e}^{2\pi\epsilon_3} h_4^-(z) &= \frac{\boldsymbol{w}_3^T \boldsymbol{v}(z)}{\boldsymbol{w}_3^T \overline{\boldsymbol{M}}_* \overline{\boldsymbol{w}}_3},
\end{aligned}\right\} \quad z \in L_c, \tag{40}$$

$$h_j^+(z) - h_j^-(z) = 0, \quad j = 1, 2, 3, 4, \quad z \in L_b.$$

The solutions to the four decoupled nonhomogeneous Riemann–Hilbert problems of scalar form in equation (40) are conveniently given by [Muskhelishvili 1953]:

$$h_1(z) = \frac{1}{\overline{\boldsymbol{w}}_1^T \overline{\boldsymbol{M}}_* \boldsymbol{w}_1} \frac{\chi_1(z)}{2\pi\mathrm{i}} \int_{L_c} \frac{\overline{\boldsymbol{w}}_1^T \boldsymbol{v}(t)\,\mathrm{d}t}{\chi_1^+(t)(t-z)}, \qquad h_3(z) = \frac{1}{\overline{\boldsymbol{w}}_3^T \overline{\boldsymbol{M}}_* \boldsymbol{w}_3} \frac{\chi_3(z)}{2\pi\mathrm{i}} \int_{L_c} \frac{\overline{\boldsymbol{w}}_3^T \boldsymbol{v}(t)\,\mathrm{d}t}{\chi_3^+(t)(t-z)},$$

$$h_2(z) = \frac{1}{\boldsymbol{w}_1^T \overline{\boldsymbol{M}}_* \overline{\boldsymbol{w}}_1} \frac{\chi_2(z)}{2\pi\mathrm{i}} \int_{L_c} \frac{\boldsymbol{w}_1^T \boldsymbol{v}(t)\,\mathrm{d}t}{\chi_2^+(t)(t-z)}, \qquad h_4(z) = \frac{1}{\boldsymbol{w}_3^T \overline{\boldsymbol{M}}_* \overline{\boldsymbol{w}}_3} \frac{\chi_4(z)}{2\pi\mathrm{i}} \int_{L_c} \frac{\boldsymbol{w}_3^T \boldsymbol{v}(t)\,\mathrm{d}t}{\chi_4^+(t)(t-z)}, \tag{41}$$

where

$$\chi_1(z) = (z-a)^{-\frac{1}{2}-\mathrm{i}\epsilon_1}(z-\bar{a})^{-\frac{1}{2}+\mathrm{i}\epsilon_1}, \qquad \chi_3(z) = (z-a)^{-\frac{1}{2}-\mathrm{i}\epsilon_3}(z-\bar{a})^{-\frac{1}{2}+\mathrm{i}\epsilon_3},$$

$$\chi_2(z) = (z-a)^{-\frac{1}{2}+\mathrm{i}\epsilon_1}(z-\bar{a})^{-\frac{1}{2}-\mathrm{i}\epsilon_1}, \qquad \chi_4(z) = (z-a)^{-\frac{1}{2}+\mathrm{i}\epsilon_3}(z-\bar{a})^{-\frac{1}{2}-\mathrm{i}\epsilon_3}. \tag{42}$$

The branch cuts for the Plemelj functions $\chi_1(z)$, $\chi_2(z)$, $\chi_3(z)$ and $\chi_4(z)$ are chosen to be the debonded part of the interface; i.e., $z \in L_c$ such that $\chi_1(z)$, $\chi_2(z)$, $\chi_3(z)$, $\chi_4(z) \cong z^{-1}$ as $|z| \to \infty$. We note here

that the solutions given by equation (41) are unique in view of the fact that $\boldsymbol{h}(z) \cong O(z^{-2})$ as $|z| \to \infty$ (or equivalently $h_j(z) \cong O(z^{-2})$, $j = 1, \ldots, 4$ as $|z| \to \infty$). By evaluating the Cauchy integrals in equation (41) and noting equation (39), we obtain the expression for $\boldsymbol{h}(z)$ as

$$
\boldsymbol{h}(z) = -2 \sum_{j=1}^{4} \frac{\boldsymbol{w}_j \overline{\boldsymbol{w}}_j^T \overline{\boldsymbol{M}}_* \boldsymbol{M}_*^{-1} \left[\boldsymbol{L}_2^{-1} \boldsymbol{B}_2 \boldsymbol{k} + \boldsymbol{L}_1^{-1} \overline{\boldsymbol{B}}_1 (\boldsymbol{i}_2 \overline{\phi_1'(0)} + \boldsymbol{i}_4 \overline{\Phi_1'(0)}) \right]}{\overline{\boldsymbol{w}}_j^T \overline{\boldsymbol{M}}_* \boldsymbol{w}_j (1 + e^{-2\pi\epsilon_j})} \left[1 - \chi_j(z) [z - \operatorname{Re}\{a(1 + 2i\epsilon_j)\}] \right]
$$

$$
+ 2R^2 \sum_{j=1}^{4} \frac{\boldsymbol{w}_j \overline{\boldsymbol{w}}_j^T \left[\boldsymbol{L}_2^{-1} \overline{\boldsymbol{B}}_2 \overline{\boldsymbol{k}} + \boldsymbol{L}_1^{-1} \boldsymbol{B}_1 (\boldsymbol{i}_2 \phi_1'(0) + \boldsymbol{i}_4 \Phi_1'(0)) \right]}{\overline{\boldsymbol{w}}_j^T \overline{\boldsymbol{M}}_* \boldsymbol{w}_j (1 + e^{-2\pi\epsilon_j})} \left[\frac{1}{z^2} - \frac{\chi_j(z)}{\chi_j(0) z^2} + \frac{\chi_j(z) \chi_j'(0)}{[\chi_j(0)]^2 z} \right], \quad (43)
$$

where $\boldsymbol{w}_2 = \overline{\boldsymbol{w}}_1$, $\boldsymbol{w}_4 = \overline{\boldsymbol{w}}_3$, $\epsilon_2 = -\epsilon_1$, $\epsilon_4 = -\epsilon_3$.

There remain two complex constants $\phi'(0)$ and $\Phi'(0)$ to be determined in the expression for $\boldsymbol{h}(z)$. The consistency conditions for $\phi'(0)$ and $\Phi'(0)$ can be derived from equation (28a) as

$$
\phi_1'(0) - R^2 \boldsymbol{i}_1^T \boldsymbol{B}_1^{-1} \sum_{j=1}^{4} \frac{\boldsymbol{w}_j \overline{\boldsymbol{w}}_j^T \left[2[\chi_j'(0)]^2 - \chi_j(0) \chi_j''(0) \right]}{\overline{\boldsymbol{w}}_j^T \overline{\boldsymbol{M}}_* \boldsymbol{w}_j (1 + e^{-2\pi\epsilon_j}) [\chi_j(0)]^2} \boldsymbol{L}_1^{-1} \boldsymbol{B}_1 (\boldsymbol{i}_2 \phi_1'(0) + \boldsymbol{i}_4 \Phi_1'(0))
$$

$$
+ \boldsymbol{i}_1^T \boldsymbol{B}_1^{-1} \left[\boldsymbol{M}_*^{-1} (\overline{\boldsymbol{M}}_2^{-1} - \overline{\boldsymbol{M}}_1^{-1}) + 2 \sum_{j=1}^{4} \frac{\boldsymbol{w}_j \overline{\boldsymbol{w}}_j^T \left[1 + \chi_j(0) \operatorname{Re}\{a(1 + 2i\epsilon_j)\} \right]}{\overline{\boldsymbol{w}}_j^T \overline{\boldsymbol{M}}_* \boldsymbol{w}_j (1 + e^{-2\pi\epsilon_j})} \overline{\boldsymbol{M}}_* \boldsymbol{M}_*^{-1} \boldsymbol{L}_1^{-1} \right]
$$

$$
\times \overline{\boldsymbol{B}}_1 (\boldsymbol{i}_2 \overline{\phi_1'(0)} + \boldsymbol{i}_4 \overline{\Phi_1'(0)})
$$

$$
= 2 \boldsymbol{i}_1^T \boldsymbol{B}_1^{-1} \left[\boldsymbol{I} - \sum_{j=1}^{4} \frac{\boldsymbol{w}_j \overline{\boldsymbol{w}}_j^T \left[1 + \chi_j(0) \operatorname{Re}\{a(1 + 2i\epsilon_j)\} \right]}{\overline{\boldsymbol{w}}_j^T \overline{\boldsymbol{M}}_* \boldsymbol{w}_j (1 + e^{-2\pi\epsilon_j})} \overline{\boldsymbol{M}}_* \right] \boldsymbol{M}_*^{-1} \boldsymbol{L}_2^{-1} \boldsymbol{B}_2 \boldsymbol{k}
$$

$$
+ R^2 \boldsymbol{i}_1^T \boldsymbol{B}_1^{-1} \sum_{j=1}^{4} \frac{\boldsymbol{w}_j \overline{\boldsymbol{w}}_j^T \left[2[\chi_j'(0)]^2 - \chi_j(0) \chi_j''(0) \right]}{\overline{\boldsymbol{w}}_j^T \overline{\boldsymbol{M}}_* \boldsymbol{w}_j (1 + e^{-2\pi\epsilon_j}) [\chi_j(0)]^2} \boldsymbol{L}_2^{-1} \overline{\boldsymbol{B}}_2 \overline{\boldsymbol{k}}, \quad (44)
$$

$$
\Phi_1'(0) - R^2 \boldsymbol{i}_3^T \boldsymbol{B}_1^{-1} \sum_{j=1}^{4} \frac{\boldsymbol{w}_j \overline{\boldsymbol{w}}_j^T \left[2[\chi_j'(0)]^2 - \chi_j(0) \chi_j''(0) \right]}{\overline{\boldsymbol{w}}_j^T \overline{\boldsymbol{M}}_* \boldsymbol{w}_j (1 + e^{-2\pi\epsilon_j}) [\chi_j(0)]^2} \boldsymbol{L}_1^{-1} \boldsymbol{B}_1 (\boldsymbol{i}_2 \phi_1'(0) + \boldsymbol{i}_4 \Phi_1'(0))
$$

$$
+ \boldsymbol{i}_3^T \boldsymbol{B}_1^{-1} \left[\boldsymbol{M}_*^{-1} (\overline{\boldsymbol{M}}_2^{-1} - \overline{\boldsymbol{M}}_1^{-1}) + 2 \sum_{j=1}^{4} \frac{\boldsymbol{w}_j \overline{\boldsymbol{w}}_j^T \left[1 + \chi_j(0) \operatorname{Re}\{a(1 + 2i\epsilon_j)\} \right]}{\overline{\boldsymbol{w}}_j^T \overline{\boldsymbol{M}}_* \boldsymbol{w}_j (1 + e^{-2\pi\epsilon_j})} \overline{\boldsymbol{M}}_* \boldsymbol{M}_*^{-1} \boldsymbol{L}_1^{-1} \right]
$$

$$
\times \overline{\boldsymbol{B}}_1 (\boldsymbol{i}_2 \overline{\phi_1'(0)} + \boldsymbol{i}_4 \overline{\Phi_1'(0)})
$$

$$
= 2 \boldsymbol{i}_3^T \boldsymbol{B}_1^{-1} \left[\boldsymbol{I} - \sum_{j=1}^{4} \frac{\boldsymbol{w}_j \overline{\boldsymbol{w}}_j^T \left[1 + \chi_j(0) \operatorname{Re}\{a(1 + 2i\epsilon_j)\} \right]}{\overline{\boldsymbol{w}}_j^T \overline{\boldsymbol{M}}_* \boldsymbol{w}_j (1 + e^{-2\pi\epsilon_j})} \overline{\boldsymbol{M}}_* \right] \boldsymbol{M}_*^{-1} \boldsymbol{L}_2^{-1} \boldsymbol{B}_2 \boldsymbol{k}
$$

$$
+ R^2 \boldsymbol{i}_3^T \boldsymbol{B}_1^{-1} \sum_{j=1}^{4} \frac{\boldsymbol{w}_j \overline{\boldsymbol{w}}_j^T \left[2[\chi_j'(0)]^2 - \chi_j(0) \chi_j''(0) \right]}{\overline{\boldsymbol{w}}_j^T \overline{\boldsymbol{M}}_* \boldsymbol{w}_j (1 + e^{-2\pi\epsilon_j}) [\chi_j(0)]^2} \boldsymbol{L}_2^{-1} \overline{\boldsymbol{B}}_2 \overline{\boldsymbol{k}}. \quad (45)
$$

The two complex constants $\phi'(0)$ and $\Phi'(0)$ can then be uniquely determined by solving the coupled linear algebraic equations in (44) and (45).

Remark 3. Equations (44) and (45) can be obtained in a straightforward manner by evaluating $\boldsymbol{h}(0)$ from the expression for $\boldsymbol{h}(z)$ in equation (43) and by noting that

$$\boldsymbol{i}_1^T \boldsymbol{B}_1^{-1} \boldsymbol{h}(0) = \boldsymbol{\phi}_1'(0) - \boldsymbol{i}_1^T \boldsymbol{B}_1^{-1} \boldsymbol{M}_*^{-1}\big[(\overline{\boldsymbol{M}}_1^{-1} - \overline{\boldsymbol{M}}_2^{-1})\overline{\boldsymbol{B}}_1(\boldsymbol{i}_2\overline{\boldsymbol{\phi}_1'(0)} + \boldsymbol{i}_4\overline{\Phi_1'(0)}) + 2\boldsymbol{L}_2^{-1}\boldsymbol{B}_2\boldsymbol{k}\big],$$

$$\boldsymbol{i}_3^T \boldsymbol{B}_1^{-1} \boldsymbol{h}(0) = \Phi_1'(0) - \boldsymbol{i}_3^T \boldsymbol{B}_1^{-1} \boldsymbol{M}_*^{-1}\big[(\overline{\boldsymbol{M}}_1^{-1} - \overline{\boldsymbol{M}}_2^{-1})\overline{\boldsymbol{B}}_1(\boldsymbol{i}_2\overline{\boldsymbol{\phi}_1'(0)} + \boldsymbol{i}_4\overline{\Phi_1'(0)}) + 2\boldsymbol{L}_2^{-1}\boldsymbol{B}_2\boldsymbol{k}\big].$$

In addition, $\int \boldsymbol{h}(z)\,\mathrm{d}z$ can also be found exactly as

$$\int \boldsymbol{h}(z)\,\mathrm{d}z = -2\sum_{j=1}^4 \frac{\boldsymbol{w}_j\overline{\boldsymbol{w}}_j^T \overline{\boldsymbol{M}}_* \boldsymbol{M}_*^{-1}\big[\boldsymbol{L}_2^{-1}\boldsymbol{B}_2\boldsymbol{k} + \boldsymbol{L}_1^{-1}\overline{\boldsymbol{B}}_1(\boldsymbol{i}_2\overline{\boldsymbol{\phi}_1'(0)} + \boldsymbol{i}_4\overline{\Phi_1'(0)})\big]}{\overline{\boldsymbol{w}}_j^T \overline{\boldsymbol{M}}_* \boldsymbol{w}_j(1 + \mathrm{e}^{-2\pi\epsilon_j})}\big[z - \mathrm{X}_j(z)\big]$$

$$-2R^2 \sum_{j=1}^4 \frac{\boldsymbol{w}_j\overline{\boldsymbol{w}}_j^T\big[\boldsymbol{L}_2^{-1}\overline{\boldsymbol{B}}_2\overline{\boldsymbol{k}} + \boldsymbol{L}_1^{-1}\boldsymbol{B}_1(\boldsymbol{i}_2\boldsymbol{\phi}_1'(0) + \boldsymbol{i}_4\Phi_1'(0))\big]}{\overline{\boldsymbol{w}}_j^T \overline{\boldsymbol{M}}_* \boldsymbol{w}_j(1 + \mathrm{e}^{-2\pi\epsilon_j})}\Big[\frac{1}{z} - \frac{\mathrm{X}_j(z)}{\mathrm{X}_j(0)z}\Big], \quad (46)$$

where

$$\mathrm{X}_j(z) = (z - a)^{\frac{1}{2} - \mathrm{i}\epsilon_j}(z - \bar{a})^{\frac{1}{2} + \mathrm{i}\epsilon_j}, \quad j = 1, 2, 3, 4. \tag{47}$$

The branch cuts for $\mathrm{X}_j(z)$ are again chosen along the arc crack L_c such that $\mathrm{X}_j(z) \cong z$ as $|z| \to \infty$.

5. The elastic field along the interface

Using equations (43), (46) and (28), we can obtain expressions for the two sets of four analytic functions $\phi_1(z), \psi_1(z), \Phi_1(z), \Psi_1(z)$ and $\phi_2(z), \psi_2(z), \Phi_2(z), \Psi_2(z)$ together with their derivatives defined in the inhomogeneity and in the matrix, respectively. Consequently, we can find the stress resultants, in-plane displacements and slopes everywhere in the inhomogeneity and in the matrix. In particular, the surface membrane shear stress resultant $\widehat{N}_{\theta r}$, surface membrane normal stress resultant $\widehat{N}_{rr}$ and surface bending moment $\widehat{M}_{rr}$ along the bonded portion of the circular interface are given by

$$\boldsymbol{t}_r = [-\widehat{N}_{\theta r} \ \ \widehat{N}_{rr} \ * \ \widehat{M}_{rr}]^T = \boldsymbol{\Omega}(\theta)\boldsymbol{t}, \quad z = R\mathrm{e}^{\mathrm{i}\theta}, \quad -\theta_0 < \theta < \theta_0, \tag{48}$$

where $\boldsymbol{t} = -\mathrm{d}\hat{\boldsymbol{\varphi}}_1/(R\,\mathrm{d}\theta)$ is given explicitly by the expression

$$\boldsymbol{t} = \frac{4}{R}\,\mathrm{Im}\left\{\sum_{j=1}^4 \frac{\mathrm{e}^{2\pi\epsilon_j}\boldsymbol{w}_j\overline{\boldsymbol{w}}_j^T\big[\boldsymbol{L}_2^{-1}\boldsymbol{B}_2\boldsymbol{k} + \boldsymbol{L}_1^{-1}\overline{\boldsymbol{B}}_1(\boldsymbol{i}_2\overline{\boldsymbol{\phi}_1'(0)} + \boldsymbol{i}_4\overline{\Phi_1'(0)})\big]}{\overline{\boldsymbol{w}}_j^T \overline{\boldsymbol{M}}_* \boldsymbol{w}_j} z\chi_j(z)[z - \mathrm{Re}\{a(1 + 2\mathrm{i}\epsilon_j)\}]\right\}, \quad (49)$$

and the 4×4 orthogonal matrix $\boldsymbol{\Omega}(\theta)$ is defined by

$$\boldsymbol{\Omega}(\theta) = \begin{bmatrix} \sin\theta & -\cos\theta & 0 & 0 \\ \cos\theta & \sin\theta & 0 & 0 \\ 0 & 0 & \sin\theta & -\cos\theta \\ 0 & 0 & \cos\theta & \sin\theta \end{bmatrix}. \tag{50}$$

In addition, the jump in the generalized displacement vector across the debonded part of the interface is given by

$$\hat{\boldsymbol{u}}_1 - \hat{\boldsymbol{u}}_2 = 4\,\mathrm{Im}\left\{\sum_{j=1}^4 \frac{\mathrm{e}^{4\pi\epsilon_j}\boldsymbol{M}_*\boldsymbol{w}_j\overline{\boldsymbol{w}}_j^T\big[\boldsymbol{L}_2^{-1}\boldsymbol{B}_2\boldsymbol{k} + \boldsymbol{L}_1^{-1}\overline{\boldsymbol{B}}_1(\boldsymbol{i}_2\overline{\boldsymbol{\phi}_1'(0)} + \boldsymbol{i}_4\overline{\Phi_1'(0)})\big]}{\overline{\boldsymbol{w}}_j^T \overline{\boldsymbol{M}}_* \boldsymbol{w}_j}\mathrm{X}_j^+(z)\right\}, \quad z \in L_c. \tag{51}$$

It is further deduced from equations (48) and (49) that the surface membrane stress resultants and surface bending moment are singularly distributed near the crack tips as

$$t_r = (2\pi r)^{-\frac{1}{2}} \Omega(+\theta_0)[K_1 r^{i\epsilon_1} w_1 + \overline{K}_1 r^{-i\epsilon_1} \overline{w}_1 + K_3 r^{i\epsilon_3} w_3 + \overline{K}_3 r^{-i\epsilon_3} \overline{w}_3], \quad r = |z-a| \to 0, \quad z \in L_b;$$

$$t_r = (2\pi r)^{-\frac{1}{2}} \Omega(-\theta_0)[K_1 r^{i\epsilon_1} w_1 + \overline{K}_1 r^{-i\epsilon_1} \overline{w}_1 + K_3 r^{i\epsilon_3} w_3 + \overline{K}_3 r^{-i\epsilon_3} \overline{w}_3], \quad r = |z-\bar{a}| \to 0, \quad z \in L_b,$$

$$(52)$$

where K_1 and K_3 are two complex intensity factors derived as

$$K_1 = 2(1 + 2i\epsilon_1)(\pi R)^{\frac{1}{2}}(2R)^{-i\epsilon_1}(\sin \theta_0)^{\frac{1}{2} - i\epsilon_1}$$

$$\times \left(\frac{w_1^T e^{\epsilon_1(\pi + \theta_0) - \frac{\theta_0}{2}i}[L_2^{-1} \overline{B}_2 \overline{k} + L_1^{-1} B_1(i_2 \phi_1'(0) + i_4 \Phi_1'(0))]}{\overline{w}_1^T \overline{M}_* w_1} \right.$$

$$\left. + \frac{w_1^T e^{\epsilon_1(\pi - \theta_0) + \frac{\theta_0}{2}i}[L_2^{-1} B_2 k + L_1^{-1} \overline{B}_1(i_2 \overline{\phi_1'(0)} + i_4 \overline{\Phi_1'(0)})]}{\overline{w}_1^T \overline{M}_* w_1} \right),$$

$$K_3 = 2(1 + 2i\epsilon_3)(\pi R)^{\frac{1}{2}}(2R)^{-i\epsilon_3}(\sin \theta_0)^{\frac{1}{2} - i\epsilon_3}$$

$$\times \left(\frac{w_3^T e^{\epsilon_3(\pi + \theta_0) - \frac{\theta_0}{2}i}[L_2^{-1} \overline{B}_2 \overline{k} + L_1^{-1} B_1(i_2 \phi_1'(0) + i_4 \Phi_1'(0))]}{\overline{w}_3^T \overline{M}_* w_3} \right.$$

$$\left. + \frac{w_3^T e^{\epsilon_3(\pi - \theta_0) + \frac{\theta_0}{2}i}[L_2^{-1} B_2 k + L_1^{-1} \overline{B}_1(i_2 \overline{\phi_1'(0)} + i_4 \overline{\Phi_1'(0)})]}{\overline{w}_3^T \overline{M}_* w_3} \right)$$

$$(53)$$

at the upper crack tip $z = a$, and

$$K_1 = -2(1 + 2i\epsilon_1)(\pi R)^{\frac{1}{2}}(2R)^{-i\epsilon_1}(\sin \theta_0)^{\frac{1}{2} - i\epsilon_1}$$

$$\times \left(\frac{\overline{w}_1^T e^{\epsilon_1(\pi - \theta_0) + \frac{\theta_0}{2}i}[L_2^{-1} \overline{B}_2 \overline{k} + L_1^{-1} B_1(i_2 \phi_1'(0) + i_4 \Phi_1'(0))]}{\overline{w}_1^T \overline{M}_* w_1} \right.$$

$$\left. + \frac{\overline{w}_1^T e^{\epsilon_1(\pi + \theta_0) - \frac{\theta_0}{2}i}[L_2^{-1} B_2 k + L_1^{-1} \overline{B}_1(i_2 \overline{\phi_1'(0)} + i_4 \overline{\Phi_1'(0)})]}{\overline{w}_1^T \overline{M}_* w_1} \right),$$

$$K_3 = -2(1 + 2i\epsilon_3)(\pi R)^{\frac{1}{2}}(2R)^{-i\epsilon_3}(\sin \theta_0)^{\frac{1}{2} - i\epsilon_3}$$

$$\times \left(\frac{\overline{w}_3^T e^{\epsilon_3(\pi - \theta_0) + \frac{\theta_0}{2}i}[L_2^{-1} \overline{B}_2 \overline{k} + L_1^{-1} B_1(i_2 \phi_1'(0) + i_4 \Phi_1'(0))]}{\overline{w}_3^T \overline{M}_* w_3} \right.$$

$$\left. + \frac{\overline{w}_3^T e^{\epsilon_3(\pi + \theta_0) - \frac{\theta_0}{2}i}[L_2^{-1} B_2 k + L_1^{-1} \overline{B}_1(i_2 \overline{\phi_1'(0)} + i_4 \overline{\Phi_1'(0)})]}{\overline{w}_3^T \overline{M}_* w_3} \right)$$

$$(54)$$

at the lower crack tip $z = \bar{a}$.

If the crack propagates along the circular interface, the energy release rate can then be conveniently obtained as [Wang and Schiavone 2013]

$$G = \frac{\overline{\boldsymbol{w}}_1^T (\boldsymbol{L}_1^{-1} + \boldsymbol{L}_2^{-1}) \boldsymbol{w}_1 |K_1|^2}{2 \cosh^2 \pi \epsilon_1} + \frac{\overline{\boldsymbol{w}}_3^T (\boldsymbol{L}_1^{-1} + \boldsymbol{L}_2^{-1}) \boldsymbol{w}_3 |K_3|^2}{2 \cosh^2 \pi \epsilon_3}. \tag{55}$$

6. Conclusions

We undertake a rigorous analysis of a challenging problem associated with a circular inhomogeneity partially bonded to an infinite isotropic laminated thin plate subjected to remote uniform membrane stress resultants and bending moments. A novel Stroh-type formalism is used to obtain a closed-form solution by reducing the boundary value problem to a nonhomogeneous Riemann–Hilbert problem of vector form which is solved analytically using a decoupling method and by evaluating the ensuing Cauchy integrals. The stress resultants, in-plane displacements and slopes everywhere in the composite are determined from the resulting analytic functions. The pertinent elastic fields on the circular interface such as the surface membrane shear stress resultant, surface membrane normal stress resultant and surface bending moment along the bonded part of the interface, the jump in the generalized displacement vector across the debonded section of the interface and the complex intensity factors at the two crack tips are all determined explicitly.

Acknowledgements

References

[Beom and Earmme 1998] H. G. Beom and Y. Y. Earmme, "Complex variable method for problems of a laminate composed of multiple isotropic layers", *Int. J. Fract.* **92**:4 (1998), 305–324.

[Cheng and Reddy 2002] Z.-Q. Cheng and J. N. Reddy, "Octet formalism for Kirchhoff anisotropic plates", *Proc. R. Soc. Lond. A* **458**:2022 (2002), 1499–1517.

[Cheng and Reddy 2005] Z.-Q. Cheng and J. N. Reddy, "Structure and properties of the fundamental elastic plate matrix", *Z. Angew. Math. Mech.* **85**:10 (2005), 721–739.

[England 1965] A. H. England, "A crack between dissimilar media", *J. Appl. Mech.* (*ASME*) **32**:2 (1965), 400–402.

[England 1966] A. H. England, "An arc crack around a circular elastic inclusion", *J. Appl. Mech.* (*ASME*) **33**:3 (1966), 637–640.

[Erdogan 1965] F. Erdogan, "Stress distribution in bonded dissimilar materials with cracks", *J. Appl. Mech.* (*ASME*) **32**:2 (1965), 403–410.

[Herrmann 1991] J. M. Herrmann, "The limitations of the model of a crack along the interface of an inclusion in an elastic matrix", *Int. J. Solids Struct.* **28**:8 (1991), 1023–1039.

[Herrmann 1994] J. M. Herrmann, "The displacement field due to an interface crack along an elastic inclusion in a differing elastic matrix", *Acta Mech.* **105**:1 (1994), 207–226.

[Lekhnitskii 1968] S. G. Lekhnitskii, *Anisotropic plates*, 2nd ed., Gordon and Breach, New York, 1968.

[Muskhelishvili 1953] N. I. Muskhelishvili, *Some basic problems of the mathematical theory of elasticity: fundamental equations, plane theory of elasticity, torsion and bending*, P. Noordhoff, Groningen, 1953.

[Perlman and Sih 1967] A. B. Perlman and G. C. Sih, "Elastostatic problems of curvilinear cracks in bonded dissimilar materials", *Int. J. Eng. Sci.* **5**:11 (1967), 845–867.

[Reddy 1997] J. N. Reddy, *Mechanics of laminated composite plates: theory and analysis*, CRC Press, Boca Raton, FL, 1997.

[Rice 1988] J. R. Rice, "Elastic fracture mechanics concepts for interfacial cracks", *J. Appl. Mech.* (*ASME*) **55**:1 (1988), 98–103.

[Rice and Sih 1965] J. R. Rice and G. C. Sih, "Plane problems of cracks in dissimilar media", *J. Appl. Mech.* (*ASME*) **32**:2 (1965), 418–423.

[Sih 1966] G. C. Sih, "Flexural problems of cracks in mixed media", pp. 391–409 in *Proceedings of the 1st International Conference on Fracture* (Sendai, 1965), vol. 1, edited by T. Yokobori et al., Japanese Society for Strength and Fracture of Materials, Sendai, Japan, 1966.

[Sih and Rice 1964] G. C. Sih and J. R. Rice, "The bending of plates in dissimilar materials with cracks", *J. Appl. Mech.* **31**:3 (1964), 477–482.

[Stroh 1958] A. N. Stroh, "Dislocations and cracks in anisotropic elasticity", *Philos. Mag.* (8) **3**:30 (1958), 625–646.

[Stroh 1962] A. N. Stroh, "Steady state problems in anisotropic elasticity", *J. Math. Phys.* (*MIT*) **41** (1962), 77–103.

[Suo 1989] Z. Suo, "Singularities interacting with interfaces and cracks", *Int. J. Solids Struct.* **25**:10 (1989), 1133–1142.

[Timoshenko and Woinowsky-Krieger 1959] S. P. Timoshenko and S. Woinowsky-Krieger, *Theory of plates and shells*, 2nd ed., McGraw-Hill, New York, 1959.

[Ting 1996] T. C. T. Ting, *Anisotropic elasticity: theory and applications*, Oxford Engineering Science Series **45**, Oxford University Press, New York, 1996.

[Toya 1974] M. Toya, "A crack along the interface of a circular inclusion embedded in an infinite solid", *J. Mech. Phys. Solids* **22**:5 (1974), 325–348.

[Wang and Schiavone 2013] X. Wang and P. Schiavone, "Interface cracks in Kirchhoff anisotropic thin plates of dissimilar materials", *J. Appl. Mech.* (*ASME*) **80**:4 (2013), art. id. 041025, 4 pp.

[Wang and Zhou 2014a] X. Wang and K. Zhou, "Green's functions for infinite and semi-infinite isotropic laminated plates", *Int. J. Mech. Sci.* **80** (2014), 169–174.

[Wang and Zhou 2014b] X. Wang and K. Zhou, "An inclusion of arbitrary shape in an infinite or semi-infinite isotropic multilayered plate", *Int. J. Appl. Mech.* **6**:1 (2014), art. id. 1450001, 21 pp.

[Williams 1959] M. L. Williams, "The stresses around a fault or crack in dissimilar media", *Bull. Seismol. Soc. Am.* **49** (1959), 199–204.

XU WANG: xuwang@ecust.edu.cn
School of Mechanical and Power Engineering, East China University of Science and Technology, 130 Meilong Road, Shanghai, 200237, China

CUIYING WANG: cuiyingwang@126.com
School of Mechanical and Power Engineering, East China University of Science and Technology, 130 Meilong Road, Shanghai, 200237, China

PETER SCHIAVONE: p.schiavone@ualberta.ca
Department of Mechanical Engineering, University of Alberta, 10-203 Donadeo Innovation Center for Engineering, 9211-116 Street NW, Edmonton AB T6G 1H9, Canada

∎msp

HIERARCHICAL MULTISCALE MODELING OF THE EFFECT OF CARBON NANOTUBE DAMAGE ON THE ELASTIC PROPERTIES OF POLYMER NANOCOMPOSITES

G. Domínguez-Rodríguez, A. K. Chaurasia, G. D. Seidel, A. Tapia and F. Avilés

The influence of various levels of carbon nanotube (CNT) structural damage on the transversely isotropic elastic properties of CNTs and CNT/polymer composites is investigated through a hierarchical multiscale modeling strategy. Assessment of the effect of structural damage on the CNTs is first conducted by removing C-C bonds and using atomistic finite element analysis. The composite cylinder method is then used to model composites whose effective properties are obtained from the Mori–Tanaka method. The axial, radial, transverse shear and in-plane shear moduli of CNTs decrease $\sim$ 70% for 10% damage. This decrease is more pronounced for CNTs with small radii, and when the broken bonds coalesce. The transverse Poisson's ratio of CNTs increases about six times for 10% damage. When these defective CNTs are used in polymer composites, the axial elastic modulus of the composite reduces by $\sim$80% while the transverse Poisson's ratio increases about three times.

1. Introduction

The engineering applications of carbon nanotube (CNT) reinforced polymers are numerous [De Volder et al. 2013]. It is well-known that adding small quantities of CNTs can enhance the mechanical and electrical properties of their host polymer, creating multifunctional materials [Gates et al. 2005; Fukushima et al. 2006; Spitalsky et al. 2010]. The transportation and aerospace industries are examples of potential users, where low density, high strength, and multifunctionality are important for service and design.

Different forms of structural damage have been reported for CNTs and other sp^2/sp^3 carbon-based nanostructures. Structural defects are commonly generated during the CNT synthesis, or by postsynthesis treatments such as electron/ion irradiation or chemical methods [Balog et al. 2010; Banhart 1999; Banhart et al. 2011; Kim et al. 2009; Krasheninnikov and Banhart 2007; Lucchese et al. 2010]. A common kind of topological CNT defect is the one frequently called "Stone–Wales" defect (although it has been suggested that a "Thrower" defect is a more proper name [Monthioux and Charlier 2014]), where two carbon atoms rotate to transform four hexagons into two heptagons and two pentagons [Araujo et al. 2012; Banhart et al. 2011]; see Figure 1, left. A second kind of defect are vacancies, i.e., places where an atom is missing; vacancies can be single (Figure 1, center) or formed by more than one missing atom (Figure 1, right).

Defects are associated with a degradation of mechanical properties of CNTs [Shet et al. 2005], with vacancies being more influential than Thrower-type defects [Sammalkorpi et al. 2004; Zandiatashbar et al. 2014]. According to Talukdar and Mitra [2010] and Sharma et al. [2012], a Thrower defect can reduce the axial elastic modulus of a singlewall CNT (SWCNT) up to 6%. In contrast, molecular dynamics
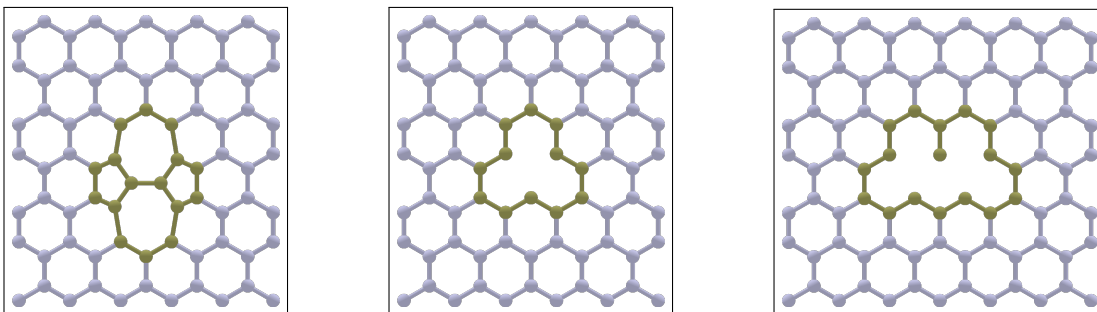
Figure 1. Different kinds of topological defects present in carbon nanostructures: left, Thrower defect; center, single vacancy; right, double vacancy.

simulations predict a reduction of about 10% in the elastic modulus for a concentration of vacancies of 2.5% [Fefey et al. 2011] and about 40% for a concentration of vacancies of 8%[Yuan and Liew 2009]. Mielke et al. [2004] and Tserpes et al. [2007] showed that Thrower defects and vacancies are important causes of tensile fracture.

Structural defects such as vacancies are able to rearrange their topology to minimize their formation energy [Yuan and Liew 2009; Berber and Oshiyama 2006]. During this rearrangement, new bonds are formed and others broken. Some defects, such as Thrower-type, do not reduce the number of bonds, while others, such as vacancies, reduce the number of bonds by two or three bonds, with a corresponding energy reconfiguration [Mielke et al. 2004; Tserpes and Papanikos 2007]. Modeling the dynamic rearrangement process after bond elimination is a complex task which demands dedicated *ab initio* computations [Gallo et al. 2007; Prasomsri et al. 2010; Ahangari et al. 2013] that are very limited in size. Traditional density functional theory computations are in the range of a few hundreds of atoms and can only reach thousands for clusters with hundreds of cores [Kohn 1995; Fonseca Guerra et al. 1998; Hine et al. 2009]. An alternative approach to tackle this problem is by finite element analysis (FEA). Although FEA does not account for quantum effects needed to predict the rearrangement of structural defects after relaxation, within the Newtonian mechanics framework FEA is a versatile and accurate tool to efficiently predict elastic properties of nanostructures [Giannopoulos et al. 2013; Haghbin and Khalili 2014; Domínguez-Rodríguez et al. 2014]. To date, bridging scales to predict elastic properties of polymer composites seems to be plausible only by using classical mechanics modeling tools. Continuous homogenization models have been previously conducted for macroscopic lattices in order to simplify the prediction of the mechanical properties of beam structures [Noor et al. 1978; Sun et al. 1981; Noor 1988; Dow and Huyer 1989; Sun and Liebbe 1990; Usik 1994]; more recently they have also been applied to nanostructures such as graphene sheets and CNTs [Odegard et al. 2002; Blanc et al. 2002; Caillerie et al. 2006]. In the present work, a hierarchical multiscale modeling approach is undertaken, wherein FEA is used at the smallest scale to predict the (transversely isotropic) elastic properties of SWCNTs. In order to damage the CNTs, carbon-carbon (C-C) bonds are sequentially eliminated. Two approaches for bond elimination are used. In the first one, bonds are randomly broken without consideration of the previous damage state; in the second one, the sequential bond breaking process is conducted only at adjacent bonds, simulating clustering damage. These properties are then used as an input to compute the influence of such CNT structural defects on the elastic properties of SWCNT/polymer composites, using classical

micromechanics theories. The composite cylinder method [Hashin and Rosen 1964] is then used to model the elastic properties of a CNT/polymer composite using the local orientation scale and including an interphase, whereas the Mori–Tanaka (MT) method [1973] is used to predict the elastic properties of composites including CNTs with multiple orientations, chiralities, and damage severity.

2. Methodology

2.1. *Elastic properties of a transversely isotropic CNT.* CNTs can be treated as transverse isotropic materials, which means that five independent elastic properties are needed to construct their stiffness tensor. The five independent elastic properties chosen for investigation in the current work are the axial elastic modulus (E_{11}), the in-plane bulk modulus (K_{23}), the transverse Poisson's ratio (v_{12}), the transverse shear modulus (μ_{12}) and the in-plane shear modulus (μ_{23}). Here, 1, 2 and 3 represent the axial, radial and angular directions of the local material coordinates of the CNT, respectively, whereas x, y, and z are the orthogonal axes of the global Cartesian coordinates as shown in Figure 2. Here, r is the radial position and θ is the angle between the axes x and 2. The CNT stiffness tensor is defined by [Qu and Cherkaoui 2006]

$$C_{ij} = \begin{pmatrix} C_{11} & C_{12} & C_{12} & 0 & 0 & 0 \\ C_{12} & C_{22} & C_{23} & 0 & 0 & 0 \\ C_{12} & C_{23} & C_{22} & 0 & 0 & 0 \\ 0 & 0 & 0 & \mu_{23} & 0 & 0 \\ 0 & 0 & 0 & 0 & \mu_{12} & 0 \\ 0 & 0 & 0 & 0 & 0 & \mu_{12} \end{pmatrix}, \tag{1}$$

where $C_{11} = E_{11} + 4v_{12}^2 K_{23}$ and $C_{12} = 2v_{12}K_{23}$ and $C_{22} = K_{23} + \mu_{23}$ and $C_{23} = K_{23} - \mu_{23}$.

The definition of the transverse Poisson's ratio for defective CNTs may be ambiguous, since structural defects produce localized perturbations in the displacement field that can differ greatly from the free transverse contraction. Therefore, the axial component of the stiffness tensor (C_{11}) was obtained from
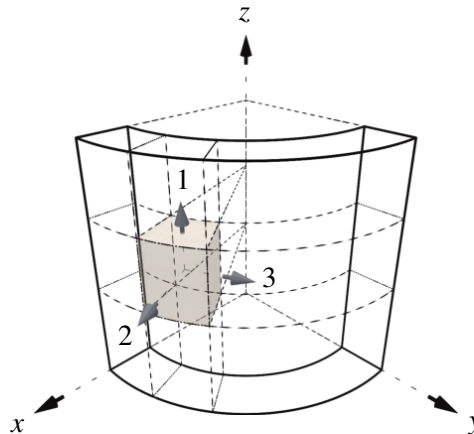

Figure 2. Material coordinates used in this work.

an energy balance and is used here to predict the transverse Poisson's ratio as

$$\nu_{12} = \sqrt{\frac{C_{11} - E_{11}}{4K_{23}}}. \tag{2}$$

The radial elastic modulus (E_{22}) was obtained from the axial elastic modulus (E_{11}), the transverse Poisson's ratio (ν_{12}), the in-plane bulk (K_{23}), and shear moduli (μ_{23}) as

$$E_{22} = \frac{4K_{23}\mu_{23}}{K_{23} + \mu_{23} + 4\nu_{12}^2 K_{23}\mu_{23}/E_{11}}. \tag{3}$$

2.2. *Finite element analysis of defective CNTs.* The atomistic FEA proposed by Li and Chou [2003b] was used here to predict the elastic properties of CNTs. In this method, the atoms are considered as nodes and the C-C bonds are modeled as solid beams with a circular cross section, whose elastic modulus (E_{beam}) and shear modulus (G_{beam}) are obtained from an equivalence between the structural deformation energies and the molecular mechanics potentials associated with tension, bending, and torsion of the atomic bonds. The selection of the beam's cross-section does not affect the calculations as long as the area and moment of inertia are preserved [Li and Chou 2003b]. Each type of bond deformation is associated with a bond force constant, representing tension (k_T), bending (k_B), and torsion (k_τ) [Li and Chou 2003b]. The elastic and geometric properties of the beams that model the C-C bonds are defined as [Li and Chou 2003b; Sakhaee-Pour 2009]

$$d_{\text{beam}} = 4\sqrt{\frac{k_B}{k_T}}, \quad E_{\text{beam}} = \frac{k_T^2 L_{\text{beam}}}{4\pi k_B}, \quad G_{\text{beam}} = \frac{k_T^2 k_\tau L_{\text{beam}}}{8\pi k_B^2}, \tag{4}$$

where d_{beam} is the beam's diameter, E_{beam} is the beam's elastic modulus, G_{beam} its shear modulus, and L_{beam} is the C-C bond length. Following the recommendations of Li and Chou [2003b], a C-C bond length of $L_{\text{beam}} = 0.142$ nm and bond force constants of $k_T = 6.52 \cdot 10^{-7}$ N·nm^{-1} and $k_B = 8.76 \cdot 10^{-10}$ N·nm^{-1}·rad^2 and $k_\tau = 2.78 \cdot 10^{-10}$ N·nm^{-1}·rad^2 were employed, as reported by Cornell et al. [1995] and Jorgensen and Severance [1990] for benzene.

The numerical solution was conducted through the commercial code ANSYS 13.0, using the "BEAM4" element which allows bending, torsion, axial compression, and tension.

Following the method of Li and Chou [2003b], nonbonded interactions such as van der Waals forces are neglected, given their significantly lower contribution when compared to covalent interactions, especially for SWCNTs [Li and Chou 2003a; Kalamkarov et al. 2006]. However, it is important to notice that van der Waals forces might be relevant for interactions between layers for the case of multiwall CNTs [Li and Chou 2003a].

Armchair SWCNTs of different chiralities were considered ranging from (3,3) (with a radius of $R \approx$ 0.2 nm) to (10,10) ($R \approx 0.7$ nm), containing a total number of 200 unit cells of height $H = 2.46$ Å (see Figure 3) for a total CNT length of $L = 49.2$ nm. This length, albeit short, keeps the problem computationally tractable and was proven to yield mechanical properties which are independent of the CNT length in a previous analysis [Domínguez-Rodríguez et al. 2014]. An equivalent wall thickness of $t = 3.4$ Å was considered for homogenization purposes, which is equivalent to the interlayer distance between graphene sheets [Ferrari and Basko 2013; Gao et al. 2008; Ni et al. 2007; Blake et al. 2007;
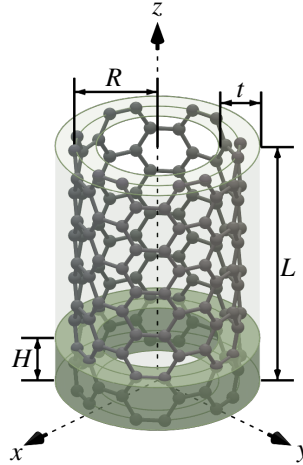
Figure 3. Geometric parameters of a representative SWCNT.

Burnett et al. 2012; Novoselov et al. 2005; Obraztsova et al. 2008]; see Figure 3. The selection of other wall thicknesses may significantly change the elastic properties of CNTs when homogenized as a hollow cylinder [Demczyk et al. 2002; Zhang et al. 2002; Srivastava et al. 2003; Natsuki et al. 2004; Tserpes and Papanikos 2005]. However, if homogenized as an effective solid cylinder, the values of the effective CNT properties would change marginally with the wall thickness.

2.2.1. *Loading cases.* The five loading cases depicted in Figure 4 were chosen in order to calculate the five independent elastic properties of the SWCNT considered as a transversely isotropic material. The total strain energy was computed for each loading case and the corresponding elastic property was obtained through an energy balance, to be further discussed. Specific boundary conditions for each loading case were imposed by applying linear equations representing the constraints on the displacement field as functions of the radial (u_r), angular (u_θ), and axial (u_z) displacement fields. The applied strain (ϵ_r, $\epsilon_{r\theta}$, ϵ_{zr} or ϵ_z) was set to 0.02, although the resulting elastic properties are independent of this input value.

In order to obtain the axial elastic modulus of the CNT (E_{11}^{CNT}), an axial (z) strain ($\epsilon_z = 0.02$) was applied through a displacement field $u_z = \epsilon_z L$ at the atoms located at the top edge of the CNT ($z = L$), whereas all degrees of freedom were restricted at the bottom edge ($z = 0$) of the SWCNT ($u_r|_{z=0} = u_z|_{z=0} = u_\theta|_{z=0} = 0$); see Figure 4a. The rest of the atoms were allowed to move freely in this loading case.

For simulation of the radial expansion to determine K_{23}^{CNT}, the top and bottom atoms were restricted to prevent contraction or expansion along the axial direction ($u_z|_{z=0} = u_z|_{z=L} = 0$), and a radial displacement $u_r = r\epsilon_r$ was applied to all of the nodes; see Figure 4b.

In order to obtain C_{11}^{CNT}, an axial strain (ϵ_z) was applied through a displacement $u_z = \epsilon_z L$ at the top edge atoms ($z = L$), whereas u_z was set to zero at the bottom edge atoms ($z = 0$). Displacements u_r and u_θ were restricted for all atoms in this loading case, as shown in Figure 4c.

For defective CNTs, the conventional definition of the transverse Poisson's ratio (ν_{12}^{CNT}) extracted directly from the transverse contraction of the axial strain loading case (Figure 4a) may be ambiguous, given the excessive localized transverse deformation in the vicinity of the defect. Thus, ν_{12}^{CNT} was calculated here from a combination of E_{11}^{CNT}, C_{11}^{CNT} and K_{23}^{CNT} as stated in (2).
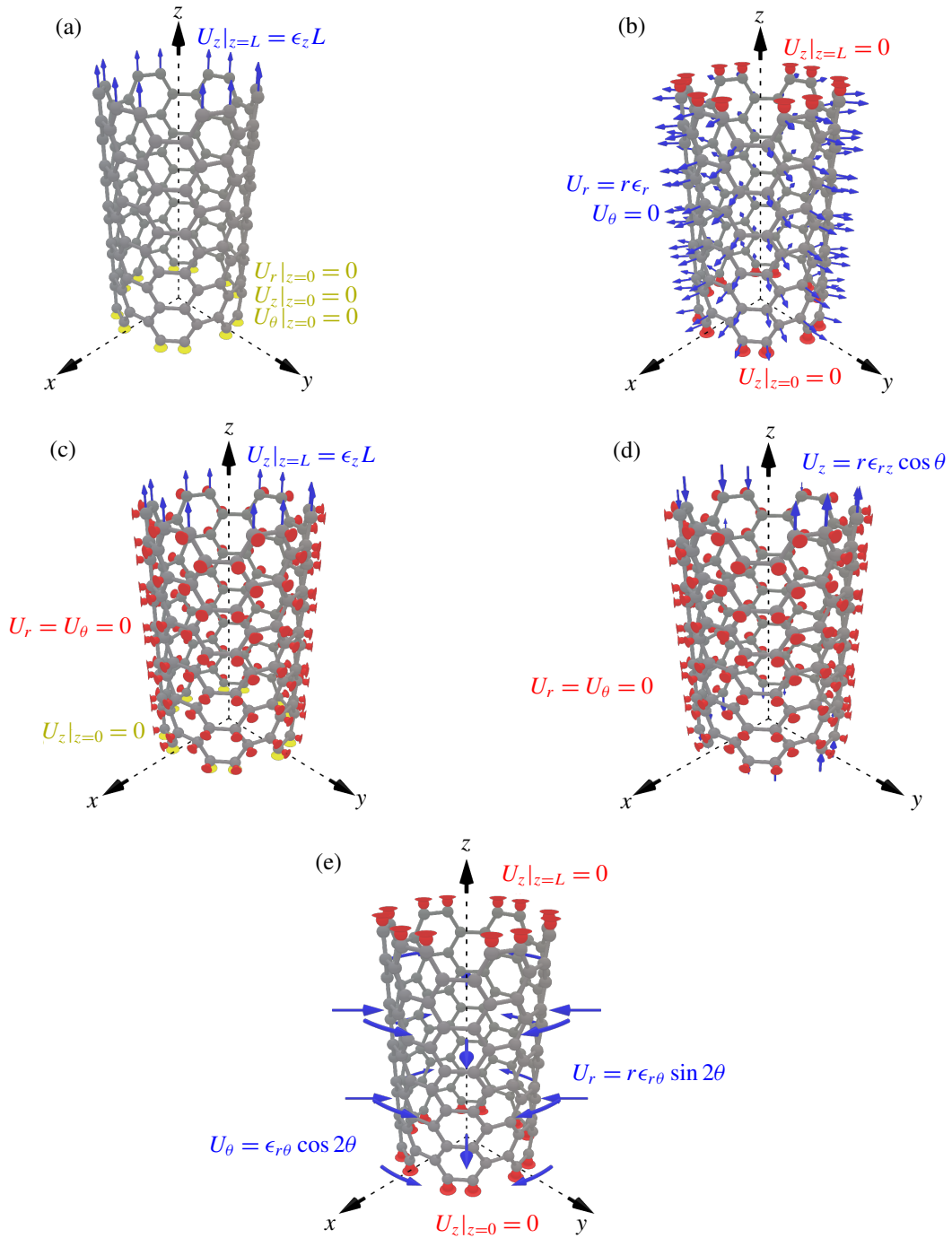
Figure 4. Loading cases used in FEA to determine the five independent elastic constants of the SWCNT: a, axial strain (E_{11}^{CNT}); b, radial expansion (K_{23}^{CNT}); c, axial strain with radial restriction (C_{11}^{CNT}, ν_{12}^{CNT}); d, transverse shear strain (μ_{12}^{CNT}); and e, in-plane shear strain (μ_{23}^{CNT}).

The transverse shear modulus (μ_{12}^{CNT}) was determined by applying a transverse shear strain (ϵ_{rz}) modeled as a nonuniform displacement field $u_z = r\epsilon_{rz}\cos(\theta)$ for all atoms, while u_r and u_θ were restricted to zero for all nodes to prevent contraction and rotation of the CNT; see Figure 4d.

Finally, to compute the in-plane shear modulus (μ_{23}^{CNT}), nonuniform radial and tangential displacement fields of magnitude $u_r = r\epsilon_{r\theta}\sin(2\theta)$ and $u_\theta = \epsilon_{r\theta}\cos(2\theta)$ were applied, whereas the top and bottom atoms were restricted to prevent contraction or expansion along the axial direction ($u_z|_{z=0} = u_z|_{z=L} = 0$); see Figure 4e. This loading case simulates the application of an in-plane (xy) shear strain.

2.2.2. *Energy balance.* In order to obtain the elastic properties of the investigated SWCNTs, the strain energy of the CNT's structural model was set equal to the strain energy of a solid cylinder under the same boundary conditions [Hashin and Rosen 1964], i.e.,

$$\frac{1}{V_C}\sum_{n=1}^{N} E_n^{(B)} = \frac{1}{2V_C}\int_0^L\int_0^{2\pi}\int_0^{R+t/2} (\boldsymbol{\sigma}:\boldsymbol{\epsilon})r\,\partial r\,\partial\theta\,\partial z, \tag{5a}$$

where $E_n^{(B)}$ is the total strain energy of the n-th C-C beam, N is the number of beams (or C-C bonds), V_C is the volume of the CNT considered as a solid cylinder (to avoid interdependency among the five elastic properties) and : represents the Frobenius inner product defined for dyadics [Meyer 2000].

Since the strains are not functions of z and $V_C = \pi\left(R + \frac{1}{2}t\right)^2 L$, (5a) becomes

$$\frac{1}{L}\sum_{n=1}^{N} E_n^{(B)} = \frac{1}{2}\int_0^{2\pi}\int_0^{R+t/2} (\boldsymbol{\sigma}:\boldsymbol{\epsilon})r\,\partial r\,\partial\theta. \tag{5b}$$

The evaluation of (5b) provides three linear equations for E_{11}^{CNT} and C_{11}^{CNT} and μ_{12}^{CNT} and a set of two linear algebraic equations whose solution yields μ_{23}^{CNT} and K_{23}^{CNT}. Because of the CNT central hollow area, (5b) shows a dependency of R and t on the CNT elastic properties. All five independent elastic properties are used to construct the stiffness tensor listed in (1).

2.2.3. *Damage generation.* The approach used here to simulate structural defects was to sequentially eliminate C-C bonds. Two configurations were investigated depending on the sequence of bond elimination followed, viz. randomly generated damage (Figure 5, top) or clustered damage (Figure 5, bottom). Since each carbon atom has three bonds, breakage of the three bonds may be considered as a vacancy in terms of missing bonds. In the random evolution scenario, the bonds are removed by generating random numbers following a uniform distribution of probability from 0 to 1. The bond is deemed broken if the randomly generated number is lower than the fraction of broken bonds to be simulated (broken bonds/total number of bonds). Due to the random nature of the process, the computations were repeated numerous times and the results averaged, reporting the average value of the computed elastic property. A dedicated convergence analysis showed that 40 repetitions yielded differences less than 0.2% for all elastic properties and damage states with respect to results with 80 of repetitions; thus 40 iterations was deemed convergent.

CNT damage was also modeled following a clustering pattern. In this approach, the first broken bond was randomly generated, and the following broken bonds were restricted to be chosen from the neighbors of the already broken bonds, generating clustered damage (Figure 5, bottom). The clustering pattern produces coalescence of CNT damage and is expected to severely affect the SWCNT properties;
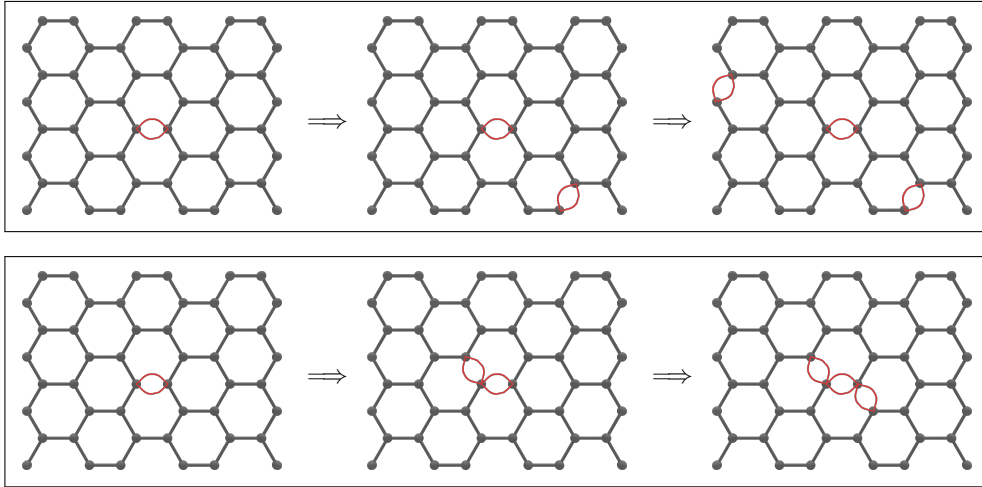
Figure 5. Schematic representation of the two cases of damage evolution investigated: top, random; bottom, clustered.

see, e.g., [Sammalkorpi et al. 2004]. Therefore, even when quantum bond reconstruction is not addressed in our classical mechanics approach, the clustered damage is expected to represent an upper bound for the same fraction of broken bonds.

2.3. *Prediction of the elastic properties of axially oriented CNT/polymer composites.*

2.3.1. *Composite cylinder method.* The composite cylinder method (CCM), initially proposed by Hashin and Rosen [1964], was used to predict the elastic properties of composite materials represented by concentric cylindrical layers. In the CCM, each layer (numbered from 1 to N) represents a phase with its own elastic properties, schematically represented as C^i for illustration purposes in Figure 6. The CCM method was employed here to predict the elastic properties of perfectly oriented polymer composites containing CNTs, including an interphase, whose stiffness tensor varies as a piecewise constant from that of the CNT (C^{CNT}) to the one of the matrix (C^m) [Hernández-Pérez and Avilés 2010]; see Figure 6. The stiffness tensor of the CNT was obtained from the energy balance between the strain energies of the CNT structure and the solid cylinder; see (5). The interface between two adjacent interphases is considered perfect, i.e., the stress tensor transfers from one layer to the other without loss. The number of interphase layers was set to 5. While a higher number of interphase layers may increase precision, it also increases the computational burden and more than 5 interphase layers was not deemed necessary in this work, provided a proper convergence analysis. The center (first phase) represents the CNT (including the central hollow region), whose stiffness tensor was previously homogenized by using the strain energy of the CNT, while the outermost phase (N-th phase) represents the matrix; all phases in between (from 2 to $N-1$) correspond to different layers modeling the interphase; see Figure 6. The matrix was considered to be an isotropic material with an elastic modulus of 1 GPa and a Poisson's ratio of 0.35, simulating a typical engineering polymer [Fink 2010; Mittal 2011]. In order to model different CNT volume fractions in a composite, the thickness of the outermost phase was varied. The first phase (CNT) starts at $r = 0$ and ends at $r = R + \frac{1}{2}t$, which represents the interface with the first layer of interphase. The last layer
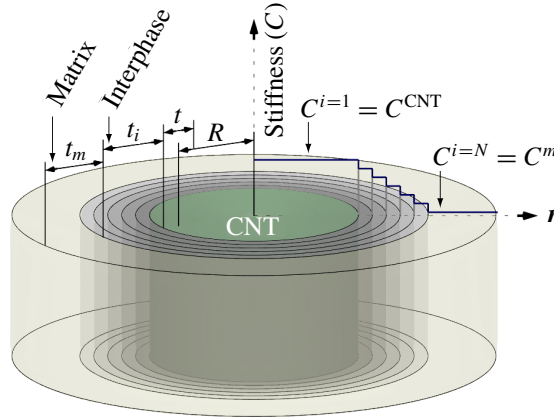
Figure 6. Schematic of the composite cylinder model.

of the interphase $(N - 1)$ ends at $r = r_{N-1} = R + \frac{1}{2}t + t_i$, where t_i is the i-th interphase thickness. The thickness of the CNT/matrix interphase was set equal to the SWCNT wall thickness $(t_i = t)$ as suggested in [Hernández-Pérez and Avilés 2010]. Finally, the matrix ends at $r = r_N = R + \frac{1}{2}t + t_i + t_m$, where t_m is the matrix thickness.

Since all phases have the same length and axial direction, the volume fraction of the CNT/polymer composite (v_f) is calculated as

$$v_f = \left[\frac{R + \frac{1}{2}t}{R + \frac{1}{2}t + t_i + t_m} \right]^2. \tag{6}$$

The maximum volume fraction available for each CNT $(v_{f\,\text{max}})$ is obtained when $t_m = 0$, i.e.,

$$v_{f\,\text{max}} = \left[\frac{R + \frac{1}{2}t}{R + \frac{1}{2}t + t_i} \right]^2. \tag{7}$$

The CCM was conducted for each armchair CNT chirality discussed in Section 2.2 — (3, 3) to (10, 10) — as well as for the two scenarios of damage generation depicted in Figure 5.

2.3.2. *Loading cases.* Four loading cases were used to obtain the five independent transversely isotropic elastic properties of CNT/polymer composites containing defective CNTs. These loading cases are similar to those depicted in Figure 4 for the CNTs, but for the continuous composites E_{11} and v_{12} were extracted directly from the axial strain loading case. The four loading cases used to compute the elastic properties of the axially oriented CNT/polymer composites by the CCM are illustrated in Figure 7.

Figure 7a shows the loading case used to calculate the axial elastic modulus (E_{11}) and transverse Poisson's ratio (v_{12}) of the composites. An axial displacement is applied and radial contraction is allowed. Detailed information about the system of equations for the boundary conditions, continuity, and displacement fields is included in Section A.1 of the Appendix. Once the system of equations is solved, the axial elastic modulus, E_{11}, is obtained as

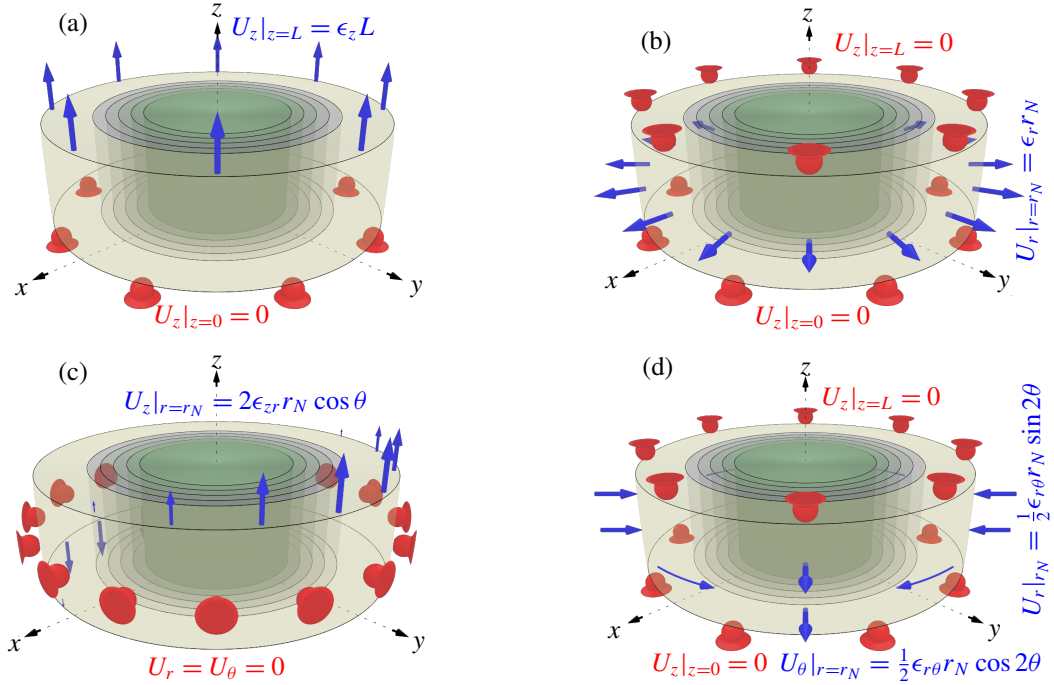$$E_{11} = \bar{\sigma}_{11}/\bar{\epsilon}_{11}, \tag{8}$$

Figure 7. Loading cases used in the composite cylinder method: a, axial strain; b, in-plane bulk strain; c, transverse shear strain; and d, in-plane shear strain.

where $\bar{\sigma}_{11}$ and $\bar{\epsilon}_{11}$ are volumetric averages of the axial stress (σ_{11}) and axial strain (ϵ_{11}). The Poisson's ratio is calculated as

$$\nu_{12} = -\bar{\epsilon}_{22}/\bar{\epsilon}_{11}, \tag{9}$$

where $\bar{\epsilon}_{22}$ is the volumetric averaged radial strain which is equal to the radial strain at the outer surface ($r = r_N$).

Figure 7b shows the loading case used to calculate the in-plane bulk modulus of the composite (K_{23}). The axial displacements are restricted at $z = 0$ and $z = L$ and a radial displacement is applied at $r = r_N$. The system of equations stated in Section A.2 of the Appendix is solved and the in-plane bulk modulus is obtained as

$$K_{23} = \bar{\sigma}_{22}/2\bar{\epsilon}_{22}, \tag{10}$$

where $\bar{\sigma}_{22}$ and $\bar{\epsilon}_{22}$ are volumetric averages of the radial stress (σ_{22}) and the radial strain (ϵ_{22}).

Figure 7c shows the loading case used to calculate the transverse shear modulus of the composite (μ_{12}). For this loading case, all radial and tangential displacements are restricted and a transverse shear strain is produced by applying an axial displacement at $r = r_N$ as a function of θ. Analytical expressions for modeling such displacement conditions are presented in Section A.3 of the Appendix. The transverse shear modulus is then obtained from statement of equivalent surface tractions between the composite cylinder assemblage and the effective homogeneous cylinder, i.e.,

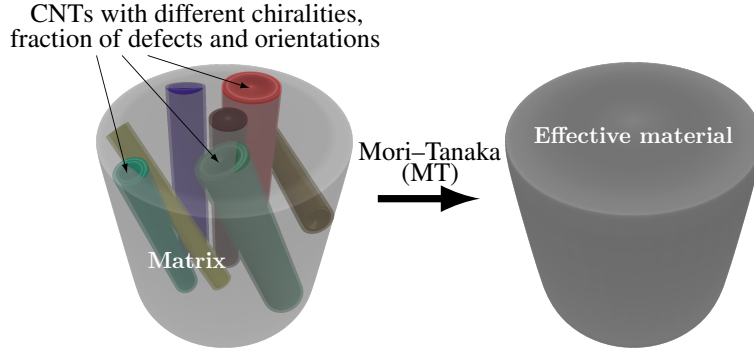$$\mu_{12}^N \epsilon_{12}^N|_{r=r_N} = \mu_{12}\epsilon_{12}|_{r=r_N}, \tag{11}$$

Figure 8. Mori–Tanaka approach for CNT/polymer composites.

where μ_{12}^N and ϵ_{12}^N are the transverse shear modulus and strain of the N-th phase, and μ_{12} and ϵ_{12} are the transverse shear modulus and strain of the effective homogeneous cylinder.

Figure 7c shows the loading case used to calculate the in-plane shear modulus of the composite (μ_{23}). Following Seidel and Lagoudas' methodology [2006], the generalized self-consistent composite cylinder method is employed to obtain the in-plane shear modulus (μ_{23}). This method is different from the conventional CCM because μ_{23} is not calculated by using its definition once the strains are obtained, but μ_{23} is explicitly included as an additional variable in the system of equations; see Section A.4 of the Appendix.

2.4. *Mori–Tanaka approach for CNT/polymer composites.* The Mori-Tanaka (MT) method allows for the prediction of elastic properties of a composite material constituted by different phases, each of them with its own geometry and material properties [Mori and Tanaka 1973]. The MT method is used here to predict the stiffness tensor of a CNT/polymer composite containing CNTs with different chiralities, fractions of broken bonds, and orientations; see Figure 8. The elastic properties of each phase are obtained from the CCM calculations in order to include the interphase.

In the MT method, the stiffness tensor (C) of the composite material is obtained as [Mori and Tanaka 1973]

$$C = \left(v_m C_m A_m + \sum_{i=1}^N v_i C_i A_i \right) \cdot \left(v_m I + \sum_{i=1}^N v_i A_i \right)^{-1}, \tag{12}$$

where I is the identity tensor (in Voigt's notation), C_m is the stiffness tensor of the polymer matrix, C_i is the stiffness tensor of the i-th phase, v_m is the volume fraction of the matrix phase, v_i is the volume fraction of the i-th phase, N is the total number of phases, A_i is the dilute strain concentration tensor for the i-th phase, transferring the strain applied on the composite to the coordinate system of each embedded phase. There are different ways to obtain A_i, one of those is by using an Eshelby [1957; 1959] tensor. Herein, the tensors are solved as matrices using Voigt's notation. Using an Eshelby tensor and an energetic equivalence between an inclusion with residual stresses and the phase to be modeled, the dilute strain concentration tensor for the i-th phase is [Lagoudas et al. 1991]

$$A_i = [I + S_i C_m^{-1}(C_i - C_m)]^{-1}, \tag{13}$$

where S_i is the Eshelby tensor for the i-th phase assumed as a cylindrical inclusion.

In order to compute the stiffness tensor of composites reinforced with randomly oriented CNTs, a rotational transformation is applied to both the strain concentration tensor and the stiffness matrix of each phase. The rotational transformations applied are of the form

$$X^* = \tilde{Q} \cdot X \cdot \tilde{Q}^T, \tag{14}$$

where X is the tensor (Voigt's notation) to be rotated and $\tilde{Q}$ is a 6×6 matrix constructed from $Q = Q(\theta, \phi)$, which is a 3×3 rotation matrix defined by

$$Q(\theta, \phi) = \begin{pmatrix} \cos(\theta)\sin(\phi) & \sin(\theta)\sin(\phi) & \cos(\phi) \\ -\sin(\theta) & \cos(\theta) & 0 \\ -\cos(\theta)\cos(\phi) & -\sin(\theta)\cos(\phi) & \sin(\phi) \end{pmatrix}, \tag{15}$$

where θ and ϕ are the two angular spherical coordinates.

In order to model a random orientation of CNTs, a volumetric average is applied to (12) to obtain

$$C = (v_m C_m A_m + O_1) \cdot (v_m I + O_2)^{-1}, \tag{16}$$

where

$$O_1 = \sum_{i=1}^{N} \frac{v_i}{4\pi} \int_0^{2\pi} \int_0^{\pi} \tilde{Q} \cdot C_i \cdot \tilde{Q}^T \cdot \tilde{Q} \cdot A_i \cdot \tilde{Q}^T \sin\phi \, \partial\phi \, \partial\theta, \tag{17a}$$

$$O_2 = \sum_{i=1}^{N} \frac{v_i}{4\pi} \int_0^{2\pi} \int_0^{\pi} \tilde{Q} \cdot A_i \cdot \tilde{Q}^T \sin\phi \, \partial\phi \, \partial\theta. \tag{17b}$$

3. Results

3.1. *Transversely isotropic elastic properties of pristine and defective CNTs.*

3.1.1. *Pristine CNTs.* The five transversely isotropic elastic properties of CNTs predicted by atomistic FEA are shown in Figure 9. The axial elastic modulus (E_{11}^{CNT}) presents a linearly decreasing trend with increased CNT's radius. The radial elastic modulus (E_{22}^{CNT}; see Figure 9, left) and both shear moduli (μ_{12}^{CNT} and μ_{23}^{CNT}; see Figure 9, right) present also a slightly decreasing trend with increased CNT radius. This trend is produced as a consequence of the larger proportion of inner hollow area inside the CNT as the radius increases, whereas all the considered carbon atoms are located at the outer ring. The proportion between the hollow center and the outer ring is larger for CNTs with larger radii. The results of E_{11}^{CNT} are within the range of previous predictions [Li and Chou 2003b; Lu 1997; Chang and Gao 2003; Xiao et al. 2005; Ávila and Lacerda 2008] and experiments [Treacy et al. 1996; Yu et al. 2000] by other authors, and also agrees with a previous work [Domínguez-Rodríguez et al. 2014] where CNTs were homogenized as hollow tubes. Those predictions of E_{11}^{CNT} are around 1 TPa and in the range of our calculations for small radius CNTs, i.e., $(3, 3)$ and $(4, 4)$ CNTs, where the central hollow area is much smaller than the tubular one. Using molecular mechanics, Shen and Li [2004] modeled the elastic properties of CNTs homogenized as solid cylinders and found a similar decreasing trend of the axial elastic modulus as a function of the CNT radius. However, some other authors have predicted higher values of E_{11}^{CNT} ($1 - 7$ TPa) [Tserpes and Papanikos 2005; Yakobson et al. 1996; Pantano et al. 2004] as a consequence of the CNT transverse area, which was assumed smaller [Ávila and Lacerda 2008]. The
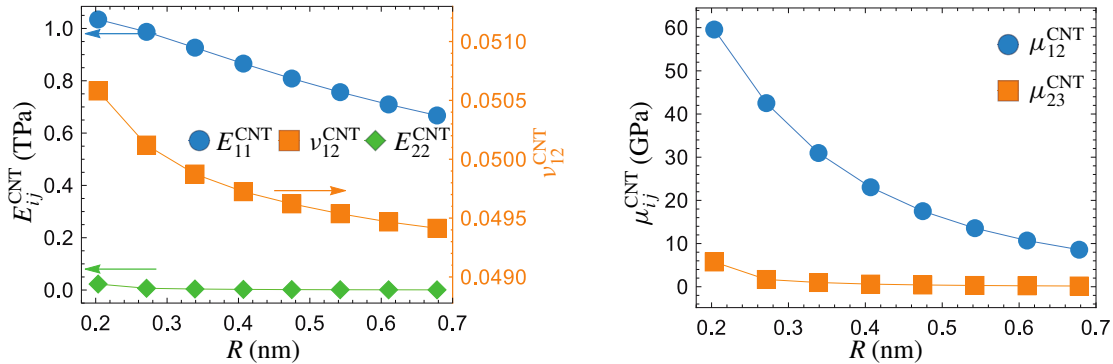
Figure 9. Elastic properties of SWCNTs as a function of their radius: left, axial and radial elastic moduli and transverse Poisson's ratio; right, transverse and in-plane shear moduli.

Poisson's ratio also presented a slight decreasing trend as a function of the CNT radius, but the difference in ν_{12} (Figure 9, left) for the different CNTs investigated is less than 2%. The radial elastic modulus of CNTs (E_{22}^{CNT}) is two orders of magnitude smaller than E_{11}^{CNT} (see Figure 9, left) which has similarly been observed experimentally [Palaci et al. 2005]. A possible explanation can be based on the loading paths. During axial strain, the deformation requires the stretching of the C-C bonds, whereas for a radial strain, most of the deformation is due to the more compliant bending of the C-C bonds.

3.1.2. *Damaged CNTs.* When the C-C bonds break, there is a probability for the CNT to become discontinuous, which renders singularities in the FEA displacement matrix. This probability is different if the bonds are removed randomly or by using a clustering pattern. In order to investigate the maximum fraction of broken bonds feasible in the CNT models, the bonds were removed following random and clustering damage processes. The process was repeated 200 times for a (3, 3) CNT and the continuity of the CNT structure was observed for each fraction of broken bonds. The fragmentation probability was defined as the number of fragmented CNTs divided by the total number of evaluated CNTs (200). According to Figure 10, this fragmentation probability resembles a sigmoid function of the fraction of broken bonds, especially for clustered damage. For random damage — Figure 10, left — the plotted interval (from 0 to 10%) only covers the first half of the sigmoid function. This phenomenon is markedly more pronounced for clustered damage (Figure 10, right), whose fragmentation probability is ~ 0.9 at a fraction of broken bonds of 8%, in comparison to ~ 0.25 for random damage at the same fraction of broken bonds. Fractions of defects higher than 8% render fragmentation probabilities for clustered damage close to 1, which is inappropriate for modeling purposes. Therefore, the highest fraction of broken bonds considered hereafter for clustered damage is 8%, whereas for random damage the maximum fraction of broken bonds was 10%.

The elastic properties of the defective CNTs were computed for the eight studied chiralities, varying the fraction of broken bonds. Figure 11 shows normalized plots of the axial elastic modulus for the studied SWCNTs with both random (Figure 11, left) or clustered (Figure 11, right) damage. E_{11}^{CNT} represents the axial elastic modulus of the defective CNT, while $E_{11}^{CNT^0}$ represents that of the pristine (defect-free) one. The axial elastic modulus of all the investigated SWCNTs decreases drastically as the fraction of broken bonds increases, which is in qualitative agreement with previous works [Sammalkorpi et al. 2004; Talukdar and Mitra 2010; Fefey et al. 2011; Yuan and Liew 2009]. This decrement is as
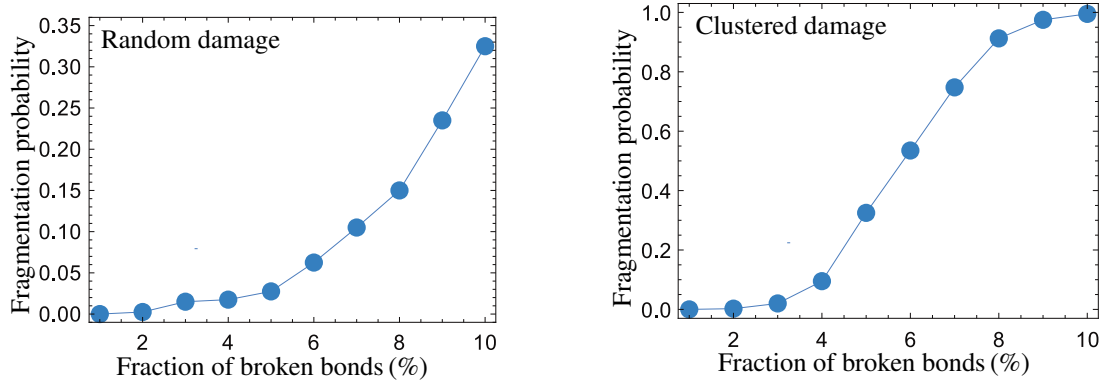
Figure 10. Probability of fragmentation as a function of the CNT fraction of broken bonds for a (3, 3) SWCNT: left, random damage; right, clustered damage.
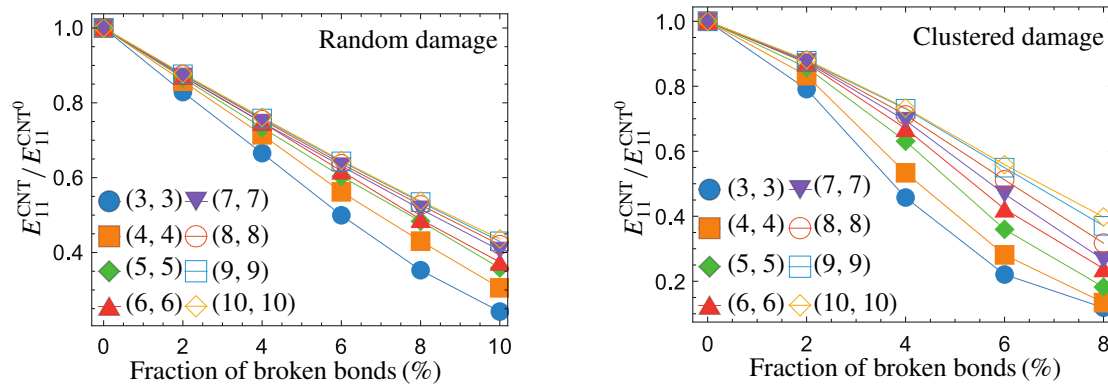

Figure 11. Normalized axial elastic modulus of defective CNTs as a function of the damage fraction: left, random damage; right, clustered damage.

high as $\sim 80\%$ for a 10% fraction of randomly distributed broken bonds (Figure 11, left) and as high as $\sim 85\%$ for a fraction of 8% clustered broken bonds (Figure 11, right). SWCNTs with smaller radii are more affected by structural defects because their unit cells have less C-C bonds (18 bonds for a unit cell of a (3, 3) SWCNT) than those of larger radii (60 bonds for a unit cell of a (10, 10) SWCNT).

The transverse Poisson's ratio of SWCNTs presents an increasing trend with an increased fraction of broken bonds (Figure 12). The value of ν_{12}^{CNT} increases six times with respect to the value of pristine CNTs for a fraction of 10% randomly distributed broken bonds (Figure 12, left). For clustered damage (Figure 12, right) the effect is more severe, reaching seven times the pristine value for an 8% fraction of broken bonds. This means that a defective CNT is significantly more compliant in the radial direction by Poisson's contraction than a pristine one. As for the case of the normalized axial elastic modulus, the difference from the pristine property is more prominent for defective SWCNTs with small radii, whose unit cells have less C-C bonds.

Similar to the case of E_{11}^{CNT}, the normalized radial elastic modulus (E_{22}^{CNT}) of defective CNTs (Figure 13) shows a linear decreasing trend with an increasing fraction of broken bonds. However, the reduction in E_{22}^{CNT} with the fraction of broken bonds is less severe than for E_{11}^{CNT} for both kinds of damage considered
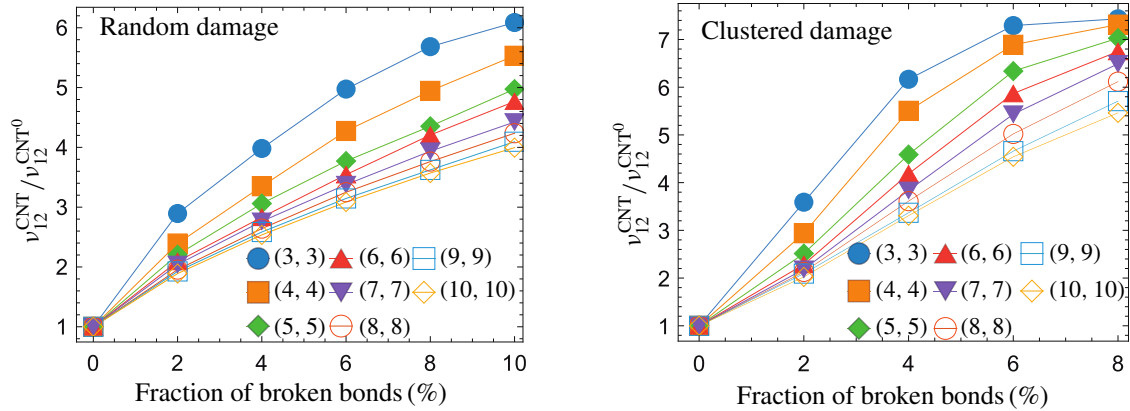
Figure 12. Normalized transverse Poisson's ratio of defective CNTs as a function of the damage fraction: left, random damage; right, clustered damage.
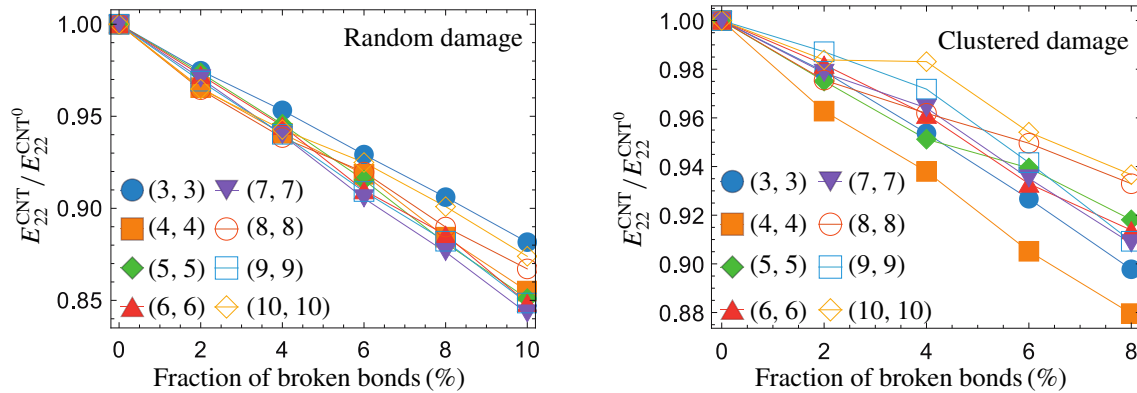

Figure 13. Normalized radial elastic modulus of defective CNTs as a function of the damage fraction: left, random damage; right, clustered damage.

herein. This is a consequence of the loading paths, because the probability of breaking a loading path is higher in the axial direction than in the radial one. The maximum reduction in E_{22}^{CNT} is $\sim 15\%$ for the case of random damage (Figure 13, left) and $\sim 12\%$ for the case of clustering damage (Figure 13, right).

The transverse shear modulus (μ_{12}^{CNT}, Figure 14) and the in-plane shear modulus (μ_{23}^{CNT}, Figure 15) of defective CNTs also present a decreasing trend as a function of the fraction of broken bonds. The decrease in the transverse shear modulus, Figure 14, is $\sim 14\%$ for a fraction of broken bonds of 10% for random damage, and $\sim 10\%$ for a fraction of broken bonds of 8% for clustered damage. The maximum reduction in the in-plane shear modulus, Figure 15, is $\sim 15\%$ for random damage and $\sim 12\%$ for clustered damage. As seen from these figures, the influence of the fraction of broken bonds on the transverse and in-plane elastic properties is smaller than on the axial elastic modulus, as a consequence of the loading paths.

3.2. *Influence of CNT fraction of broken bonds on the transversely isotropic elastic properties of axially oriented CNT/polymer composites.* The transversely isotropic elastic properties of CNT/polymer composites containing axially oriented (aligned) CNTs were first obtained by the CCM for each damaged SWCNT investigated. The computations were also conducted using the MT method to simulate
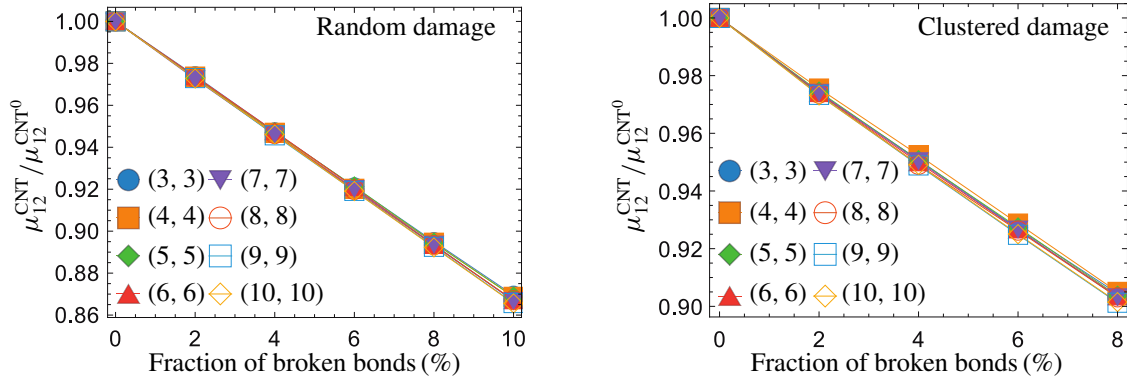
Figure 14. Normalized transverse shear modulus of defective CNTs as a function of the damage fraction: left, random damage; right, clustered damage.
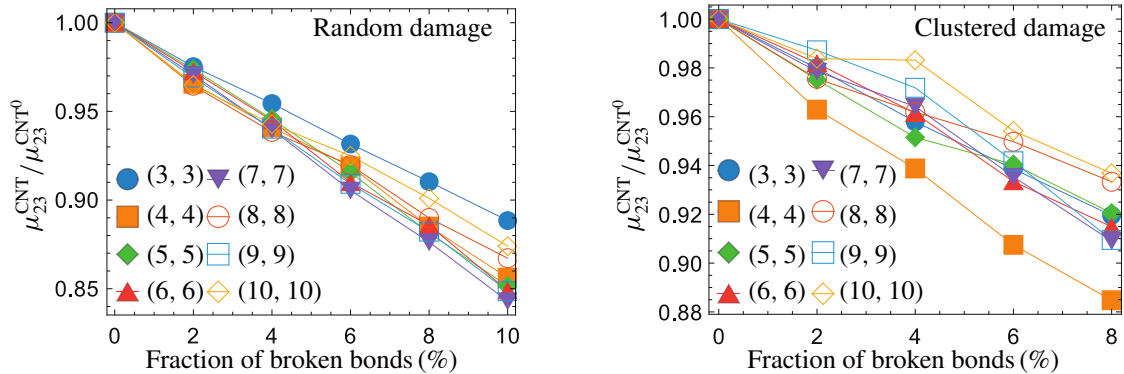

Figure 15. Normalized in-plane shear modulus of defective CNTs as a function of the damage fraction: left, random damage; right, clustered damage.

a CNT/polymer composite containing a full variety of axially oriented SWCNTs, including the eight studied chiralities and all different fractions of broken bonds, as could be expected in an experimental situation. For the MT method, the volume fraction of each chirality and fraction of broken bonds was calculated by sampling a random number from 0 to 1 following a uniform distribution of probability, and then weighted by the summation of volume fractions.

The influence of the fraction of broken bonds on the elastic properties of aligned CNT/polymer composites with a fixed CNT volume fraction of 1% was investigated for both random and clustered damage. The elastic properties reported in Figures 16–18 are normalized by the elastic property of the composite containing pristine CNTs (without defects), which are labeled with a superscript "0". The normalized axial elastic modulus of the composite (E_{11}/E_{11}^0) is plotted in Figure 16. E_{11} decreases linearly with increased fraction of broken bonds, regardless of the CNT size/chirality. The composite containing $(3, 3)$ SWCNTs shows a more pronounced influence of the fraction of broken bonds as a consequence of the higher elastic properties of the $(3, 3)$ CNT. For a fraction of SWCNT defects of 8%, the composite presents a knockdown in E_{11} of $\sim 60\%$ for random damage (Figure 16, left) and $\sim 80\%$ for clustered damage (Figure 16, right).
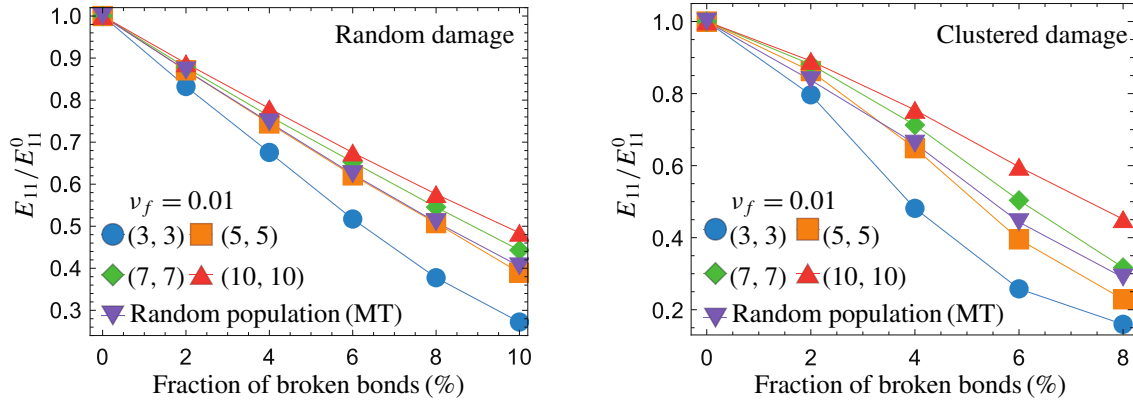
Figure 16. Normalized transverse axial elastic modulus of CNT/polymer composites as a function of CNT fraction of broken bonds for composites containing axially oriented CNTs: left, random damage; right, clustered damage.
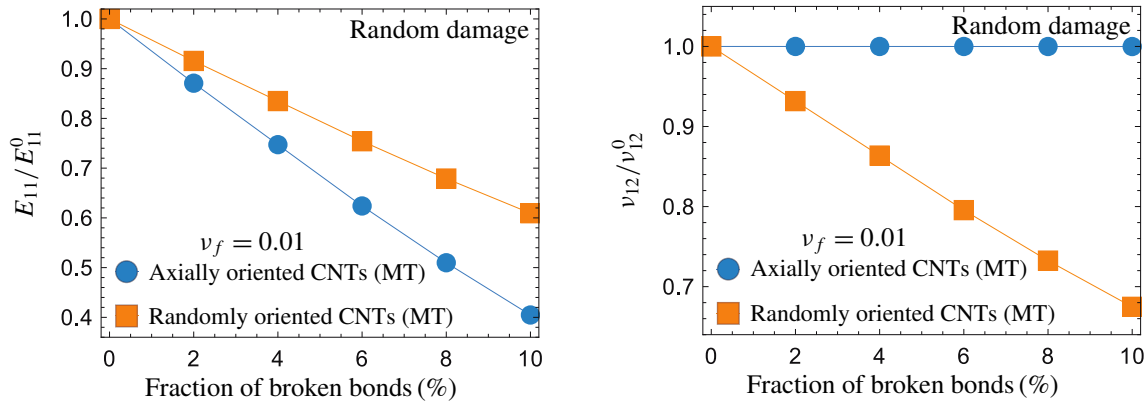
Figure 17. Normalized elastic properties of CNT/polymer composites as a function of the fraction of broken bonds for composites containing axially and randomly oriented CNTs: left, axial elastic modulus; right, transverse shear modulus.

The normalized transverse Poisson's ratio (ν_{12}/ν_{12}^0) of the composite as a function of the fraction of broken bonds is shown in Figure 18 for composites with axially oriented CNTs and a volume fraction of 1%. The value of ν_{12} increases as the fraction of CNT broken bonds increases due to lost of radial rigidity caused by the breakage of C-C bonds. This increase in ν_{12} is more pronounced for composites containing SWCNTs with smaller radii and clustered damage. However, the increments of ν_{12} are less than 5% for the maximum clustered fraction broken bonds investigated herein (8%).

The radial elastic modulus (E_{22}), the in-plane shear modulus (μ_{23}), and the transverse shear modulus (μ_{12}) were not significantly affected by the fraction of broken bonds for composites with axially oriented CNTs and therefore are not shown. This is because the in-plane and transverse elastic properties of unidirectional composites are matrix dominated, which also applies for the case of aligned CNTs.

3.3. *Elastic properties of randomly oriented CNT/polymer composites.* The elastic properties of CNT/polymer composites were also computed for SWCNTs with a variety of random orientations considering

Figure 18. Normalized transverse Poisson's ratio of CNT/polymer composites as a function of CNT fraction of broken bonds for composites containing axially oriented CNTs: left, random damage; right, clustered damage.
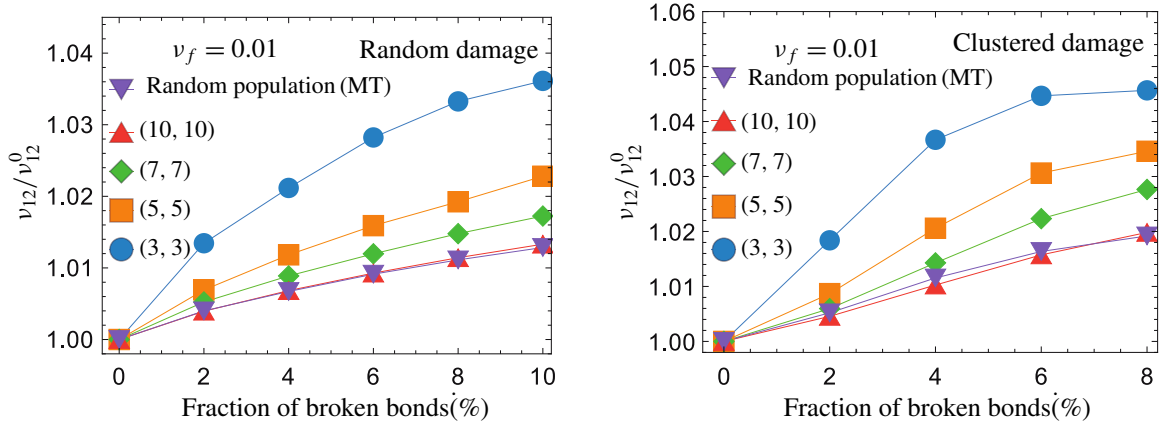
pristine and defective CNTs and a fixed CNT volume fraction of 1% ($v_f = 0.01$). The MT formulation and (16) are used to average the elastic properties of CNT/polymer composites for all angle orientations, chirality, and fraction of defects. The normalized axial elastic modulus of CNT/polymer composites (E_{11}/E_{11}^0) as a function of the fraction of broken bonds is shown in Figure 17, left, for composites with axially and randomly oriented CNTs. Both random and clustered damage presented similar results; therefore, only plots for random damage are shown. The decreasing rate of E_{11}/E_{11}^0 for composites with axially oriented SWCNTs is larger, which is a consequence of the higher SWCNT influence on the composite elastic properties when the CNTs are axially oriented in the (unidirectional) composite.

The transverse shear modulus (μ_{12}), in-plane shear modulus (μ_{23}), and radial elastic modulus (E_{22}) are dominated by the matrix properties. As such, the contribution of the SWCNT (defective or not) is negligible when the SWCNTs are axially oriented, as shown in Figure 17, right, for the normalized transverse shear modulus. The in-plane shear modulus (μ_{23}) and the radial elastic modulus (E_{22}) as functions of the fraction of broken bonds present a similar trend to μ_{12} and therefore are not plotted. When the SWCNTs are randomly oriented, some of them reinforce the transverse direction and some others the axial one. Therefore, for a random orientation of SWCNTs, μ_{12}, μ_{23}, and E_{22} are significantly affected.

4. Conclusions

A multiscale hierarchical (sequential) approach was carried out to predict the influence of CNT structural defects on the elastic properties of CNT/polymer composites. As the initial step, the elastic properties of armchair SWCNTs were modeled using atomistic finite element analysis. Structural defects were generated in the SWCNTs by removing carbon-carbon bonds. SWCNT damage was produced progressively by randomly selecting the bonds to eliminate and also as a clustered (coalesced) damage by removing only bonds that are adjacent to the already eliminated bonds. The next step was the computation of the elastic properties of CNT/polymer composites, which was performed through the composite cylinder and Mori–Tanaka methods. The composite cylinder method was used to model the elastic properties of a composite

material containing axially oriented (aligned) CNTs surrounded by an interphase and matrix. The Mori–Tanaka method was used to model composite materials containing axially and randomly oriented CNTs with a random combination of chiralities and fractions of broken bonds. Regarding the elastic properties of CNTs, the knockdown in the axial elastic modulus of CNTs is on the order of $\sim 60\%$ with an 8% fraction of randomly broken bonds, whereas the knockdown with an 8% fraction of clustered broken bonds is $\sim 80\%$. The transverse Poisson's ratio of CNTs increases ~ 7 times with an 8% fraction of randomly or clustered broken bonds with respect to its pristine value. The radial elastic modulus, transverse shear modulus, and in-plane shear modulus of CNTs present a knockdown of about 10% for an 8% fraction of broken bonds. Regarding the elastic properties of CNT/polymer composites reinforced with axially oriented CNTs, the axial elastic modulus and the transverse Poisson's ratio are the elastic properties most influenced by the SWCNTs, and as such those properties are more affected by CNT defects. The knockdown in the axial elastic modulus for CNT/polymer composites containing a 1% volume fraction of randomly oriented CNTs with a fraction of broken bonds of 8% is on the order of $\sim 50\%$. The radial elastic modulus, the axial shear and the in-plane shear moduli of the CNT/polymer composites are only influenced by structural defects when the CNTs are randomly oriented. The knockdown in those properties are on the order of $\sim 30\%$ with a 1% CNT volume fraction and 8% fraction of defects. For randomly oriented CNTs, the five studied elastic properties are strongly influenced by the fraction of broken bonds. In comparison to random damage, clustered damage showed a larger influence of defects on the axial elastic modulus and transverse Poisson's ratio of CNTs (especially for those with smaller radius) and therefore, their polymer composites.

Appendix: Loading cases in the composite cylinder method

This appendix provides explicit equations concerning displacement fields, boundary conditions and continuity equations for the four loading cases used in the composite cylinder method.

A.1. *Axial elastic modulus and transverse Poisson's ratio.* For the axial elastic modulus (E_{11}), the radial (u_r^i), axial (u_z^i), and angular (u_θ^i) displacements of each phase (i) are defined in the interval $r_{i-1} \leq r \leq r_i$ as

$$u_r^i = B_1^i r + B_2^i/r, \quad u_\theta^i = 0, \quad u_z^i = \epsilon_z z, \tag{A.1}$$

where B_1^i and B_2^i are constants.

The outer surface of the composite at $r = r_N$ is free from radial stress, i.e.,

$$\sigma_{rr}^N|_{r=r_N} = 0. \tag{A.2}$$

In order to avoid a mathematical singularity, $B_2^{(1)}$ is set to 0 for the first layer.

The continuity equations for stresses and displacements of each layer are

$$u_r^i|_{r=r_i} = u_r^{i+1}|_{r=r_i}, \tag{A.3a}$$

$$\sigma_{rr}^i|_{r=r_i} = \sigma_{rr}^{i+1}|_{r=r_i}. \tag{A.3b}$$

A.2. *In-plane bulk modulus.* The in-plane bulk modulus (K_{23}) is calculated by using displacement equations for the interval $r_{i-1} \leq r \leq r_i$, which are similar to those of (A.1) except for the condition in u_z,

i.e.,

$$u_r^i = D_1^i r + D_2^i/r, \quad u_\theta^i = 0, \quad u_z^i = 0, \tag{A.4}$$

where D_1^i and D_2^i are constants.

The boundary conditions state that maximum radial displacement occurs at the outer surface ($r = r_N$), i.e.,

$$u_r^N|_{r=r_N} = \epsilon_r r_N. \tag{A.5}$$

$D_2^{(1)}$ is again set to 0 to avoid singularities.

The continuity conditions for stresses and displacements are those stated in (A.3).

A.3. *Transverse shear modulus*. The transverse shear modulus is calculated by applying an axial displacement field as function of θ for the interval $r_{i-1} \leq r \leq r_i$:

$$u_r^i = 0, \quad u_\theta^i = 0, \quad u_z^i = (F_1^i r + F_2^i/r)\cos\theta. \tag{A.6}$$

This displacement field produces a pure transverse shear strain ($\epsilon_{z\theta} \neq 0$, $\epsilon_{zz} = \epsilon_{rr} = \epsilon_{\theta\theta} = \epsilon_{r\theta} = 0$).

The boundary conditions require that the maximum radial deformation occurs at $r = r_N$ (see Figure 7c), i.e.,

$$u_z^N|_{r=r_N} = 2\epsilon_{z\theta} r_N \cos\theta, \tag{A.7}$$

where $F_2^{(1)}$ is set to 0 for the first layer.

The continuity equation for displacements is represented by (A.3a), while that for stresses is

$$\mu_i \frac{\partial u_z^i}{\partial r}\bigg|_{r=r_i} = \mu_{i+1} \frac{\partial u_z^{i+1}}{\partial r}\bigg|_{r=r_i}. \tag{A.8}$$

A.4. *In-plane shear modulus*. The displacement conditions used in the in-plane shear strain loading case are [Christensen and Lo 1979]

$$u_r^i = \left[H_1^i r + H_2^i r^3 \left(\frac{v_{zr}^i}{3 - 2v_{zr}^i} \right) - H_3^i \frac{1}{r^3} + 2H_4^i \frac{1}{r} \left(\frac{v_{zr}^i - 1}{2v_{zr}^i - 1} \right) \right] \sin(2\theta), \tag{A.9a}$$

$$u_\theta^i = \left(H_1^i r + H_2^i r^3 + H_3^i \frac{1}{r^3} + 2H_4^i \frac{1}{r} \right) \cos(2\theta), \tag{A.9b}$$

$$u_z^i = 0. \tag{A.9c}$$

Both $H_3^{(1)}$ and $H_4^{(1)}$ are set to 0 in order to avoid a mathematical singularity at the first layer.

The generalized self-consistent composite cylinder model includes an extra $(N+1)$ layer of material which does not represent one of the N phases of the composite cylinder but the homogenized composite material. This layer explicitly includes the in-plane shear modulus of the composite material (μ_{23}^{eff}) instead of the shear modulus of a specific layer. The displacement fields for this layer are defined as [Seidel and

Lagoudas 2006]

$$u_r^{N+1} = \frac{r_{N+1}}{4\mu_{23}^{\text{eff}}} \left[\frac{2r}{r_{N+1}} + H_5 \left(\frac{r_{N+1}}{r} \right)^3 + 4(1 - \nu_{23}^{\text{eff}}) H_6 \frac{r_{N+1}}{r} \right] \sin(2\theta), \tag{A.10a}$$

$$u_\theta^{N+1} = \frac{-r_{N+1}}{4\mu_{23}^{\text{eff}}} \left[-\frac{2r}{r_{N+1}} + H_5 \left(\frac{r_{N+1}}{r} \right)^3 - 2(1 - 2\nu_{23}^{\text{eff}}) H_6 \frac{r_{N+1}}{r} \right] \cos(2\theta), \tag{A.10b}$$

$$u_z^{N+1} = 0. \tag{A.10c}$$

The continuity equations for u_r, u_θ, σ_{rr}, and $\sigma_{r\theta}$ are similar to those stated in (A.3).

In order to achieve an energetic homogenization, the whole composite is considered an effective homogeneous solid cylinder whose displacements are

$$u_r^* = \frac{r_{N+1}}{4\mu_{23}^{\text{eff}}} \left(\frac{2r}{r_{N+1}} \right) \sin(2\theta), \tag{A.11a}$$

$$u_\theta^* = \frac{-r_{N+1}}{4\mu_{23}^{\text{eff}}} \left(-\frac{2r}{r_{N+1}} \right) \cos(2\theta), \tag{A.11b}$$

$$u_z^* = 0. \tag{A.11c}$$

The composite cylinder and the homogenized solid cylinder are energetically equated through the use of the Eshelby [1957; 1959] formula

$$\int_0^{2\pi} \left[\sigma_{rr}^{N+1} u_r^* + \sigma_{r\theta}^{N+1} u_\theta^* - (\sigma_{rr}^* u_r^{N+1} + \sigma_{r\theta}^* u_\theta^{N+1}) \right]_{r=r_N} d\theta = 0. \tag{A.12}$$

Then the system of equations from (A.9) to (A.12) is solved and μ_{23}^{eff} corresponds to the reported value for μ_{23}.

Acknowledgments

References

[Ahangari et al. 2013] M. G. Ahangari, A. Fereidoon, M. Jahanshahi, and M. Ganji, "Electronic and mechanical properties of single-walled carbon nanotubes interacting with epoxy: a DFT study", *Physica E* **48** (2013), 148–156.

[Araujo et al. 2012] P. T. Araujo, M. Terrones, and M. S. Dresselhaus, "Defects and impurities in graphene-like materials", *Mater. Today* **15**:3 (2012), 98–109.

[Ávila and Lacerda 2008] A. F. Ávila and G. S. R. Lacerda, "Molecular mechanics applied to single-walled carbon nanotubes", *Mat. Res.* **11** (09 2008), 325–333.

[Balog et al. 2010] R. Balog, B. Jorgensen, L. Nilsson, M. Andersen, E. Rienks, M. Bianchi, M. Fanetti, E. Laegsgaard, A. Baraldi, S. Lizzit, Z. Sljivancanin, F. Besenbacher, B. Hammer, T. G. Pedersen, P. Hofmann, and L. Hornekaer, "Bandgap opening in graphene induced by patterned hydrogen adsorption", *Nat. Mater.* **9**:4 (2010), 315–319.

[Banhart 1999] F. Banhart, "Irradiation effects in carbon nanostructures", *Rep. Progr. Phys.* **62**:8 (1999), 1181–1221.

[Banhart et al. 2011] F. Banhart, J. Kotakoski, and A. V. Krasheninnikov, "Structural defects in graphene", *ACS Nano* **5**:1 (2011), 26–41.

[Berber and Oshiyama 2006] S. Berber and A. Oshiyama, "Reconstruction of mono-vacancies in carbon nanotubes: atomic relaxation vs. spin polarization", *Physica B* **376–377** (2006), 272–275.

[Blake et al. 2007] P. Blake, E. W. Hill, A. H. C. Neto, K. S. Novoselov, D. Jiang, R. Yang, T. J. Booth, and A. K. Geim, "Making graphene visible", *Appl. Phys. Lett.* **91**:6 (2007), 063124.

[Blanc et al. 2002] X. Blanc, C. Le Bris, and P.-L. Lions, "From molecular models to continuum mechanics", *Arch. Ration. Mech. Anal.* **164**:4 (2002), 341–381.

[Burnett et al. 2012] T. L. Burnett, R. Yakimova, and O. Kazakova, "Identification of epitaxial graphene domains and adsorbed species in ambient conditions using quantified topography measurements", *J. Appl. Phys.* **112**:5 (2012), 054308.

[Caillerie et al. 2006] D. Caillerie, A. Mourad, and A. Raoult, "Discrete homogenization in graphene sheet modeling", *J. Elasticity* **84**:1 (2006), 33–68.

[Chang and Gao 2003] T. Chang and H. Gao, "Size-dependent elastic properties of a single-walled carbon nanotube via a molecular mechanics model", *J. Mech. Phys. Solids* **51**:6 (2003), 1059–1074.

[Christensen and Lo 1979] R. M. Christensen and K. H. Lo, "Solutions for effective shear properties in three phase sphere and cylinder models", *J. Mech. Phys. Solids* **27**:4 (1979), 315–330.

[Cornell et al. 1995] W. D. Cornell, P. Cieplak, C. I. Bayly, I. R. Gould, K. M. Merz, D. M. Ferguson, D. C. Spellmeyer, T. Fox, J. W. Caldwell, and P. A. Kollman, "A second generation force field for the simulation of proteins, nucleic acids, and organic molecules", *J. Am. Chem. Soc.* **117**:19 (1995), 5179–5197.

[De Volder et al. 2013] M. F. L. De Volder, S. H. Tawfick, R. H. Baughman, and A. J. Hart, "Carbon nanotubes: present and future commercial applications", *Science* **339** (2013), 535–539.

[Demczyk et al. 2002] B. G. Demczyk, Y. M. Wang, J. Cumings, M. Hetman, W. Han, A. Zettl, and R. O. Ritchie, "Direct mechanical measurement of the tensile strength and elastic modulus of multiwalled carbon nanotubes", *Mater. Sci. Eng. A* **334**:1–2 (2002), 173–178.

[Domínguez-Rodríguez et al. 2014] G. Domínguez-Rodríguez, A. Tapia, and F. Avilés, "An assessment of finite element analysis to predict the elastic modulus and Poisson's ratio of singlewall carbon nanotubes", *Comput. Mat. Sci.* **82** (2014), 257–263.

[Dow and Huyer 1989] J. O. Dow and S. A. Huyer, "Continuum models of space station structures", *J. Aerospace Eng.* **2**:4 (1989), 220–238.

[Eshelby 1957] J. D. Eshelby, "The determination of the elastic field of an ellipsoidal inclusion, and related problems", *Proc. Roy. Soc. London. Ser. A.* **241** (1957), 376–396.

[Eshelby 1959] J. D. Eshelby, "The elastic field outside an ellipsoidal inclusion", *Proc. Roy. Soc. London. Ser. A* **252** (1959), 561–569.

[Fefey et al. 2011] E. G. Fefey, R. Mohan, and A. Kelkar, "Computational study of the effect of carbon vacancy defects on the Young's modulus of (6, 6) single wall carbon nanotube", *Mater. Sci. Eng. B* **176**:9 (2011), 693–700.

[Ferrari and Basko 2013] A. C. Ferrari and D. M. Basko, "Raman spectroscopy as a versatile tool for studying the properties of graphene", *Nat. Nano.* **8**:4 (2013), 235–246.

[Fink 2010] J. K. Fink, *Handbook of engineering and speciality thermoplastics*, Scrivener, Salem, Massachusetts, 2010.

[Fonseca Guerra et al. 1998] C. Fonseca Guerra, J. G. Snijders, G. te Velde, and E. J. Baerends, "Towards an order-N DFT method", *Theor. Chem. Acc.* **99**:6 (1998), 391–403.

[Fukushima et al. 2006] T. Fukushima, A. Kosaka, Y. Yamamoto, T. Aimiya, S. Notazawa, T. Takigawa, T. Inabe, and T. Aida, "Dramatic effect of dispersed carbon nanotubes on the mechanical and electroconductive properties of polymers derived from ionic liquids", *Small* **2**:4 (2006), 554–560.

[Gallo et al. 2007] M. Gallo, A. Favila, and D. Glossman-Mitnik, "DFT studies of functionalized carbon nanotubes and fullerenes as nanovectors for drug delivery of antitubercular compounds", *Chem. Phys. Lett.* **447**:1–3 (2007), 105–109.

[Gao et al. 2008] L. Gao, W. Ren, F. Li, and H.-M. Cheng, "Total color difference for rapid and accurate identification of graphene", *ACS Nano* **2**:8 (2008), 1625–1633.

[Gates et al. 2005] T. S. Gates, G. M. Odegard, S. J. V. Frankland, and T. C. Clancy, "Computational materials: multi-scale modeling and simulation of nanostructured materials", *Compos. Sci. Tech.* **65**:15–16 (2005), 2416–2434.

[Giannopoulos et al. 2013] G. I. Giannopoulos, A. P. Tsiros, and S. K. Georgantzinos, "Prediction of elastic mechanical behavior and stability of single-walled carbon nanotubes using bar elements", *Mech. Adv. Mater. Struct.* **20**:9 (2013), 730–741.

[Haghbin and Khalili 2014] A. Haghbin and S. M. R. Khalili, "Effect of chiral angle on tensile behavior modeling of single-walled carbon nanotubes", *Mech. Adv. Mater. Struct.* **21**:6 (2014), 505–515.

[Hashin and Rosen 1964] Z. Hashin and B. W. Rosen, "The elastic moduli of fiber-reinforced materials", *J.Appl. Mech.* **31**:2 (1964), 223–232.

[Hernández-Pérez and Avilés 2010] A. Hernández-Pérez and F. Avilés, "Modeling the influence of interphase on the elastic properties of carbon nanotube composites", *Comput. Mat. Sci.* **47**:4 (2010), 926–933.

[Hine et al. 2009] N. D. M. Hine, P. D. Haynes, A. A. Mostofi, C.-K. Skylaris, and M. C. Payne, "Linear-scaling density-functional theory with tens of thousands of atoms: expanding the scope and scale of calculations with ONETEP", *Comput. Phys. Comm.* **180**:7 (2009), 1041–1053.

[Jorgensen and Severance 1990] W. L. Jorgensen and D. L. Severance, "Aromatic-aromatic interactions: free energy profiles for the benzene dimer in water, chloroform, and liquid benzene", *J. Am. Chem. Soc.* **112**:12 (1990), 4768–4774.

[Kalamkarov et al. 2006] A. L. Kalamkarov, A. V. Georgiades, S. K. Rokkam, V. P. Veedu, and M. N. Ghasemi-Nejhad, "Analytical and numerical techniques to predict carbon nanotubes properties", *Int. J. Solids Struct.* **43**:22–23 (2006), 6832–6854.

[Kim et al. 2009] K. S. Kim, Y. Zhao, H. Jang, S. Y. Lee, J. M. Kim, K. S. Kim, J.-H. Ahn, P. Kim, J.-Y. Choi, and B. H. Hong, "Large-scale pattern growth of graphene films for stretchable transparent electrodes", *Nature* **457**:7230 (2009), 706–710.

[Kohn 1995] W. Kohn, "Density functional theory for systems of very many atoms", *Int. J. Quantum Chem.* **56**:4 (1995), 229–232.

[Krasheninnikov and Banhart 2007] A. V. Krasheninnikov and F. Banhart, "Engineering of nanostructured carbon materials with electron or ion beams", *Nat. Mater.* **6**:10 (2007), 723–733.

[Lagoudas et al. 1991] D. C. Lagoudas, A. C. Gavazzi, and H. Nigam, "Elastoplastic behavior of metal matrix composites based on incremental plasticity and the Mori–Tanaka averaging scheme", *Comput. Mech.* **8**:3 (1991), 193–203.

[Li and Chou 2003a] C. Li and T.-W. Chou, "Elastic moduli of multi-walled carbon nanotubes and the effect of van der Waals forces", *Compos. Sci. Tech.* **63**:11 (2003), 1517–1524.

[Li and Chou 2003b] C. Li and T.-W. Chou, "A structural mechanics approach for the analysis of carbon nanotubes", *Int. J. Solids Struct.* **40**:10 (2003), 2487–2499.

[Lu 1997] J. P. Lu, "Elastic properties of carbon nanotubes and nanoropes", *Phys. Rev. Lett.* **79** (1997), 1297–1300.

[Lucchese et al. 2010] M. Lucchese, F. Stavale, E. M. Ferreira, C. Vilani, M. Moutinho, R. B. Capaz, C. Achete, and A. Jorio, "Quantifying ion-induced defects and Raman relaxation length in graphene", *Carbon* **48**:5 (2010), 1592–1597.

[Meyer 2000] C. Meyer, *Matrix analysis and applied linear algebra and solutions manual*, Society for Industrial and Applied Mathematics, Philadelphia, 2000.

[Mielke et al. 2004] S. L. Mielke, D. Troya, S. Zhang, J.-L. Li, S. Xiao, R. Car, R. S. Ruoff, G. C. Schatz, and T. Belytschko, "The role of vacancy defects and holes in the fracture of carbon nanotubes", *Chem. Phys. Lett.* **390**:4–6 (2004), 413–420.

[Mittal 2011] V. Mittal, *High performance polymers and engineering plastics*, Scrivener, Salem, Massachusetts, 2011.

[Monthioux and Charlier 2014] M. Monthioux and J.-C. Charlier, "Giving credit where credit is due: the Stone–(Thrower)–Wales designation revisited", *Carbon* **75** (2014), 1–4.

[Mori and Tanaka 1973] T. Mori and K. Tanaka, "Average stress in matrix and average elastic energy of materials with misfitting inclusions", *Acta Metall.* **21**:5 (1973), 571–574.

[Natsuki et al. 2004] T. Natsuki, K. Tantrakarn, and M. Endo, "Effects of carbon nanotube structures on mechanical properties", *Appl. Phys. A* **79**:1 (2004), 117–124.

[Ni et al. 2007] Z. H. Ni, H. M. Wang, J. Kasim, H. M. Fan, T. Yu, Y. H. Wu, Y. P. Feng, and Z. X. Shen, "Graphene thickness determination using reflection and contrast spectroscopy", *Nano Lett.* **7**:9 (2007), 2758–2763.

[Noor 1988] A. K. Noor, "Continuum modeling for repetitive lattice structures", *Appl. Mech. Rev.* **41**:7 (1988), 285–296.

[Noor et al. 1978] A. K. Noor, M. S. Anderson, and W. H. Greene, "Continuum models for beam- and platelike lattice structures", *AIAA Journal* **16**:12 (1978), 1219–1228.

[Novoselov et al. 2005] K. S. Novoselov, D. Jiang, F. Schedin, T. J. Booth, V. V. Khotkevich, S. V. Morozov, and A. K. Geim, "Two-dimensional atomic crystals", *Proc. Nat. Acad. Sci. USA* **102**:30 (2005), 10451–10453.

[Obraztsova et al. 2008] E. A. Obraztsova, A. V. Osadchy, E. D. Obraztsova, S. Lefrant, and I. V. Yaminsky, "Statistical analysis of atomic force microscopy and Raman spectroscopy data for estimation of graphene layer numbers", *Physica Status Solidi (B)* **245**:10 (2008), 2055–2059.

[Odegard et al. 2002] G. M. Odegard, T. S. Gates, L. M. Nicholson, and K. E. Wise, "Equivalent-continuum modeling of nano-structured materials", *Compos. Sci. Tech.* **62**:14 (2002), 1869–1880.

[Palaci et al. 2005] I. Palaci, S. Fedrigo, H. Brune, C. Klinke, M. Chen, and E. Riedo, "Radial elasticity of multiwalled carbon nanotubes", *Phys. Rev. Lett.* **94** (2005), 175502–1–175502–4.

[Pantano et al. 2004] A. Pantano, D. M. Parks, and M. C. Boyce, "Mechanics of deformation of single- and multi-wall carbon nanotubes", *J. Mech. Phys. Solids* **52**:4 (2004), 789–821.

[Prasomsri et al. 2010] T. Prasomsri, D. Shi, and D. E. Resasco, "Anchoring Pd nanoclusters onto pristine and functionalized single-wall carbon nanotubes: a combined DFT and experimental study", *Chem. Phys. Lett.* **497**:1–3 (2010), 103–107.

[Qu and Cherkaoui 2006] J. Qu and M. Cherkaoui, *Fundamentals of micromechanics of solids*, Wiley, Hoboken, New Jersey, 2006.

[Sakhaee-Pour 2009] A. Sakhaee-Pour, "Elastic properties of single-layered graphene sheet", *Solid State Comm.* **149**:1–2 (2009), 91–95.

[Sammalkorpi et al. 2004] M. Sammalkorpi, A. Krasheninnikov, A. Kuronen, K. Nordlund, and K. Kaski, "Mechanical properties of carbon nanotubes with vacancies and related defects", *Phys. Rev. B* **70** (2004), 245416.

[Seidel and Lagoudas 2006] G. D. Seidel and D. C. Lagoudas, "Micromechanical analysis of the effective elastic properties of carbon nanotube reinforced composites", *Mech. Mater.* **38**:8–10 (2006), 884–907.

[Sharma et al. 2012] K. Sharma, K. K. Saxena, and M. Shukla, "Effect of multiple Stone–Wales and vacancy defects on the mechanical behavior of carbon nanotubes using molecular dynamics", *Procedia Engineering* **38** (2012), 3373–3380.

[Shen and Li 2004] L. Shen and J. Li, "Transversely isotropic elastic properties of single-walled carbon nanotubes", *Phys. Rev. B* **69** (2004), 045414–1–045414–10.

[Shet et al. 2005] C. Shet, N. Chandra, and S. Namilae, "Defect-defect interaction in carbon nanotubes under mechanical loading", *Mech. Adv. Mater. Struct.* **12**:1 (2005), 55–65.

[Spitalsky et al. 2010] Z. Spitalsky, D. Tasis, K. Papagelis, and C. Galiotis, "Carbon nanotube-polymer composites: chemistry, processing, mechanical and electrical properties", *Prog. Polymer Sci.* **35**:3 (2010), 357–401.

[Srivastava et al. 2003] D. Srivastava, C. Wei, and K. Cho, "Nanomechanics of carbon nanotubes and composites", *Appl. Mech. Rev.* **56**:2 (2003), 215–230.

[Sun and Liebbe 1990] C. T. Sun and S. W. Liebbe, "Global-local approach to solving vibration of large truss structures", *AIAA Journal* **28**:2 (1990), 303–308.

[Sun et al. 1981] C. Sun, B. Kim, and J. Bogdanoff, "On the derivation of equivalent simple models for beam- and plate-like structures in dynamic analysis", in *Structures, structural dynamics, and materials and co-located conferences*, American Institute of Aeronautics and Astronautics, 1981.

[Talukdar and Mitra 2010] K. Talukdar and A. K. Mitra, "Comparative MD simulation study on the mechanical properties of a zigzag single-walled carbon nanotube in the presence of Stone–Thrower–Wales defects", *Compos. Struct.* **92**:7 (2010), 1701–1705.

[Treacy et al. 1996] M. M. J. Treacy, T. W. Ebbesen, and J. M. Gibson, "Exceptionally high Young's modulus observed for individual carbon nanotubes", *Nature* **381**:6584 (1996), 678–680.

[Tserpes and Papanikos 2005] K. I. Tserpes and P. Papanikos, "Finite element modeling of single-walled carbon nanotubes", *Compos. B* **36**:5 (2005), 468–477.

[Tserpes and Papanikos 2007] K. I. Tserpes and P. Papanikos, "The effect of Stone–Wales defect on the tensile behavior and fracture of single-walled carbon nanotubes", *Compos. Struct.* **79**:4 (2007), 581–589.

[Usik 1994] L. Usik, "Equivalent continuum models of large platelike lattice structures", *Int. J. Solids Struct.* **31**:4 (1994), 457–467.

[Xiao et al. 2005] J. R. Xiao, B. A. Gama, and J. W. Gillespie Jr., "An analytical molecular structural mechanics model for the mechanical properties of carbon nanotubes", *Int. J. Solids Struct* **42**:11–12 (2005), 3075–3092.

[Yakobson et al. 1996] B. I. Yakobson, C. J. Brabec, and J. Bernholc, "Nanomechanics of carbon tubes: instabilities beyond linear response", *Phys. Rev. Lett.* **76** (1996), 2511–2514.

[Yu et al. 2000] M.-F. Yu, B. S. Files, S. Arepalli, and R. S. Ruoff, "Tensile loading of ropes of single wall carbon nanotubes and their mechanical properties", *Phys. Rev. Lett.* **84** (2000), 5552–5555.

[Yuan and Liew 2009] J. Yuan and K. Liew, "Effects of vacancy defect reconstruction on the elastic properties of carbon nanotubes", *Carbon* **47**:6 (2009), 1526–1533.

[Zandiatashbar et al. 2014] A. Zandiatashbar, G.-H. Lee, S. J. An, S. Lee, N. Mathew, M. Terrones, T. Hayashi, C. R. Picu, J. Hone, and N. Koratkar, "Effect of defects on the intrinsic strength and stiffness of graphene", *Nat. Comm.* **5** (2014), 1–8.

[Zhang et al. 2002] P. Zhang, Y. Huang, P. H. Geubelle, P. A. Klein, and K. C. Hwang, "The elastic modulus of single-wall carbon nanotubes: a continuum analysis incorporating interatomic potentials", *Int. J. Solids Struct.* **39**:13–14 (2002), 3893–3906.

GUSTAVO DOMÍNGUEZ-RODRÍGUEZ: gashdmi@gmail.com
Centro de Investigación Científica de Yucatán, Calle 43 No. 130, Colonia Chuburná de Hidalgo, 97200 Mérida,, Yucatan, Mexico

ADARSH CHAURASIA: adarsh.chaurasia@vt.edu
Department of Engineering Science and Mechanics, Virginia Polytechnic Institute and State University, 495 Ol d Turner Street, Norris Hall, Room 223, Blacksburg, VA 24061, United States

GARY SEIDEL: gary.seidel@vt.edu
Department of Aerospace and Ocean Engineering, Virginia Polytechnic Institute and State University, 228 Randolph Hall (0203), Blacksburg, VA 24061, United States

ALEJANDRO TAPIA: jorge.tapia@correo.uady.mx
Facultad de Ingeniería, Universidad Autónoma de Yucatán, Av. Industrias no Contaminantes por Periférico, Norte, Cordemex, 97310 Mérida,, Mexico

FRANCIS AVILÉS: faviles@cicy.mx
Centro de Investigación Científica de Yucatán, Calle 43 No. 130, Colonia Chuburná de Hidalgo, 97200 Mérida,, Mexico

COUPLED THERMALLY GENERAL IMPERFECT AND MECHANICALLY COHERENT ENERGETIC INTERFACES SUBJECT TO IN-PLANE DEGRADATION

ALI ESMAEILI, PAUL STEINMANN AND ALI JAVILI

To date, the effects of interface in-plane damage on the thermomechanical response of a thermally general imperfect (GI) and mechanically coherent energetic interface are not taken into account. A thermally GI interface allows for a discontinuity in temperature as well as in the normal heat flux across the interface. A mechanically coherent energetic interface permits a discontinuity in the normal traction but not in the displacement field across the interface. The temperature of a thermally GI interface is a degree of freedom and is computed using a material parameter known as the sensitivity. The current work is the continuation of the model developed by Esmaeili et al. (2016a) where a degrading highly conductive (HC) and mechanically coherent energetic interface is considered. An HC interface only allows for the jump in normal heat flux and not the jump in temperature across the interface. In this contribution, a thermodynamically consistent theory for thermally GI and mechanically coherent energetic interfaces subject to in-plane degradation is developed. A computational framework to model this class of interfaces using the finite element method is established. In particular, the influence of the interface in-plane degradation on the sensitivity is captured. To this end, the equations governing a fully nonlinear transient problem are given. They are solved using the finite element method. The results are illustrated through a series of three-dimensional numerical examples for various interfacial parameters. In particular, a comparison is made between the results of the intact and the degraded thermally GI interface formulation.

A list of symbols can be found on page 310.

1. Introduction

Interfaces possess different thermomechanical properties from those of the bulk. The interface properties become dominating as the length scale reduces: the smaller the scale, the larger the interface area to bulk volume ratio [Cammarata 1994; Dingreville et al. 2005; Duan et al. 2009]. This dominating influence motivates one to devise a more realistic model to better capture the physics of interface materials. The following are a few additional motivations to develop a more general interface model:

- increasing applications of thermal interfaces [Prasher 2006],

- unusual thermal behavior of surface and interfaces at the nanoscale [Berber et al. 2000; Che et al. 2000; Cahill et al. 2003; Prasher 2005],

- the study of interface mechanical characteristics by the vast majority of the literature is mainly based on cohesive zone models.

Therefore, in this contribution, we follow the work of Javili et al. [2014] and Kaessmair et al. [2014], where the interface theory was extended to mechanically coherent energetic and thermally general imperfect (GI) interfaces. A thermally GI interface permits discontinuities in both temperature and normal heat flux. The extreme cases of thermally GI interfaces are highly conductive (HC) and lowly conductive (LC) interfaces, where the former allows a discontinuity in the normal heat flux but not in the temperature across the interface, and the latter permits a discontinuity in the temperature but not in the normal heat flux across the interface. Among the various thermal interfaces introduced above, an HC interface is termed thermally coherent due to the vanishing temperature jump. We point out that the thermally GI interface presented here may be specialized to all the other types of thermal interfaces. For further details on the different types of thermal imperfections, see [Esmaeili et al. 2016a; 2016b; Kaessmair et al. 2014; Javili et al. 2014] and references therein.

A mechanically coherent energetic interface is based on the *interface elasticity theory* proposed in [Gurtin and Murdoch 1975; Murdoch 1976]. Note that the coherence of the interface refers to the continuity in the displacement field across the interface. This manuscript is limited to mechanically coherent energetic interfaces. For further details, see, for instance, [Moeckel 1975; Daher and Maugin 1986; dell'Isola and Romano 1987; Gurtin 1998; Steigmann and Ogden 1999; Fried and Todres 2005; Fried and Gurtin 2007; Levitas and Javanbakht 2010; Javili and Steinmann 2010; Benveniste and Miloh 2001; Sharma et al. 2003; Dingreville et al. 2005; Duan et al. 2005a; 2005b; 2009; Benveniste 2013; Huang and Sun 2007; Fischer and Svoboda 2010; Yvonnet et al. 2011; Altenbach et al. 2012; Davydov et al. 2013] and the references therein. A restriction of the interface elasticity theory is that it only captures elastic interface behavior.

The nucleation of microvoids and strong discontinuities, such as cracks, can act as shields or amplify stress intensity in other regions of an interface. Consequently, this can influence the temperature distribution and thus the thermomechanical response of a body. Noting that the interface elasticity theory can only capture elastic behavior of energetic interfaces, the development of a more general interface model, in which interface inelasticity is taken into account, seems necessary.

Very recently in [Esmaeili et al. 2016a] we have considered thermally highly conductive (HC) interfaces in a thermomechanical body, whereby due to the highly conductive property the (otherwise mechanically coherent) interfaces allow for jumps in the normal heat flux. Moreover, they are equipped with interface stresses that are coupled to in-plane damage. In this contribution, we formulate a follow up version of [Esmaeili et al. 2016a] that generalizes the thermal part of the above interfaces to the thermally GI case, whereas the mechanical part is as before. Thereby this formulation embraces the two limiting cases of the previous HC interfaces (jump in normal heat flux) and the lowly conductive (LC) Kapitza interfaces, see [Esmaeili et al. 2016b], that allow for a jump in the temperature. Thus arbitrary combinations of HC and LC (jump in normal heat flux and jump in the temperature) are analyzed numerically.

To take into account the in-plane damage, a nonlocal continuum damage approach is utilized. For further details on this approach with application to bulk materials, see, for instance, [Kachanov 1958; Rabotnov 1963; Chaboche 1981; de Souza Neto and Perić 1996; de Souza Neto et al. 1998; Steinmann et al. 1994], among others. There are a few reasons to use a nonlocal damage model: first, mesh-objective finite element simulation of strain softening materials; second, determining the growth of microcracks by the energy release from the volume encompassing the microcrack [Bažant and Xi 1991]; third, the influence of the presence of a microcrack on the stress level of other neighboring microcracks; and finally

capturing size effects [Bažant and Jirásek 2002]. The nonlocality in this work is of integral-type, which then requires the use of an interactive (cut-off) radius, capturing size effects. The interactive radius is a function of the molecular structure of the intact material and the distribution and growth of the microc-racks in the damaging material. It is not yet well-established how to determine the interactive radius from experiments (see [Bažant and Jirásek 2002] for further details). The degradation of the interface material here is measured using a tangential (in-plane) damage variable denoted by $\overline{D}_{\parallel}$. Consequently, as the damage variable evolves, all the mechanical and in-plane thermal properties of the interface are reduced. However, the out-of-plane thermal properties, i.e., the interface Kapitza resistance coefficient $\bar{r}_Q^0$ and the sensitivity $\bar{s}_0$, will increase as the damage evolves. The damage variable here is a function of the interface effective (undamaged) free energy $\overline{\Psi}^0$, which in turn depends on both the interface temperature $\overline{\Theta}$ and the interface deformation gradient $\overline{F}$. Here, no distinction between thermal and mechanical damage has been made for the sake of simplicity and the fact that such distinction has not yet been physically motivated.

In summary, the key contributions of this work are as follows:

- To derive the governing equations of a thermomechanical solid possessing thermally GI and mechanically coherent energetic interface subject to in-plane degradation, within the fully nonlinear three dimensional setting.

- To present a thermodynamically consistent formulation and derive the dissipation inequality on the interface.

- To account for the effects of in-plane damage on the thermomechanical properties of the interface.

- To derive the thermal and mechanical weak forms.

- To derive the consistent tangent stiffness matrices in the bulk and on the interface.

- To present details of the computation of solids possessing thermally GI and mechanically coherent energetic interfaces within the three-dimensional, nonlinear and transient setting.

- To illustrate the theory with the help of numerical examples using the finite element method.

This paper is organized as follows. First the notation and certain key concepts are briefly introduced. Section 2 summarizes the kinematics of nonlinear continuum mechanics. The local governing equations, including the additional contributions from the interface, together with the constitutive relations are given in Section 3. A numerical framework for the interface is established in Section 4. The framework includes the weak formulation of the governing equations, the corresponding finite element implementation and the derivation of the consistent stiffness matrices. A series of numerical examples, based on the finite element approximation of the weak form, is presented in Section 5 to elucidate the theory. Section 6 concludes this work.

2. Problem definition

This section summarizes the kinematics of nonlinear continuum mechanics, including thermally general imperfect and mechanically coherent energetic interfaces and introduces the notation adopted here. Further details on the kinematics of deformable interfaces can be found in [Javili et al. 2013]. All over-lined
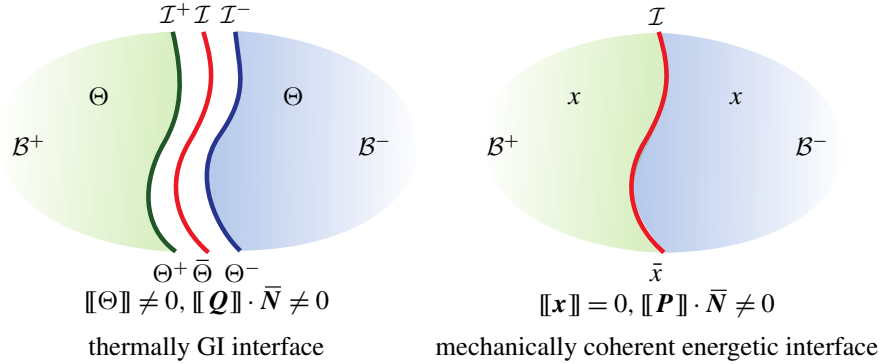
$\mathcal{I}^+\mathcal{I}\ \mathcal{I}^-$ $\mathcal{I}$

Θ Θ x x

$\mathcal{B}^+$ $\mathcal{B}^-$ $\mathcal{B}^+$ $\mathcal{B}^-$

$\Theta^+\ \bar{\Theta}\ \Theta^-$ $\bar{x}$

$[\![\Theta]\!]\neq 0,\ [\![\boldsymbol{Q}]\!]\cdot\bar{\boldsymbol{N}}\neq 0$ $[\![\boldsymbol{x}]\!]=0,\ [\![\boldsymbol{P}]\!]\cdot\bar{\boldsymbol{N}}\neq 0$

thermally GI interface   mechanically coherent energetic interface

Figure 1. Thermally general imperfect interface, left, and mechanically coherent energetic interface, right. The interface in this work is mechanically coherent, thus no jump in deformation is allowed across the interface, $[\![\boldsymbol{\varphi}]\!]=\mathbb{0}$, $[\![\boldsymbol{x}]\!]=\mathbb{0}$, and energetic, thus the jump of the normal traction across the interface does not vanish, i.e., $[\![\boldsymbol{P}]\!]\cdot\bar{\boldsymbol{N}}\neq\mathbb{0}$. A thermally GI interface allows for the jump in temperature $[\![\Theta]\!]\neq 0$, and in normal heat flux $[\![\boldsymbol{Q}]\!]\cdot\bar{\boldsymbol{N}}\neq 0$ across the interface. The bulk and interface are denoted here by $\mathcal{B}$ and $\mathcal{I}$. The normal to the interface is denoted by $\bar{\boldsymbol{N}}$, see Figure 2. The in-plane degradation of the interface causes the degradation of mechanical and thermal properties of the interface through a tangential damage variable $\bar{D}_\parallel$.

quantities correspond to the interface.[1] The List of symbols gathers a list of notations frequently used in this manuscript.

Consider a continuum body $\mathcal{B}$ that takes the material configuration $\mathcal{B}_0\subset\mathbb{E}^3$ at time $t=0$, and the spatial configuration $\mathcal{B}_t$ at $t>0$, as depicted in Figure 1. The body $\mathcal{B}$ is partitioned into two disjoint subdomains, $\mathcal{B}_0^+$ and $\mathcal{B}_0^-$, by an interface $\mathcal{I}_0$, thus the bulk is defined by $\mathcal{B}_0:=\mathcal{B}_0^+\bigcup\mathcal{B}_0^-$, with reference placements of material particles labeled $\boldsymbol{X}$. The two sides of the interface $\mathcal{I}_0$ are denoted $\mathcal{I}_0^+:=\partial\mathcal{B}_0^+\bigcap\mathcal{I}_0$ and $\mathcal{I}^-:=\partial\mathcal{B}_0^-\bigcap\mathcal{I}_0$. The material particles on the interface are labeled $\bar{\boldsymbol{X}}$. The outward unit normal to $\partial\mathcal{B}_0$ is denoted $\boldsymbol{N}$. The outward unit normal to the boundary of the interface $\partial\mathcal{I}_0$, tangent to the interface $\mathcal{I}_0$, is denoted $\widetilde{\boldsymbol{N}}$. The unit normal to $\mathcal{I}_0$ is denoted $\bar{\boldsymbol{N}}$, whose direction is conventionally taken to point from the negative side of the interface to the positive side. The spatial counterparts of the various unit normals are $\boldsymbol{n}$, $\widetilde{\boldsymbol{n}}$ and $\bar{\boldsymbol{n}}$, respectively. The deformation maps of the bulk, and the negative and positive sides of the interface are denoted $\boldsymbol{\varphi}$, $\boldsymbol{\varphi}^-$ and $\boldsymbol{\varphi}^+$, respectively. The restriction of the motion $\boldsymbol{\varphi}$ to the interface is

---

[1]Direct notation is adopted throughout. Occasional use is made of index notation, the summation convention for repeated indices being implied. The three-dimensional Euclidean space is denoted by $\mathbb{E}^3$. The scalar product of two vectors $\boldsymbol{a}$ and $\boldsymbol{b}$ is denoted by $\boldsymbol{a}\cdot\boldsymbol{b}=[\boldsymbol{a}]_i[\boldsymbol{b}]_i$. The scalar product of two second-order tensors $\boldsymbol{A}$ and $\boldsymbol{B}$ is denoted by $\boldsymbol{A}:\boldsymbol{B}=[\boldsymbol{A}]_{ij}[\boldsymbol{B}]_{ij}$. The composition of two second-order tensors $\boldsymbol{A}$ and $\boldsymbol{B}$, denoted $\boldsymbol{A}\cdot\boldsymbol{B}$, is a second-order tensor with coefficients $[\boldsymbol{A}\cdot\boldsymbol{B}]_{ij}=[\boldsymbol{A}]_{im}[\boldsymbol{B}]_{mj}$. The nonstandard products of a fourth-order tensor $\mathbb{C}$ and a vector $\boldsymbol{b}$ is defined by $[\boldsymbol{b}\vdots\mathbb{C}]_{ikl}=[\mathbb{C}]_{ijkl}[\boldsymbol{b}]_j$. The action of a second-order tensor $\boldsymbol{A}$ on a vector $\boldsymbol{a}$ is given by $[\boldsymbol{A}\cdot\boldsymbol{a}]_i=[\boldsymbol{A}]_{ij}[\boldsymbol{a}]_j$. The standard product of a fourth-order tensor $\mathbb{C}$ and a second-order tensor $\boldsymbol{A}$ is defined by $[\mathbb{C}:\boldsymbol{A}]_{ij}=[\mathbb{C}]_{ijkl}[\boldsymbol{A}]_{kl}$. The dyadic product of two vectors $\boldsymbol{a}$ and $\boldsymbol{b}$ is a second-order tensor $\boldsymbol{D}=\boldsymbol{a}\otimes\boldsymbol{b}$ with $[\boldsymbol{D}]_{ij}=[\boldsymbol{a}]_i[\boldsymbol{b}]_j$. Two nonstandard dyadic products of two second-order tensors $\boldsymbol{A}$ and $\boldsymbol{B}$ are the fourth-order tensors $[\boldsymbol{A}\,\bar{\otimes}\,\boldsymbol{B}]_{ijkl}=[\boldsymbol{A}]_{ik}[\boldsymbol{B}]_{jl}$ and $[\boldsymbol{A}\,\underline{\otimes}\,\boldsymbol{B}]_{ijkl}=[\boldsymbol{A}]_{il}[\boldsymbol{B}]_{jk}$. The average and jump of a quantity $\{\bullet\}$ over an interface are defined by $\{\!\{\bullet\}\!\}=\frac{1}{2}[\{\bullet\}^++\{\bullet\}^-]$ and $[\![\{\bullet\}]\!]=\{\bullet\}^+-\{\bullet\}^-$, respectively.
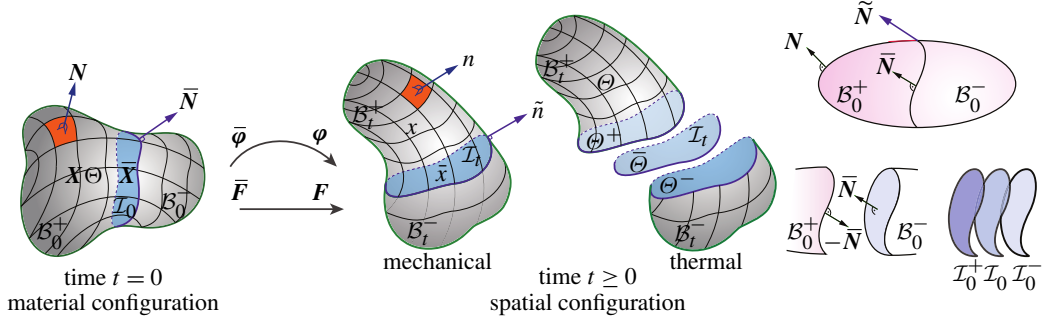
Figure 2. The bulk domain $\mathcal{B}_0$, the bulk subdomains $\mathcal{B}_0^{\pm}$, the interface $\mathcal{I}_0$, the two sides of the interface $\mathcal{I}_0^{\pm}$ and the unit normals to the surface $\boldsymbol{N}$, the interface $\bar{\boldsymbol{N}}$, and boundary of the interface $\widetilde{\boldsymbol{N}}$, all defined in the material configuration. The bulk, interface and the two sides of interface deformation maps, denoted as $\boldsymbol{\varphi}$, $\bar{\boldsymbol{\varphi}}$ and $\boldsymbol{\varphi}^{\pm}$, respectively, map the material configuration to the spatial configuration at time t. The bulk domain $\mathcal{B}_t$, the bulk subdomains $\mathcal{B}_t^{\pm}$, the interface $\mathcal{I}_t$ and its two sides $\mathcal{I}_t^{\pm}$, the unit normals to the surface $\boldsymbol{n}$, interface $\bar{\boldsymbol{n}}$, and boundary of the interface $\widetilde{\boldsymbol{n}}$, all defined in the spatial configuration. The bulk temperatures on plus and minus side of the interface and the interface temperature are denoted by Θ^+, Θ^- and $\bar{\Theta}$, respectively. The interface unit normal is pointing from the negative side of the interface to the positive side. The bulk and (rank-deficient) interface deformation gradients are $\boldsymbol{F}$ and $\bar{\boldsymbol{F}}$, respectively. The interface is mechanically coherent and thermally noncoherent.

defined by $\bar{\boldsymbol{\varphi}}$. The current placements of particles in the bulk and on the two sides of the interface are denoted $\boldsymbol{x}$ and $\boldsymbol{x}^{\mp}$ where the spatial placement of particles on the interface are designated as $\bar{\boldsymbol{x}}$. One should note that $\boldsymbol{\varphi}^+ = \boldsymbol{\varphi}^- = \bar{\boldsymbol{\varphi}}$ and $\boldsymbol{x}^+ = \boldsymbol{x}^- = \bar{\boldsymbol{x}}$ for mechanically coherent interfaces. This means the interface placement is always between the two lateral sides of the interface. The interface and bulk temperature on two sides of the interface are denoted by $\bar{\Theta}$, Θ^+ and Θ^-, respectively.

Remark 1. Since the interface is thermally general imperfect, the bulk temperatures Θ^+ and Θ^- can differ from each other. This is in contrast with a highly conductive interface where the jump of temperature across the interface vanishes and thus $\bar{\Theta} = \Theta^+ = \Theta^-$. Moreover, on a thermally general imperfect interface, the relation between the bulk and the interface temperature $\bar{\Theta}$ is (in general) unknown. In other words, the interface temperature does not necessarily take a value between the bulk temperatures on the two sides of the interface (for further details, see [Javili et al. 2014; Esmaeili et al. 2016a]).

The bulk and the (rank-deficient) interface deformation gradients $\boldsymbol{F}$ and $\bar{\boldsymbol{F}}$, together with the corresponding velocities $\boldsymbol{V}$ and $\bar{\boldsymbol{V}}$ are respectively defined by

$$\boldsymbol{F}(\boldsymbol{X}, t) := \operatorname{Grad} \boldsymbol{\varphi}(\boldsymbol{X}, t), \quad \boldsymbol{V} := \mathrm{D}_t \boldsymbol{\varphi}(\boldsymbol{X}, t) \quad \text{and} \quad \bar{\boldsymbol{F}}(\bar{\boldsymbol{X}}, t) := \overline{\operatorname{Grad}} \, \bar{\boldsymbol{\varphi}}(\bar{\boldsymbol{X}}, t), \quad \bar{\boldsymbol{V}} := \mathrm{D}_t \bar{\boldsymbol{\varphi}}(\bar{\boldsymbol{X}}, t). \quad (1)$$

Thereby the interface gradient and divergence operators respectively read

$$\overline{\operatorname{Grad}}\{\bullet\} := \operatorname{Grad}\{\bullet\} \cdot \bar{\boldsymbol{I}} \quad \text{and} \quad \overline{\operatorname{Div}}\{\bullet\} := \overline{\operatorname{Grad}}\{\bullet\} : \bar{\boldsymbol{I}} \quad \text{with} \quad \bar{\boldsymbol{I}} := \boldsymbol{I} - \bar{\boldsymbol{N}} \otimes \bar{\boldsymbol{N}}, \quad (2)$$

where $\bar{\boldsymbol{I}}$ and $\boldsymbol{I}$ denote the interface and bulk unit tensors. Their spatial counterparts are denoted $\bar{\boldsymbol{i}}$ and $\boldsymbol{i}$. Finally the bulk and interface Jacobians are denoted by

$$J := \det \boldsymbol{F} > 0 \quad \text{and} \quad \bar{J} := \overline{\det} \, \bar{\boldsymbol{F}} > 0,$$

respectively, with $\overline{\det}\{\bullet\}$ denoting the area determinant [Steinmann 2008].

3. Governing equations

The local balance equations of force, energy and entropy in the bulk and on the interface together with the associated boundary conditions are listed in Table 1 (for further details, see [Esmaeili et al. 2016a]). The considered interface model deals with interfaces that are

- mechanically coherent, $[\![\boldsymbol{\varphi}]\!] = \mathbb{0}$,

- mechanically energetic, thus $[\![\boldsymbol{P}]\!] \cdot \bar{\boldsymbol{N}} \neq \mathbb{0}$ and

- thermally general imperfect, $[\![\boldsymbol{Q}]\!] \cdot \bar{\boldsymbol{N}} \neq 0$ and $[\![\Theta]\!] \neq 0$.

The third property, i.e., thermal general imperfection of the interface, is characterized by allowing a jump both in the temperature and the normal heat flux ($[\![\Theta]\!] \neq 0$ and $[\![\boldsymbol{Q}]\!] \cdot \bar{\boldsymbol{N}} \neq 0$, respectively) across the interface. Also note that a thermally GI interface is fully dissipative. See Section 3 for further elaborations.

Remark 2. In what follows we briefly discuss different kinds of thermal interfaces:

force balance:	$\operatorname{Div} \boldsymbol{P} + \boldsymbol{B}^{\mathrm{p}} = \mathbb{0}$	in $\mathcal{B}_0$	$\widehat{\boldsymbol{B}}^{\mathrm{p}} = \boldsymbol{P} \cdot \boldsymbol{N}$	on $\partial \mathcal{B}_0^{\mathrm{N}}$
	$\overline{\operatorname{Div}} \, \bar{\boldsymbol{P}} + \bar{\boldsymbol{B}}^{\mathrm{p}} = -[\![\boldsymbol{P}]\!] \cdot \bar{\boldsymbol{N}}$	on $\mathcal{I}_0$	$\widetilde{\boldsymbol{B}}^{\mathrm{p}} = \bar{\boldsymbol{P}} \cdot \widetilde{\boldsymbol{N}}$	on $\partial \mathcal{I}_0^{\mathrm{N}}$
energy:	$-\boldsymbol{P} : \operatorname{Grad} \boldsymbol{V} + \operatorname{Div} \boldsymbol{Q} - Q^{\mathrm{p}} + \mathrm{D}_t \mathcal{E} = 0$	in $\mathcal{B}_0$	$\widehat{Q}^{\mathrm{p}} = -\boldsymbol{Q} \cdot \boldsymbol{N}$	on $\partial \mathcal{B}_0^{\mathrm{N}}$
	$-\bar{\boldsymbol{P}} : \overline{\operatorname{Grad}} \, \bar{\boldsymbol{V}} + \overline{\operatorname{Div}} \, \bar{\boldsymbol{Q}} - \bar{Q}^{\mathrm{p}} + \mathrm{D}_t \bar{\mathcal{E}} = -[\![\boldsymbol{Q}]\!] \cdot \bar{\boldsymbol{N}}$	on $\mathcal{I}_0$		
entropy:	$\operatorname{Div} \boldsymbol{H} - H^{\mathrm{p}} + \mathrm{D}_t \Xi \geq 0$	in $\mathcal{B}_0$	$\widehat{H}^{\mathrm{p}} = -\boldsymbol{H} \cdot \boldsymbol{N}$	on $\partial \mathcal{B}_0^{\mathrm{N}}$
	$\overline{\operatorname{Div}} \, \bar{\boldsymbol{H}} - \bar{H}^{\mathrm{p}} + \mathrm{D}_t \bar{\Xi} \geq -[\![\boldsymbol{H}]\!] \cdot \bar{\boldsymbol{N}}$	on $\mathcal{I}_0$	$\widetilde{H}^{\mathrm{p}} = -\bar{\boldsymbol{H}} \cdot \widetilde{\boldsymbol{N}}$	on $\partial \mathcal{I}_0^{\mathrm{N}}$

$\boldsymbol{B}^{\mathrm{p}}$	force vector per unit volume	$\widehat{\boldsymbol{B}}^{\mathrm{p}}$	surface traction per unit area
$\bar{\boldsymbol{B}}^{\mathrm{p}}$	force vector per unit area	$\widetilde{\boldsymbol{B}}^{\mathrm{p}}$	curve traction per unit length
$\boldsymbol{Q}$	bulk heat flux vector per unit area	$\bar{\boldsymbol{Q}}$	interface heat flux vector per unit length
$\boldsymbol{H}$	bulk entropy flux vector per unit area	$\bar{\boldsymbol{H}}$	interface entropy flux vector per unit length
Q^{p}	bulk heat source per unit volume	$\widehat{Q}^{\mathrm{p}}$	surface heat source per unit area
$\bar{Q}^{\mathrm{p}}$	interface heat source per unit area	$\widetilde{Q}^{\mathrm{p}}$	curve heat source per unit length
H^{p}	bulk entropy source per unit volume	$\widehat{H}^{\mathrm{p}}$	surface entropy source per unit area
$\bar{H}^{\mathrm{p}}$	interface entropy source per unit area	$\widetilde{H}^{\mathrm{p}}$	curve entropy source per unit length
$\mathcal{E}$	bulk internal energy per unit volume	$\bar{\mathcal{E}}$	interface internal energy per unit area

Table 1. Localized force, energy and entropy balances in the bulk and on the interface in the material configuration. The notation $\{\bullet\}^{\mathrm{p}}$ is to denote prescribed quantities. Balance of angular momentum results in the symmetry of the bulk Cauchy stress, i.e., $\boldsymbol{P} \cdot \boldsymbol{F}^t = \boldsymbol{F} \cdot \boldsymbol{P}^t$, and the interface Cauchy stress, i.e., $\bar{\boldsymbol{P}} \cdot \bar{\boldsymbol{F}}^t = \bar{\boldsymbol{F}} \cdot \bar{\boldsymbol{P}}^t$, in the material configuration.

- A thermally perfect interface is recovered when $[\![\boldsymbol{Q}]\!]\cdot\overline{N} = 0$ and $[\![\Theta]\!] = 0$.

- A highly conductive interface imposes a vanishing temperature jump across the interface while allowing for the jump of normal heat flux across the interface, i.e., $[\![\Theta]\!] = 0$ and $[\![\boldsymbol{Q}]\!]\cdot\overline{N} \neq 0$. Note that a continuous temperature distribution across the interface does not necessary imply a HC interface (see [Javili et al. 2014] for further details). Furthermore, an HC interface is nondissipative due to the vanishing temperature jump across the interface, which results in the interface temperature being identical to the bulk temperatures on the two sides of the interface.

- A lowly conductive (LC) interface allows for a temperature jump but not for a jump in the normal heat flux across the interface, i.e., $[\![\Theta]\!] \neq 0$ and $[\![\boldsymbol{Q}]\!]\cdot\overline{N} = 0$. This model is subject to Kapitza's assumption of thermal resistance. Note that an LC interface is semidissipative (possessing only one dissipation contribution, see Section 3 for further discussions). For this interface, a connection between the interface and the bulk temperature (in general) can not be drawn.

- A semidissipative (SD) interface is a generalization of the LC interface so that the jump in both the temperature and the normal heat flux is admissible, i.e., $[\![\boldsymbol{Q}]\!]\cdot\overline{N} \neq 0$ and $[\![\Theta]\!] \neq 0$. Analogous to the LC interface, the same dissipation contribution is nonvanishing for an SD interface. However, unlike an LC interface, the SD interface imposes a relation between the interface and the bulk temperature, or more precisely between what we call interface and bulk coldness. The coldness here is defined as the inverse of the temperature.

- A fully dissipative (FD) interface is a GI interface similar to an SD interface in the sense that both $[\![\boldsymbol{Q}]\!]\cdot\overline{N} \neq 0$ and $[\![\Theta]\!] \neq 0$ are admissible. Nonetheless, an FD interface is generalized to possess two dissipation contributions. Consequently, a relation (in general) between interface and bulk temperature cannot be established (analogously to an LC interface). Additionally, for an FD interface, the interface temperature shall be considered as an independent degree of freedom.

Furthermore, both thermal and mechanical properties of the interface are affected by the interface in-plane degradation. In doing so, a reduction factor $[1 - \overline{D}_\parallel]$ is introduced, which reduces the mechanical and in-plane thermal properties of the interface as the damage $\overline{D}_\parallel$ evolves. The out-of-plane thermal properties of the interface, the sensitivity $\bar{s}_0$ and the Kapitza thermal resistance $\bar{r}_Q^0$, are inversely affected by the reduction factor, i.e., $\bar{s} = \bar{s}_0/[1 - \overline{D}_\parallel]$ and $\bar{r}_Q = \bar{r}_Q^0/[1 - \overline{D}_\parallel]$. Note that in this work the damage variable is a function of the nonlocal equivalent distortion $\overline{F}_{\mathrm{nloc}}$, which in turn depends on the interface deformation gradient $\overline{F}$ and temperature $\overline{\Theta}$. The interface Piola stress $\overline{P}$ is a superficial tensor field possessing the property $\overline{P} \cdot \overline{N} = \mathbb{0}$. It is noteworthy to mention that the interface is mechanically coherent and, due to the interface energetics, a discontinuity in the traction across the interface is allowed and hence $[\![\boldsymbol{P}]\!]\cdot\overline{N} \neq \mathbb{0}$.

Next are the bulk and interface free energies. The corresponding constitutive relations and temperature evolution equations are given in Table 2. Note that $0 \leq \overline{D}_\parallel(\overline{F}, \overline{\Theta}) \leq 1$ and $\bar{\vartheta}$ is an internal variable; $\boldsymbol{k}$ and $\bar{\boldsymbol{k}}_0$ denote the bulk and interface positive (semi) definite thermal conductivity tensors. For thermally isotropic materials in the spatial configuration, $\boldsymbol{k} = k\boldsymbol{i}$ and $\bar{\boldsymbol{k}}_0 = \bar{k}_0\bar{\boldsymbol{i}}$, where the scalars $k \geq 0$ and $\bar{k}_0 \geq 0$ are the thermal conductivity coefficients in the bulk and on the interface, respectively. The heat capacity coefficients in the bulk and on the interface are denoted by c_F and $\bar{c}_{\overline{F}} = [1 - \overline{D}_\parallel]\bar{c}_{\overline{F}}^0$, where $\bar{c}_{\overline{F}}^0$ is the interface heat capacity coefficient associated with the undamaged (virgin) state of the interface material.

free energy:	$\Psi \equiv \Psi(\boldsymbol{F}, \Theta)$	in $\mathcal{B}_0$
	$\overline{\Psi} \equiv \overline{\Psi}(\overline{\boldsymbol{F}}, \overline{\Theta}, \overline{D}_\parallel, \bar{\vartheta}) = [1 - \overline{D}_\parallel]\overline{\Psi}^0$	on $\mathcal{I}_0$
constitutive relations:	$\boldsymbol{P} := \partial \Psi / \partial \boldsymbol{F}$ and $\Xi := -\partial \Psi / \partial \Theta$	in $\mathcal{B}_0$
	$\overline{\boldsymbol{P}} := \partial \overline{\Psi} / \partial \overline{\boldsymbol{F}} = [1 - \overline{D}_\parallel]\overline{\boldsymbol{P}}_0$ and $\overline{\Xi} := -\partial \overline{\Psi} / \partial \overline{\Theta} = [1 - \overline{D}_\parallel]\overline{\Xi}^0$	on $\mathcal{I}_0$
	$\boldsymbol{Q} = -J\boldsymbol{F}^{-1} \cdot \boldsymbol{k} \cdot \boldsymbol{F}^{-\mathrm{t}} \cdot \mathrm{Grad}\,\Theta$	in $\mathcal{B}_0$
	$\overline{\boldsymbol{Q}} = -\bar{J}\overline{\boldsymbol{F}}^{-1} \cdot [1 - \overline{D}_\parallel]\bar{\boldsymbol{k}}_0 \cdot \overline{\boldsymbol{F}}^{-\mathrm{t}} \cdot \overline{\mathrm{Grad}}\,\overline{\Theta}$	on $\mathcal{I}_0$
temperature evolution:	$c_F \mathrm{D}_t \Theta = -\mathrm{Div}\,\boldsymbol{Q} + \Theta \partial_\Theta \boldsymbol{P} : \mathrm{D}_t \boldsymbol{F} + Q^{\mathrm{p}}$ with $c_F := -\Theta \partial^2 \Psi / \partial \Theta^2$	in $\mathcal{B}_0^{\mathrm{N}}$
	$\bar{c}_{\overline{F}} \mathrm{D}_t \overline{\Theta} = -\overline{\mathrm{Div}}\,\overline{\boldsymbol{Q}} + \overline{\Theta} \partial_{\overline{\Theta}} \overline{\boldsymbol{P}} : \mathrm{D}_t \overline{\boldsymbol{F}} + \overline{Q}^{\mathrm{p}} - [\![\boldsymbol{Q}]\!] \cdot \overline{\boldsymbol{N}}$ with $\bar{c}_{\overline{F}} := -[1 - \overline{D}_\parallel]\overline{\Theta} \partial^2 \overline{\Psi}^0 / \partial \overline{\Theta}^2$	on $\mathcal{I}_0^{\mathrm{N}}$

Table 2. Bulk and interface free energies, the corresponding constitutive relations and temperature evolution equations.

To proceed, a Helmholtz energy[2] is considered for the interface containing the following arguments [Esmaeili et al. 2016a]:

$$\overline{\Psi}(\overline{\boldsymbol{F}}, \overline{\Theta}, \overline{D}, \bar{\vartheta}) = [1 - \overline{D}]\overline{\Psi}_0(\overline{\boldsymbol{F}}, \overline{\Theta}) + \int_0^{\bar{\vartheta}} \overline{\mathcal{H}}(\bar{\vartheta}^*)\,\mathrm{d}\bar{\vartheta}^*, \tag{3}$$

where $\overline{\mathcal{H}}(\bar{\vartheta})$ denotes a monotonically increasing function depending on the internal variable $\bar{\vartheta}$. Now by differentiating (3) with respect to time, particularizing the Clausius–Plank inequality and making use of the constitutive relations, one expresses the interface reduced dissipation $\overline{\mathcal{D}}_{\mathrm{red}}$ as (for further details, see [Esmaeili et al. 2016a])

$$\overline{\mathcal{D}}_{\mathrm{red}} = \underbrace{\overline{Y}\dot{\overline{D}}_\parallel - \overline{\mathcal{H}}(\bar{\vartheta})\dot{\bar{\vartheta}}}_{\overline{\mathcal{D}}_\parallel} + \underbrace{\overline{\Theta}\big[[\![\Theta^{-1}]\!]\{\!\{\boldsymbol{Q}\}\!\} - \big[\overline{\Theta}^{-1} - \{\!\{\Theta^{-1}\}\!\}\big][\![\boldsymbol{Q}]\!]\big] \cdot \overline{\boldsymbol{N}}}_{\overline{\mathcal{D}}_\nparallel} \geq 0 \text{ with } \overline{Y} = \overline{\Psi}^0(\overline{\boldsymbol{F}}, \overline{\Theta}) = -\frac{\partial \overline{\Psi}}{\partial \overline{D}_\parallel}, \tag{4}$$

where the quantity $\overline{Y}$ is the thermodynamic force conjugate to the interface damage variable $\overline{D}_\parallel$. Next, together with satisfying $\overline{\mathcal{D}}_\parallel \geq 0$, a damage condition $\overline{\Upsilon}$ is introduced as [Steinmann 1999]

$$\overline{\Upsilon}(\overline{Y}, \overline{\mathcal{H}}) = \bar{\upsilon}(\overline{Y}) - \overline{\mathcal{H}}(\bar{\vartheta}) \leq 0, \tag{5}$$

with $\bar{\upsilon}$ being a monotonically increasing function. The damage evolution law and the Kuhn–Tucker conditions can be obtained from the postulate of maximum dissipation using the Lagrange-multiplier method. Now by choosing $\bar{\upsilon}(\bullet) = \overline{\mathcal{H}}(\bullet)$, and defining the change of variables $\overline{F}_{\max} := f(\bar{\vartheta})$ and $\overline{F}_{\mathrm{nloc}} := f(\overline{Y})$ and assuming f to be a monotonically increasing function with the property $f(0) = 0$, an alternative damage condition to (5) takes the form extended to integral-type nonlocality [Esmaeili et al. 2016a]:

$$\overline{\phi}(\overline{F}_{\mathrm{nloc}}, \overline{F}_{\max}) = \overline{F}_{\mathrm{nloc}} - \overline{F}_{\max} \leq 0, \text{ with } \overline{F}_{\mathrm{nloc}}(\overline{\boldsymbol{x}}_{\mathrm{r}}) = \int_{\mathcal{I}_0} \overline{\omega}(\overline{\boldsymbol{x}}_{\mathrm{r}}, \overline{\boldsymbol{x}}_s)\overline{F}_{\mathrm{loc}}(\boldsymbol{x}_s)\,\mathrm{d}A \text{ and } \overline{F}_{\mathrm{loc}} := \sqrt{\frac{2\overline{Y}}{\overline{E}}}, \tag{6}$$

---

[2]The integral term in (3) is introduced in analogy with that of [Simo and Hughes 1998, §1.3.3] and is the energy storage in the material due to the accumulation of microscopic defects.
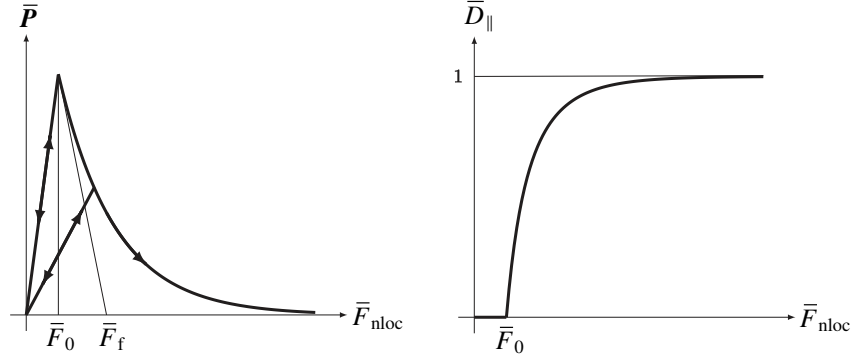
Figure 3. Stress vs. nonlocal equivalent distortion with exponential softening on the interface, left. Damage variable vs. nonlocal equivalent distortion associated with (8), right. The parameters $\bar{F}_0$ and $\bar{F}_f$ are the interface critical equivalent distortion and ductility response.

where $\bar{F}_{\max}(t) = \max_{s \in [0,\,t]}\{\bar{F}_0, \bar{F}_{\mathrm{nloc}}|_s\}$, $\bar{F}_0$ is the damage threshold, $\bar{F}_{\mathrm{loc}}$ is the local equivalent distortion, and $\bar{E}$ is the interface Young's modulus. Note that the damage variable is eventually simply a function of $\bar{F}_{\max}$, i.e., $\bar{D}_{\|} = \bar{\mathscr{D}}_{\|}(\bar{F}_{\max})$. In $(6)_2$, $\bar{\omega}(\bar{x}_{\mathrm{r}},\ \bar{x}_{\mathrm{s}})$ is a given nonlocal weight function depending on the geodesic distance $\bar{r} = \|\bar{x}_{\mathrm{r}} - \bar{x}_{\mathrm{s}}\|_{\mathcal{I}}$ between the source point $\bar{x}_{\mathrm{s}}$ and the receiver point $\bar{x}_{\mathrm{r}}$. On the interface, the weight function $\bar{\omega}$ here is defined as

$$\bar{\omega}(\bar{x}_{\mathrm{r}}, \bar{x}_{\mathrm{s}}) = \frac{\bar{\omega}_0(\bar{r})}{\int_{\mathcal{I}_0} \bar{\omega}_0(\bar{r}) \, dA} \quad \text{with} \quad \bar{\omega}_0(\bar{r}) = \begin{cases} [1 - \bar{r}^2/\bar{R}^2]^2 & \text{if } |\bar{r}| \leq \bar{R}, \\ 0 & \text{if } |\bar{r}| \geq \bar{R}, \end{cases} \tag{7}$$

where $\bar{\omega}_0(\bar{r})$ is a nonnegative and monotonically decreasing (for $\bar{r} \geq 0$) piecewise polynomial bell-shaped function. The interface interaction radius is denoted by $\bar{R}$. The damage function, relating $\bar{D}_{\|}$ to the history variable $\bar{F}_{\max}$, is given as follows (see Figure 3, right):

$$\bar{D}_{\|} = \bar{\mathscr{D}}_{\|}(\bar{F}_{\max}) = \begin{cases} 0 & \text{if } \bar{F}_{\max} \leq \bar{F}_0, \\ 1 - \dfrac{\bar{F}_0}{\bar{F}_{\max}} \exp\left(-\dfrac{\bar{F}_{\max} - \bar{F}_0}{\bar{F}_f - \bar{F}_0}\right) & \text{if } \bar{F}_{\max} \geq \bar{F}_0, \end{cases} \tag{8}$$

where $\bar{F}_f$ affects the ductility of the response. An illustration is depicted in Figure 3, left.

To satisfy $\bar{\mathcal{D}}_{\|} \geq 0$ in $(4)_1$, using the relation $[\![\Theta^{-1}]\!] = -[\![\Theta]\!]\{\!\{\Theta^{-1}\}\!\}\{\!\{\Theta\}\!\}^{-1}$, we enforce the fulfillment of the following two conditions:

$$^1\bar{\mathcal{D}}_{\|} = -[\![\Theta]\!]\{\!\{Q\}\!\} \cdot \bar{N} \geq 0 \quad \text{and} \quad ^2\bar{\mathcal{D}}_{\|} = -[\bar{\Theta}^{-1} - \{\!\{\Theta^{-1}\}\!\}][\![Q]\!] \cdot \bar{N} \geq 0. \tag{9}$$

Remark 3. For the interface considered here, both dissipation contributions in (9) are positive and hence the interface is termed fully dissipative. For an HC interface, both of these dissipation contributions vanish since $[\![\Theta]\!] = 0$. Both SD and LC interfaces allow for $^1\bar{\mathcal{D}}_{\|}$ to be nonzero since $[\![\Theta]\!] \neq 0$. The difference is that for an SD interface $[\![Q]\!] \cdot \bar{N} \neq 0$ and $[\bar{\Theta}^{-1} - \{\!\{\Theta^{-1}\}\!\}] = 0$, whereas for an LC interface $[\![Q]\!] \cdot \bar{N} = 0$ and a relation between the interface and the bulk temperatures is (in general) unknown (see also Remark 2).

To this end, Fourier-like relations are introduced as follows:

$$[\![\Theta]\!] = -\frac{\bar{r}_Q^0}{[1-\overline{D}_\parallel]}\{\!\{Q\}\!\}\cdot\overline{N} \quad \text{and} \quad \overline{\Theta}^{-1} - \{\!\{\Theta^{-1}\}\!\} = -\frac{\bar{s}_0}{[1-\overline{D}_\parallel]}[\![Q]\!]\cdot\overline{N}, \tag{10}$$

where $\bar{r}_Q^0 \geq 0$ and $\bar{s}_0 \geq 0$ are the undamaged (virgin) Kapitza resistance coefficient and the thermal sensitivity, respectively. As the interface damage grows and thus the reduction factor $[1-D_\parallel]$ decreases, one expects a more pronounced jump in the temperature across the interface and a less strong coupling between the bulk and the interface temperatures due to $\bar{r}_Q^0/[1-\overline{D}_\parallel]$ and $\bar{s}_0/[1-\overline{D}_\parallel]$ taking higher values. This observation is illustrated by the numerical results, which will be presented later.

4. Computational framework

Here we establish a numerical framework that encompasses thermohyperelasticity combined with a nonlocal damage model on the thermally general imperfect (GI) and mechanically coherent energetic interface. The weak form, together with its temporal and spatial discretizations, will be presented next.

The localized force balance equations in the bulk and on the interface given in Table 1 are tested with vector valued test functions $\delta\boldsymbol{\varphi} \in \mathcal{H}^1(\mathcal{B}_0)$ and $\delta\overline{\boldsymbol{\varphi}} \in \mathcal{H}^1(\mathcal{I}_0)$, respectively. By integrating the result over all domains in the material configuration, using the bulk and interface divergence theorems and the superficiality properties of the interface Piola stress, the weak form of the balance of linear momentum reads

$$\int_{\mathcal{B}_0}\boldsymbol{P}:\text{Grad}\,\delta\boldsymbol{\varphi}\,dV + \int_{\mathcal{I}_0}[1-\overline{D}_\parallel]\overline{\boldsymbol{P}}_0:\overline{\text{Grad}}\,\delta\overline{\boldsymbol{\varphi}}\,dA - \int_{\mathcal{B}_0}\delta\boldsymbol{\varphi}\cdot\boldsymbol{B}^{\text{p}}\,dV - \int_{\mathcal{I}_0}\delta\overline{\boldsymbol{\varphi}}\cdot\overline{\boldsymbol{B}}^{\text{p}}\,dA - \int_{\partial\mathcal{B}_0^{\text{N}}}\delta\boldsymbol{\varphi}\cdot\widehat{\boldsymbol{B}}_{\text{N}}^{\text{p}}\,dA$$

$$-\int_{\partial\mathcal{I}_0^{\text{N}}}\delta\overline{\boldsymbol{\varphi}}\cdot\widetilde{\boldsymbol{B}}_{\text{N}}^{\text{p}}\,dL = 0, \quad \forall\delta\boldsymbol{\varphi}\in\mathcal{H}^1(\mathcal{B}_0) \text{ and } \forall\delta\overline{\boldsymbol{\varphi}}\in\mathcal{H}^1(\mathcal{I}_0) \quad \text{with} \quad \delta\overline{\boldsymbol{\varphi}} = \{\!\{\delta\boldsymbol{\varphi}\}\!\}|_{\mathcal{I}_0} \text{ and } [\![\delta\boldsymbol{\varphi}]\!] = \mathbb{0}. \tag{11}$$

Analogously, the thermal weak form is derived first by testing the local temperature evolutions (see Table 2) in the bulk and on the interface with the scalar-valued test function $\delta\Theta \in \mathcal{H}_0^1(\mathcal{B}_0)$ and $\delta\overline{\Theta} \in \mathcal{H}_0^1(\mathcal{I}_0)$, respectively. The result is then integrated over the corresponding domains in the material configuration, resulting in the global weak form of the temperature evolution equation as follows:

$$\int_{\mathcal{B}_0}\boldsymbol{Q}\cdot\text{Grad}\,\delta\Theta - \delta\Theta c_{\boldsymbol{F}}\text{D}_t\Theta + \delta\Theta\,Q^{\text{p}} + \delta\Theta\Theta\partial_\Theta\boldsymbol{P}:\text{D}_t\boldsymbol{F}\,dV + \int_{\partial\mathcal{B}_0^{\text{N}}}\delta\Theta\,\widehat{Q}_{\text{N}}^{\text{p}}\,dA$$

$$+\int_{\mathcal{I}_0}[1-\overline{D}_\parallel]\overline{\boldsymbol{Q}}_0\cdot\overline{\text{Grad}}\,\delta\overline{\Theta} - \delta\overline{\Theta}[1-\overline{D}_\parallel]\bar{c}_{\overline{\boldsymbol{F}}}^0\text{D}_t\overline{\Theta} + \delta\overline{\Theta}\,\overline{Q}^{\text{p}} + \delta\overline{\Theta}\,\overline{\Theta}\big[[1-\overline{D}_\parallel]\partial_{\overline{\Theta}}\overline{\boldsymbol{P}}_0 - \partial_{\overline{\Theta}}\overline{\mathcal{D}}_\parallel\overline{\boldsymbol{P}}_0\big]:\text{D}_t\overline{\boldsymbol{F}}\,dA$$

$$-\int_{\mathcal{I}_0}[\![\delta\Theta]\!][1-\overline{D}_\parallel]\frac{1}{\bar{r}_Q^0}[\![\Theta]\!] - [\delta\overline{\Theta} - \{\!\{\delta\Theta\}\!\}][1-\overline{D}_\parallel]\frac{1}{\bar{s}_0}[\overline{\Theta}^{-1} - \{\!\{\Theta^{-1}\}\!\}]\,dA = 0,$$

$$\forall\delta\Theta\in\mathcal{H}^1(\mathcal{B}_0) \quad \text{and} \quad \forall\delta\overline{\Theta}\in\mathcal{H}^1(\mathcal{I}_0), \tag{12}$$

where $\overline{\boldsymbol{Q}}_0 = -\bar{J}\overline{\boldsymbol{F}}^{-1}\cdot\bar{\boldsymbol{k}}_0\cdot\overline{\boldsymbol{F}}^{-\text{t}}\cdot\overline{\text{Grad}}\,\overline{\Theta}$ is the undamaged heat conduction along the interface.

It is of great importance to mention that the current model can be simplified into other interface models. By setting the damage variable to zero, the model in [Kaessmair et al. 2014] is retrieved, where a nondegrading thermally GI and mechanically coherent energetic interface is studied. A degrading HC interface model is obtained as in [Esmaeili et al. 2016a] by setting $[\![\Theta]\!] = 0$, and consequently $\{\!\{\Theta\}\!\} = \overline{\Theta}$,

		bulk		interface
Lamé constant:	μ	80193.8 N/mm^2	$\bar{\mu}$	2×80193.8 N/mm
Lamé constant:	λ	110743.5 N/mm^2	$\bar{\lambda}$	2×110743.5 N/mm
compression modulus:	κ	164206.03 N/mm^2	$\bar{\kappa}$	2×190937.3 N/mm
specific heat capacity:	c_F	3.588 N/[mm^{2}K]	$\bar{c}_F^0$	3.588 N/[mmK]
heat conduction coeff.:	k	45 N/[sK]	$\bar{k}_0$	100×45 Nmm/[sK]
heat expansion coeff.:	α	10^{-5} 1/K	$\bar{\alpha}$	$[0-1.5] \times 10^{-5}$ 1/K
initial temperature:	Θ_0	298 K	$\bar{\Theta}_0$	298 K

		only interface		
	$\bar{F}_0$	0.005	$\bar{F}_\mathrm{f}$	0.1
thermal resistance	$\bar{r}_Q^0$	0.1 mm sK/N	$\bar{R}$	0.1 mm

Table 3. Material properties assumed in the numerical examples. Note that $\kappa = \lambda + 2/3\,\mu$ and $\bar{\kappa} = \bar{\lambda} + \bar{\mu}$.

which then results in the last integral in (12) to vanish. A degrading LC interface can be modeled as in [Esmaeili et al. 2016b] by removing the second term in the last integral, due to the fact that the jump of normal heat flux across interface vanishes (see relation (10)$_2$). The finite element implementation is given in Appendix A.

5. Numerical examples

In this section we study the computational aspects of thermally GI and mechanically coherent energetic interfaces subject to in-plane degradation and their effects on the overall response of the body. The in- and out-of-plane thermomechanical response of the interface is affected by the interface in-plane degradation. In particular, we focus on the influence of interface damage on the out-of-plane thermal properties of the interface, i.e., $\bar{s}_0$ and $\bar{r}_Q^0$. It is important to point out that the solution procedure is robust and shows the asymptotically quadratic rate of convergence associated with the Newton–Raphson scheme. The computational domain is discretized using 1600 trilinear hexahedral elements.

The reversible material behavior in the bulk and on the interface is characterized by a thermohyperelastic Helmholtz energy functions. The damage affects the interface response by reducing the interface stiffness, heat capacity and heat conduction coefficient, and increasing the Kapitza coefficient $\bar{r}_Q^0$ and thermal sensitivity $\bar{s}_0$. Appendix B gathers the effective (undamaged) Helmholtz energy functions together with their corresponding derivatives both in the bulk and on the interface. The corresponding material parameters for the bulk and interface are given in Table 3.

Consider now the strip shown in Figure 4, where a constant displacement is prescribed at the two opposite faces. The strip is partitioned into two homogeneous domains by an interface. The width and the thickness of the strip are kept constant. The thermal boundary condition is globally adiabatic, i.e., $\widehat{Q}^\mathrm{p} = \widetilde{Q}^\mathrm{p} = \mathbb{0}$. The thermal initial condition is a uniformly distributed temperature $\Theta_0 = 298$ K. In order to better understand the influence of a thermomechanical GI interface on the overall response of the body, all thermomechanical properties of the bulk are fixed. Similar examples of intact (nondegrading)
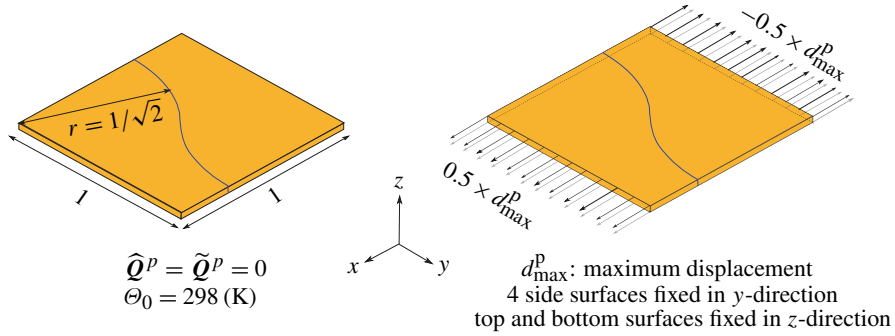
Figure 4. Strip with curved interface: geometry, left, and applied boundary conditions, right. Dimensions are in mm. The thickness is 0.05.
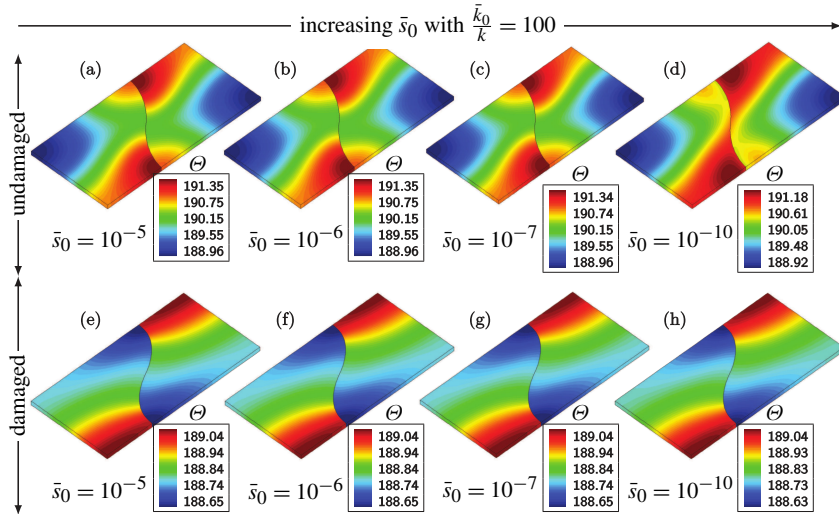

Figure 5. The bulk temperature distribution of the strip stretched up to 100% of its original length for $\bar{\mu}/\mu = \bar{\lambda}/\lambda = 2$ mm, $\bar{r}_Q^0 = 0.1$ and $\bar{k}_0/k = 100$ mm. Results a–d correspond to the intact interface, whereas results e–h correspond to the degrading interface.

LC, HC and GI interfaces can be found respectively in [Javili et al. 2012; 2013; Kaessmair et al. 2014]. Degrading HC and LC interfaces are studied in the recent contributions [Esmaeili et al. 2016a; 2016b], respectively. It is mentioned that to obtain an HC interface behavior from the current model, one can assign infinitesimal values to $\bar{s}_0$ and $\bar{r}_Q^0$, which causes both dissipation contributions in (9) to vanish. An LC interface is obtained by setting only $\bar{s}_0 \approx 0$, while $\bar{r}_Q^0$ is assigned a finite value. Note that we use Fourier-like relations (10) to fulfill the inequalities in (9).

In the first example we focus on the conductivity of a degrading interface. The domain is stretched up to 100% of its initial length in 40 equal steps where the total time is 10 ms. Note that for this example, $c_{\bar{F}}^0 = \bar{\alpha} = 0$ and $\bar{k}_0/k = 100$ mm, $\bar{r}_Q^0 = 0.1$, and $\bar{s}_0$ varies from 10^{-5} to 10^{-10}. The results of the two cases, undamaged and damaged interface, are compared and depicted in Figure 5. It is observed that the temperature distribution along the intact interface is more uniform (see Figure 5a–d) than the
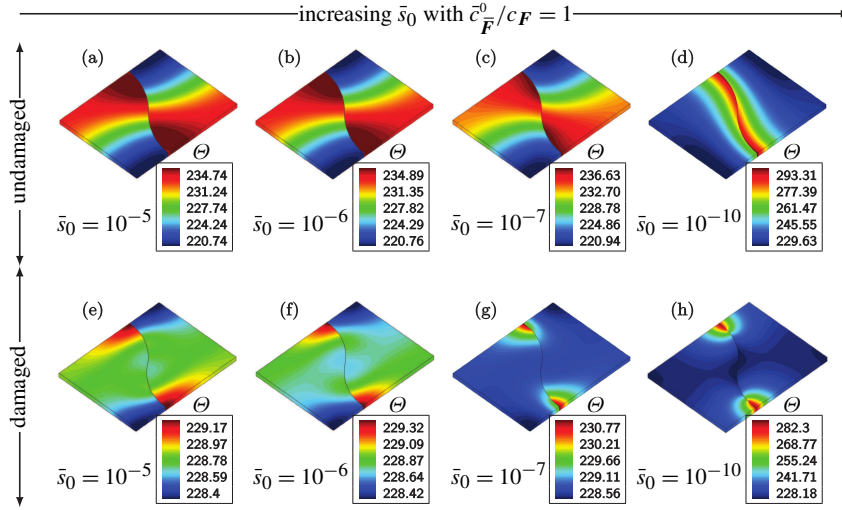
Figure 6. The bulk temperature distribution of the strip stretched up to 30% of its original length for $\bar{\mu}/\mu = \bar{\lambda}/\lambda = 2\,\text{mm}$, $\bar{r}_Q^0 = 0.1$ and $c_{\bar{F}}^0/c_F = 1\,\text{mm}$. Results a–d correspond to the intact interface, whereas results e–h correspond to the degrading interface.
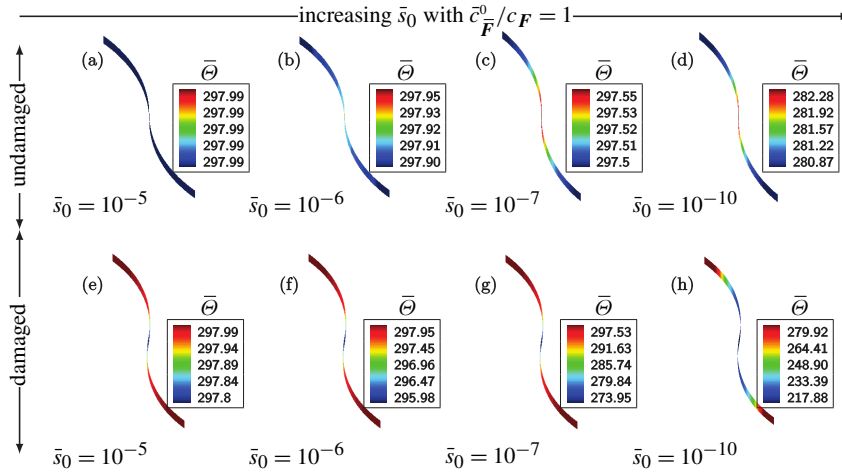

Figure 7. The interface temperature distribution of the strip stretched up to 30% of its original length for $\bar{\mu}/\mu = \bar{\lambda}/\lambda = 2\,\text{mm}$, $\bar{r}_Q^0 = 0.1$ and $c_{\bar{F}}^0/c_F = 1\,\text{mm}$. Results a–d correspond to the intact interface, whereas results e–h correspond to the degrading interface.

one along the damaging interface (see Figure 5e–h). Moreover, a degrading interface causes a higher temperature jump across the interface due to the fact that $\bar{r}_Q^0/[1 - \overline{D}_\parallel]$ assumes higher values as damage evolves. One should note that the simplified interface evolution equation of this example takes the form $\overline{\text{Div}}([1 - \overline{D}_\parallel]\overline{Q}) = -[\![\Theta]\!]$, thus a jump in the normal heat flux shall be observed. We point out that since the interface here is fully dissipative, in contrast to an HC interface, it allows for a jump in the
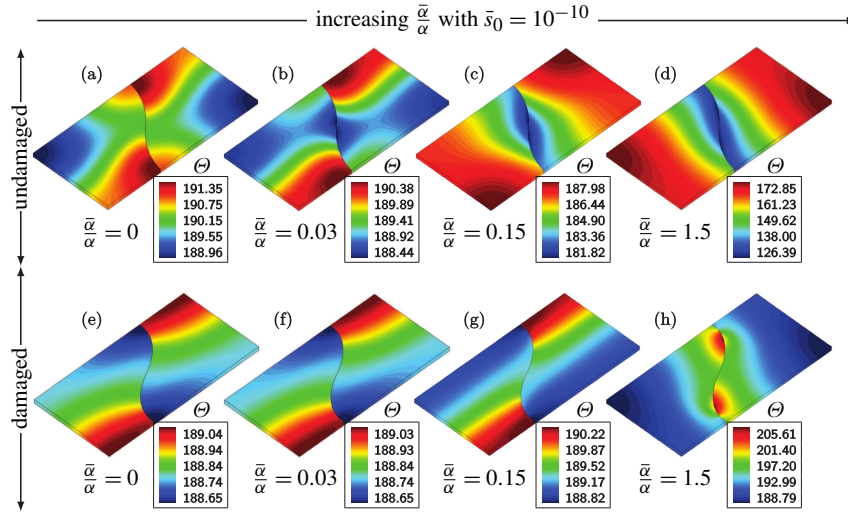
Figure 8. The bulk temperature distribution of the strip stretched up to 100% of its original length for $\bar{\mu}/\mu = \bar{\lambda}/\lambda = 2$ mm, $\bar{r}_Q^0 = 0.1$ and $\bar{s}_0 = 10^{-10}$. Results a–d correspond to the intact interface, whereas results e–h correspond to the degrading interface.
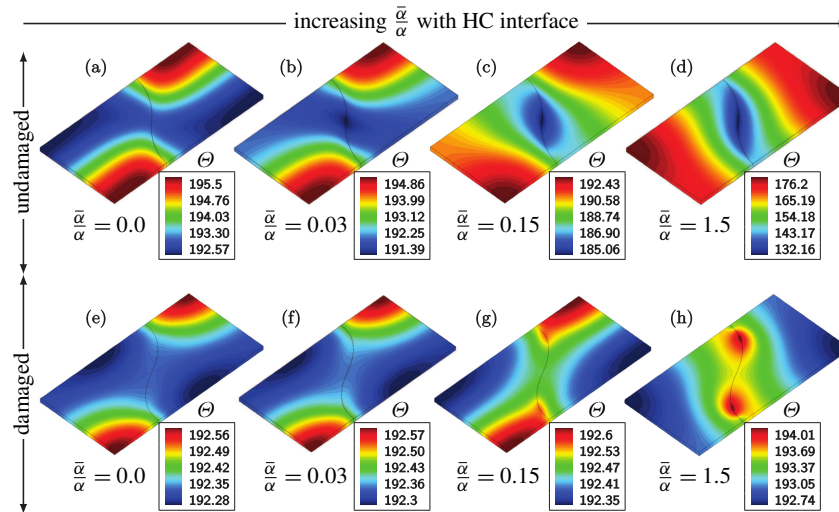
Figure 9. The bulk temperature distribution of the strip stretched up to 100% of its original length for $\bar{\mu}/\mu = \bar{\lambda}/\lambda = 2$ mm. Results a–d correspond to the intact highly conductive interface, whereas results e–h correspond to the degrading highly conductive interface. See [Esmaeili et al. 2016a] for further details.

temperature across the interface. Also, along a nondegrading HC interface with a high enough value for the interface conduction coefficient (such as $\bar{k}_0/k = 100$ mm), a uniform temperature distribution is achieved. This observation cannot be made for either an intact or a degrading GI interface (see Figure 5d and h, respectively).

Figure 10. The interface temperature distribution of the strip stretched up to 100% of its original length for $\bar{u}/\mu = \bar{\lambda}/\lambda = 2$ mm, $\bar{r}_Q^0 = 0.1$ and $\bar{s}_0 = 10^{-10}$. Results a–d correspond to the intact interface, whereas results e–h correspond to the degrading interface.
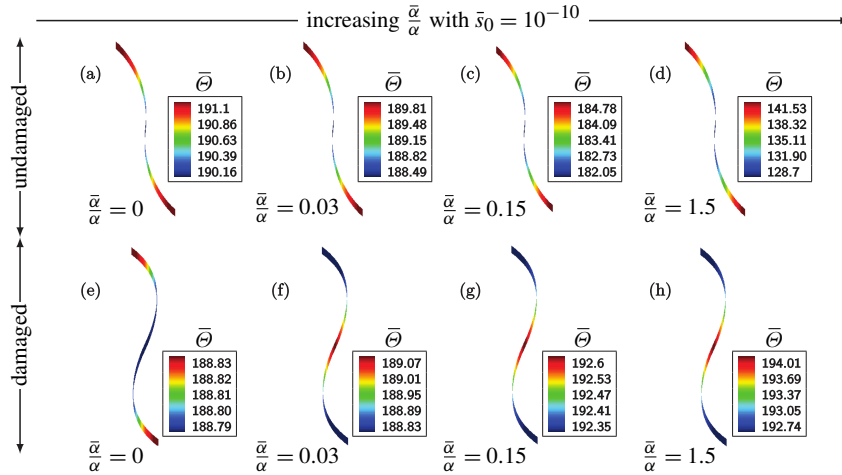
In the second example the effects of the interface heat capacity are studied. The domain here is stretched up to 30% of its initial length in 15 equal steps where the total time is 10 ms. Note that for this example, $\bar{k}_0 = \bar{\alpha} = 0$ and $\bar{c}_{\bar{F}}^0/c_F = 1$ mm, and $\bar{s}_0$ ranges from 10^{-5} to 10^{-10}. Analogous to the previous example, two cases of intact and damaged interface are considered here and shown in Figure 6 and Figure 7. From Figure 6 one finds that the intact interface is more capable of maintaining its initial temperature (also see Figure 7a–d). On the other hand, the domain cools down due to the Gough–Joule effect. These two different responses create the nonuniform temperature distribution in the domain containing the intact interface, as depicted in Figure 6a–d. On the contrary, a degrading interface can not retain its initial temperature (see Figure 7e–h), causing (in general) a more uniform temperature distribution in the domain as shown in Figure 6e–h. Note that for this example, the interface temperature evolution simplifies to $[1 - \bar{D}_\parallel]\bar{c}_{\bar{F}}^0 D_t \bar{\Theta} = -[\![\boldsymbol{Q}]\!]\cdot\bar{\boldsymbol{N}}$, meaning that a jump in the normal heat flux across the interface is present. Here we draw our attention to the difference between a thermally GI and HC interface. As mentioned before, an HC interface implies no temperature jump across the interface, and consequently the interface temperature becomes the average of the bulk temperatures on the two sides of the interface. Observing Figure 6 and Figure 7, one concludes that a jump in the temperature is clearly present across the interface, and the interface temperature is not the average of the surrounding bulk temperatures.

In the final example we turn our attention to the interface Gough–Joule effect by setting $\bar{k}_0 = \bar{c}_{\bar{F}}^0 = 0$ and $\bar{s}_0 = 10^{-10}$ and ranging $\bar{\alpha}/\alpha$ from 0 to 1.5. The domain here is stretched up to 100% of its initial length in 40 equal steps where the total time is 10 ms. The temperature evolution equation in this case simplifies to

$$[\![\boldsymbol{Q}]\!]\cdot\bar{\boldsymbol{N}} = \bar{\Theta}\partial_{\bar{\Theta}}([1 - \bar{D}_\parallel]\bar{\boldsymbol{P}}_0) : D_t\bar{\boldsymbol{F}} = \left[\bar{\Theta}[1 - \bar{D}_\parallel]\partial_{\bar{\Theta}}P_0 - \bar{\Theta}\partial_{\bar{\Theta}}\bar{D}_\parallel\bar{\boldsymbol{P}}_0\right] : D_t\bar{\boldsymbol{F}}.$$

From Figure 8 and Figure 10 we observe that the intact interface cools down under the increasing load due to the Gough–Joule effect more than the degrading interface. Moreover, it is shown that higher

temperature jumps and less strong coupling between the interface and bulk temperatures are achieved when the interface is allowed to degrade since

$$\bar{r}_Q^0/[1 - \overline{D}_\parallel] \quad \text{and} \quad \bar{s}_0/[1 - \overline{D}_\parallel]$$

assume higher values as damage evolves (compare Figure 8f–h to Figure 8a–d). Finally, the highest level of interface deformation is observed in this example due to the presence of the thermomechanical coupling term ($\bar{\alpha} \neq 0$) in the interface effective Helmholtz energy. A comparison is also made between a thermally GI and HC interface in Figure 9, which illustrates an HC interface under the same conditions as the thermally GI interface shown in Figure 8. The first observation, as expected, is the vanishing temperature jump across the HC interface. One can also notice that the HC interface (in general) retains to a larger extent its initial temperature. Although the intact thermally GI and HC interfaces have the lowest temperatures in the middle of the interface (see Figure 10a–d and Figure 9), the thermally GI interface temperature, unlike the HC interface temperature, is not coupled to its surrounding bulk temperatures. This means a thermally GI interface is allowed to be colder or warmer than the bulk (see Figure 10h and Figure 8h, where the interface is colder than the bulk). Note that for an HC interface the temperature is strongly coupled to that of the bulk by being the average of the adjacent bulk temperatures. Finally, the difference between a thermally GI and an HC interface becomes even more pronounced when in-plane degradation is allowed to initiate. Now, a degrading thermally GI interface loses its initial temperature at its two ends more drastically, while on an HC interface the coldest region is the middle of the interface.

6. Summary and conclusion

A theoretical and computational framework for continua containing thermally general imperfect and mechanically coherent energetic interfaces was outlined. The corresponding mechanical and thermal weak forms of the balance equations were given. The balance equations were fully discretized using the finite element method in space. The effects of the in-plane degradation on the in- and out-of-plane thermomechanical properties of the interface and the overall response of the body were also taken into account by introducing a tangential reduction factor. With the evolution of damage, the in-plane properties, i.e., interface stiffness, heat expansion coefficient, conduction coefficient and heat capacity coefficient, are reduced, whereas the out-of-plane properties, i.e., the Kapitza resistance coefficient and sensitivity, are increased. The increase of the out-of-plane thermal properties results in a higher temperature jump and a weaker coupling between interface and bulk temperatures. The tangential damage variable is a function of the equivalent distortion, which is nonlocalized using integral-type averaging.

A series of numerical examples served to elucidate the theory presented in this work. It was shown that the degraded interface undergoes more deformation. In addition, as the heat conduction coefficient is reduced while the damage evolves, higher temperature gradients along the interface were observed. It was also illustrated that an interface retains its initial temperature to a larger extent due to the reduced heat expansion coefficient. The degrading interface was shown to be less capable of being resistant to temperature changes as a result of the reduced specific heat capacity. We also observed that (in general) in all the examples higher temperature jumps across the interface and less strong coupling between the interface and bulk temperatures are attributed to the damage of the interface. Finally, in all the examples, asymptotically quadratic convergence associated with the Newton–Raphson scheme was achieved.

One consequent extension to this work is to study the role of the out-of-plane degradation of the interface material (cohesive damage) on the thermomechanical response of a thermally general imperfect and mechanically energetic interface. This includes introducing noncoherent deformation into the current formulation by allowing a displacement jump across the interface, which requires the use of a cohesive zone model. Such an extension shall be discussed in later contributions.

Appendix A: Finite element implementation

In order to apply the finite element method to the present problem, the weak forms (11) and (12) are discretized in space and time. The time interval $\mathcal{T}$ is subdivided into a set of intervals $\Delta t := t_{\tau+1} - t_{\tau}$ with

$$\mathcal{T} = \bigcup_{\tau=0}^{n_{\text{ts}}} [t_{\tau}, t_{\tau+1}], \tag{A.1}$$

where n_{ts} denotes the number of time steps. The spatial discretization is performed using the Bubnov–Galerkin finite element method. The geometry and temperature of the bulk and interface together with the jump and average of temperature over the interface are approximated as a function of the natural coordinates $\xi \in [-1, 1]^3$ and $\bar{\xi} \in [-1, 1]^2$ assigned to the bulk and the interface, respectively. Using standard interpolations according to the isoparametric concepts, we obtain

$$
\begin{aligned}
\boldsymbol{X}|_{\mathcal{B}_0^{\beta}} &\approx \boldsymbol{X}^{\text{h}}(\xi) = \sum_{i=1}^{n_{\text{nB}}} N^i(\xi)\boldsymbol{X}^i, & \overline{\boldsymbol{X}}|_{\mathcal{I}_0^{\gamma}} &\approx \overline{\boldsymbol{X}}^{\text{h}}(\bar{\xi}) = \sum_{i=1}^{n_{\text{nI}}} \overline{N}^i(\bar{\xi})\overline{\boldsymbol{X}}^i, \\
\boldsymbol{\varphi}|_{\mathcal{B}_0^{\beta}} &\approx \boldsymbol{\varphi}^{\text{h}}(\xi) = \sum_{i=1}^{n_{\text{nB}}} N^i(\xi)\boldsymbol{\varphi}^i, & \overline{\boldsymbol{\varphi}}|_{\mathcal{I}_0^{\gamma}} &\approx \overline{\boldsymbol{\varphi}}^{\text{h}}(\bar{\xi}) = \sum_{i=1}^{n_{\text{nI}}} \overline{N}^i(\bar{\xi})\overline{\boldsymbol{\varphi}}^i, \\
\Theta|_{\mathcal{B}_0^{\beta}} &\approx \Theta^{\text{h}}(\xi) = \sum_{i=1}^{n_{\text{nB}}} N^i(\xi)\Theta^i, & \overline{\Theta}|_{\mathcal{I}_0^{\gamma}} &\approx \overline{\Theta}^{\text{h}}(\bar{\xi}) = \sum_{i=1}^{n_{\text{nI}}} \overline{N}^i(\bar{\xi})\overline{\Theta}^i, \\
[\![\Theta]\!]|_{\mathcal{I}_0^{\gamma}} &\approx [\![\Theta]\!]^{\text{h}}(\bar{\xi}) = \sum_{i=1}^{n_{\text{nI}}} \overline{N}^i(\bar{\xi})[\![\Theta]\!]^i, & \{\!\{\Theta\}\!\}|_{\mathcal{I}_0^{\gamma}} &\approx \{\!\{\Theta\}\!\}^{\text{h}}(\bar{\xi}) = \sum_{i=1}^{n_{\text{nI}}} \overline{N}^i(\bar{\xi})\{\!\{\Theta\}\!\}^i,
\end{aligned}
\tag{A.2}
$$

where $\mathcal{B}_0^{\beta}$ and $\mathcal{I}_0^{\gamma}$ are the βth and γ^{th} element in the bulk and on the interface, respectively. The shape functions of the bulk and interface elements at a local node i are denoted by N^i and $\overline{N}^i$, respectively. Every bulk and interface element consists of n_{nB} and n_{nI} nodes, respectively.

For the sake of brevity, homogeneous Neumann boundary conditions are assumed and hence some integrals vanish. The integrals are standard and require no additional care. Now, the fully discrete (spatially and temporally) form of mechanical and thermal residuals associated with the global node I are defined by

$$
\begin{aligned}
[^{\text{tot}}\boldsymbol{R}_{\boldsymbol{\varphi}}^I]_{\tau+1} = \int_{\mathcal{B}_0} \boldsymbol{P}_{\tau+1} \cdot \operatorname{Grad} N^I \, \mathrm{d}V &- \int_{\mathcal{B}_0} N^I \boldsymbol{B}_{\tau+1}^{\text{p}} \, \mathrm{d}V \\
&+ \int_{\mathcal{I}_0} \left[[1 - \overline{D}_{\|}]\overline{\boldsymbol{P}}_0\right]_{\tau+1} \cdot \overline{\operatorname{Grad}} \, \overline{N}^I \, \mathrm{d}A - \int_{\mathcal{I}_0} \overline{N}^I \overline{\boldsymbol{B}}_{\tau+1}^{\text{p}} \, \mathrm{d}A, \quad \text{(A.3)}
\end{aligned}
$$

and

$$
\begin{aligned}
[^{\mathrm{tot}}\mathrm{R}_{\Theta}^{I}]_{\tau+1} =&-\int_{\mathcal{B}_0} \boldsymbol{Q}_{\tau+1}\cdot\mathrm{Grad}\,N^{I}+Q_{\tau+1}^{\mathrm{p}}N^{I}\,\mathrm{d}V -\int_{\mathcal{I}_0}\big[[1-D_{\parallel}]\overline{\boldsymbol{Q}}_0\big]_{\tau+1}\cdot\overline{\mathrm{Grad}}\,\overline{N}^{I}+\overline{Q}_{\tau+1}^{\mathrm{p}}\overline{N}^{I}\,\mathrm{d}A\\
&-\int_{\mathcal{B}_0}\Theta_{\tau+1}[\partial_{\Theta}\boldsymbol{P}]_{\tau+1}:\frac{1}{\Delta t}[\boldsymbol{F}_{\tau+1}-\boldsymbol{F}_{\tau}]N^{I}-c_{F}\frac{1}{\Delta t}[\Theta_{\tau+1}-\Theta_{\tau}]N^{I}\,\mathrm{d}V\\
&-\int_{\mathcal{I}_0}\overline{\Theta}_{\tau+1}[\partial_{\overline{\Theta}}([1-\overline{D}_{\parallel}]\overline{\boldsymbol{P}}_0)]_{\tau+1}:\frac{1}{\Delta t}[\overline{\boldsymbol{F}}_{\tau+1}-\overline{\boldsymbol{F}}_{\tau}]\overline{N}^{I}-[1-\overline{D}_{\parallel}]\overline{c}_{\overline{F}}^{\,0}\frac{1}{\Delta t}[\overline{\Theta}_{\tau+1}-\overline{\Theta}_{\tau}]\overline{N}^{I}\,\mathrm{d}A\\
&-\int_{\mathcal{I}_0}[1-\overline{D}_{\parallel}]\frac{1}{\overline{s}_0}[\overline{\Theta}^{-1}-\{\!\{\Theta^{-1}\}\!\}]\overline{N}^{I}\,\mathrm{d}A\\
&-\int_{\mathcal{I}_0^-}[1-\overline{D}_{\parallel}]\frac{1}{\overline{r}_Q^{\,0}}\overline{N}^{I}[\![\Theta]\!]_{\tau+1}\,\mathrm{d}A+\int_{\mathcal{I}_0^+}[1-\overline{D}_{\parallel}]\frac{1}{\overline{r}_Q^{\,0}}\overline{N}^{I}[\![\Theta]\!]_{\tau+1}\,\mathrm{d}A.
\end{aligned}\tag{A.4}
$$

Note that mechanical and thermal residuals are composed of contributions from both the bulk and inter-face. Moreover, although the integrands of the last two integrals in (A.4) are identical, the domains over which these integrals are taken are different. This is due to the fact that the interface is thermally general imperfect. The global mechanical and thermal residual vectors take the form

$$
^{\mathrm{tot}}\boldsymbol{R}=[^{\mathrm{tot}}\boldsymbol{R}_{\varphi}\ \boldsymbol{R}_{\Theta}\ ^{\mathrm{tot}}\overline{\boldsymbol{R}}_{\Theta}]^{T}\quad\text{with }^{\mathrm{tot}}\boldsymbol{R}_{\varphi}=[\boldsymbol{R}_{\varphi}^{1}\cdots\boldsymbol{R}_{\varphi}^{I}\cdots\boldsymbol{R}_{\varphi}^{n_{\mathrm{Bn}}}]^{T}+[\overline{\boldsymbol{R}}_{\varphi}^{1}\cdots\overline{\boldsymbol{R}}_{\varphi}^{I}\cdots\overline{\boldsymbol{R}}_{\varphi}^{n_{\mathrm{In}}}]^{T},
$$

$$
\boldsymbol{R}_{\Theta}=[\mathrm{R}_{\Theta}^{1}\cdots\mathrm{R}_{\Theta}^{I}\cdots\mathrm{R}_{\Theta}^{n_{\mathrm{Bn}}}]^{T}\text{and }^{\mathrm{tot}}\overline{\boldsymbol{R}}_{\Theta}=\underbrace{[\,\overline{\mathrm{R}}_{\Theta}^{1}\cdots\overline{\mathrm{R}}_{\Theta}^{I}\cdots\overline{\mathrm{R}}_{\Theta}^{n_{\mathrm{In}}}]^{T}}_{\overline{\boldsymbol{R}}_{\Theta}}+\underbrace{[\,\overline{\mathrm{R}}_{\Theta}^{1\pm}\cdots\overline{\mathrm{R}}_{\Theta}^{I\pm}\cdots\overline{\mathrm{R}}_{\Theta}^{n_{\mathrm{In}}^{\pm}}]^{T}}_{\overline{\boldsymbol{R}}_{\Theta\pm}},\tag{A.5}
$$

where n_{Bn} and n_{In} denote the number of bulk and interface nodes. The summation operator implies the (conventional) residual assembly of the finite element method. Note that total interface thermal residual $^{\mathrm{tot}}\overline{\boldsymbol{R}}_{\Theta}$ is composed of contributions from interface residuals corresponding to the degrees of freedom $\overline{\Theta}$ and $\Theta^{\pm}$, respectively denoted by $\overline{\boldsymbol{R}}_{\Theta}$ and $\overline{\boldsymbol{R}}_{\Theta\pm}$. Both of the above thermal residuals contribute to the total thermal residual, i.e., $^{\mathrm{tot}}\boldsymbol{R}_{\Theta}=\boldsymbol{R}_{\Theta}+^{\mathrm{tot}}\overline{\boldsymbol{R}}_{\Theta}$.

The fully discrete coupled nonlinear system of governing equations can be stated as follows:

$$
^{\mathrm{tot}}\boldsymbol{R}(^{\mathrm{tot}}\boldsymbol{d})\overset{!}{=}\mathbb{0}\quad\text{with}\quad {}^{\mathrm{tot}}\boldsymbol{d}=[\boldsymbol{d}_{\varphi}\,\boldsymbol{d}_{\Theta}\,\boldsymbol{d}_{\overline{\Theta}}]^{T},\tag{A.6}
$$

where $^{\mathrm{tot}}\boldsymbol{d}$ is the unknown global vector of spatial coordinates $\boldsymbol{d}_{\varphi}$ and temperature $\boldsymbol{d}_{\Theta}$ and $\boldsymbol{d}_{\overline{\Theta}}$. To solve (A.6)$_1$, a Newton–Raphson scheme is utilized. Thus, the consistent linearization of the resulting system of equations yields the total (algorithmic) tangent stiffness matrix for every pair of global nodes I and J as

$$
^{\mathrm{tot}}\boldsymbol{K}^{IJ}:=\frac{\partial^{\mathrm{tot}}\boldsymbol{R}^{I}}{\partial^{\mathrm{tot}}\boldsymbol{d}^{J}}\quad\text{where}\quad {}^{\mathrm{tot}}\boldsymbol{K}^{IJ}=\begin{bmatrix}\boldsymbol{K}_{\varphi\varphi}^{IJ}&\boldsymbol{K}_{\varphi\Theta}^{IJ}&\mathbb{0}\\[2pt]\boldsymbol{K}_{\Theta\varphi}^{IJ}&\mathrm{K}_{\Theta\Theta}^{IJ}&0\\[2pt]\mathbb{0}&0&0\end{bmatrix}+\underbrace{\begin{bmatrix}^{\mathrm{tot}}\overline{\boldsymbol{K}}_{\varphi\varphi}^{IJ}&^{\mathrm{tot}}\overline{\boldsymbol{K}}_{\varphi\Theta}^{IJ}&^{\mathrm{tot}}\overline{\boldsymbol{K}}_{\varphi\overline{\Theta}}^{IJ}\\[2pt]^{\mathrm{tot}}\overline{\boldsymbol{K}}_{\Theta\varphi}^{IJ}&^{\mathrm{tot}}\overline{\mathrm{K}}_{\Theta\Theta}^{IJ}&^{\mathrm{tot}}\overline{\mathrm{K}}_{\Theta\overline{\Theta}}^{IJ}\\[2pt]^{\mathrm{tot}}\overline{\boldsymbol{K}}_{\overline{\Theta}\varphi}^{IJ}&^{\mathrm{tot}}\overline{\mathrm{K}}_{\overline{\Theta}\Theta}^{IJ}&^{\mathrm{tot}}\overline{\mathrm{K}}_{\overline{\Theta}\overline{\Theta}}^{IJ}\end{bmatrix}}_{^{\mathrm{tot}}\overline{\boldsymbol{K}}^{IJ}},\tag{A.7}
$$

with $^{\mathrm{tot}}\overline{\boldsymbol{K}}^{IJ}$ being defined as

$$
\begin{bmatrix}^{\mathrm{tot}}\overline{\boldsymbol{K}}_{\varphi\varphi}^{IJ}=\overline{\boldsymbol{K}}_{\varphi\varphi}^{IJ}&^{\mathrm{tot}}\overline{\boldsymbol{K}}_{\varphi\Theta}^{IJ}=\overline{\boldsymbol{K}}_{\varphi\Theta+}^{IJ}+\overline{\boldsymbol{K}}_{\varphi\Theta-}^{IJ}&^{\mathrm{tot}}\overline{\boldsymbol{K}}_{\varphi\overline{\Theta}}^{IJ}=\overline{\boldsymbol{K}}_{\varphi\overline{\Theta}}^{IJ}\\[3pt]^{\mathrm{tot}}\overline{\boldsymbol{K}}_{\Theta\varphi}^{IJ}=\overline{\boldsymbol{K}}_{\Theta+\varphi}^{IJ}+\overline{\boldsymbol{K}}_{\Theta-\varphi}^{IJ}&^{\mathrm{tot}}\overline{\mathrm{K}}_{\Theta\Theta}^{IJ}=\overline{\mathrm{K}}_{\Theta+\Theta+}^{IJ}+\overline{\mathrm{K}}_{\Theta+\Theta-}^{IJ}+\overline{\mathrm{K}}_{\Theta-\Theta+}^{IJ}+\overline{\mathrm{K}}_{\Theta-\Theta-}^{IJ}&^{\mathrm{tot}}\overline{\mathrm{K}}_{\Theta\overline{\Theta}}^{IJ}=\overline{\mathrm{K}}_{\Theta+\overline{\Theta}}^{IJ}+\overline{\mathrm{K}}_{\Theta-\overline{\Theta}}^{IJ}\\[3pt]^{\mathrm{tot}}\overline{\boldsymbol{K}}_{\overline{\Theta}\varphi}^{IJ}=\overline{\boldsymbol{K}}_{\overline{\Theta}\varphi}^{IJ}&^{\mathrm{tot}}\overline{\mathrm{K}}_{\overline{\Theta}\Theta}^{IJ}=\overline{\mathrm{K}}_{\overline{\Theta}\Theta+}^{IJ}+\overline{\mathrm{K}}_{\overline{\Theta}\Theta-}^{IJ}&^{\mathrm{tot}}\overline{\mathrm{K}}_{\overline{\Theta}\overline{\Theta}}^{IJ}=\overline{\mathrm{K}}_{\overline{\Theta}\overline{\Theta}}^{IJ}\end{bmatrix}.\tag{A.8}
$$

Note that $^{\text{tot}}\boldsymbol{K}$ is also decomposed into contributions from the bulk and the interface. The bulk contributions to the total stiffness matrix are given as

$$\boldsymbol{K}_{\boldsymbol{\varphi\varphi}}^{IJ} = \frac{\partial \boldsymbol{R}_{\boldsymbol{\varphi}}^{I}}{\partial \boldsymbol{\varphi}^{J}} = \int_{\mathcal{B}_0} \text{Grad } N^I \mathbin{\vdots} [\partial_{\boldsymbol{F}} \boldsymbol{P}] \cdot \text{Grad } N^J \, \mathrm{d}V, \quad \boldsymbol{K}_{\boldsymbol{\varphi}\Theta}^{IJ} = \frac{\partial \boldsymbol{R}_{\boldsymbol{\varphi}}^{I}}{\partial \Theta^{J}} = \int_{\mathcal{B}_0} N^J \, [\partial_{\Theta} \boldsymbol{P}] \cdot \text{Grad } N^I \, \mathrm{d}V,$$

$$\boldsymbol{K}_{\Theta\boldsymbol{\varphi}}^{IJ} = \frac{\partial \mathrm{R}_{\Theta}^{I}}{\partial \boldsymbol{\varphi}^{J}} = \int_{\mathcal{B}_0} -N^I \left[\frac{\partial (\Theta \partial_{\Theta} \boldsymbol{P} : \mathrm{D}_t \boldsymbol{F})}{\partial \boldsymbol{F}} \right] \cdot \text{Grad } N^J - \text{Grad } N^I \cdot [\partial_{\boldsymbol{F}} \boldsymbol{Q}] \cdot \text{Grad } N^J \, \mathrm{d}V, \qquad \text{(A.9)}$$

$$\mathrm{K}_{\Theta\Theta}^{IJ} = \frac{\partial \mathrm{R}_{\Theta}^{I}}{\partial \Theta^{J}} = \int_{\mathcal{B}_0} - \text{Grad } N^I \cdot \left[\frac{\partial \boldsymbol{Q}}{\partial \, \text{Grad } \Theta} \right] \cdot \text{Grad } N^J + N^I \left[\frac{c_F}{\Delta t} - \left[\frac{\partial (\Theta \partial_{\Theta} \boldsymbol{P} : \mathrm{D}_t \boldsymbol{F})}{\partial \Theta} \right] \right] N^J \, \mathrm{d}V.$$

The interface contributions to the total stiffness matrix consist of local ($^{\text{loc}}\overline{\boldsymbol{K}}$) and nonlocal ($^{\text{nloc}}\overline{\boldsymbol{K}}$) contributions. The local contributions $^{\text{loc}}\overline{\boldsymbol{K}}$, uniquely derived for a GI interface, are as follows:

$$^{\text{loc}}\overline{\mathrm{K}}_{\Theta^{\pm}\overline{\Theta}}^{IJ} = \frac{\partial \overline{\mathrm{R}}_{\Theta}^{I\pm}}{\partial \overline{\Theta}^{J}} = \int_{\mathcal{I}_0^{\pm}} [1 - \overline{D}_{\parallel}(\bar{\boldsymbol{x}}_{\mathrm{r}})] \frac{1}{2\bar{s}_0} \frac{1}{\overline{\Theta}^2} \overline{N}^I \overline{N}^J \, \mathrm{d}A_{\mathrm{r}},$$

$$^{\text{loc}}\overline{\mathrm{K}}_{\overline{\Theta}\Theta^{\pm}}^{IJ} = \frac{\partial \overline{\mathrm{R}}_{\overline{\Theta}}^{I}}{\partial \Theta^{J\pm}} = \int_{\mathcal{I}_0} [1 - \overline{D}_{\parallel}(\bar{\boldsymbol{x}}_{\mathrm{r}})] \frac{1}{2\bar{s}_0} \frac{1}{[\Theta^{\pm}]^2} \overline{N}^I \overline{N}^J \, \mathrm{d}A_{\mathrm{r}}, \qquad \text{(A.10)}$$

$$^{\text{loc}}\overline{\mathrm{K}}_{\Theta^{\pm}\Theta^{\pm}}^{IJ} = \frac{\partial \overline{\mathrm{R}}_{\Theta}^{I\pm}}{\partial \Theta^{J\pm}} = \int_{\mathcal{I}_0^{\pm}} [1 - \overline{D}_{\parallel}(\bar{\boldsymbol{x}}_{\mathrm{r}})] \frac{1}{4\bar{s}_0} \frac{1}{[\Theta^{\pm\pm}]^2} \overline{N}^I \overline{N}^J \, \mathrm{d}A_{\mathrm{r}} \pm \pm \int_{\mathcal{I}_0^{\pm}} [1 - \overline{D}_{\parallel}(\bar{\boldsymbol{x}}_{\mathrm{r}})] \frac{1}{r_Q^0} \overline{N}^I \overline{N}^J \, \mathrm{d}A_{\mathrm{r}},$$

where $\mathrm{d}A_{\mathrm{r}} = \mathrm{d}A(\bar{\boldsymbol{x}}_{\mathrm{r}})$. The rest of interface local contributions to the total stiffness matrix are given as

$$^{\text{loc}}\overline{\boldsymbol{K}}_{\boldsymbol{\varphi\varphi}}^{IJ} = \frac{\partial \overline{\boldsymbol{R}}_{\boldsymbol{\varphi}}^{I}}{\partial \overline{\boldsymbol{\varphi}}^{J}} = \int_{\mathcal{I}_0} \overline{\text{Grad}} \, \overline{N}^I \mathbin{\vdots} [1 - \overline{D}_{\parallel}(\bar{\boldsymbol{x}}_{\mathrm{r}})] \partial_{\overline{\boldsymbol{F}}} \overline{\boldsymbol{P}}_0(\bar{\boldsymbol{x}}_{\mathrm{r}}) \cdot \overline{\text{Grad}} \, \overline{N}^J \, \mathrm{d}A_{\mathrm{r}},$$

$$^{\text{loc}}\overline{\boldsymbol{K}}_{\boldsymbol{\varphi}\overline{\Theta}}^{IJ} = \frac{\partial \overline{\boldsymbol{R}}_{\boldsymbol{\varphi}}^{I}}{\partial \overline{\Theta}^{J}} = \int_{\mathcal{I}_0} \overline{N}^J [1 - \overline{D}_{\parallel}(\bar{\boldsymbol{x}}_{\mathrm{r}})] \partial_{\overline{\Theta}} \overline{\boldsymbol{P}}_0(\bar{\boldsymbol{x}}_{\mathrm{r}}) \cdot \overline{\text{Grad}} \, \overline{N}^I \, \mathrm{d}A_{\mathrm{r}},$$

$$^{\text{loc}}\overline{\boldsymbol{K}}_{\overline{\Theta}\boldsymbol{\varphi}}^{IJ} = \frac{\partial \overline{\mathrm{R}}_{\Theta}^{I}}{\partial \overline{\boldsymbol{\varphi}}^{J}} = \int_{\mathcal{I}_0} -\overline{N}^I [1 - \overline{D}_{\parallel}(\bar{\boldsymbol{x}}_{\mathrm{r}})] \left[\frac{\partial (\overline{\Theta} \partial_{\overline{\Theta}} \overline{\boldsymbol{P}}_0(\bar{\boldsymbol{x}}_{\mathrm{r}}) : \mathrm{D}_t \overline{\boldsymbol{F}})}{\partial \overline{\boldsymbol{F}}} \right] \cdot \overline{\text{Grad}} \, \overline{N}^J \, \mathrm{d}A_{\mathrm{r}}$$

$$- \int_{\mathcal{I}_0} \overline{N}^I [-\partial_{\overline{\Theta}} \overline{\mathcal{D}}_{\parallel}(\bar{\boldsymbol{x}}_{\mathrm{r}})] \left[\frac{\partial (\overline{\Theta} \overline{\boldsymbol{P}}_0(\bar{\boldsymbol{x}}_{\mathrm{r}}) : \mathrm{D}_t \overline{\boldsymbol{F}})}{\partial \overline{\boldsymbol{F}}} \right] \cdot \overline{\text{Grad}} \, \overline{N}^J \, \mathrm{d}A_{\mathrm{r}}$$

$$- \int_{\mathcal{I}_0} \overline{\text{Grad}} \, \overline{N}^I \cdot [1 - \overline{D}_{\parallel}(\bar{\boldsymbol{x}}_{\mathrm{r}})] [\partial_{\overline{\boldsymbol{F}}} \overline{\boldsymbol{Q}}_0(\bar{\boldsymbol{x}}_{\mathrm{r}})] \cdot \overline{\text{Grad}} \, \overline{N}^J \, \mathrm{d}A_{\mathrm{r}}, \qquad \text{(A.11)}$$

$$^{\text{loc}}\overline{\mathrm{K}}_{\overline{\Theta}\,\overline{\Theta}}^{IJ} = \frac{\partial \overline{\mathrm{R}}_{\Theta}^{I}}{\partial \overline{\Theta}^{J}} = \int_{\mathcal{I}_0} - \overline{\text{Grad}} \, \overline{N}^I \cdot [1 - \overline{D}_{\parallel}(\bar{\boldsymbol{x}}_{\mathrm{r}})] \left[\frac{\partial \overline{\boldsymbol{Q}}_0(\bar{\boldsymbol{x}}_{\mathrm{r}})}{\partial \, \overline{\text{Grad}} \, \overline{\Theta}} \right] \cdot \overline{\text{Grad}} \, \overline{N}^J \, \mathrm{d}A_{\mathrm{r}}$$

$$+ \int_{\mathcal{I}_0} \overline{N}^I [1 - \overline{D}_{\parallel}(\bar{\boldsymbol{x}}_{\mathrm{r}})] \left[\frac{\bar{c}_{\overline{F}}^0}{\Delta t} + \frac{1}{\bar{s}_0 \overline{\Theta}^2} - \left[\frac{\partial (\overline{\Theta} \partial_{\overline{\Theta}} \overline{\boldsymbol{P}}_0(\bar{\boldsymbol{x}}_{\mathrm{r}}) : \mathrm{D}_t \overline{\boldsymbol{F}})}{\partial \overline{\Theta}} \right] \right] \overline{N}^J \, \mathrm{d}A_{\mathrm{r}}$$

$$- \int_{\mathcal{I}_0} \overline{N}^I [-\partial_{\overline{\Theta}} \overline{\mathcal{D}}_{\parallel}(\bar{\boldsymbol{x}}_{\mathrm{r}})] \left[\frac{\partial (\overline{\Theta} \overline{\boldsymbol{P}}_0(\bar{\boldsymbol{x}}_{\mathrm{r}}) : \mathrm{D}_t \overline{\boldsymbol{F}})}{\partial \overline{\Theta}} \right] \overline{N}^J \, \mathrm{d}A_{\mathrm{r}},$$

where $\partial_{\overline{\Theta}} \overline{\mathcal{D}}_\parallel$, and using $(6)_{2,3}$, is computed as

$$\partial_{\overline{\Theta}} \overline{\mathcal{D}}_\parallel(\bar{x}_r) = \overline{\mathcal{D}}_\parallel' \partial_{\overline{\Theta}} F_{nloc} \Rightarrow \partial_{\overline{\Theta}} F_{nloc}(\bar{x}_r) = \int_{\mathcal{I}_0} \omega(\bar{x}_r, \bar{x}_s) \frac{1}{\overline{E} F_{loc}(\bar{x}_s)} \partial_{\overline{\Theta}} \overline{\Psi}^0(\bar{x}_s) \, dA_s \tag{A.12}$$

with $\overline{\mathcal{D}}_\parallel' = \partial_{F_{nloc}} \overline{\mathcal{D}}_\parallel$.

Next, the nonlocal corrections to the interface stiffness matrix are given as

$$^{nloc}\overline{K}_{\varphi\varphi}^{IJ} = \frac{\partial \overline{R}_\varphi^I}{\partial \overline{\varphi}^J} = \int_{\mathcal{I}_0} \overline{\text{Grad}}\, \overline{N}^I \stackrel{.}{\cdot} \overline{P}_0(\bar{x}_r) \otimes [-\partial_{\overline{\varphi}^J} \overline{\mathcal{D}}_\parallel(\bar{x}_r)] \, dA_r,$$

$$^{nloc}\overline{K}_{\varphi\overline{\Theta}}^{IJ} = \frac{\partial \overline{R}_\varphi^I}{\partial \overline{\Theta}^J} = \int_{\mathcal{I}_0} [-\partial_{\overline{\Theta}^J} \overline{\mathcal{D}}_\parallel(\bar{x}_r)] \overline{P}_0(\bar{x}_r) \cdot \overline{\text{Grad}}\, \overline{N}^I \, dA_r,$$

$$^{nloc}\overline{K}_{\overline{\Theta}\varphi}^{IJ} = \frac{\partial \overline{R}_\Theta^I}{\partial \overline{\varphi}^J} = \int_{\mathcal{I}_0} -\overline{N}^I \overline{\Theta} D_t \overline{F} : [-\partial_{\overline{\Theta}} \overline{P}_0 \otimes \partial_{\overline{\varphi}^J} \overline{\mathcal{D}}_\parallel - \overline{P}_0 \otimes \partial_{\overline{\varphi}^J \overline{\Theta}} \overline{\mathcal{D}}_\parallel]_{\bar{x}_r} \, dA_r$$

$$- \int_{\mathcal{I}_0} \overline{\text{Grad}}\, \overline{N}^I \cdot \overline{Q}_0(\bar{x}_r) \otimes [-\partial_{\overline{\varphi}^J} \overline{\mathcal{D}}_\parallel(\bar{x}_r)]$$

$$+ \overline{N}^I [-\partial_{\overline{\varphi}^J} \overline{\mathcal{D}}_\parallel(\bar{x}_r)] \left[\bar{c}_{\overline{F}}^0 D_t \overline{\Theta} - \frac{1}{\bar{s}_0} [\overline{\Theta}^{-1} - \{\!\{\Theta\}\!\}^{-1}] \right]_{\bar{x}_r} \, dA_r, \tag{A.13}$$

$$^{nloc}\overline{K}_{\Theta^\pm \varphi}^{IJ} = \frac{\partial \overline{R}_\Theta^{I\pm}}{\partial \overline{\varphi}^J} = \int_{\mathcal{I}_0^\pm} \overline{N}^I [-\partial_{\overline{\varphi}^J} \overline{\mathcal{D}}_\parallel(\bar{x}_r)] \left[\frac{1}{2\bar{s}_0}[\overline{\Theta}^{-1} - \{\!\{\Theta\}\!\}^{-1}] \pm \frac{1}{\bar{r}_Q^0} [\![\Theta]\!] \right]_{\bar{x}_r} \, dA_r,$$

$$^{nloc}\overline{K}_{\overline{\Theta}\overline{\Theta}}^{IJ} = \frac{\partial \overline{R}_\Theta^I}{\partial \overline{\Theta}^J} = \int_{\mathcal{I}_0} - \overline{\text{Grad}}\, \overline{N}^I \cdot [-\partial_{\overline{\Theta}^J} \overline{\mathcal{D}}_\parallel(\bar{x}_r)] \overline{Q}_0(\bar{x}_r)$$

$$- \overline{N}^I \overline{\Theta} [-\partial_{\overline{\Theta}^J} \overline{\mathcal{D}}_\parallel \partial_{\overline{\Theta}} \overline{P}_0 - \partial_{\overline{\Theta}^J \overline{\Theta}} \overline{\mathcal{D}}_\parallel \overline{P}_0]_{\bar{x}_r} : D_t \overline{F}(\bar{x}_r) \, dA_r$$

$$+ \int_{\mathcal{I}_0} \overline{N}^I [-\partial_{\overline{\Theta}^J} \overline{\mathcal{D}}_\parallel(\bar{x}_r)] \left[\bar{c}_{\overline{F}}^0 D_t \overline{\Theta} - \frac{1}{\bar{s}_0} [\overline{\Theta}^{-1} - \{\!\{\Theta^{-1}\}\!\}] \right]_{\bar{x}_r} \, dA_r,$$

where

$$D_t \overline{F} = \frac{[\overline{F}_{\tau+1} - \overline{F}_\tau]}{\Delta t} \quad \text{and} \quad D_t \overline{\Theta} = \frac{[\overline{\Theta}_{\tau+1} - \overline{\Theta}_\tau]}{\Delta t}.$$

The notation $[\{\bullet\}]_{\bar{x}_r}$ means that the quantity $\{\bullet\}$ is evaluated at point $\bar{x}_r$. In the derivation of the nonlocal corrections to the interface stiffness matrix, the first and second derivatives of the damage variable with respect to the nodal coordinates and temperature $\overline{\varphi}^J$ and $\overline{\Theta}^J$ at an arbitrary point $\bar{x}_r$ on the interface using $(6)_{2,3}$ are calculated as follows:

$$\partial_{\overline{\Theta}^J} \overline{\mathcal{D}}_\parallel(\bar{x}_r) = \overline{\mathcal{D}}_\parallel' \partial_{\overline{\Theta}^J} F_{nloc} \Rightarrow \partial_{\overline{\Theta}^J} F_{nloc}(\bar{x}_r) = \int_{\mathcal{I}_0} \omega(\bar{x}_r, \bar{x}_s) \frac{1}{\overline{E} F_{loc}(\bar{x}_s)} \partial_{\overline{\Theta}} \overline{\Psi}^0(\bar{x}_s) \overline{N}^J(\bar{x}_s) \, dA_s, \tag{A.14}$$

$$\partial_{\overline{\varphi}^J} \overline{\mathcal{D}}_\parallel(\bar{x}_r) = \overline{\mathcal{D}}_\parallel' \partial_{\overline{\varphi}^J} F_{nloc} \Rightarrow \partial_{\overline{\varphi}^J} F_{nloc}(\bar{x}_r) = \int_{\mathcal{I}_0} \omega(\bar{x}_r, \bar{x}_s) \frac{1}{\overline{E} F_{loc}(\bar{x}_s)} \partial_{\overline{F}} \overline{\Psi}^0(\bar{x}_s) \cdot \overline{\text{Grad}}\, \overline{N}^J(\bar{x}_s) \, dA_s, \tag{A.15}$$

$$\partial_{\overline{\varphi}^J \overline{\Theta}} \overline{\mathcal{D}}_\parallel(\bar{x}_r) = \overline{\mathcal{D}}_\parallel'' \partial_{\overline{\Theta}} F_{nloc} \partial_{\overline{\varphi}^J} F_{nloc} + \overline{\mathcal{D}}_\parallel' \partial_{\overline{\varphi}^J \overline{\Theta}} F_{nloc} \quad \text{and}$$

$$\partial_{\overline{\Theta}^J \overline{\Theta}} \overline{\mathcal{D}}_\parallel(\bar{x}_r) = \overline{\mathcal{D}}_\parallel'' \partial_{\overline{\Theta}^J} F_{nloc} \partial_{\overline{\Theta}} F_{nloc} + \overline{\mathcal{D}}_\parallel' \partial_{\overline{\Theta}^J \overline{\Theta}} F_{nloc}, \tag{A.16}$$

where $\overline{\mathscr{D}}''_{\parallel} = \partial_{F_{\mathrm{nloc}}} \overline{\mathscr{D}}'_{\parallel}$ and $\mathrm{d}A_{\mathrm{s}} = \mathrm{d}A(\bar{\boldsymbol{x}}_{\mathrm{s}})$ and

$$\partial_{\overline{\boldsymbol{\varphi}}^J \overline{\Theta}} F_{\mathrm{nloc}}(\bar{\boldsymbol{x}}_{\mathrm{r}}) = \int_{\mathcal{I}_0} \omega(\bar{\boldsymbol{x}}_{\mathrm{r}}, \bar{\boldsymbol{x}}_{\mathrm{s}}) \left[\frac{-1}{\overline{E}^2 F_{\mathrm{loc}}^3} \partial_{\bar{F}} \overline{\Psi}^0 \partial_{\overline{\Theta}} \overline{\Psi}^0 + \frac{1}{\overline{E} F_{\mathrm{loc}}} \partial_{\bar{F}\overline{\Theta}} \overline{\Psi}^0 \right]_{\bar{\boldsymbol{x}}_{\mathrm{s}}} \cdot \overline{\mathrm{Grad}} \, \overline{N}^J(\bar{\boldsymbol{x}}_{\mathrm{s}}) \, \mathrm{d}A_{\mathrm{s}}, \quad \text{(A.17)}$$

$$\partial_{\overline{\Theta}^J \overline{\Theta}} F_{\mathrm{nloc}}(\bar{\boldsymbol{x}}_{\mathrm{r}}) = \int_{\mathcal{I}_0} \omega(\bar{\boldsymbol{x}}_{\mathrm{r}}, \bar{\boldsymbol{x}}_{\mathrm{s}}) \left[\frac{-1}{\overline{E}^2 F_{\mathrm{loc}}^3} [\partial_{\overline{\Theta}} \overline{\Psi}^0]^2 + \frac{1}{\overline{E} F_{\mathrm{loc}}} \partial_{\overline{\Theta}\overline{\Theta}} \overline{\Psi}^0 \right]_{\bar{\boldsymbol{x}}_{\mathrm{s}}} \overline{N}^J(\bar{\boldsymbol{x}}_{\mathrm{s}}) \, \mathrm{d}A_{\mathrm{s}}. \quad \text{(A.18)}$$

Similarly the notation $[\{\bullet\}]_{\bar{\boldsymbol{x}}_{\mathrm{s}}}$ means that the quantity $\{\bullet\}$ is evaluated at point $\bar{\boldsymbol{x}}_{\mathrm{s}}$. Note that by using the derivatives (A.14)−(A.18) in the nonlocal corrections (A.13), the double integrals are introduced into the formulation due to nonlocality of the damage model. Furthermore, during unloading we set $\overline{\mathscr{D}}' = \overline{\mathscr{D}}'' = 0$.

Appendix B: Constitutive relations in the bulk and on the interface

bulk
$\Psi = \frac{1}{2}\lambda \ln^2 J + \frac{1}{2}\mu[\boldsymbol{F} : \boldsymbol{F} - 3 - 2\ln J] - 3\alpha\kappa[\Theta - \Theta_0]J^{-1}\ln J + c_F[\Theta - \Theta_0 - \Theta \ln(\Theta/\Theta_0)] - \Xi_0[\Theta - \Theta_0]$
$\boldsymbol{P} = \lambda \ln J \boldsymbol{F}^{-\mathrm{t}} + \mu[\boldsymbol{F} - \boldsymbol{F}^{-\mathrm{t}}] - 3\alpha\kappa J^{-1}[\Theta - \Theta_0][1 - \ln J]\boldsymbol{F}^{-\mathrm{t}}$
$\Xi = 3\alpha\kappa J^{-1}\ln J + c_F \ln(\Theta/\Theta_0) + \Xi_0$
$\partial_F \boldsymbol{P} = \lambda[\boldsymbol{F}^{-\mathrm{t}} \otimes \boldsymbol{F}^{-\mathrm{t}} + \ln J \, \mathbb{D}] + \mu[\mathbb{I} - \mathbb{D}] + 3\alpha\kappa[\Theta - \Theta_0][J^{-1}[2 - \ln J]\boldsymbol{F}^{-\mathrm{t}} \otimes \boldsymbol{F}^{-\mathrm{t}} - J^{-1}[1 - \ln J]\mathbb{D}]$
$\partial_\Theta \boldsymbol{P} = -3\alpha\kappa J^{-1}[1 - \ln J]\boldsymbol{F}^{-\mathrm{t}}$
$\partial_\Theta(\Theta\partial_\Theta \boldsymbol{P} : \mathrm{D}_t \boldsymbol{F}) = -3\alpha\kappa J^{-1}[1 - \ln J]\mathrm{div}\,\boldsymbol{V}$
$\partial_F(\Theta\partial_\Theta \boldsymbol{P} : \mathrm{D}_t \boldsymbol{F}) = -3\alpha\kappa\Theta[J^{-1}[\ln J - 2]\mathrm{div}\,\boldsymbol{V}\boldsymbol{F}^{-\mathrm{t}} + J^{-1}[1 - \ln J][\mathrm{D}_t \boldsymbol{F} : \mathbb{D} + [1/\triangle t]\boldsymbol{F}^{-\mathrm{t}} : \mathbb{I}]]$
$\partial_F \boldsymbol{Q} = -Jk[\boldsymbol{F}^{-1} \cdot \boldsymbol{F}^{-\mathrm{t}} \otimes \boldsymbol{F}^{-\mathrm{t}} + \mathbb{B}] : \mathrm{Grad}\,\Theta, \qquad\qquad \partial_{\mathrm{Grad}\,\Theta} \boldsymbol{Q} = -Jk\boldsymbol{G}$
$\mathbb{D} = \partial_F \boldsymbol{F}^{-\mathrm{t}} = -\boldsymbol{F}^{-\mathrm{t}} \underline{\otimes} \boldsymbol{F}^{-1}, \qquad\qquad\qquad \mathbb{I} = \partial_F \boldsymbol{F} = \boldsymbol{i} \,\overline{\otimes}\, \boldsymbol{I}$
$\mathbb{B} = \partial_F(\boldsymbol{F}^{-1} \cdot \boldsymbol{F}^{-\mathrm{t}}) = -[\boldsymbol{F}^{-1} \,\overline{\otimes}\, \boldsymbol{F}^{-1}] \cdot \boldsymbol{F}^{-\mathrm{t}} - \boldsymbol{F}^{-1} \cdot [\boldsymbol{F}^{-\mathrm{t}} \underline{\otimes} \boldsymbol{F}^{-\mathrm{t}}], \quad \boldsymbol{G} = \boldsymbol{F}^{-1} \cdot \boldsymbol{F}^{-\mathrm{t}}$

interface
$\overline{\Psi}^0 = \frac{1}{2}\bar{\lambda} \ln^2 \bar{J} + \frac{1}{2}\bar{\mu}[\bar{\boldsymbol{F}} : \bar{\boldsymbol{F}} - 2 - 2\ln \bar{J}] - 2\bar{\alpha}\bar{\kappa}[\overline{\Theta} - \overline{\Theta}_0]\bar{J}^{-1}\ln \bar{J} + \bar{c}_{\bar{F}}^0[\overline{\Theta} - \overline{\Theta}_0 - \overline{\Theta}\ln(\overline{\Theta}/\overline{\Theta}_0)] - \overline{\Xi}_{\mathrm{s}}[\overline{\Theta} - \overline{\Theta}_0]$
$\overline{\boldsymbol{P}}_0 = \partial_{\bar{F}} \overline{\Psi}^0 = \bar{\lambda} \ln \bar{J} \bar{\boldsymbol{F}}^{-\mathrm{t}} + \bar{\mu}[\bar{\boldsymbol{F}} - \bar{\boldsymbol{F}}^{-\mathrm{t}}] - 2\bar{\alpha}\bar{\kappa}\bar{J}^{-1}[\overline{\Theta} - \overline{\Theta}_0][1 - \ln \bar{J}]\bar{\boldsymbol{F}}^{-\mathrm{t}}$
$\overline{\Xi}_0 = 2\bar{\alpha}\bar{\kappa}\bar{J}^{-1}\ln \bar{J} + \bar{c}_{\bar{F}}^0 \ln(\overline{\Theta}/\overline{\Theta}_0) + \overline{\Xi}_{\mathrm{s}}, \qquad\qquad \partial_{\overline{\Theta}} \overline{\Psi}^0 = -\overline{\Xi}_0$
$\partial_{\bar{F}} \overline{\boldsymbol{P}}_0 = \bar{\lambda}[\bar{\boldsymbol{F}}^{-\mathrm{t}} \otimes \bar{\boldsymbol{F}}^{-\mathrm{t}} + \ln \bar{J}\overline{\mathbb{D}}] + \bar{\mu}[\overline{\mathbb{I}} - \overline{\mathbb{D}}] + 2\bar{\alpha}\bar{\kappa}[\overline{\Theta} - \overline{\Theta}_0][\bar{J}^{-1}[2 - \ln \bar{J}]\bar{\boldsymbol{F}}^{-\mathrm{t}} \otimes \bar{\boldsymbol{F}}^{-\mathrm{t}} - \bar{J}^{-1}[1 - \ln \bar{J}]\overline{\mathbb{D}}]$
$\partial_{\overline{\Theta}} \overline{\boldsymbol{P}}_0 = \partial_{\bar{F}\overline{\Theta}} \overline{\Psi}^0 = -2\bar{\alpha}\bar{\kappa}\bar{J}^{-1}[1 - \ln \bar{J}]\bar{\boldsymbol{F}}^{-\mathrm{t}}, \qquad\qquad \partial_{\overline{\Theta}\overline{\Theta}} \overline{\Psi}^0 = -\bar{c}_{\bar{F}}^0\overline{\Theta}^{-1}$
$\partial_{\overline{\Theta}}(\overline{\Theta}\partial_{\overline{\Theta}} \overline{\boldsymbol{P}}_0 : \mathrm{D}_t \bar{\boldsymbol{F}}) = -2\bar{\alpha}\bar{\kappa}\bar{J}^{-1}[1 - \ln \bar{J}]\overline{\mathrm{div}}\,\overline{\boldsymbol{V}}$
$\partial_{\bar{F}}(\overline{\Theta}\partial_{\overline{\Theta}} \overline{\boldsymbol{P}}_0 : \mathrm{D}_t \bar{\boldsymbol{F}}) = -2\bar{\alpha}\bar{\kappa}\overline{\Theta}[\bar{J}^{-1}[\ln \bar{J} - 2]\overline{\mathrm{div}}\,\overline{\boldsymbol{V}}\bar{\boldsymbol{F}}^{-\mathrm{t}} + \bar{J}^{-1}[1 - \ln \bar{J}][\mathrm{D}_t \bar{\boldsymbol{F}} : \overline{\mathbb{D}} + [1/\triangle t]\bar{\boldsymbol{F}}^{-\mathrm{t}} : \overline{\mathbb{i}}]]$
$\partial_{\bar{F}} \overline{\boldsymbol{Q}}_0 = -J\bar{k}_0[\bar{\boldsymbol{F}}^{-1} \cdot \bar{\boldsymbol{F}}^{-\mathrm{t}} \otimes \bar{\boldsymbol{F}}^{-\mathrm{t}} + \overline{\mathbb{B}}] : \overline{\mathrm{Grad}}\,\overline{\Theta}, \qquad\qquad \partial_{\overline{\mathrm{Grad}}\,\overline{\Theta}} \overline{\boldsymbol{Q}}_0 = -J\bar{k}_0\overline{\boldsymbol{G}}$
$\overline{\mathbb{D}} = \partial_{\bar{F}} \bar{\boldsymbol{F}}^{-\mathrm{t}} = -\bar{\boldsymbol{F}}^{-\mathrm{t}} \underline{\otimes} \bar{\boldsymbol{F}}^{-1} + [\boldsymbol{i} - \bar{\boldsymbol{i}}] \,\overline{\otimes}\, \bar{\boldsymbol{F}}^{-1} \cdot \bar{\boldsymbol{F}}^{-\mathrm{t}}, \qquad\qquad \overline{\mathbb{i}} = \partial_{\bar{F}} \bar{\boldsymbol{F}} = \boldsymbol{i} \,\overline{\otimes}\, \bar{\boldsymbol{I}}$
$\overline{\mathbb{B}} = \partial_{\bar{F}}(\bar{\boldsymbol{F}}^{-1} \cdot \bar{\boldsymbol{F}}^{-\mathrm{t}}) = \,^{\mathrm{t}}[\bar{\boldsymbol{F}}^{-1} \cdot \overline{\mathbb{D}}] + \bar{\boldsymbol{F}}^{-1} \cdot \overline{\mathbb{D}}, \qquad\qquad \overline{\boldsymbol{G}} = \bar{\boldsymbol{F}}^{-1} \cdot \bar{\boldsymbol{F}}^{-\mathrm{t}}$

List of symbols

F	bulk material deformation gradient	$\overline{F}$	interface material deformation gradient
φ	bulk deformation map	$\overline{\varphi}$	interface deformation map
X	bulk material coordinates	$\overline{X}$	interface material coordinates
x	bulk spatial coordinates	$\bar{x}$	interface spatial coordinates
Θ	bulk temperature	$\overline{\Theta}$	interface temperature
Θ_0	bulk initial temperature	$\overline{\Theta}_0$	interface initial temperature
N	bulk material normal to surface	$\overline{N}$	interface material normal to interface
n	bulk spatial normal to surface	$\overline{n}$	interface spatial normal to interface
Ψ	bulk Helmholtz energy	$\overline{\Psi}$	interface nominal Helmholtz energy
Ξ_s	bulk specific entropy	$\overline{\Xi}_s$	interface specific entropy
Ξ	bulk entropy	$\overline{\Xi}$	interface nominal entropy
P	bulk Piola stress	$\overline{P}$	interface nominal Piola stress

only interface			
$\varphi^{\pm}$	deformation maps of $\pm$ side	$x^{\pm}$	spatial coordinates of $\pm$ side
$\widetilde{n}$	spatial normal to interface boundary	$\widetilde{N}$	material normal to interface boundary
$\overline{\Psi}^0$	undamaged Helmholtz energy	$\overline{D}_{\parallel}$	damage variable
$\overline{P}_0$	undamaged Piola stress tensor	$\overline{\Xi}^0$	undamaged entropy
$\overline{F}_{\mathrm{loc}}$	local equivalent distortion	$\overline{F}_{\mathrm{nloc}}$	nonlocal equivalent distortion
$\overline{F}_0$	elastic limit	$\overline{F}_{\mathrm{max}}$	maximum attained $\overline{F}_{\mathrm{nloc}}$
$\bar{s}_0$	undamaged sensitivity	$\bar{r}_Q^0$	undamaged Kapitza resistance coefficient

Acknowledgments

References

[Altenbach et al. 2012] H. Altenbach, V. A. Eremeyev, and N. F. Morozov, "Surface viscoelasticity and effective properties of thin-walled structures at the nanoscale", *Int. J. Eng. Sci.* **59** (2012), 83–89.

[Bažant and Jirásek 2002] Z. P. Bažant and M. Jirásek, "Nonlocal integral formulations of plasticity and damage: survey of progress", *J. Eng. Mech.* **128**:11 (2002), 1119–1149.

[Bažant and Xi 1991] Z. P. Bažant and Y. Xi, "Statistical size effect in quasi-brittle structures, II: Nonlocal theory", *J. Eng. Mech.* **117**:11 (1991), 2623–2640.

[Benveniste 2013] Y. Benveniste, "Models of thin interphases and the effective medium approximation in composite media with curvilinearly anisotropic coated inclusions", *Int. J. Eng. Sci.* **72** (2013), 140–154.

[Benveniste and Miloh 2001] Y. Benveniste and T. Miloh, "Imperfect soft and stiff interfaces in two-dimensional elasticity", *Mech. Mater.* **33**:6 (2001), 309–323.

[Berber et al. 2000] S. Berber, Y.-K. Kwon, and D. Tománek, "Unusually high thermal conductivity of carbon nanotubes", *Phys. Rev. Lett.* **84** (2000), 4613–4616.

[Cahill et al. 2003] D. G. Cahill, W. K. Ford, K. E. Goodson, G. D. Mahan, A. Majumdar, H. J. Maris, R. Merlin, and S. R. Phillpot, "Nanoscale thermal transport", *J. Appl. Phys.* **93** (2003), 793–818.

[Cammarata 1994] R. C. Cammarata, "Surface and interface stress effects in thin films", *Prog. Surf. Sci.* **46** (1994), 1–38.

[Chaboche 1981] J.-L. Chaboche, "Continuous damage mechanics — a tool to describe phenomena before crack initiation", *Nuc. Eng. Des.* **64**:2 (1981), 233–247.

[Che et al. 2000] J. Che, T. Çagin, and W. A. Goddard III, "Thermal conductivity of carbon nanotubes", *Nanotechnology* **11** (2000), 65–69.

[Daher and Maugin 1986] N. Daher and G. A. Maugin, "The method of virtual power in continuum mechanics: application to media presenting singular surfaces and interfaces", *Acta Mech.* **60**:3–4 (1986), 217–240.

[Davydov et al. 2013] D. Davydov, A. Javili, and P. Steinmann, "On molecular statics and surface-enhanced continuum modeling of nano-structures", *Comput. Mater. Sci.* **69** (2013), 510–519.

[dell'Isola and Romano 1987] F. dell'Isola and A. Romano, "On the derivation of thermomechanical balance equations for continuous systems with a nonmaterial interface", *Int. J. Eng. Sci.* **25**:11–12 (1987), 1459–1468.

[Dingreville et al. 2005] R. Dingreville, J. Qu, and M. Cherkaoui, "Surface free energy and its effect on the elastic behavior of nano-sized particles, wires and films", *J. Mech. Phys. Solids* **53**:8 (2005), 1827–1854.

[Duan et al. 2005a] H. L. Duan, J. Wang, Z. P. Huang, and B. L. Karihaloo, "Eshelby formalism for nano-inhomogeneities", *Proc. R. Soc. Lond. A* **461**:2062 (2005), 3335–3353.

[Duan et al. 2005b] H. L. Duan, J. Wang, Z. P. Huang, and B. L. Karihaloo, "Size-dependent effective elastic constants of solids containing nano-inhomogeneities with interface stress", *J. Mech. Phys. Solids* **53**:7 (2005), 1574–1596.

[Duan et al. 2009] H. L. Duan, J. Wang, and B. L. Karihaloo, "Theory of elasticity at the nanoscale", pp. 1–68 Elsevier, 2009.

[Esmaeili et al. 2016a] A. Esmaeili, A. Javili, and P. Steinmann, "Highly-conductive energetic coherent interfaces subject to in-plane degradation", *Math. Mech. Solids* (2016).

[Esmaeili et al. 2016b] A. Esmaeili, A. Javili, and P. Steinmann, "A thermo-mechanical cohesive zone model accounting for mechanically energetic Kapitza interfaces", *Int. J. Solids Struct.* **92–93** (2016), 29–44.

[Fischer and Svoboda 2010] F. D. Fischer and J. Svoboda, "Stresses in hollow nanoparticles", *Int. J. Solids Struct.* **47**:20 (2010), 2799–2805.

[Fried and Gurtin 2007] E. Fried and M. E. Gurtin, "Thermomechanics of the interface between a body and its environment", *Contin. Mech. Thermodyn.* **19**:5 (2007), 253–271.

[Fried and Todres 2005] E. Fried and R. E. Todres, "Mind the gap: the shape of the free surface of a rubber-like material in proximity to a rigid contactor", *J. Elasticity* **80**:1-3 (2005), 97–151.

[Gurtin 1998] M. E. Gurtin, "A general theory of curved deformable interfaces in solids at equilibrium", *Philos. Mag. A* **78**:5 (1998), 1093–1109.

[Gurtin and Murdoch 1975] M. E. Gurtin and A. I. Murdoch, "A continuum theory of elastic material surfaces", *Arch. Rational Mech. Anal.* **57**:4 (1975), 291–323.

[Huang and Sun 2007] Z. P. Huang and L. Sun, "Size-dependent effective properties of a heterogeneous material with interface energy effect: from finite deformation theory to infinitesimal strain analysis", *Acta Mech.* **190**:1–4 (2007), 151–163.

[Javili and Steinmann 2010] A. Javili and P. Steinmann, "On thermomechanical solids with boundary structures", *Int. J. Solids Struct.* **47**:24 (2010), 3245–3253.

[Javili et al. 2012] A. Javili, A. McBride, and P. Steinmann, "Numerical modelling of thermomechanical solids with mechanically energetic (generalised) Kapitza interfaces", *Comput. Mat. Sci.* **65** (2012), 542–551.

[Javili et al. 2013] A. Javili, A. McBride, and P. Steinmann, "Numerical modelling of thermomechanical solids with highly conductive energetic interfaces", *Int. J. Numer. Methods Eng.* **93**:5 (2013), 551–574.

[Javili et al. 2014] A. Javili, S. Kaessmair, and P. Steinmann, "General imperfect interfaces", *Comput. Methods Appl. Mech. Eng.* **275** (2014), 76–97.

[Kachanov 1958] L. M. Kachanov, "Time of the rupture process under creep conditions", *Izv. Akad. Nauk. S.S.R. Otd. Tech. Nauk.* **8** (1958), 26–31. In Russian; translated in *International Journal of Fracture* **97**:11 (1999), xi–xviii.

[Kaessmair et al. 2014] S. Kaessmair, A. Javili, and P. Steinmann, "Thermomechanics of solids with general imperfect coherent interfaces", *Arch. Appl. Mech.* **84**:9 (2014), 1409–1426.

[Levitas and Javanbakht 2010] V. I. Levitas and M. Javanbakht, "Surface tension and energy in multivariant martensitic trans-formations: phase-field theory, simulations, and model of coherent interface", *Phys. Rev. Lett.* **105**:16 (2010), 165701.

[Moeckel 1975] G. P. Moeckel, "Thermodynamics of an interface", *Arch. Rational Mech. Anal.* **57** (1975), 255–280.

[Murdoch 1976] A. I. Murdoch, "A thermodynamical theory of elastic material interfaces", *Quart. J. Mech. Appl. Math.* **29**:3 (1976), 245–275.

[Prasher 2005] R. Prasher, "Predicting the thermal resistance of nanosized constrictions", *Nano Letters* **5**:11 (2005), 2155–2159.

[Prasher 2006] R. Prasher, "Thermal interface materials: historical perspective, status, and future directions", *Proc. IEEE* **94**:8 (2006), 1571–1586.

[Rabotnov 1963] Y. N. Rabotnov, "On the equation of state of creep", *P. I. Mech. Eng. Conf. Proc.* **178**:1 (1963), 2–117–2–122.

[Sharma et al. 2003] P. Sharma, S. Ganti, and N. Bhate, "Effect of surfaces on the size-dependent elastic state of nano-inhomogeneities", *Appl. Phys. Lett.* **82**:4 (2003), 535–537.

[Simo and Hughes 1998] J. C. Simo and T. J. R. Hughes, *Computational inelasticity*, Springer, New York, 1998.

[de Souza Neto and Perić 1996] E. A. de Souza Neto and D. Perić, "A computational framework for a class of fully coupled models for elastoplastic damage at finite strains with reference to the linearization aspects", *Comput. Meth. Appl. Mech. Eng.* **130**:1 (1996), 179–193.

[de Souza Neto et al. 1998] E. A. de Souza Neto, D. Perić, and D. R. J. Owen, "Continuum modelling and numerical simulation of material damage at finite strains", *Arch. Comput. Methods Eng.* **5**:4 (1998), 311–384.

[Steigmann and Ogden 1999] D. J. Steigmann and R. W. Ogden, "Elastic surface-substrate interactions", *Proc. R. Soc. Lond. A* **455**:1982 (1999), 437–474.

[Steinmann 1999] P. Steinmann, "Formulation and computation of geometrically non-linear gradient damage", *Int. J. Num. Methods Eng.* **46**:5 (1999), 757–779.

[Steinmann 2008] P. Steinmann, "On boundary potential energies in deformational and configurational mechanics", *J. Mech. Phys. Solids* **56**:3 (2008), 772–800.

[Steinmann et al. 1994] P. Steinmann, C. Miehe, and E. Stein, "Comparison of different finite deformation inelastic damage models within multiplicative elastoplasticity for ductile materials", *Comput. Mech.* **13**:6 (1994), 458–474.

[Yvonnet et al. 2011] J. Yvonnet, A. Mitrushchenkov, G. Chambaud, and Q.-C. He, "Finite element model of ionic nanowires with size-dependent mechanical properties determined by ab initio calculations", *Comput. Methods Appl. Mech. Eng.* **200**:5–8 (2011), 614–625.

ALI ESMAEILI: ali.esmaeili@ltm.uni-erlangen.de
Department of Applied Mechanics, University of Erlangen-Nuremberg, Egerlandstrasse 5, D-91058 Erlangen, Germany

PAUL STEINMANN: paul.steinmann@ltm.uni-erlangen.de
Department of Applied Mechanics, University of Erlangen-Nuremberg, Egerlandstrasse 5, D-91058 Erlangen, Germany

ALI JAVILI: ajavili@bilkent.edu.tr
Department of Mechanical Engineering, Bilkent University, 06800 Ankara, Turkey

■msp

TRANSIENT GROWTH OF A PLANAR CRACK
IN THREE DIMENSIONS: MIXED MODE

Louis Milton Brock

Transient growth in 3D of a semi-infinite, plane brittle crack in an isotropic, elastic solid is considered. Growth is mixed-mode, caused by in-plane and normal point forces on each face of an existing semi-infinite crack. An analytic solution is obtained for the case of dynamic similarity, i.e., crack edge speed is subcritical and may vary continuously with direction, but is time-invariant. The dynamic energy release rate criterion, with kinetic energy included, is imposed. A nonlinear differential equation for crack edge speed results, and allows the description of crack contour, i.e., the curve formed by the crack edge in the crack plane. Study indicates that forces of a type that increase rapidly from zero can create a fracture initiation phase in which crack growth rate indeed does not vary with time.

Introduction

In 2D dynamic fracture, the rectilinear crack edge can be defined by an equation of motion for the crack tip [Freund 1972; 1990]. In a 3D study, such an equation must describe the crack contour, i.e., curve formed by the crack edge in the crack plane. For the dynamic steady state case, this goal is considered in [Brock 2015a; 2015b]. A semi-infinite crack, driven by compressive point forces that translate on its surfaces, extends at subcritical constant speed in an unbounded, isotropic solid. Results indicate that the crack edge is rectilinear away from the point force path, but forms a bulge near the forces.

This paper treats a transient version of a similar problem. Stationary point forces are applied at the edge of an initially undisturbed, plane semi-infinite crack. The forces include both normal and in plane components, and mixed-mode, brittle fracture occurs. A (presumably) concave region of new crack surface grows out from the point forces. Region behavior is dynamically similar, i.e., points on its edge move at subcritical speeds that may vary with position, but not with time. The process is governed by dynamic energy release rate [Freund 1990; Brock 2015a; 2015b]. In contrast to [Brock 2015a; 2015b] however, the concept of surface energy density [Freund 1990] is employed. In contrast to [Freund 1990; Brock 2015a], kinetic energy [Gdoutos 2005; Brock 2015b] is included in the energy rate balance.

Problem statement

Closed crack $A_C(x_3^0 = 0, x_1^0 < 0)$, with boundary $C(x_1^0, x_3^0) = 0$, exists in an unbounded elastic solid. Cartesian coordinates are denoted by $\boldsymbol{x}_0 = \boldsymbol{x}_0(x_k^0)$, and $k = (1, 2, 3)$. The solid is at rest for time $t \leq 0$, but point forces (compression and shear) appear for $t > 0$ on both crack faces at points $(x_1^0 = 0-, x_2^0 = 0, x_3^0 = 0\pm)$. Brittle fracture is instantaneous, and the crack extends outward from $\boldsymbol{x}_0 = 0$. The crack now

---

occupies region $A_C + \delta A$ and boundary C now includes a concave bulge [Brock 2015a; 2015b] that can be defined as

$$\sqrt{(x_1^0)^2 + (x_2^0)^2} = l(\theta, t), \quad l(\theta, t) = V(\theta)t, \tag{1a}$$

$$0 < V < V_R, \quad \theta = \tan^{-1}\frac{x_2^0}{x_1^0}\left(|\theta| < \tfrac{1}{2}\pi\right). \tag{1b}$$

Equation (1) imposes a dynamically similar geometry on the crack. Equations that govern displacement $\boldsymbol{u}(u_k)$ and traction $\boldsymbol{T}(\sigma_{ik})$ for $t > 0$ are [Achenbach 1973]

$$\nabla \cdot \boldsymbol{T} - \rho\ddot{\boldsymbol{u}} = 0, \tag{2a}$$

$$\frac{1}{\mu}\boldsymbol{T} = \frac{2\nu}{1-2\nu}(\nabla \cdot \boldsymbol{u})\mathbb{1} + \nabla\boldsymbol{u} + \boldsymbol{u}\nabla. \tag{2b}$$

In (2), components $u_k = u_k(\boldsymbol{x}_0, t)$ and $\sigma_{ik} = \sigma_{ik}(\boldsymbol{x}_0, t)$; respectively, $(\nabla, \nabla^2, \mathbb{1})$ are gradient, Laplacian, and identity tensor. Operations $(Df, \dot{f})$ signify differentiation with respect to t in the fixed frame of $\boldsymbol{x}_0$, and (μ, ρ, ν) respectively are shear modulus, mass density and Poisson's ratio. Uncoupling of (2a) gives

$$\boldsymbol{u} = \boldsymbol{u}_S + \boldsymbol{u}_D, \tag{3a}$$

$$V_S^2\nabla^2\boldsymbol{u}_S - \ddot{\boldsymbol{u}}_S = 0, \quad V_D^2\nabla^2\boldsymbol{u}_D - \ddot{\boldsymbol{u}}_D = 0, \tag{3b}$$

$$\nabla \cdot \boldsymbol{u}_S = 0, \qquad \nabla \times \boldsymbol{u}_D = 0. \tag{3c}$$

Equation (1b) indicates that Rayleigh speed $V_R < V_S$ is the bound for subcritical crack extension. In (3b) (V_S, V_D) are speeds of shear and dilatational waves:

$$V_S = \sqrt{\frac{\mu}{\rho}}, \quad V_D = c_D V_S, \quad c_D = \sqrt{2\frac{1-\nu}{1-2\nu}}. \tag{4}$$

For $x_3^0 = 0\pm$ and $(x_1^0, x_2^0) \in A_C + \delta A$ (for $t > 0$),

$$\sigma_{3k} = -P_k\delta(x_1^0)\delta(x_2^0). \tag{5a}$$

For $x_3^0 = 0$ and $(x_1^0, x_2^0) \notin A_C + \delta A$ (for $t > 0$),

$$[u_k] = 0. \tag{5b}$$

In (5), force P_k is a positive constant, $\delta(f)$ denotes Dirac function, and $[f] = f^{(+)} - f^{(-)}$ where $f^{(\pm)} = f(x_1^0, x_2^0, 0\pm, t)$. Also $[u_k]$ in $A_C + \delta A$ must vanish continuously on C, but σ_{3k} for $(x_1^0, x_2^0) \notin A_C + \delta A$ can exhibit (integrable) singular behavior on C. For $t \leq 0$, then $(\boldsymbol{u}, \boldsymbol{T}) \equiv 0$, and for finite $t > 0$, then $(\boldsymbol{u}, \boldsymbol{T})$ must be bounded as $|\boldsymbol{x}_0| \to \infty$.

Discontinuity problem

A common, e.g., [Barber 1992], procedure for solving crack problems is to represent the relative motion of crack faces as unknown discontinuities in displacement. To implement this procedure for the present initial/boundary value problem, the related problem of discontinuities in $(\boldsymbol{u}, \boldsymbol{T})$ is now considered. The

unbounded solid is again at rest when at time $t = 0$ the discontinuities are imposed in the same region A_C of the $x_1^0 x_2^0$-plane. That is, conditions (5b) still hold, but for $x_3 = 0$ and $(x_1^0, x_2^0) \in A_C + \delta A$ (for $t > 0$):

$$[u_k] = \Delta_k, \quad [\sigma_{3k}] = \Sigma_k. \tag{6}$$

Here (Δ_k, Σ_k) are continuous functions of (x_1^0, x_2^0, t). They are bounded in $A_C + \delta A$ for $\sqrt{(x_1^0)^2 + (x_2^0)^2} \to \infty$ and vanish on C and for $t \le 0$. The requirements for (Δ_k, Σ_k) suggest that conditions for $t \le 0$ and for finite $t > 0$ and $|x_0| \to \infty$ are again satisfied.

Transform solution

An effective procedure, e.g., [Brock and Achenbach 1973], for 2D transient study of semi-infinite crack extension at constant speed employs coordinates that translate with the crack edge, and unilateral temporal and bilateral spatial integral transforms [Sneddon 1972]. In view of (1), translating base x is defined as

$$x_1 = x_1^0 - [c(\theta)\cos\theta]s, \quad x_2 = x_2^0 - [c(\theta)\sin\theta]s, \quad x_3 = x_3^0, \tag{7a}$$

$$s = V_S t, \quad c(\theta) = \frac{V(\theta)}{V_S}, \tag{7b}$$

$$\dot{f} = Df = V_S[\partial_s f - c(\theta)(\partial_1 f \cos\theta + \partial_2 f \sin\theta)], \tag{7c}$$

$$\partial_s f = \frac{\partial f}{\partial s}, \quad \partial_k f = \frac{\partial f}{\partial x_k} \quad k = (1, 2, 3). \tag{7d}$$

The temporal Laplace transform operation is

$$L(f) = \hat{f}(p) = \int f(s) \exp(-ps) \, ds. \tag{8a}$$

Integration is over positive real s and $\text{Re}(p) > 0$. A double spatial integral transform is now required. The operation in terms of (x_1, x_2) and the corresponding inverse operation are [Sneddon 1972]

$$\tilde{f}(p, q_1, q_2) = \iint \hat{f}(p, x_1, x_2) \exp[-p(q_1 x_1 + q_2 x_2)] \, dx_1 \, dx_2, \tag{8b}$$

$$\hat{f}(p, x_1, x_2) = \left(\frac{p}{2\pi i}\right)^2 \iint \tilde{f}(p, q_1, q_2) \exp[p(q_1 x_1 + q_2 x_2)] \, dq_1 \, dq_2. \tag{8c}$$

Integration in (8b) is over real (x_1, x_2); integration in (8c) is along the imaginary (q_1, q_2)-axes. It is noted that (x, s) have dimensions of length, p has dimensions of inverse length, and (q_1, q_2) are dimensionless. Because (1) involves a speed that varies with direction, application of (8b) to (2)–(4), (5b) and (6) is complicated. Despite the role of θ, the problem is not axially symmetric. Nevertheless, 3D studies of sliding contact [Brock 2012] and crack growth [Brock 2015a; 2015b] suggest transformations

$$\text{Im}(q_1) = \text{Im}(q)\cos\psi, \quad \text{Im}(q_2) = \text{Im}(q)\sin\psi, \tag{9a}$$

$$x_1 = x\cos\psi, \qquad x_2 = x\sin\psi. \tag{9b}$$

Here $\text{Re}(q) = 0+$ and $|\text{Im}(q), x| < \infty$ and $|\psi| < \frac{1}{2}\pi$. Parameters (q, ψ) and (x, ψ) resemble quasipolar coordinates, i.e.,

$$dx_1 \, dx_2 = |x| \, dx \, d\psi, \quad dq_1 \, dq_2 = |q| \, dq \, d\psi. \tag{9c}$$

The uncoupling effect of (9) leads to the combination

$$\tilde{f}(p, q_1, q_2) \rightarrow \bar{f}(p, q, \psi), \tag{10a}$$

$$\hat{f}(p, x, \psi) = -\frac{p^2}{2\pi} \int \frac{|q|}{q} \bar{f}(p, q, \psi) \exp(pqx) \, dq. \tag{10b}$$

Integration is along the positive $(\text{Re}(q) = 0+)$ side of the $\text{Im}(q)$-axis. In view of (7), (9) and (10a) the transform of differential equations (3b) take the respective form

$$[\partial_3^2 - p^2(1 - cq)^2]\bar{u}_S = 0, \tag{11a}$$

$$[c_D^2\partial_3^2 - p^2(1 - cq)^2]\bar{u}_D = 0. \tag{11b}$$

In view of (11), (3c) and conditions for $s \leq 0$ and finite $s > 0$ and $|x| \rightarrow \infty$, the displacement transforms for $x_3 > 0(+)$ and $x_3 < 0(-)$ are

$$\bar{u}_1^{(\pm)} = q \cos \psi \, U_\pm \exp(-pA|x_3|) + U_1^\pm \exp(-pB|x_3|), \tag{12a}$$

$$\bar{u}_2^{(\pm)} = q \sin \psi \, U_\pm \exp(-pA|x_3|) + U_2^\pm \exp(-pB|x_3|), \tag{12b}$$

$$\bar{u}_3^{(\pm)} = (\mp)AU_\pm \exp(-pA|x_3|)(\pm)\frac{q}{B}(U_1^\pm \cos \psi + U_2^\pm \sin \psi) \exp(-pB|x_3|). \tag{12c}$$

In (11) and (12), $c = c(\psi)$ and coefficients $(U_\pm, U_1^\pm, U_2^\pm)$ are functions of (p, q, ψ). Terms (A, B) are

$$A = \sqrt{\frac{1}{c_D^2}(1 - cq)^2 - q^2},$$

$$B = \sqrt{(1 - cq)^2 - q^2}. \tag{13a}$$

Therefore, bounded behavior for $\hat{u}_k$ as $|x_3| \rightarrow \infty$ requires that $\text{Re}(A) > 0$ in the q-plane with branch cut

$$\text{Im}(q) = 0,$$

$$\frac{-1}{c_D - c} < \text{Re}(q) < \frac{1}{c_D + c}. \tag{13b}$$

Similarly $\text{Re}(B) > 0$ in the q-plane with branch cut

$$\text{Im}(q) = 0,$$

$$-\frac{1}{1 - c} < \text{Re}(q) < \frac{1}{1 + c}. \tag{13c}$$

Restriction (1b) guarantees that $c_D - c > 1 - c > 0$. Equations (2b), (5b) and (6) for $x_3^0 = x_3 = 0$ can be operated upon with (8) in light of (7) and (9)–(11). Coefficients $(U_\pm, U_1^\pm, U_2^\pm)$ in (12) can then be found in terms of transforms $(\bar{\Delta}_k, \bar{\Sigma}_k)$. Results lead to six homogeneous equations that relate $(\bar{u}_k, \bar{\sigma}_{3k})$ for $x_3 = 0\pm$ and $(\bar{\Delta}_k, \bar{\Sigma}_k)$ (Appendix A).

Application to crack growth problem

Study of (5a) shows that Σ_k is either not specified or is required to vanish. Therefore, $\bar{\Sigma}_k$ can be dropped from the analysis. Equations (A.2) reduce to

$$\bar{\tau}_1^+ + \bar{\tau}_{1P} + \mu p \tfrac{1}{2} B \bar{\Delta}_1 - \mu p \frac{q^2 M \cos \psi}{2B(1-cq)^2}(\bar{\Delta}_1 \cos \psi + \bar{\Delta}_2 \sin \psi) = 0, \tag{14a}$$

$$\bar{\tau}_2^+ + \bar{\tau}_{2P} + \mu p \tfrac{1}{2} B \bar{\Delta}_2 - \mu p \frac{q^2 M \sin \psi}{2B(1-cq)^2}(\bar{\Delta}_1 \cos \psi + \bar{\Delta}_2 \sin \psi) = 0, \tag{14b}$$

$$\bar{\tau}_3^+ + \bar{\tau}_{3P} + \frac{\mu p M_R \bar{\Delta}_3}{2A(1-cq)^2} = 0. \tag{14c}$$

Here τ_{kP} is the point-force contribution to σ_{3k}. In view of (5) and (8)–(10),

$$\bar{\tau}_{kP} = -\frac{P_k}{p(1-cq)}, \quad \mathrm{Re}(1-cq) > 0. \tag{15}$$

The contribution to σ_{3k} for $x > 0$ is $\tau_k^+(x, \psi, s)$, which is generated behind wave front $c_D s - x - cs > 0$ and is unknown. In view of (8)–(10) therefore, transform $\bar{\tau}_k^+$ exists for $\mathrm{Re}(q) > -1/(c_D - c)$. Term $\Delta_k(x, \psi, s) = 0$ (for $x > 0$) and is an unknown function for $x < 0$ that is generated behind wave front $c_D s + x + cs > 0$. Therefore transform $\bar{\Delta}_k$ exists for $\mathrm{Re}(q) < 1/(c_D + c)$.

Equations (14a) and (14b) are coupled, and are considered first. Elimination of the M-term and use of (15) gives

$$\left[\bar{\tau}_1^+ - \frac{P_1}{p(1-cq)}\right]\sin \psi - \left[\bar{\tau}_2^+ - \frac{P_2}{p(1-cq)}\right]\cos \psi + \mu p \tfrac{1}{2} B(\bar{\Delta}_2 \cos \psi - \bar{\Delta}_1 \sin \psi) = 0. \tag{16}$$

Equation (16) is of the Wiener–Hopf type [Morse and Feshbach 1953; Achenbach 1973] and can be solved as follows: (A, B) are written as products $(A_+ A_-, B_+ B_-)$, where

$$A_\pm = \sqrt{\frac{1}{c_D} \pm q\left(1 \mp \frac{c}{c_D}\right)}, \quad B_\pm = \sqrt{1 \pm q(1 \mp c)}. \tag{17}$$

In (17) $A_\pm$ are analytic in, respectively, overlapping half-planes $\mathrm{Re}(q) > -1/(c_D - c)$ and $\mathrm{Re}(q) < 1/(c_D + c)$. In (17) $B_\pm$ are analytic in, respectively, overlapping half-planes $\mathrm{Re}(q) > -1/(1-c)$ and $\mathrm{Re}(q) < 1/(1+c)$. Equation (16) can be rearranged as

$$\frac{2}{\mu B_+}(\bar{\tau}_1^+ \sin \psi - \bar{\tau}_2^+ \cos \psi) + \frac{2}{\mu p(1-cq)}\left(\frac{1}{B_+} - \sqrt{c}\right)(P_2 \cos \psi - P_1 \sin \psi)$$

$$= p B_-(\bar{\Delta}_1 \sin \psi - \bar{\Delta}_2 \cos \psi) - \frac{2\sqrt{c}}{\mu p(1-cq)}(P_2 \cos \psi - P_1 \sin \psi), \tag{18a}$$

$$A_+(1/c) = B_+(1/c) = 1/\sqrt{c}. \tag{18b}$$

The left-hand and right-hand sides of (18a) are analytic, respectively, in overlapping half-plane $\mathrm{Re}(q) > -1/(c_D - c)$ and $\mathrm{Re}(q) < 1/(c_D + c)$, so that each side is an analytic continuation of the same entire function. In connection with (6), Δ_k must vanish continuously on C for $x \to 0-$. Equations (8a) and (10b)

therefore require that $pq\bar{\Delta}_k$, and also the right-hand side of (18a), vanish for $|q| \to \infty$. The entire function itself must then in light of Liouville's theorem [Morse and Feshbach 1953] vanish, and (18a) yields

$$\bar{\tau}_1^+ \sin\psi - \vec{\tau}_2^+ \cos\psi = \frac{1}{p(1-cq)}(\sqrt{c}B_+ - 1)(P_2\cos\psi - P_1\sin\psi), \tag{19a}$$

$$\bar{\Delta}_1 \sin\psi - \bar{\Delta}_2 \cos\psi = \frac{2\sqrt{c}}{\mu p^2(1-cq)B_-}(P_2\cos\psi - P_1\sin\psi). \tag{19b}$$

In (A.3) it can be shown that

$$B^2(1-cq)^2 - q^2 M = M_R. \tag{20}$$

Use of (15), (19a) and (20) in (14a) gives

$$\bar{\tau}_1^+ - \frac{P_1}{p(1-cq)} - \frac{\sqrt{c}B_+ \sin\psi}{p(1-cq)}(P_2\cos\psi - P_1\sin\psi) = \frac{\mu p M_R \cos\psi}{2B(1-cq)^2}(\bar{\Delta}_1\cos\psi + \bar{\Delta}_2\sin\psi). \tag{21}$$

Equation (21) is also of the Wiener–Hopf type, and it is noted that M_R in (A.3a) is the Rayleigh function in (q, ψ)-space. Its branch points on the $\mathrm{Re}(q)$-axis are ascertained in (13a). It also exhibits two roots on the $\mathrm{Re}(q)$-axis, $-1/(c_R - c)$ and $1/(c_R - c)$. Here $V_R = c_R V_S$ is the Rayleigh wave speed in the solid, and $c_R < 1 < c_D$. In view of (1b) and (A.3a),

$$\frac{-1}{c_R - c} < \frac{-1}{1-c} < \frac{-1}{c_D - c} < 0 < \frac{1}{c_D + c} < \frac{1}{1+c} < \frac{1}{c_R + c} < \frac{1}{c}, \tag{22a}$$

$$M_R \approx -Rq^4 (|q| \to \infty), \tag{22b}$$

$$R = 4ab - K^2, \quad R(\pm c_R) = 0, \tag{22c}$$

$$a(c) = \sqrt{1 - \frac{c^2}{c_D^2}}, \quad b(c) = \sqrt{1 - c^2}, \quad K(c) = c^2 - 2. \tag{22d}$$

In view of (22), function $G(q, \psi)$ with the property $G \to 1$ (as $|q| \to \infty$) is defined as

$$G = \frac{c^2(c_R^2 - c^2)}{R(1-cq)^2}\frac{M_R}{(1-cq)^2 - c_R^2 q^2}. \tag{23a}$$

One can write $G = G_+ G_-$, where $G_\pm$ respectively are analytic in overlapping half-planes $\mathrm{Re}(q) > -1/(c_D - c)$ and $\mathrm{Re}(q) < 1/(c_D + c)$:

$$G_\pm = \exp\left(\frac{1}{\pi}\int \tan^{-1}\frac{4\sqrt{u^2 - 1}\sqrt{c_D^2 - u^2}}{c_D(u^2 - 2)^2}\frac{du}{(u \mp c)[q(u \mp c) \pm 1]}\right). \tag{23b}$$

Integration is over range $1 < u < c_D$. This result and the behavior discussed in connection with (17) allows (21) to be treated in the same fashion as (16), and here solved for $\bar{\tau}_1^+$ and $\bar{\Delta}_1\cos\psi + \bar{\Delta}_2\sin\psi$.

Combining the latter result with (19b) and (23b) then gives

$$
\vec{\Delta}_1 = \frac{2\sqrt{c}\sin\psi}{\mu p^2(1-cq)B_-}(P_2\cos\psi - P_1\sin\psi)
$$

$$
- \frac{2\sqrt{c}\cos\psi}{\mu p^2 c_R}\frac{B_-G_+}{M_R g_+}(1-cq)[1+q(c_R-c)](P_1\cos\psi + P_2\sin\psi), \qquad (24a)
$$

$$
\vec{\Delta}_2 = \frac{2\sqrt{c}\cos\psi}{\mu p^2(1-cq)B_-}(P_1\sin\psi - P_2\cos\psi)
$$

$$
- \frac{2\sqrt{c}\sin\psi}{\mu p^2 c_R}\frac{B_-G_+}{M_R g_+}(1-cq)[1+q(c_R-c)](P_2\sin\psi + P_1\cos\psi), \qquad (24b)
$$

$$
g_+ = G_+(1/c). \qquad (24c)
$$

It is noted that identical results follow upon substitution of (19b) into (14b). Equation (14c) is studied in the same fashion as (14a) and (14b), and solved for $(\bar{\tau}_3^+, \bar{\Delta}_3)$, e.g.,

$$
\bar{\Delta}_3 = \frac{2\sqrt{c}}{\mu p^2 c_R}\frac{A_-G_+}{M_R g_+}(1-cq)[1+q(c_R-c)]P_3. \qquad (24d)
$$

Transform inversion valid on crack plane near C

In view of (7b), (7c) and (9),

$$
\dot{\Delta}_k = V_S(\partial_S - c\partial)\Delta_k, \quad \partial f = \frac{\partial f}{\partial x}. \qquad (25)
$$

Therefore, (8a), (10) and (24c) give for $x < 0$

$$
L(\dot{\Delta}_3) = -\frac{P_3}{\mu\pi}\frac{\sqrt{c}V_S}{g_+ c_R}p\int\frac{|q|}{qM_R}\,dq\,G_+A_-(1-cq)^2[1+q(c_R-c)]\exp(pqx). \qquad (26a)
$$

For $x < 0$, Cauchy theory is used to transform the integration to the upper ($\text{Im}(q) = 0+$) side of the positive real q-axis. An expression valid for $x \to 0-$ is then extracted:

$$
L(\dot{\Delta}_3) \approx \frac{2P_3}{\mu\pi}\sqrt{1+\frac{c}{c_D}}\left(1-\frac{c}{c_R}\right)\frac{\sqrt{c}V_S}{g_+ R}\frac{p}{\sqrt{-x}}\int\frac{du}{\sqrt{u}}\exp(-pu). \qquad (26b)
$$

Integration is over the entire positive u-axis and, in fact, gives $\sqrt{\pi/p}$ [Gradshteyn and Ryzhik 2014]. However $p\exp(-pu)$ is the transform of function $\partial_S\delta(s-u)$ [Abramowitz and Stegun 1972]. Point-force loading (5a) represents a step-function in time. For generality therefore, we consider the case

$$
P_k = P_k(V_S t), \quad P_k(0) = 0. \qquad (27)
$$

Solution behavior is more discernible if points in the $x_1^0 x_2^0$-plane are defined with respect to $x_0 = 0$. Therefore, upon inversion [Abramowitz and Stegun 1972; Sneddon 1972] of the modified (26b), coordinates (x_0, ψ, s), where $x_0 = x + cs$, are introduced, and for $\left(s > 0, x_0 \to cs-, |\psi| < \frac{1}{2}\pi\right)$,

$$
\dot{\Delta}_3 \approx \frac{2V_S}{\mu\pi}\sqrt{1+\frac{c}{c_D}}\frac{\sqrt{c}K_I}{\sqrt{cs-x_0}}, \quad K_I = \left(1-\frac{c}{c_R}\right)\frac{c^2\partial_S}{Rg_+}\int_0^s\frac{\partial_S P_3}{\sqrt{s-u}}\,du. \qquad (28)
$$

A similar procedure for (24a) and (24b) give for $(s > 0, x_0 \to cs-)$

$$\dot{\Delta}_1 \approx \frac{2V_S}{\mu\pi} \frac{\sqrt{c}}{\sqrt{cs - x_0}} \left(-\frac{\sin\psi}{\sqrt{1+c}} K_{\mathrm{III}} + \cos\psi \sqrt{1+c} K_{\mathrm{II}} \right), \tag{29a}$$

$$\dot{\Delta}_2 \approx \frac{2V_S}{\mu\pi} \frac{\sqrt{c}}{\sqrt{cs - x_0}} \left(\frac{\cos\psi}{\sqrt{1+c}} K_{\mathrm{III}} + \sin\psi \sqrt{1+c} K_{\mathrm{II}} \right), \tag{29b}$$

$$K_{\mathrm{II}} = \left(1 - \frac{c}{c_R} \right) \frac{c^2 \partial_S}{R g_+} \int_0^s \frac{\mathrm{d}u}{\sqrt{s-u}} \partial_S (\cos\psi \, P_1 + \sin\psi \, P_2), \tag{29c}$$

$$K_{\mathrm{III}} = \partial_S \int_0^s \frac{\mathrm{d}u}{\sqrt{s-u}} \partial_S (\sin\psi \, P_1 - \cos\psi \, P_2). \tag{29d}$$

Subscripts (I, II, III) indicate that the K-terms are, based on the role of (c_D, c_R, g_+), related to what are referred to [Freund 1990], respectively, as the opening, in-plane and antiplane modes of fracture. The K-terms are finite for all $0 < V(\psi) < c_R V_S$, e.g.,

$$\frac{c^2}{R} \to \frac{2c_D^2}{c_D^2 - 1} \ (c = 0), \quad \left(1 - \frac{c}{c_R} \right) \frac{1}{R} \to \frac{1}{F_R} \left(\frac{c_D}{2c_R} \right)^2 \ (c = c_R), \tag{30a}$$

$$F_R = c_R^2 - 2 + \frac{1}{c_D} \left(\sqrt{\frac{c_D^2 - c_R^2}{1 - c_R^2}} + \sqrt{\frac{1 - c_R^2}{c_D^2 - c_R^2}} \right) > 0. \tag{30b}$$

The analogous results for σ_{3k} when $(s > 0, x_3^0 = 0, x_0 \to cs+)$ are

$$\sigma_{31}^0 \approx \frac{1}{\pi\sqrt{c}\sqrt{x_0 - cs}} \left(-\sin\psi \sqrt{1-c} K_{\mathrm{III}} + \frac{\cos\psi}{\sqrt{1-c}} \frac{R}{c^2} K_{\mathrm{II}} \right), \tag{31a}$$

$$\sigma_{32}^0 \approx \frac{1}{\pi\sqrt{c}\sqrt{x_0 - cs}} \left(\cos\psi \sqrt{1-c} K_{\mathrm{III}} + \frac{\sin\psi}{\sqrt{1-c}} \frac{R}{c^2} K_{\mathrm{II}} \right), \tag{31b}$$

$$\sigma_{33}^0 \approx \frac{\sqrt{c_D}}{\pi\sqrt{c}\sqrt{c_D - c}} \frac{R}{c^2} \frac{K_{\mathrm{I}}}{\sqrt{x_0 - cs}}. \tag{31c}$$

For a rectilinear crack edge, e.g., [Freund 1972; 1990], an orthogonal basis is chosen so that the crack plane, crack edge and normal to the crack edge can each be defined in terms of one coordinate direction. Here the outwardly directed normal to C forms angle φ with respect to the positive (x, x_0)-direction, where

$$\varphi = \tan^{-1} \frac{c'}{c} \left(|\varphi| < \tfrac{1}{2}\pi \right), \quad f' = \frac{\mathrm{d}f}{\mathrm{d}\psi}. \tag{32}$$

Therefore for each point $(x_0 = cs, \psi)$ on C traction $(\sigma_{3\tau}^0, \sigma_{3\nu}^0, \sigma_{33}^0)$ and velocity discontinuity $(\dot{\Delta}_\tau, \dot{\Delta}_\nu, \dot{\Delta}_3)$ set can be defined in terms of a local coordinate system $(\tau, \nu, x_3^0 = x_3)$. Here τ is the tangent to C, taken in the clockwise sense, and ν is the outwardly directed normal to C. Equation (28) is still valid, and the other members of the set are listed in Appendix B.

Criterion: dynamic energy release rate

A standard criterion for brittle fracture, e.g., [Freund 1972], equates the rate at which surface energy is released to the rate of work associated with traction and relative displacements in the fracture zone $\Im$. If

kinetic energy is included [Gdoutos 2005; Brock 2015b], the equation takes the form

$$D \iint_{\delta A} e_F \, dx_1^0 \, dx_2^0 = \iint_{\Im} \sigma_{3k}^0 \dot{\Delta}_k \, dx_1^0 \, dx_2^0 + D \iiint_{123} \tfrac{1}{2} \rho \dot{u}_k \dot{u}_k \, dx_1^0 \, dx_2^0 \, dx_3^0. \tag{33}$$

Here e_F is the surface energy per unit area, and is generally assumed to be constant [deBoer et al. 1988; Skriver and Rosengaard 1992]. Fracture zone $\Im$ of course is a strip of infinitesimal thickness in the $x_1^0 x_2^0$-plane that straddles the portion of C that borders δA. Subscript 123 signifies integration over the unbounded solid. Use of Green's theorem [Malvern 1969] and translating basis x expressed in terms of $(x_0, \psi, x_3 = 0)$ gives for the left-hand side of (33)

$$V e_F s \int_{\Psi} d\psi \, c \sqrt{c^2 + (c')^2}. \tag{34a}$$

Here Ψ denotes integration over range $|\psi| < \tfrac{1}{2}\pi$. Use of the translating basis for the integration over $\Im$ in (33) gives

$$\int_{\Psi} d\psi \int_{cs-}^{cs+} |x_0| \sigma_{3k}^0 \dot{\Delta}_k \, dx_0. \tag{34b}$$

Use of (28)–(30) in (34b) gives rise to Dirac function $\delta(x_0 - cs)$ [Freund 1972]. It is also recognized [Achenbach and Brock 1973] that the linear behavior in s displayed by (34a) places a restriction on the behavior of $\partial_S P(s)$. That is, $V(\psi)$ in general must vary with time. One case, however, for which time-invariance is valid is

$$\partial_S P_k(s) = p_k \sqrt{s}. \tag{35a}$$

Equation (34b) then gives

$$\pi \frac{s}{\mu} \int_{\Psi} d\psi \, V \left[\frac{R}{c^2} \left(K_{\mathrm{I}}^2 \sqrt{\frac{c_D + c}{c_D - c}} + K_{\mathrm{II}}^2 \sqrt{\frac{1 + c}{1 - c}} \right) + K_{\mathrm{III}}^2 \sqrt{\frac{1 - c}{1 + c}} \right]. \tag{35b}$$

In light of (28), (29c) and (29d),

$$K_{\mathrm{I}} = \left(1 - \frac{c}{c_R} \right) \frac{c^2 p_3}{R g_+}, \tag{36a}$$

$$K_{\mathrm{II}} = \left(1 - \frac{c}{c_R} \right) \frac{c^2}{R g_+} (p_1 \cos \psi + p_2 \sin \psi), \tag{36b}$$

$$K_{\mathrm{III}} = p_1 \sin \psi - p_2 \cos \psi. \tag{36c}$$

In view of (7c) and (9) the transforms of $\dot{u}_k$ are $p(1 - cq)\bar{u}_k$, where $\bar{u}_k$ and coefficients $(U_{\pm}, U_1^{\pm}, U_2^{\pm})$ are given by (12) and (C.1). Therefore the last integral in (33) requires inversion for $x_3 \neq 0$, and a more explicit version of (10) is useful:

$$\tilde{f}(p, q_1, q_2, x_3) \rightarrow f_{\Psi}(p, q, \psi) \exp(-p\Omega |x_3|), \quad \Omega = (A, B), \tag{37a}$$

$$\hat{f}(p, x, \psi, x_3) = -\frac{p^2}{2\pi} \int \frac{|q|}{q} f_{\Psi}(p, q, \psi) \exp[p(qx - \Omega |x_3|)] \, dq. \tag{37b}$$

Derivation of (28)–(30) is based on changing the integration path in (10b) to the $\mathrm{Re}(q)$-axis. After [Achenbach 1973], the integration path in (37b) can be changed, via Cauchy theory, to a contour defined

in the complex q-plane such that the exponential term takes the form $\exp(-pu)$, where u is real and positive. In carrying out this procedure, it is recognized that the singular behavior displayed by $\dot{\Delta}_k$ in (28) and (29) is manifest in $\dot{u}$ near C. Therefore, Green's theorem [Malvern 1969] is invoked to write the last term in (33) as an integral over the surface of a tube of radius $r_C \to 0$ that encloses the portion of C that borders δA. Translating basis x is employed, but with local coordinates (r, ψ, ϕ), centered on C, where

$$r = \sqrt{x^2 + x_3^2}, \quad \phi = \tan^{-1} \frac{x_3}{x} \ (|\phi| < \pi). \tag{38}$$

Equations (C.2) and (C.3) define the integration contour functions, parameterized by (38) and $u > 0$. For $r_C \to 0$, however, asymptotic forms (C.4) can be used, and it can then be shown that (37b) gives a linear combination of terms defined as the real or imaginary parts of (compare (26b))

$$\frac{p}{\sqrt{r Q_\Omega^\pm}} \int \frac{du}{\sqrt{u}} \exp(-pu), \tag{39a}$$

$$\frac{1}{\sqrt{Q_A^\pm}} = \frac{1}{\sqrt{2}}(A_\Phi^+ \pm i A_\Phi^-), \quad A_\Phi^\pm = \sqrt{1 \pm \frac{\cos\phi}{A_\Phi}}, \tag{39b}$$

$$\frac{1}{\sqrt{Q_B^\pm}} = \frac{1}{\sqrt{2}}(B_\Phi^+ \pm i B_\Phi^-), \quad B_\Phi^\pm = \sqrt{1 \pm \frac{\cos\phi}{B_\Phi}}. \tag{39c}$$

In view of (12), (27)–(29), (35a) and (39) the asymptotic forms of $\dot{u}_k$ are given listed in Appendix D. Use of (D.1) and (D.2) gives for the last term in (33)

$$-\frac{s}{\mu} \int_\Psi d\psi \, V\sqrt{c^2 + (c')^2} \left[\left(1 + \frac{c}{c_D}\right) \frac{K_I^2}{c^3} E_I + (1+c) \frac{K_{II}^2}{c^3} E_{II} + \frac{K_{III}^2}{c(1+c)} E_{III} \right]. \tag{40}$$

In (40) coefficients (E_I, E_{II}, E_{III}) are functions of $c(\psi)$ and defined by

$$E_I = \int_\Phi \cos\phi [(Q_3^+)^2 + (Q_3^-)^2] \, d\phi, \tag{41a}$$

$$E_{II} = \int_\Phi \cos\phi [(Q_{12}^+)^2 + (Q_{12}^-)^2] \, d\phi, \tag{41b}$$

$$E_{III} = \int_\Phi \cos\phi \left(\tfrac{1}{2} B_\Phi^-\right)^2 d\phi. \tag{41c}$$

Here Φ signifies integration over range $|\phi| < \pi$, and it can also be shown for $c \to 0$ that $(E_I, E_{II}) \approx O(c^4)$ and $E_{III} \approx O(c^2)$. Equations (34a), (35b) and (40) all involve integration with respect to ψ, and thus (33) reduces to the nonlinear differential equation for $c(\psi)$:

$$\mu e_F \sqrt{c^2 + (c')^2} = \left(1 + \frac{c}{c_D}\right) K_I^2 \left[\frac{\pi R}{c^2 a} - \frac{E_I}{c^3} \sqrt{c^2 + (c')^2} \right]$$

$$+ (1+c) K_{II}^2 \left[\frac{\pi R}{c^2 b} - \frac{E_{II}}{c^3} \sqrt{c^2 + (c')^2} \right] + \frac{K_{III}^2}{1+c} \left[\pi b - \frac{E_{III}}{c} \sqrt{c^2 + (c')^2} \right]. \tag{42}$$

Special cases: aspects of solution behavior

Knowledge of $c(\psi)$ provides a contour function $x_0 = V(\psi)t$ (where $t > 0$, $|\psi| < \frac{1}{2}\pi$) that defines C for the extending portion of crack A_C. Extension of each crack edge point is of course $V(\psi)t \cos \psi$ in the positive x_1^0-direction. Analysis of (42) must deal with its nonlinear form and ψ-dependent coefficient $(K_I^2, K_{II}^2, K_{III}^2)$. Nevertheless experience [Brock 2015a; 2015b] suggests that some aspects of solution behavior can be determined from (42). In particular, Rayleigh limit case $c(\psi) \to c_R$ arises only when

$$e_F + \frac{\pi}{\mu c_R^3}\left(\frac{p_3}{4F_R g_R^+}\right)^2 \left(1 + \frac{c_R}{c_D}\right)E_I = 0, \quad g_R^+ = G_+\left(\frac{1}{c_R}\right). \tag{43}$$

On the other hand, a low-speed assumption $c(\psi) \ll c_R$ and expansions in c^2 give (42) the more explicit form

$$\frac{\mu e_F}{\pi}\sqrt{c^2 + (c')^2} \approx \frac{c_D^2}{2(c_D^2 - 1)}p_3^2[1 + E_I c\sqrt{c^2 + (c')^2}] + (p_1 \sin \psi - p_2 \cos \psi)^2[1 + E_{III}c\sqrt{c^2 + (c')^2}]$$

$$+ \frac{c_D^2}{2(c_D^2 - 1)}(p_1 \cos \psi + p_2 \sin \psi)^2[1 + E_{II}c\sqrt{c^2 + (c')^2}], \tag{44a}$$

$$E_I = \frac{5}{32}\left(1 + \frac{1}{c_D^2}\right), \quad E_{II} = \frac{1}{32}\left(3 + \frac{8}{c_D^2}\right), \quad E_{III} = \frac{1}{4}. \tag{44b}$$

Crack contour behavior for the low-speed assumption

We treat two cases governed by (44):

Case A: $p_3 = p_A$ (pure compression).

Case B: $p_2 = 0$, $p_1 = p_3 = p_B$ (combined loading).

Problem symmetry exists with respect to the $x_2^0 x_3^0$-plane for both cases, and the effect of kinetic energy is considered for each.

Case A. For $c(\psi) < 0.5$, Equation (44) for Case A reduces to

$$\sqrt{z^2 + (z')^2}(1 - c_A^2 E_I z) = 1, \tag{45a}$$

$$z = \frac{c}{c_A}, \quad c_A = \frac{c_D^2}{2(c_D^2 - 1)}\frac{\pi p_A^2}{\mu e_F}. \tag{45b}$$

When kinetic energy is, respectively, neglected ($E_I = 0$) and included, (45) gives

$$c(\psi) = c_A, \tag{46a}$$

$$c(\psi) = \frac{1}{2E_I c_A}(1 - \sqrt{1 - \Gamma_A}), \quad \Gamma_A = \frac{(2c_A)^2}{E_I}. \tag{46b}$$

Equation (46) describes semicircular crack edge extension zone contours. To illustrate, consider a generic metal with properties [deBoer et al. 1988; Skriver and Rosengaard 1992; Brock 2015a; 2015b]

$$\mu = 79\,\text{GPa}, \quad e_F = 2.2\,\text{J/m}^2, \quad V_S = 3094\,\text{m/s}, \quad c_D = 2, \quad c_R = 0.933.$$

α_A	5	10	14.4	15	20
c_A	0.03013	0.12051	0.25	0.27114	0.48202
$c(0)$	0.04163	0.13581	0.2703	0.29212	0.50889

Table 1. Case A: parameters c_A and $c(0)$ for values of $p_A = \alpha_A (10^4)$ N/m$^{3/2}$.

Calculations for c_A and $c(0)$ are presented in Table 1 for various values of p_A. It is noted that $c(0) > c_A$. Therefore neglect of kinetic energy under-predicts crack extension speed $V \cos \psi$. This effect decreases with increasing p_A, however. For example, c_A and $c(0)$ for $p_A = 5(10^4)$ N/m$^{3/2}$ in Table 1 differ by 38.2%, but for $p_A = 15(10^4)$ N/m$^{3/2}$ the difference is 7.7%.

Case B. For $c(\psi) < 0.5$, Equation (44) now reduces to

$$2\sqrt{z^2 + (z')^2}\left[1 - \left(\tfrac{1}{8}c_B\right)^2 z(E_0 + E_\Psi \cos^2 \psi)\right] = A_0 + \frac{\cos^2 \psi}{c_D^2}, \tag{47a}$$

$$z = \frac{c}{c_B}, \quad c_B = \frac{c_D^2}{c_D^2 - 1}\frac{\pi p_B^2}{\mu e_F}, \quad A_0 = 2 - \frac{1}{c_D^2}. \tag{47b}$$

Coefficients $(E_0, E_\Psi) = 0$ when kinetic energy is neglected. If it is included,

$$E_0 = 13 - \frac{3}{c_D^2}, \quad E_\Psi = \frac{16}{c_D^2} - 5. \tag{47c}$$

Explicit ψ-dependence of (47a) implies that the crack extension zone contour is not circular, and that obtaining an analytical solution for $c(\psi)$ may be difficult. The form of (47a) suggests use of the series representation:

$$z(\psi) = \alpha\left[1 + \sum_{1}^{N} a_{2j} \cos^{2j} \psi\right]. \tag{48}$$

Substitution into (47a) and equating coefficients of terms $\cos^{2j} \psi$ (for $j \geq 0$) when kinetic energy is included gives recursive equations for (dimensionless) coefficients (α, a_{2j}). Terms (α, a_2) are the solutions to quadratic equations

$$\alpha = \frac{A_0}{1 + \Omega}, \quad a_2 = \frac{1}{4}\left[\sqrt{1 + 8\left(\frac{\omega E_0}{1 + \Omega} + \frac{1}{c_D^2 A_0}\right)} - 1\right], \tag{49a}$$

$$\Omega = \sqrt{1 - \omega A_0 E_0}, \quad \omega = \frac{1}{2}\left(\frac{1}{4}c_B\right)^2. \tag{49b}$$

Terms $(a_4, a_6, \dots)$ satisfy linear equations, but are complicated. Some simplicity is achieved by not expressing them completely in explicit form, e.g.,

$$a_4 = \frac{1}{2A_0^2(1 + 8a_2)}\left[\frac{1}{c_D^4} + a_2^2 A_0(3A_0 + 8\alpha\omega E_0) + 6\alpha\omega A_0 E_0 a_2 - (\omega E_\Psi a_2^2)^2\right]. \tag{50}$$

Kinetic energy neglected

ψ	0°	15°	30°	45°	60°	75°	90°
c	0.148	0.138	0.116	0.095	0.081	0.074	0.071
c'	0	−0.043	−0.059	−0.51	−0.035	−0.018	0
$c \cos \psi$	0.148	0.133	0.101	0.067	0.041	0.019	0

Kinetic energy included

ψ	0°	15°	30°	45°	60°	75°	90°
c	0.169	0.164	0.152	0.139	0.13	0.126	0.125
c'	0	−0.038	−0.052	−0.043	−0.024	−0.009	0
$c \cos \psi$	0.169	0.158	0.132	0.098	0.015	0.033	0

Table 2. Case B: parameters c, c' and $c \cos \psi$ for $p_B = 7.7(10^4)\,\text{N/m}^{3/2}$ and various ψ.

The coefficients exhibit simpler forms, of course, when kinetic energy is neglected, e.g.,

$$\alpha = \frac{1}{2}A_0, \quad a_2 = \frac{1}{4}\left[\sqrt{1 + \frac{8}{c_D^2 A_0}} - 1\right], \quad a_4 = \frac{1}{2A_0^2(1 + 8a_2)}\left[\frac{1}{c_D^4} + 3a_2^2 A_0^2\right]. \tag{51}$$

Calculations of (c, c') and dimensionless crack extension speed $c \cos \psi$ for $0 < \psi < \frac{1}{2}\pi$ based on (48) are given in Table 2 for the generic metal featured in Table 1. In view of the observations concerning p_A, only the single value $p_B = 7.7(10^4)\,\text{N/m}^{3/2}$ is considered. This corresponds to a dimensionless speed parameter $c_B = 0.1429$ and $\omega = 6.378(10^{-4})$, so that use of zero-order expansions of the kinetic energy-dependent coefficients $(\alpha, a_2, a_4, a_6, \dots)$ generates negligible error. For clarity, ψ-values in Table 2 are given in degrees.

Table 2 entries indicate that combined loading creates an elliptical crack contour for which the maximum rate of crack extension into the solid exceeds the rate at which new crack surface spreads along the original, semi-infinite crack contour. Neglect of kinetic energy exaggerates this effect while it (see Case A) under-predicts both rates.

Some observations

This paper extends the range of studies for 3D dynamic crack growth [Brock 2015a; 2015b] by considering a transient problem with mixed-mode loading. The crack is initially a closed, semi-infinite slit, with a rectilinear edge, and point forces applied on the surfaces just behind the edge. The dynamically similar case is treated, i.e., crack edge extension rate is constant in time, but can vary with direction. Unilateral temporal and bilateral spatial Laplace transforms are employed. However, the latter, and their inverses, make use of variable transformations based on quasipolar coordinates. An equation associated with crack-opening mode, and two coupled equations associated with shear mode, are produced in transform space. Both sets are put in Wiener–Hopf form [Morse and Feshbach 1953] and solved exactly.

Inversion is carried out analytically, and results subjected to a dynamic energy release rate criterion, with kinetic energy included. As is predictable [Achenbach and Brock 1973], the assumption of dynamic

similarity restricts the time-variation of the point forces. Under this restriction, examples of pure compression loading (Case A) and mixed-mode loading (Case B) are examined. In Case A, the extending crack edge is semicircular, and inclusion of kinetic energy gives larger crack extension speeds. A similar effect on speed is noted for Case B. However, the edge is not circular, with the maximum rate of crack extension into the solid being greater than the expansion rate of new crack surface along the original crack contour.

The point force behavior considered here involves extremely rapid, but not instantaneous, growth in time. Thus, the results presented here suggest that dynamic similarity can exist, at least in a brief fracture initiation phase.

Appendix A

$$2\bar{u}_1 \mp \bar{\Delta}_1 + \frac{q\cos\psi}{(1-cq)^2}\frac{N}{A}\bar{\Delta}_3 + \frac{\overline{\Sigma}_1}{\mu B} = 0, \tag{A.1a}$$

$$2\bar{u}_2 \mp \bar{\Delta}_2 + \frac{q\sin\psi}{(1-cq)^2}\frac{N}{A}\bar{\Delta}_3 + \frac{\overline{\Sigma}_2}{\mu B} = 0, \tag{A.1b}$$

$$2\bar{u}_3 \mp \bar{\Delta}_3 - \frac{q}{(1-cq)^2}\frac{N}{B}(\bar{\Delta}_1\cos\psi + \bar{\Delta}_2\sin\psi) + \frac{q^2+AB}{(1-cq)^2}\frac{\overline{\Sigma}_3}{\mu B} = 0. \tag{A.1c}$$

$$2\bar{\sigma}_{31} \mp \overline{\Sigma}_1 + \mu pB\bar{\Delta}_1 - \frac{pq\cos\psi}{B(1-cq)^2}P = 0, \tag{A.2a}$$

$$2\bar{\sigma}_{32} \mp \overline{\Sigma}_2 + \mu pB\bar{\Delta}_2 - \frac{pq\sin\psi}{B(1-cq)^2}P = 0, \tag{A.2b}$$

$$2\bar{\sigma}_{33} \mp \overline{\Sigma}_3 + \frac{p}{A(1-cq)^2}\big[Nq(\overline{\Sigma}_1\cos\psi + \overline{\Sigma}_2\sin\psi) + \mu M_R\bar{\Delta}_3\big] = 0. \tag{A.2c}$$

$$P = N\overline{\Sigma}_3 + \mu Mq(\bar{\Delta}_1\cos\psi + \bar{\Delta}_2\sin\psi), \tag{A.3a}$$

$$N = T - 2AB, \quad M = 2N - (1-cq)^2, \quad M_R = 4q^2AB + T^2, \tag{A.3b}$$

$$T = (1-cq)^2 - 2q^2. \tag{A.3c}$$

Appendix B

$$\sigma_{3\tau}^0 \approx \frac{1}{\pi\sqrt{c}\sqrt{x_0-cs}}\left(-K_{\mathrm{III}}\sqrt{1-c}\cos\varphi + K_{\mathrm{II}}\frac{R}{c^2}\frac{\sin\varphi}{\sqrt{1-c}}\right), \tag{B.1a}$$

$$\sigma_{3\nu}^0 \approx \frac{1}{\pi\sqrt{c}\sqrt{x_0-cs}}\left(\Sigma_{\mathrm{III}}\sqrt{1-c}\sin\varphi + K_{\mathrm{II}}\frac{R}{c^2}\frac{\cos\varphi}{\sqrt{1-c}}\right). \tag{B.1b}$$

$$\dot{\Delta}_\tau \approx \frac{2V_S\sqrt{c}}{\mu\pi\sqrt{cs-x_0}}\left(-K_{\mathrm{III}}\frac{\cos\varphi}{\sqrt{1+c}} + K_{\mathrm{II}}\sqrt{1+c}\sin\varphi\right), \tag{B.2a}$$

$$\dot{\Delta}_\nu \approx \frac{2V_S\sqrt{c}}{\mu\pi\sqrt{cs-x_0}}\left(K_{\mathrm{III}}\frac{\sin\varphi}{\sqrt{1+c}} + K_{\mathrm{II}}\sqrt{1+c}\cos\varphi\right). \tag{B.2b}$$

$$\sin \varphi = \frac{c'}{\sqrt{c^2 + (c')^2}}, \quad \cos \varphi = \frac{c}{\sqrt{c^2 + (c')^2}}, \quad f' = \frac{\mathrm{d}f}{\mathrm{d}\psi}. \tag{B.3}$$

Appendix C

$$U_\pm = \pm \frac{q}{(1 - cq)^2} (\bar{\Delta}_1 \cos \psi + \bar{\Delta}_2 \sin \psi) - \frac{T\bar{\Delta}_3}{2A(1 - cq)^2}, \tag{C.1a}$$

$$U_1^\pm = \pm \tfrac{1}{2} \bar{\Delta}_1 \mp \frac{q^2 \cos \psi}{(1 - cq)^2} (\bar{\Delta}_1 \cos \psi + \bar{\Delta}_2 \sin \psi) + \frac{q B \cos \psi}{(1 - cq)^2} \bar{\Delta}_3, \tag{C.1b}$$

$$U_2^\pm = \pm \tfrac{1}{2} \bar{\Delta}_2 \mp \frac{q^2 \sin \psi}{(1 - cq)^2} (\bar{\Delta} \cos \psi + \bar{\Delta}_2 \sin \psi) + \frac{q B \sin \psi}{(1 - cq)^2} \bar{\Delta}_3. \tag{C.1c}$$

The contour function q for the case $\Omega = A$ in (37) can be written in terms of parameter u and local coordinates (r, ψ, ϕ) as

$$q = \frac{-1}{A_\Phi^2} \left[\frac{u}{r} \cos \phi + \frac{c}{c_D^2} \pm i \frac{\sin \phi}{c_D} \sqrt{\left(c_D \frac{u}{r} \right)^2 - \sin^2 \phi - \left(c \frac{u}{r} + \cos \phi \right)^2} \right] (u > u_A), \tag{C.2a}$$

$$A_\Phi = \sqrt{1 - \frac{c^2}{c_D^2} \sin^2 \phi}, \quad u_A = \frac{r}{c_D a^2} \left(\frac{c}{c_D} \cos \phi - A_\Phi^2 \right). \tag{C.2b}$$

For case $\Omega = B$ in (37),

$$q = -\frac{1}{B_\Phi^2} \left[\frac{u}{r} \cos \phi + c \sin^2 \phi \pm i \sin \phi \sqrt{\left(\frac{u}{r} \right)^2 - \sin^2 \phi - \left(c \frac{u}{r} + \cos \phi \right)^2} \right] (u > u_B), \tag{C.3a}$$

$$B_\Phi = \sqrt{1 - c^2 \sin^2 \phi}, \quad u_B = \frac{r}{b^2} (c \cos \phi - B_\Phi^2). \tag{C.3b}$$

Equations (C.2a) and (C.3a) respectively behave for $r \to 0$ as

$$q \approx -\frac{u}{r Q_A^\pm} \ (u > 0), \quad Q_A^\pm = \cos \phi \mp i a \sin \phi, \tag{C.4a}$$

$$q \approx -\frac{u}{r Q_B^\pm} \ (u > 0), \quad Q_B^\pm = \cos \phi \mp i b \sin \phi. \tag{C.4b}$$

Appendix D

$$\dot{u}_1 \approx \frac{\sqrt{2c}}{\mu \sqrt{r}} \left[\frac{Q_{12}^-}{c^2} \cos \psi \sqrt{1 + c} K_{\mathrm{II}} + B_\Phi^- \sin \psi \frac{K_{\mathrm{III}}}{\sqrt{1 + c}} \right] \mathrm{sgn}(\phi) + \frac{\sqrt{2c}}{\mu \sqrt{r}} \frac{Q_3^+}{c^2} \cos \psi \sqrt{1 + \frac{c}{c_D}} K_{\mathrm{I}}, \tag{D.1a}$$

$$\dot{u}_2 \approx \frac{\sqrt{2c}}{\mu \sqrt{r}} \left[\frac{Q_{12}^-}{c^2} \sin \psi \sqrt{1 + c} K_{\mathrm{II}} - B_\Phi^- \cos \psi \frac{K_{\mathrm{III}}}{\sqrt{1 + c}} \right] \mathrm{sgn}(\phi) + \frac{\sqrt{2c}}{\mu \sqrt{r}} \frac{Q_3^+}{c^2} \sin \psi \sqrt{1 + \frac{c}{c_D}} K_{\mathrm{I}}, \tag{D.1b}$$

$$\dot{u}_3 \approx \frac{\sqrt{2c}}{\mu \sqrt{r}} \frac{Q_{12}^+}{c^2} \sqrt{1 + c} K_{\mathrm{II}} - \frac{\sqrt{2c}}{\mu \sqrt{r}} \frac{Q_3^-}{c^2} \sqrt{1 + \frac{c}{c_D}} K_{\mathrm{I}} \mathrm{sgn}(\phi). \tag{D.1c}$$

$$Q_{12}^{+} = a A_{\Phi}^{+} + \frac{K}{2b} B_{\Phi}^{+}, \quad Q_{12}^{-} = A_{\Phi}^{-} + \tfrac{1}{2} K B_{\Phi}^{-}, \tag{D.2a}$$

$$Q_{3}^{+} = \frac{K}{2a} A_{\Phi}^{+} + b B_{\Phi}^{+}, \quad Q_{3}^{-} = \tfrac{1}{2} K A_{\Phi}^{-} + B_{\Phi}^{-}. \tag{D.2b}$$

References

[Abramowitz and Stegun 1972] M. Abramowitz and I. A. Stegun (editors), *Handbook of mathematical functions*, Dover, New York, 1972.

[Achenbach 1973] J. D. Achenbach, *Wave propagation in elastic solids*, North-Holland, Amsterdam, 1973.

[Achenbach and Brock 1973] J. D. Achenbach and L. M. Brock, *On quasistatic and dynamic fracture*, pp. 529–541, Noordhoff, Leyden, The Netherlands, 1973.

[Barber 1992] J. R. Barber, *Elasticity*, Solid Mechanics and its Applications **12**, Kluwer, Dordrecht, 1992.

[Brock 2012] L. M. Brock, "Two cases of rapid contact on an elastic half-space: the sliding ellipsoid die, rolling sphere", *J. Mech. Mater. Struct.* **7**:5 (2012), 469–483.

[Brock 2015a] L. M. Brock, "Contours for planar cracks growing in three dimensions", *J. Mech. Mater. Struct.* **10**:1 (2015), 63–77.

[Brock 2015b] L. M. Brock, "Contours for planar cracks growing in three dimensions: influence of kinetic energy", *J. Appl. Mech.* **82**:11 (2015), Art. Id #111011 (6 pages).

[Brock and Achenbach 1973] L. M. Brock and J. D. Achenbach, "Extension of an interface flaw under the influence of transient waves", *Int. J. Solids Struct.* **9**:1 (1973), 53–68.

[deBoer et al. 1988] F. R. deBoer, R. Boom, W. C. M. Mattens, A. R. Miedema, and A. K. Niessen, *Cohesion in metals*, North-Holland, Amsterdam, 1988.

[Freund 1972] L. B. Freund, "Energy flux into the tip of an extending crack in an elastic solid", *J. Elasticity* **2**:4 (1972), 341–349.

[Freund 1990] L. B. Freund, *Dynamic fracture mechanics*, Cambridge University Press, 1990.

[Gdoutos 2005] E. E. Gdoutos, *Fracture mechanics*, Solid mechanics and its applications **123**, Springer, New York, 2005.

[Gradshteyn and Ryzhik 2014] I. S. Gradshteyn and I. M. Ryzhik, *Table of integrals, series, and products*, 8th ed., Academic Press, New York, 2014.

[Malvern 1969] L. S. Malvern, *Introduction to the mechanics of continuous media*, Prentice-Hall, Englewood Cliffs (NJ), 1969.

[Morse and Feshbach 1953] P. M. Morse and H. Feshbach, *Methods of theoretical physics I*, McGraw-Hill, New York, 1953.

[Skriver and Rosengaard 1992] H. L. Skriver and N. M. Rosengaard, "Surface energy and work function of elemental metals", *Phys. Rev. B* **46** (Sep 1992), 7157–7168.

[Sneddon 1972] I. N. Sneddon, *The use of integral transforms*, McGraw-Hill, New York, 1972.

LOUIS MILTON BROCK: louis.brock@uky.edu
Department of Mechanical Engineering, College of Engineering, University of Kentucky, 204 EEX,
Lexington, KY 40506-0038, United States

STRESS CONCENTRATION AROUND A NANOVOID ECCENTRICALLY EMBEDDED IN AN ELASTIC LAMINA SUBJECTED TO FAR-FIELD LOADING

Changwen Mi

Stress concentration is one of the major challenges threatening the health and integrity of engineering structures. This paper analyzes the stress distributions around a spherical nanovoid near two parallel free surfaces. The loading is all-around uniform tension at infinity, perpendicular to the axis of symmetry of the infinite strip. Both plane surfaces of the strip assume traction free boundary conditions whereas the spherical void surface is modeled as a mathematical thin-film of Gurtin and Murdoch type. The method of Boussinesq's displacement functions is used in the analysis and the solutions are expressed semianalytically in terms of infinite series of Legendre functions and improper integrals involving Bessel functions. Numerical calculations are performed to illustrate the dependence of elastic fields on surface material properties, model size, void radius, and eccentricity. The results suggest the likelihood of optimizing stress concentrations in metallic materials and structures by the proper design of surface material properties, particularly of the residual surface stress.

1. Introduction

The presence of geometric defects such as holes, pits, and voids in elastic materials has received extensive investigation in literature because of the negative impact of stress concentrations on the integrity of engineering structures [Mura 1987]. Stress concentrations around spherically shaped voids have been one focus of micromechanics for decades, due probably to the relative simplicity in mathematical formulations. Most of these studies, however, have been concerned with spherical voids at the microscale [Tsuchida and Nakahara 1970; 1972; 1974; 1976; Tsuchida et al. 1976; Boccardo et al. 2015]. At such a length scale, stress concentration factors are typically independent of void radius provided that no additional characteristic lengths are involved. For models containing more than one characteristic length, stress concentrations typically depend on their ratios, instead of on individual length scale parameters.

Nonetheless, situations become more complicated as the characteristic length scales decrease to the nanoscale. As summarized in recent review articles on mechanics of nanostructured materials, surface effects dominate the mechanics and physics at small scales by introducing additional length scales [Duan et al. 2009; Wang et al. 2011; Chen and Yao 2014; Mi and Kouris 2014]. Stress distributions show strong dependence on void size. Several studies have been concerned with stress distributions around nanovoids embedded in an infinitely extended medium. By integrating traditionally excluded surface/interface energies and stresses into the classical Eshelby formalism for embedded inclusions, Sharma and Ganti [2004] first examined the size-dependent stress concentrations on the surface of a nanovoid. He and Li [2006] investigated the influence of surface mechanics on stress concentrations near a spherical void embedded in an infinite medium subjected to unidirectional remote load. Li et al. [2006] further solved the stress

concentration factors around a spherical nanovoid under a few combinations of biaxial uniform loads. Duan et al. [2009] calculated the stress concentration factors of a spherical nanovoid by supplementing the equations of classical theory of elasticity with generalized Young–Laplace equations of surface elasticity.

More often than not, voids are found near a free surface. Therefore, displacements and stresses are additionally disturbed due to the presence of material boundaries. By the use of a displacement functions approach, Mi and Kouris [2013] examined the stress distributions around a nanosized void near a single free surface. More recently, they further evaluated the stress concentration factors due to a nanovoid equally close to two parallel free surfaces [Mi and Kouris 2015]. In both studies, a unidirectional uniform load applied at infinity was considered. Stress concentrations due to other loading conditions are also under development. For example, Mi et al. [2016] calculated elastic fields near a hemispherical pit at the plane boundary of an elastic half-space subjected to statically equivalent shear tractions.

Here we examine the stress concentrations around a nanosized void embedded at an arbitrary position in an infinite lamina of finite thickness. An all-around tensile stress field applied at the remote boundary of the lamina is considered. In view of the symmetry in both geometry and loading, the classical method of Boussinesq displacement functions is employed [Barber 2010] to solve the three-dimensional elastic problem. In the absence of body forces and torsional loads, two harmonic functions are sufficient to provide a general solution to the displacement equations of equilibrium. However, multiple sets of displacement functions are needed due to the disturbances caused by void and dual plane boundaries. For example, the voided lamina can be treated as the common domain belonging to both a voided infinite space and a defects-free lamina. For these domains, forms of (harmonic) displacement functions are well-known.

Based on this reasoning, a general solution was constructed by superposing a few groups of displacement functions, expressed in either spherical or cylindrical coordinates. Cylindrical and spherical harmonics are in the forms of improper integrals and infinite series, respectively. Consequently, they carry either continuous or discrete unknowns, in order to make the representations general enough. Although mathematically tedious and difficult, the subsequent solution principle is straightforward. Unknown functions in cylindrical harmonics were first expressed in terms of the unknown coefficients in spherical harmonics by imposing traction-free boundary conditions at both the upper and lower surfaces of the lamina.

Next, the Gurtin and Murdoch [1978] continuum model of surface mechanics was adopted to simulate the mechanical response of the void surface. In essence, this model treats a solid surface as a mathematical layer of vanishing thickness. On such a two-dimensional domain, both surface strain and surface stress were defined and thus a surface constitutive law was proposed. Finally, surface mechanics participates in the mechanics and physics of the problem by modifying the force balance condition across the surface. The enforcement of the modified boundary conditions at the void surface, by the use of a system of truncated infinite series involving Legendre polynomials, renders us the unknown coefficients in the spherical harmonics, and thus the unknown functions in cylindrical harmonics too. As the stresses due to the disturbance of plane boundaries are improper integrals of Howland type involving Bessel functions and hyperbolic functions, special algorithms were adopted to ensure the convergence and accuracy of their evaluations [Ling 1957; 1978; Ling and Lin 1971; Ling and Wu 1982].

It is worth mentioning that in the present study only the surface mechanics at the void surface is considered. Those at both plane boundaries are ignored, due to their secondary importance. As pointed out in [Mi and Kouris 2006], surface effects at flat surfaces may be neglected when those at one or more curved boundaries with finite radii of curvature are taken into account.

In terms of semianalytical series and integral expressions for stresses, extensive numerical calculations have been performed for various combinations of surface material properties, model size, void radius, and eccentricity. The results of the nanovoid symmetrically embedded in an elastic lamina and in an infinite medium have been reproduced as special cases of the eccentric model. Special consideration has been given to the determination of stress distributions in the immediate vicinity of the void due to far-field tension, since the disturbance of geometric defects is a short-range force field [Mura 1987]. The combined analytical and numerical analyses show that the stress concentration factors along the void surface can differ drastically from their classical counterparts. It is therefore possible to optimize the stress distributions by controlling the surface material properties of the void surface. At the nanoscale, the proper control of stresses and strains is a crucial factor in self-organized growth of quantum-dot crystals [Springholz et al. 1998].

The remainder of this paper is organized as follows. In Section 2 we outline in detail the mathematical method of solution, supplemented by three Appendices documenting indispensable yet tedious components of the solution procedure. Section 3 numerically examines the impact of surface material properties, model size, void radius, and eccentricity on the elastic fields in the vicinity of the embedded nanovoid. Finally, in Section 4, conclusions are drawn.

2. Method of solution

Consider a spherical nanovoid near either plane boundary of an infinite strip of finite thickness, as shown in Figure 1. Biaxial uniform boundary loads are applied at infinity, along directions parallel to both free surfaces. Given the geometry, cylindrical (r, θ, z) and spherical (R, φ, θ) coordinates will be used alternatively in the subsequent development. The transformation rules among these coordinates and the Cartesian one are also illustrated in Figure 1. The shear modulus G and Poisson's ratio ν are selected
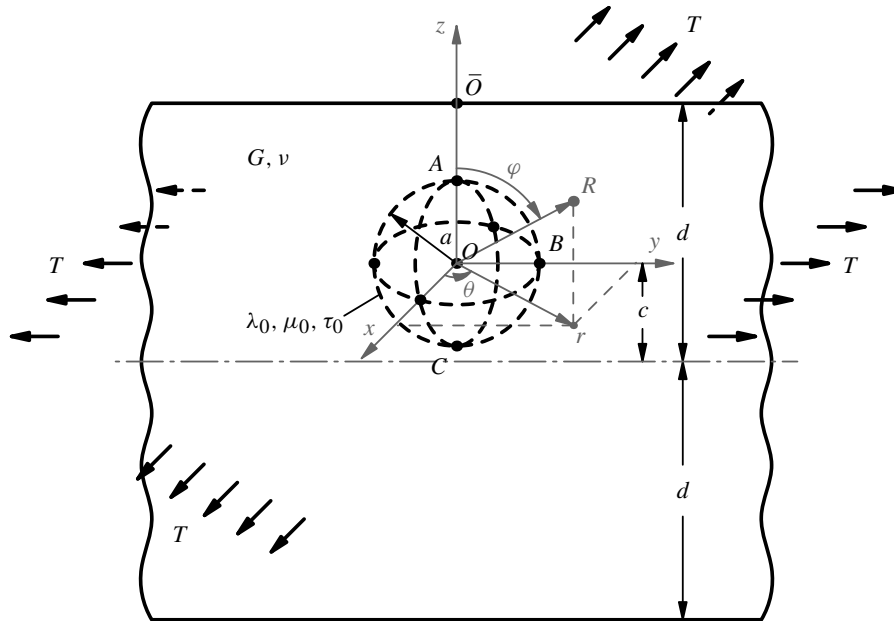
Figure 1. Geometry of the problem.

to represent the bulk material properties of the elastic lamina. Within the framework of the classical theory of micromechanics, three characteristic lengths exist in this problem, i.e., the half-thickness of the substrate d, void radius a, and the eccentricity c. Following [Gurtin and Murdoch 1978], three surface constants are required to fully accommodate the mechanical response of the void surface. Among them, τ_0 denotes residual surface stress whereas λ_0 and μ_0 are surface counterparts of Lamé constants. These surface material properties introduce a few more intrinsic length scales into the problem and thus make the solution more difficult to tackle.

In the absence of body forces, the axially symmetric equations of equilibrium in terms of displacements are given by

$$
\begin{aligned}
&\frac{\partial^2 u_r}{\partial z^2} + \frac{2(1-\nu)}{(1-2\nu)}\left\{\frac{\partial^2 u_r}{\partial r^2} + \frac{1}{r}\frac{\partial u_r}{\partial r} - \frac{u_r}{r^2}\right\} + \frac{1}{(1-2\nu)}\frac{\partial^2 u_z}{\partial r \partial z} = 0, \\
&\frac{\partial^2 u_z}{\partial r^2} + \frac{1}{r}\frac{\partial u_z}{\partial r} + \frac{2(1-\nu)}{(1-2\nu)}\frac{\partial^2 u_z}{\partial z^2} + \frac{1}{(1-2\nu)}\left\{\frac{1}{r}\frac{\partial u_r}{\partial z} + \frac{\partial^2 u_r}{\partial r \partial z}\right\} = 0.
\end{aligned}
\tag{1}
$$

Thanks to the axial symmetry, two arbitrary harmonic functions (i.e., ϕ_0 and ϕ_3) are sufficient to yield the solution

$$
2Gu_r = \frac{\partial \phi_0}{\partial r} + z\frac{\partial \phi_3}{\partial r}, \quad 2Gu_z = \frac{\partial \phi_0}{\partial z} + z\frac{\partial \phi_3}{\partial z} - (3-4\nu)\phi_3.
\tag{2}
$$

Such a simple combination was first proposed by Boussinesq and is a special case of the more general Papkovich–Neuber representation [Barber 2010]. With the help of strain-displacement relationship and Hooke's law, the corresponding stresses read

$$
\begin{aligned}
&\sigma_{rr} = \frac{\partial^2 \phi_0}{\partial r^2} - \frac{z}{r}\frac{\partial \phi_3}{\partial r} - 2\nu\frac{\partial \phi_3}{\partial z} - z\frac{\partial^2 \phi_3}{\partial z^2}, \quad \sigma_{\theta\theta} = \frac{1}{r}\frac{\partial \phi_0}{\partial r} + \frac{z}{r}\frac{\partial \phi_3}{\partial r} - 2\nu\frac{\partial \phi_3}{\partial z}, \\
&\sigma_{zz} = \frac{\partial^2 \phi_0}{\partial z^2} - 2(1-\nu)\frac{\partial \phi_3}{\partial z} + z\frac{\partial^2 \phi_3}{\partial z^2}, \qquad \sigma_{zr} = \frac{\partial^2 \phi_0}{\partial r \partial z} - (1-2\nu)\frac{\partial \phi_3}{\partial r} + z\frac{\partial^2 \phi_3}{\partial r \partial z}.
\end{aligned}
\tag{3}
$$

Spherical displacements and stresses are readily derived by using the relations

$$
\frac{\partial}{\partial r} = \sin\varphi\frac{\partial}{\partial R} + \frac{\cos\varphi}{R}\frac{\partial}{\partial \varphi}, \quad \frac{\partial}{\partial z} = \cos\varphi\frac{\partial}{\partial R} - \frac{\sin\varphi}{R}\frac{\partial}{\partial \varphi},
\tag{4}
$$

and the coordinate transformation equations

$$
\boldsymbol{e}_R = \sin\varphi\,\boldsymbol{e}_r + \cos\varphi\,\boldsymbol{e}_z, \quad \boldsymbol{e}_\varphi = \cos\varphi\,\boldsymbol{e}_r - \sin\varphi\,\boldsymbol{e}_z.
\tag{5}
$$

Traction-free boundary conditions are imposed at both plane boundaries of the infinite strip:

$$
(\sigma_{zr})_{z=d-c} = (\sigma_{zz})_{z=d-c} = 0, \quad (\sigma_{zr})_{z=-d-c} = (\sigma_{zz})_{z=-d-c} = 0.
\tag{6}
$$

At infinity,

$$
(\sigma_{rr})_{r\to\infty} = (\sigma_{\theta\theta})_{r\to\infty} = T.
\tag{7}
$$

As mentioned before, the mechanical response of the void surface is modeled by the theory of surface mechanics proposed in [Gurtin and Murdoch 1978]. In this context, the surface of the spherical void is treated as a mathematical film of vanishing thickness. The key component of the model lies in the

fact that at submicro- to nanoscales, the net traction across a solid surface is balanced by the surface divergence of surface stress ($\nabla_S \cdot \Sigma$):

$$\sigma_{ij}n_j - T_i^{(n)} = (\nabla_S \cdot \Sigma)_i, \tag{8}$$

where n_i are components of the outward unit normal to the surface under consideration and $T_i^{(n)}$ of the external traction load, which is absent in the present case. The surface stress Σ is connected to the displacement gradient, evaluated at the surface, by the relations

$$\Sigma_{\alpha\beta} = \tau_0\delta_{\alpha\beta} + (\mu_0 - \tau_0)(u_{\alpha,\beta} + u_{\beta,\alpha}) + (\lambda_0 + \tau_0)u_{\gamma,\gamma}\delta_{\alpha\beta} + \tau_0 u_{\alpha,\beta}, \quad \Sigma_{3\alpha} = \tau_0 u_{3,\alpha}. \tag{9}$$

Applying (8) and (9) to the geometry of the present problem, the boundary conditions at the void surface ($R = a$) can be expressed in spherical coordinates by

$$
\begin{aligned}
-\sigma_{RR} = (\nabla_S \cdot \Sigma)_R = &-\frac{2\tau_0}{R} - \frac{2(\lambda_0 + \mu_0)}{R^2}\left\{2u_R + \frac{\partial u_\varphi}{\partial\varphi} + \frac{\cos\varphi}{\sin\varphi}u_\varphi\right\} \\
&- \frac{\tau_0}{R^2}\left\{2u_R + 2\frac{\partial u_\varphi}{\partial\varphi} + \frac{2\cos\varphi}{\sin\varphi}u_\varphi - \frac{\partial^2 u_R}{\partial\varphi^2} - \frac{\cos\varphi}{\sin\varphi}\frac{\partial u_R}{\partial\varphi}\right\}, \\
-\sigma_{R\varphi} = (\nabla_S \cdot \Sigma)_\varphi = &\frac{\lambda_0}{R^2}\left\{2\frac{\partial u_R}{\partial\varphi} + \frac{\partial^2 u_\varphi}{\partial\varphi^2} + \frac{\cos\varphi}{\sin\varphi}\frac{\partial u_\varphi}{\partial\varphi} - \frac{u_\varphi}{\sin^2\varphi}\right\} \\
&+ \frac{\mu_0}{R^2}\left\{2\frac{\partial u_R}{\partial\varphi} + 2\frac{\partial^2 u_\varphi}{\partial\varphi^2} + \frac{2\cos\varphi}{\sin\varphi}\frac{\partial u_\varphi}{\partial\varphi} - \frac{2\cos^2\varphi}{\sin^2\varphi}u_\varphi\right\} + \frac{2\tau_0}{R^2}\left\{\frac{\partial u_R}{\partial\varphi} - u_\varphi\right\}.
\end{aligned}
\tag{10}
$$

For more details on Gurtin and Murdoch's model of surface mechanics, readers are invited to refer to their original publications [Gurtin and Murdoch 1975; 1978] and applications of the model [Benveniste 2006; Huang and Wang 2013; Mi and Kouris 2014].

To develop a solution to the present problem, forms of the two harmonic functions must be determined in advance. A few groups of displacement functions are proposed to construct the solution, the first of which is

$$\phi_0 = \frac{1-\nu}{2(1+\nu)}(r^2 - 2z^2)T, \quad \phi_3 = -\frac{z}{(1+\nu)}T. \tag{11}$$

In view of (3), this set corresponds to the applied load at infinity, $\sigma_{rr} = \sigma_{\theta\theta} = T$. The far-field boundary conditions in (7) are thus identically satisfied. Additional groups of displacement functions accommodating the disturbed elastic fields due to the presence of void and plane boundaries are also required. Let us first consider the disturbance caused by the void. In view of the solution to the harmonic equation defined outside of a sphere of radius a, we may try

$$\phi_0 = T\sum_{n=0}^{\infty} A_n \frac{d^{n+3}}{R^{n+1}}P_n[\mu], \quad \phi_3 = T\sum_{n=0}^{\infty} B_n \frac{d^{n+2}}{R^{n+1}}P_n[\mu], \tag{12}$$

where $P_n[\mu]$ denote Legendre functions of the first kind of order n and $\mu = \cos\varphi$. These functions were normalized with respect to the half-thickness d and the far-field tension T to make the unknown coefficients (A_n and B_n) dimensionless. Two additional sets of displacement functions are necessary to

accommodate the nature of finite thickness of the infinite strip:

$$\phi_0 = T \int_0^\infty \psi_1[\lambda] J_0[\lambda r] \cosh[\lambda z]\, \mathrm{d}\lambda, \quad \phi_3 = T \int_0^\infty \lambda \psi_2[\lambda] J_0[\lambda r] \sinh[\lambda z]\, \mathrm{d}\lambda; \tag{13}$$

$$\phi_0 = T \int_0^\infty \overline{\psi}_1[\lambda] J_0[\lambda r] \sinh[\lambda z]\, \mathrm{d}\lambda, \quad \phi_3 = T \int_0^\infty \lambda \overline{\psi}_2[\lambda] J_0[\lambda r] \cosh[\lambda z]\, \mathrm{d}\lambda, \tag{14}$$

where $J_0[\lambda r]$ is a Bessel function of the first kind of zeroth order and $\psi_1[\lambda]$, $\psi_2[\lambda]$, $\overline{\psi}_1[\lambda]$ and $\overline{\psi}_2[\lambda]$ are unknown functions of the integral variable, to be determined by satisfying the boundary conditions in (6). The displacement functions (13) and (14) represent the symmetric and antisymmetric components of the disturbance due to both free surfaces, respectively.

The displacement functions in (12) are expressed in spherical coordinates. In order to satisfy the boundary conditions at the plane boundaries in (6), they need be transformed into cylindrical coordinates. From [Gradshteyn and Ryzhik 2014], an integral representation of the azimuthally independent spherical harmonics can be found for the half-space $z > 0$:

$$\frac{P_n[\mu]}{R^{n+1}} = \frac{1}{n!} \int_0^\infty \lambda^n J_0[\lambda r] e^{-\lambda z}\, \mathrm{d}\lambda. \tag{15}$$

The displacement functions in (12) can therefore be transformed to

$$\begin{aligned}
\phi_0 &= T \int_0^\infty \left\{ \sum_{n=0}^\infty \frac{A_n d^{n+3} \lambda^n}{n!} \right\} J_0[\lambda r] e^{-\lambda z}\, \mathrm{d}\lambda, \\
\phi_3 &= T \int_0^\infty \lambda \left\{ \sum_{n=0}^\infty \frac{B_n d^{n+2} \lambda^{n-1}}{n!} \right\} J_0[\lambda r] e^{-\lambda z}\, \mathrm{d}\lambda.
\end{aligned} \tag{16}$$

Replacing (z) with $(-z)$, (μ) with $(-\mu)$, and employing the parity property of the Legendre function [Arfken et al. 2013], it can be found that for $z < 0$,

$$\frac{P_n[\mu]}{R^{n+1}} = \frac{(-1)^n}{n!} \int_0^\infty \lambda^n J_0[\lambda r] e^{\lambda z}\, \mathrm{d}\lambda. \tag{17}$$

Then, the displacement functions in (12) become

$$\begin{aligned}
\phi_0 &= T \int_0^\infty \left\{ \sum_{n=0}^\infty \frac{(-1)^n A_n d^{n+3} \lambda^n}{n!} \right\} J_0[\lambda r] e^{\lambda z}\, \mathrm{d}\lambda, \\
\phi_3 &= T \int_0^\infty \lambda \left\{ \sum_{n=0}^\infty \frac{(-1)^n B_n d^{n+2} \lambda^{n-1}}{n!} \right\} J_0[\lambda r] e^{\lambda z}\, \mathrm{d}\lambda,
\end{aligned} \tag{18}$$

At this point, the expressions for stresses at the upper surface of the strip can be developed by the superposition of the displacement functions (13), (14), and (16). Those at the lower surface are derived from (13), (14), and (18). The enforcement of the plane boundary conditions in (6) yields the following relations:

$$\psi_1 = \sum_{n=0}^\infty \frac{A_{2n} (d\lambda)^{2n+3}}{2(2n)!} \left\{ (3-4\nu)(K^+ - I^-) + L^+ - N^- + 2d\lambda \left(I^- + \frac{c}{d} J^+ - K^+ \right) \right\}$$

$$+ \sum_{n=0}^{\infty} \frac{A_{2n+1}(d\lambda)^{2n+4}}{2(2n+1)!} \left\{ (3-4\nu)J^+ - M^- + 2d\lambda \left(\frac{c}{d}I^- + \frac{c}{d}K^+ - J^+ \right) \right\}$$

$$+ \sum_{n=0}^{\infty} \frac{B_{2n}(d\lambda)^{2n+2}}{(2n)!} \left\{ 2(1-\nu)(1-2\nu)J^+ + c\lambda((3-4\nu)I^- + N^-) \right.$$

$$\left. + d^2\lambda^2 \left(\frac{2c}{d}K^+ - \left(1+\frac{c^2}{d^2}\right)J^+ \right) \right\}$$

$$+ \sum_{n=0}^{\infty} \frac{B_{2n+1}(d\lambda)^{2n+3}}{(2n+1)!} \left\{ 2(1-\nu)(1-2\nu)(K^+ - I^-) + c\lambda M^- \right.$$

$$\left. + d^2\lambda^2 \left(\frac{2c}{d}J^+ - \left(1+\frac{c^2}{d^2}\right)K^+ + \left(1-\frac{c^2}{d^2}\right)I^- \right) \right\},$$

(19)

$$\bar{\psi}_1 = \sum_{n=0}^{\infty} \frac{A_{2n}(d\lambda)^{2n+3}}{2(2n)!} \left\{ (3-4\nu)J^+ - M^- + 2d\lambda \left(\frac{c}{d}(K^+ - I^-) - J^+ \right) \right\}$$

$$+ \sum_{n=0}^{\infty} \frac{A_{2n+1}(d\lambda)^{2n+4}}{2(2n+1)!} \left\{ (3-4\nu)(K^+ + I^-) - L^+ - N^- + 2d\lambda \left(\frac{c}{d}J^+ - K^+ - I^- \right) \right\}$$

$$+ \sum_{n=0}^{\infty} \frac{B_{2n}(d\lambda)^{2n+2}}{(2n)!} \left\{ 2(1-\nu)(1-2\nu)(K^+ + I^-) + c\lambda M^- \right.$$

$$\left. + d^2\lambda^2 \left(\frac{2c}{d}J^+ - \left(1-\frac{c^2}{d^2}\right)I^- - \left(1+\frac{c^2}{d^2}\right)K^+ \right) \right\}$$

(20)

$$+ \sum_{n=0}^{\infty} \frac{B_{2n+1}(d\lambda)^{2n+3}}{(2n+1)!} \left\{ 2(1-\nu)(1-2\nu)J^+ + c\lambda(N^- - (3-4\nu)I^-) \right.$$

$$\left. + d^2\lambda^2 \left(\frac{2c}{d}K^+ - \left(1+\frac{c^2}{d^2}\right)J^+ \right) \right\},$$

$$\psi_2 = \sum_{n=0}^{\infty} \frac{A_{2n}(d\lambda)^{2n+3}}{(2n)!}(K^+ - I^-) + \sum_{n=0}^{\infty} \frac{A_{2n+1}(d\lambda)^{2n+4}}{(2n+1)!}J^+$$

$$+ \sum_{n=0}^{\infty} \frac{B_{2n}(d\lambda)^{2n+2}}{2(2n)!} \left\{ (3-4\nu)J^+ + M^- + 2d\lambda \left(J^+ - \frac{c}{d}(K^+ - I^-) \right) \right\}$$

(21)

$$+ \sum_{n=0}^{\infty} \frac{B_{2n+1}(d\lambda)^{2n+3}}{2(2n+1)!} \left\{ (3-4\nu)(K^+ - I^-) - L^+ + N^- + 2d\lambda \left(K^+ - I^- - \frac{c}{d}J^+ \right) \right\},$$

$$\frac{\bar{\psi}_2}{d^3} = \sum_{n=0}^{\infty} \frac{A_{2n}(d\lambda)^{2n+3}}{(2n)!}J^+ + \sum_{n=0}^{\infty} \frac{A_{2n+1}(d\lambda)^{2n+4}}{(2n+1)!}(K^+ + I^-)$$

$$+ \sum_{n=0}^{\infty} \frac{B_{2n}(d\lambda)^{2n+2}}{2(2n)!} \left\{ (3-4\nu)(K^+ + I^-) + L^+ + N^- + 2d\lambda \left(K^+ + I^- - \frac{c}{d}J^+ \right) \right\}$$

(22)

$$+ \sum_{n=0}^{\infty} \frac{B_{2n+1}(d\lambda)^{2n+3}}{2(2n+1)!} \left\{ (3-4\nu)J^+ + M^- + 2d\lambda \left(J^+ - \frac{c}{d}(K^+ + I^-) \right) \right\},$$

where

$$
I^{\pm} = \frac{1}{\sinh[2x] - 2x} \pm \frac{1}{\sinh[2x] + 2x}, \quad J^{\pm} = I^{\pm} \sinh[2cx/d], \quad K^{\pm} = I^{\pm} \cosh[2cx/d],
$$
$$
L^{\pm} = I^{\pm} e^{-2x}, \quad M^{\pm} = I^{\pm} e^{-2x} \sinh[2cx/d], \quad N^{\pm} = I^{\pm} e^{-2x} \cosh[2cx/d], \quad x = d\lambda.
$$
(23)

Next, we impose the boundary conditions at the void surface $R = a$, given in (10). For this purpose, the displacement functions (13) and (14) must be transformed into spherical coordinates. With the help of the series representations of cylindrical harmonics [Gradshteyn and Ryzhik 2014],

$$
J_0[\lambda r] \cosh \lambda z = \sum_{n=0}^{\infty} \frac{(\lambda R)^{2n}}{(2n)!} P_{2n}[\mu], \quad J_0[\lambda r] \sinh \lambda z = \sum_{n=0}^{\infty} \frac{(\lambda R)^{2n+1}}{(2n+1)!} P_{2n+1}[\mu].
$$
(24)

Equations (13) and (14) can be combined into a single group,

$$
\phi_0 = T \sum_{n=0}^{\infty} \alpha_n \frac{R^n}{d^{n-2}} P_n[\mu], \quad \phi_3 = T \sum_{n=0}^{\infty} \beta_n \frac{R^n}{d^{n-1}} P_n[\mu],
$$
(25)

where

$$
\alpha_{2n} = d^{2n-2} \int_0^{\infty} \frac{\psi_1 \lambda^{2n}}{(2n)!} \, d\lambda, \qquad \alpha_{2n+1} = d^{2n-1} \int_0^{\infty} \frac{\overline{\psi}_1 \lambda^{2n+1}}{(2n+1)!} \, d\lambda,
$$
$$
\beta_{2n} = d^{2n-1} \int_0^{\infty} \frac{\overline{\psi}_2 \lambda^{2n+1}}{(2n)!} \, d\lambda, \quad \beta_{2n+1} = d^{2n} \int_0^{\infty} \frac{\psi_2 \lambda^{2n+2}}{(2n+1)!} \, d\lambda.
$$
(26)

Substituting (19)–(22) into (26), we obtain

$$
\begin{aligned}
\alpha_{2n} = &\sum_{m=0}^{\infty} A_{2m} q_{2m}^{2n} \Bigg\{ (3-4\nu)(K_{2m+2n}^+ - I_{2m+2n}^-) + L_{2m+2n}^+ - N_{2m+2n}^- \\
&\qquad\qquad + (2m+2n+1)\Big(\frac{c}{d} J_{2m+2n+1}^+ - K_{2m+2n+1}^+ + I_{2m+2n+1}^-\Big) \Bigg\} \\
&+ \sum_{m=0}^{\infty} A_{2m+1} q_{2m+1}^{2n} \Bigg\{ (3-4\nu) J_{2m+2n+1}^+ - M_{2m+2n+1}^- \\
&\qquad\qquad + (2m+2n+2)\Big(\frac{c}{d} K_{2m+2n+2}^+ + \frac{c}{d} I_{2m+2n+2}^- - J_{2m+2n+2}^+\Big) \Bigg\} \\
&+ 2\sum_{m=0}^{\infty} B_{2m} q_{2m}^{2n} \Bigg\{ \frac{4(1-\nu)(1-2\nu)}{(2m+2n)} J_{2m+2n-1}^+ + \frac{c}{d}((3-4\nu) I_{2m+2n}^- + N_{2m+2n}^-) \\
&\qquad\qquad + (2m+2n+1)\Big(\frac{c}{d} K_{2m+2n+1}^+ - \frac{1}{2}\Big(1+\frac{c^2}{d^2}\Big) J_{2m+2n+1}^+\Big) \Bigg\} \\
&+ 2\sum_{m=0}^{\infty} B_{2m+1} q_{2m+1}^{2n} \Bigg\{ \frac{4(1-\nu)(1-2\nu)}{(2m+2n+1)} (K_{2m+2n}^+ - I_{2m+2n}^-) \\
&\qquad\qquad + (2m+2n+2)\frac{c}{d} J_{2m+2n+2}^+ + \frac{c}{d} M_{2m+2n+1}^- \\
&\qquad\qquad + (m+n+1)\Big(\Big(1-\frac{c^2}{d^2}\Big) I_{2m+2n+2}^- - \Big(1+\frac{c^2}{d^2}\Big) K_{2m+2n+2}^+\Big) \Bigg\},
\end{aligned}
$$
(27)

$$\alpha_{2n+1} = \sum_{m=0}^{\infty} A_{2m} q_{2m}^{2n+1} \left\{ (3-4\nu) J_{2m+2n+1}^{+} - M_{2m+2n+1}^{-} \right.$$
$$\left. + (2m+2n+2)\left(\frac{c}{d} K_{2m+2n+2}^{+} - \frac{c}{d} I_{2m+2n+2}^{-} - J_{2m+2n+2}^{+}\right) \right\}$$

$$+ \sum_{m=0}^{\infty} A_{2m+1} q_{2m+1}^{2n+1} \left\{ (3-4\nu)(K_{2m+2n+2}^{+} + I_{2m+2n+2}^{-}) - L_{2m+2n+2}^{+} - N_{2m+2n+2}^{-} \right.$$
$$\left. + (2m+2n+3)\left(\frac{c}{d} J_{2m+2n+3}^{+} - K_{2m+2n+3}^{+} - I_{2m+2n+3}^{-}\right) \right\}$$

$$+ 2\sum_{m=0}^{\infty} B_{2m} q_{2m}^{2n+1} \left\{ \frac{4(1-\nu)(1-2\nu)}{(2m+2n+1)}(K_{2m+2n}^{+} + I_{2m+2n}^{-}) \right. \qquad (28)$$
$$+ (2m+2n+2)\frac{c}{d} J_{2m+2n+2}^{+} + \frac{c}{d} M_{2m+2n+1}^{-}$$
$$\left. - (m+n+1)\left(\left(1-\frac{c^2}{d^2}\right) I_{2m+2n+2}^{-} + \left(1+\frac{c^2}{d^2}\right) K_{2m+2n+2}^{+}\right) \right\}$$

$$+ 2\sum_{m=0}^{\infty} B_{2m+1} q_{2m+1}^{2n+1} \left\{ \frac{4(1-\nu)(1-2\nu)}{(2m+2n+2)} J_{2m+2n+1}^{+} + \frac{c}{d}(N_{2m+2n+2}^{-} - (3-4\nu) I_{2m+2n+2}^{-}) \right.$$
$$\left. + (2m+2n+3)\left(\frac{c}{d} K_{2m+2n+3}^{+} - \frac{1}{2}\left(1+\frac{c^2}{d^2}\right) J_{2m+2n+3}^{+}\right) \right\},$$

$$\beta_{2n} = \sum_{m=0}^{\infty} A_{2m} q_{2m}^{2n} (2m+2n+1) J_{2m+2n+1}^{+}$$

$$+ \sum_{m=0}^{\infty} A_{2m+1} q_{2m+1}^{2n} (2m+2n+2)\{K_{2m+2n+2}^{+} + I_{2m+2n+2}^{-}\}$$

$$+ \sum_{m=0}^{\infty} B_{2m} q_{2m}^{2n} \left\{ (3-4\nu)(K_{2m+2n}^{+} + I_{2m+2n}^{-}) + L_{2m+2n}^{+} + N_{2m+2n}^{-} \right. \qquad (29)$$
$$\left. + (2m+2n+1)\left(K_{2m+2n+1}^{+} + I_{2m+2n+1}^{-} - \frac{c}{d} J_{2m+2n+1}^{+}\right) \right\}$$

$$+ \sum_{m=0}^{\infty} B_{2m+1} q_{2m+1}^{2n} \left\{ (3-4\nu) J_{2m+2n+1}^{+} + M_{2m+2n+1}^{-} \right.$$
$$\left. + (2m+2n+2)\left(J_{2m+2n+2}^{+} - \frac{c}{d}(K_{2m+2n+2}^{+} + I_{2m+2n+2}^{-})\right) \right\},$$

$$\beta_{2n+1} = \sum_{m=0}^{\infty} A_{2m} q_{2m}^{2n+1} (2m+2n+2)\{K_{2m+2n+2}^{+} - I_{2m+2n+2}^{-}\}$$

$$+ \sum_{m=0}^{\infty} A_{2m+1} q_{2m+1}^{2n+1} (2m+2n+3) J_{2m+2n+3}^{+}$$

$$+ \sum_{m=0}^{\infty} B_{2m} q_{2m}^{2n+1} \left\{ (3-4\nu) J_{2m+2n+1}^{+} + M_{2m+2n+1}^{-} \right. \qquad (30)$$
$$\left. + (2m+2n+2)\left(J_{2m+2n+2}^{+} - \frac{c}{d}(K_{2m+2n+2}^{+} - I_{2m+2n+2}^{-})\right) \right\}$$

$$+ \sum_{m=0}^{\infty} B_{2m+1} q_{2m+1}^{2n+1} \left\{ (3-4\nu)(K_{2m+2n+2}^{+} - I_{2m+2n+2}^{-}) - L_{2m+2n+2}^{+} + N_{2m+2n+2}^{-} \right.$$

$$\left. + (2m+2n+3)\left(K_{2m+2n+3}^{+} - I_{2m+2n+3}^{-} - \frac{c}{d} J_{2m+2n+3}^{+} \right) \right\},$$

where

$$q_m^n = \frac{(m+n)!}{m!n!2^{m+n+1}}, \quad I_k^{\pm} = \frac{2^k}{k!} \int_0^{\infty} I^{\pm} x^k \, \mathrm{d}x, \quad J_k^{\pm} = \frac{2^k}{k!} \int_0^{\infty} I^{\pm} x^k \sinh[2cx/d] \, \mathrm{d}x,$$

$$K_k^{\pm} = \frac{2^k}{k!} \int_0^{\infty} I^{\pm} x^k \cosh[2cx/d] \, \mathrm{d}x, \qquad\qquad L_k^{\pm} = \frac{2^k}{k!} \int_0^{\infty} I^{\pm} e^{-2x} x^k \, \mathrm{d}x, \qquad (31)$$

$$M_k^{\pm} = \frac{2^k}{k!} \int_0^{\infty} I^{\pm} e^{-2x} x^k \sinh[2cx/d] \, \mathrm{d}x, \qquad N_k^{\pm} = \frac{2^k}{k!} \int_0^{\infty} I^{\pm} e^{-2x} x^k \cosh[2cx/d] \, \mathrm{d}x.$$

These integrals are known as *Howland type*. Their evaluations are nontrivial and separately documented in Appendix A.

Given the displacement functions (11), (12), and (25), both the stresses and the surface divergence of surface stresses at the void surface can be evaluated. The boundary conditions in (10) then become

$$\sum_{n=0}^{\infty} \left\{ \left(i_{SA1} + i_{A1} \frac{d^{n+3}}{a^{n+3}} \right) A_n + \left(i_{SB1} + i_{B1} \frac{d^{n+1}}{a^{n+1}} \right) B_{n-1} + \left(i_{SB2} + i_{B2} \frac{d^{n+3}}{a^{n+3}} \right) B_{n+1} \right.$$

$$\left. + \left(i_{S\alpha 1} + i_{\alpha 1} \frac{a^{n-2}}{d^{n-2}} \right) \alpha_n + \left(i_{S\beta 1} + i_{\beta 1} \frac{a^{n-2}}{d^{n-2}} \right) \beta_{n-1} + \left(i_{S\beta 2} + i_{\beta 2} \frac{a^n}{d^n} \right) \beta_{n+1} \right\} P_n[\mu]$$

$$= \left\{ \frac{2\tau_0}{aT} - \frac{2}{3} + \frac{2(1-2\nu)(2\lambda_0 + 2\mu_0 + \tau_0)}{3aG(1+\nu)} \right\} P_0[\mu] + \left\{ \frac{2}{3} + \frac{2(\lambda_0 + \mu_0 - \tau_0)}{3aG} \right\} P_2[\mu],$$

$$\sum_{n=1}^{\infty} \left\{ \left(l_{SA1} + l_{A1} \frac{d^{n+3}}{a^{n+3}} \right) A_n + \left(l_{SB1} + l_{B1} \frac{d^{n+1}}{a^{n+1}} \right) B_{n-1} + \left(l_{SB2} + l_{B2} \frac{d^{n+3}}{a^{n+3}} \right) B_{n+1} \right. \qquad (32)$$

$$\left. + \left(l_{S\alpha 1} + l_{\alpha 1} \frac{a^{n-2}}{d^{n-2}} \right) \alpha_n + \left(l_{S\beta 1} + l_{\beta 1} \frac{a^{n-2}}{d^{n-2}} \right) \beta_{n-1} + \left(l_{S\beta 2} + l_{\beta 2} \frac{a^n}{d^n} \right) \beta_{n+1} \right\} P_n'[\mu]$$

$$= \left\{ \frac{(\lambda_0 + 3\mu_0 - \tau_0)}{3aG} - \frac{1}{3} \right\} P_2'[\mu],$$

where i_{SA1}, i_{A1}, i_{SB1}, i_{B1}, i_{SB2}, i_{B2}, $i_{S\alpha 1}$, $i_{\alpha 1}$, $i_{S\beta 1}$, $i_{\beta 1}$, $i_{S\beta 2}$, $i_{\beta 2}$, l_{SA1}, l_{A1}, l_{SB1}, l_{B1}, l_{SB2}, l_{B2}, $l_{S\alpha 1}$, $l_{\alpha 1}$, $l_{S\beta 1}$, $l_{\beta 1}$, $l_{S\beta 2}$, and $l_{\beta 2}$ are all dimensionless functions of the order number n, void radius a, half-thickness d, shear modulus G, Poisson's ratio ν, and the three surface material constants. For brevity, their expressions are provided in Appendix B. Equating the coefficients of Legendre functions $P_n[\mu]$ and their derivatives $P_n'[\mu]$ lead to a system of linear equations for the unknown constants A_n and B_n. The solution is obtained by solving the linear system.

A careful examination of (32) and those coefficients defined in Appendix B reveals that the strength of the void surface is governed by four intrinsic dimensionless parameters: $\lambda_0' = \lambda_0/aG$, $\mu_0' = \mu_0/aG$, $\tau_0' = \tau_0/aG$, and $\tau_0'' = \tau_0/aT$. The impact of surface mechanics becomes significant when any of these parameters approaches the order of magnitude of unity, or at least to one tenth. For smaller magnitudes, the inclusion of the model of surface mechanics only brings negligible modifications to the classical

solution. By a combined analytical and numerical analysis, Mi and Kouris [2014] recently analyzed the relative importance of these four dimensionless quantities. For a metal system, the last of these four parameters ($\tau_0'' = \tau_0/aT$) dominates since the shear modulus of a metal is about two orders of magnitude higher than its yield strength. The other three parameters become relatively more important in models composed of soft materials such as gelatin gels and rubbers [Mi et al. 2016].

Subsequently, by the superposition of the expressions that can be developed from all displacement functions, all stresses and displacements can be calculated in both cylindrical and spherical coordinates. Nonetheless, difficulties arise when evaluating stresses due to the displacement functions (13) and (14). As can be seen from the expansions in (24), in spherical coordinates the displacement functions in (25) are valid solutions to the harmonic equation only in regions near the void. For regions far away from the void, both series diverge. As a result, the representations in (25) are most helpful to the enforcement of the boundary conditions at the void surface.

On the other hand, when directly evaluating stresses from (13) and (14), integrals involving more complicated integrands than those shown in (31) are encountered. They can be represented by 24 integrals of Howland type, possessing an additional Bessel function and a hyperbolic function in the integrands. The evaluations of these integrals require special consideration, which are presented in Appendix C.

3. Results and discussion

Several numerical experiments were performed when all-around tension at infinity was considered. The infinite strip is assumed to be an isotropic continuum made of nickel, whose shear modulus and Poisson's ratio are respectively $G = 76\,\text{GPa}$ and $\nu = 0.31$. The far-field tensile stress field was chosen so as to ensure that no yielding is resulted: $T = 100\,\text{MPa}$. Stresses and displacements were calculated for various combinations of surface material properties, model size, eccentricity, and void radius.

Based on the dimension analysis presented at the end of last section, it is obvious that the effects of surface mechanics are both material and load dependent. For practical applications of the developed solution, the values of these four parameters and therefore the strength of surface mechanics must be informed from both the bulk and surface material properties of the given physical model. Even for crystalline metals, it is a primary challenge to determine accurate values for the residual surface stress and the two surface Lamé constants. Nonetheless, molecular simulations demonstrate that both the residual surface stress and the stiffness constants of a crystalline surface have a magnitude of about $1\,\text{N/m}$ [Gumbsch and Daw 1991; Shenoy 2005; Mi et al. 2008], though either sign is possible. For a nanovoid of radius $10\,\text{nm}$, τ_0/a, λ_0/a, $\mu_0/a \sim 100\,\text{MPa}$, whose magnitude is reasonably close to the practical loads of most engineering materials. In view of this fact, we have based our calculations merely on several plain crystalline surfaces and two nominal models to investigate the physical significance of surface elasticity. These case studies are sufficiently representative.

3.1. *Convergence test.* It can be observed that the displacement functions (12) and (25) are complete and the convergence of the series is guaranteed. However, these displacement functions are in the form of infinite series. As a result, the fulfillment of boundary conditions results in an infinite set of simultaneous linear equations; see (32). It is not possible to analytically solve such an infinite system without truncation. We therefore must truncate the infinite series in (32) at a finite order *N*, which inevitably introduces numerical approximation to the solution.
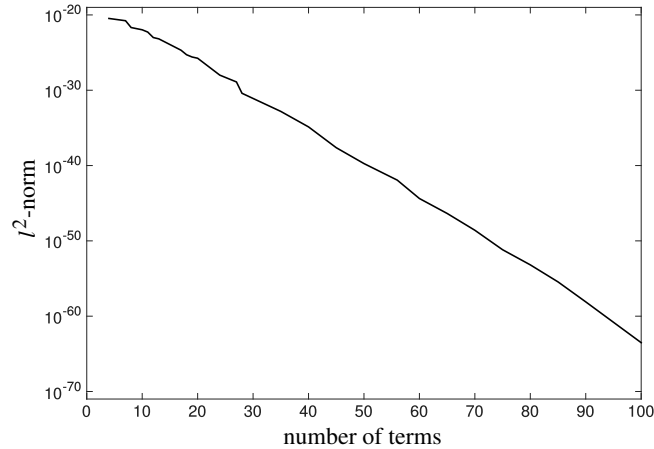
Figure 2. Variation of the l^2-norm of the error vector of the linear system (32) as a function of the number of terms included in the series after truncation.

In order to numerically test the convergence of the solution as a function of the number of terms kept in the truncated series, we computed the l^2-norm of the error vector of the linear system (32). The error vector is formed by the residuals of all linear equations after truncation. As a convention, the square root of the error vector is defined as the l^2-norm.

To evaluate numerically the semianalytical solution and analyze its sensitivity to the truncation parameter, we here take a quite general model as an example. The three characteristic lengths of the model were chosen as $d = 20\,$nm, $a = 6\,$nm, and $c = 10\,$nm. In addition, we chose to model the void surface by the mechanical behavior of a crystalline copper surface whose normal is defined by the crystalline direction [111]. A pair of square brackets is often used to denote a crystalline direction in crystallography. In this analysis, values of the truncation that number up to 100 were considered. A semilogarithmic plot with the l^2-norm of the error vector is presented in Figure 2. It can be concluded from the plot that the l^2-norm decreases exponentially as the truncation number N increases. For both the classical and the modified solutions, no more than 20 terms are needed to satisfy the boundaries conditions at the void surface, with an accuracy up to five significant figures for displacements and stresses. We therefore assume the truncation number $N = 20$ from now on.

3.2. *Effects of surface material properties.* To investigate the influence of surface material properties, we first examined the stress disturbances caused by a nanovoid of radius $6\,$nm, eccentrically embedded ($c = 10\,$nm) in an infinite strip with half-thickness $d = 20\,$nm. In addition to the classical case ($\lambda_0 = \mu_0 = \tau_0 = 0$), six additional surface models were considered. The values of the three surface constants in these models were taken or designed on the basis of [Mi et al. 2008; Shenoy 2005]. For example, we chose to treat the void surface as a plain crystalline copper or nickel surface with two representative surface orientations in four surface models. In crystallography notation, a pair of parentheses is typically used to stand for a crystalline surface. For example, the combination (111) represents a crystalline surface with the crystalline direction [111] as its surface normal. In the remaining two models, we assigned simple nominal values to all three surface constants, i.e., $\lambda_0 = \mu_0 = \tau_0 = 1$ and $\lambda_0 = \mu_0 = \tau_0 = -1$. The rationale
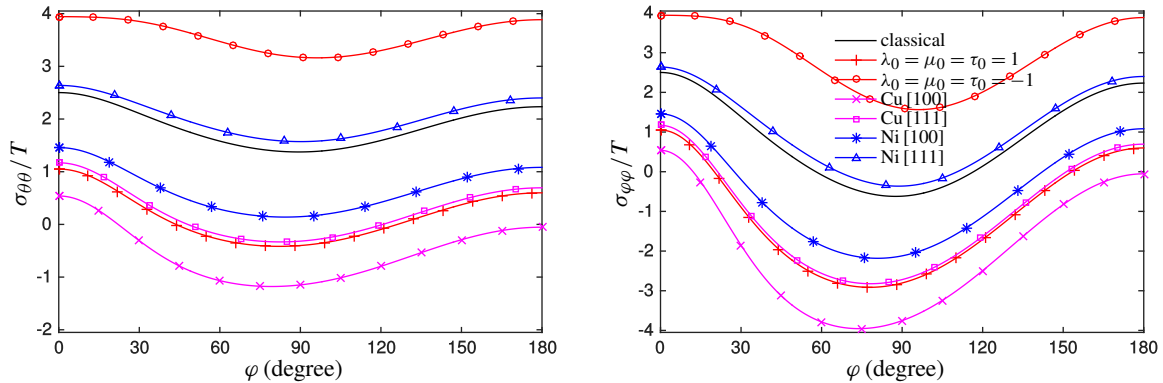
Figure 3. Distribution of hoop, left, and tangential stresses, right, along the void surface ($R = a$). Both subfigures consider six surface models, in addition to the classical solution. Three characteristic lengths of the model are chosen as: $d = 20$ nm, $a = 0.3d$, and $c = 0.5d$.
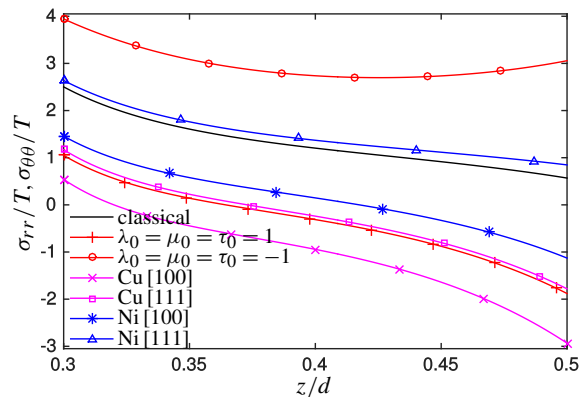

Figure 4. Variation of σ_{rr} and $\sigma_{\theta\theta}$ along the axis of symmetry ($a \leq z \leq d - c$) as a function of nondimensionalized coordinate z/d. In addition to the classical solution, six surface models are considered. Three characteristic lengths of the model are chosen as: $d = 20$ nm, $a = 0.3d$, and $c = 0.5d$.

behind such simple choices is as follows. Both experimental measurements [Cammarata 1994] and atomistic calculations [Mi et al. 2008; Shenoy 2005] have demonstrated that all surface elastic properties of a crystalline surface/interface are roughly in the order of magnitude 1 N/m. Their sign, surprisingly, can be either positive or negative. The possibility of negative surface constants, particularly of negative surface Lamé parameters, is out of expectation and has been extensively discussed [Cammarata 1994; Mi et al. 2008; Shenoy 2005].

Figure 3 shows the hoop ($\sigma_{\theta\theta}$) and tangential ($\sigma_{\varphi\varphi}$) stresses along the void surface $R = a$. For all surface models, stress concentration factors reach high tensile values at the north pole A of the void. The stress concentrations at the south pole C are slightly less severe, due to the eccentricity of the void. Low tensile/compressive values of the stress concentration factors were found near but not exactly on

the equator of the void, due again to the eccentricity of the void. It can be seen that stress distributions in the top half of the strip are more disturbed by the presence of infinite plane boundaries. For this reason, we further plotted both the cylindrical radial (σ_{rr}) and hoop ($\sigma_{\theta\theta}$) stresses along the positive z-axis, as shown in Figure 4. Along the symmetry axis, these two stress components are identical.

From the various cases shown in Figures 3 and 4, it is obvious that stress distributions depend strongly on particular models of surface mechanics. Ni (111) and one of the two nominal models ($\lambda_0 = \mu_0 = \tau_0 = -1$) resulted in more severe stress concentrations than the classical solution. The other four surface models help to reduce the stress concentrations. Among them, the nominal model ($\lambda_0 = \mu_0 = \tau_0 = -1$) and Cu (100) represent the worst and best scenarios, respectively. In the latter case, compressive hoop and tangential stresses were found in most regions of the void surface, except in the immediate vicinity of the void poles A and C. This is quite impressive, given the fact that the remote boundary loading is purely tensile.

Based on the previous dimension analysis on the four intrinsic dimensionless parameters for a metal system, the residual surface stress alone is far more important than surface elasticity. Consequently, it is reasonable to approximate the stresses around a nanovoid embedded in an infinite substrate subjected to all-around far-field tension by

$$
\begin{aligned}
\frac{\sigma_{RR}}{T} &= \frac{2\tau_0}{Ta}\frac{a^3}{R^3} + \frac{2}{3} - \frac{2}{3}\frac{a^3}{R^3} - \left\{\frac{2}{3} - \frac{10(5-\nu)}{3(7-5\nu)}\frac{a^3}{R^3} + \frac{12}{(7-5\nu)}\frac{a^5}{R^5}\right\}P_2[\mu], \\
\frac{\sigma_{\theta\theta}}{T} &= -\frac{\tau_0}{Ta}\frac{a^3}{R^3} + 1 + \frac{(4-5\nu)}{(7-5\nu)}\frac{a^3}{R^3} + \frac{1}{(7-5\nu)}\frac{a^5}{R^5} - \left\{\frac{5(1-2\nu)}{(7-5\nu)}\frac{a^3}{R^3} - \frac{5}{(7-5\nu)}\frac{a^5}{R^5}\right\}P_2[\mu], \\
\frac{\sigma_{\varphi\varphi}}{T} &= -\frac{\tau_0}{Ta}\frac{a^3}{R^3} + \frac{1}{3} + \frac{(2+5\nu)}{3(7-5\nu)}\frac{a^3}{R^3} - \frac{1}{(7-5\nu)}\frac{a^5}{R^5} + \left\{\frac{2}{3} - \frac{5(1-2\nu)}{3(7-5\nu)}\frac{a^3}{R^3} + \frac{7}{(7-5\nu)}\frac{a^5}{R^5}\right\}P_2[\mu].
\end{aligned}
\tag{33}
$$

The above solution is a simple superposition of the classical solution with the effects due to the residual surface stress alone. It now becomes obvious that for nanosized voids the first term in any stress component is in the same order of magnitude as the other ones and therefore must be taken into account. The dependence of stress distributions on surface models in Figures 3 and 4 can be qualitatively explained by (33). The values of residual surface stress are $\tau_0 = -1$, -0.11 (Ni (111)), 0 (classical), 0.7 (Ni (100)), 0.95 (Cu (111)), 1, and 1.41 N/m (Cu (100)) for the seven curves in each subfigure of Figures 3 and 4. The trend is very clear that stress distributions are significantly affected by the value of the residual surface stress. Positive values of τ_0 help to reduce stress levels whereas the negative ones tend to intensify the stress concentrations. For compressive far-field loading, the conclusions should obviously be reversed. It should also be noted that (33) cannot be used to quantitatively predict the curves in Figures 3 and 4. The errors represent the disturbances introduced by both the top and bottom plane boundaries.

3.3. *Effects of model size.* Because the impact of surface mechanics is strongly model dependent, we decided to choose a representative model ($\lambda_0 = \mu_0 = \tau_0 = 1$) in the subsequent development as a means of exploring general trends. Figures 5–8 aim to investigate the influence of surface mechanics on samples of different sizes, when both the void radius to half-thickness ratio and eccentricity are kept constant. As expected, in the absence of surface mechanics, stress distributions are independent of model sizes and are solely functions of ratios among characteristic lengths, i.e., a/d and c/d. This is not the case, however, when the nominal model of surface mechanics is incorporated. From Figures 5–8, it is clear that the
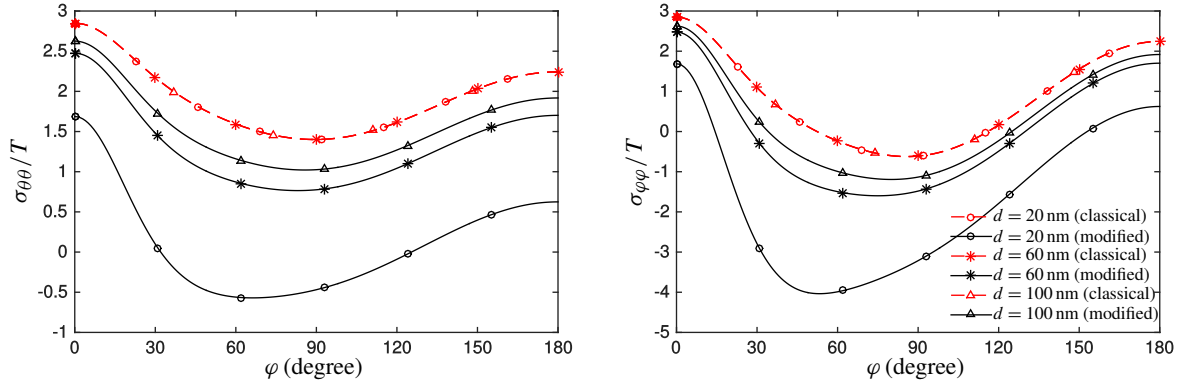
Figure 5. Distribution of hoop, left, and tangential stresses, right, along the void surface ($R = a$). The remaining adjustable parameters are set to: $a = 0.3d$, $c = 0.6d$, and $\lambda_0 = \mu_0 = \tau_0 = 1$ for nonclassical cases.
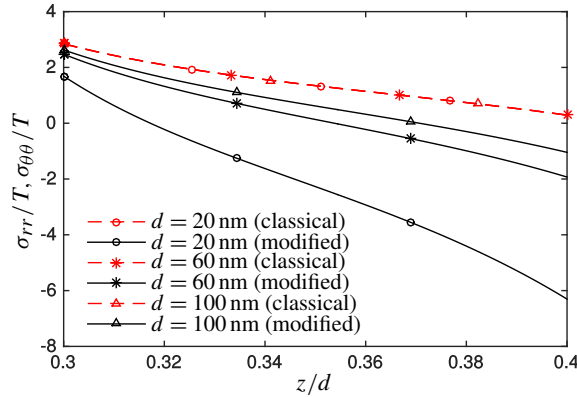

Figure 6. Variation of σ_{rr} and $\sigma_{\theta\theta}$ along the axis of symmetry ($a \leq z \leq d - c$) as a function of nondimensionalized coordinate z/d. The remaining adjustable parameters are set to: $a = 0.3d$, $c = 0.6d$, and $\lambda_0 = \mu_0 = \tau_0 = 1$ for nonclassical cases.

strength of surface mechanics decays monotonically with the model size d. The smaller the model size, the more significant the difference between the classical and modified solutions becomes.

Similar to Figures 3 and 4, Figures 5 and 6 also show the stress concentrations along the void surface and the positive z-axis, respectively. In the latter case ($\varphi = 0$), cylindrical and spherical stresses are connected: $\sigma_{rr} = \sigma_{\varphi\varphi}$ and $\sigma_{zz} = \sigma_{RR}$. Again, the strength of surface mechanics can be qualitatively analyzed by the solution due to a nanovoid embedded in an infinite matrix:

$$(\sigma_{rr}/T)_{\varphi=0} = (\sigma_{\theta\theta}/T)_{\varphi=0} = -\frac{\tau_0}{Ta}\frac{a^3}{R^3} + 1 - \frac{(1-5\nu)}{(7-5\nu)}\frac{a^3}{R^3} + \frac{6}{(7-5\nu)}\frac{a^5}{R^5}. \tag{34}$$

As before, in the above equation the contribution due to surface elasticity has been neglected because of its secondary importance.
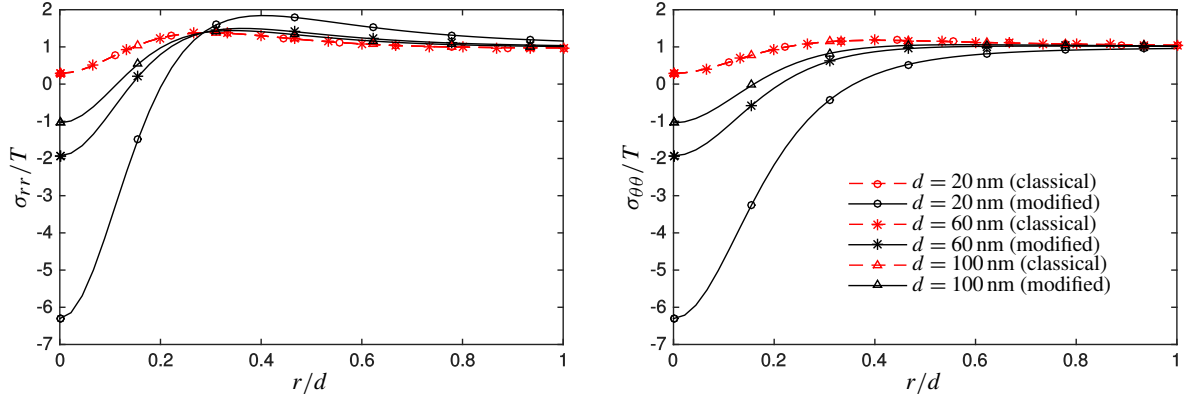
Figure 7. Variation of radial, left, and hoop stresses, right, along the top boundary ($z = d - c$) as a function of nondimensionalized radial coordinate r/d. The remaining adjustable parameters are set to: $a = 0.3d$, $c = 0.6d$, and $\lambda_0 = \mu_0 = \tau_0 = 1$ for nonclassical cases.

Figure 7 shows variations of the radial and hoop stresses on the upper surface of the infinite strip. For all three model sizes, the void surface effects resulted in compressive stress states in the central region of the upper boundary. The compressive domain decreases with model size. Due to symmetry, the maximum compressive stress always occurs at the center $\bar{O}$ of the upper boundary. The discrepancies among the classical and modified solutions are confined to only a few times the radius of the void. This is because the void defect itself is a short-range force field.

Stress distributions on the x-y plane as a function of the model size were also investigated, as shown in Figure 8. The influence of surface mechanics behaves again as a monotonic function. It is interesting to observe that high tensile normal stresses develop on and near the void surface (Figure 8a). In particular, the normal stress σ_{RR} at the free surface of the void becomes nonzero due to the inclusion of surface effects. By the essence of surface mechanics, this stress is equilibrated by the surface divergence of the surface stress ($-2\tau_0/a$). In contrast, low tensile or even compressive $\sigma_{\theta\theta}$ and $\sigma_{\varphi\varphi}$ are produced near the void, representing a relieved stress state. It is no surprise to find that all stresses converge to their far-field counterparts in regions $R \geq 3a$. Once again, the qualitative behavior of the above analysis can be accurately predicted by the closed-form approximations

$$
\begin{aligned}
(\sigma_{RR}/T)_{\varphi=\pi/2} &= \frac{2\tau_0}{Ta}\frac{a^3}{R^3} + 1 - \frac{(13-5\nu)}{(7-5\nu)}\frac{a^3}{R^3} + \frac{6}{(7-5\nu)}\frac{a^5}{R^5}, \\
(\sigma_{\theta\theta}/T)_{\varphi=\pi/2} &= -\frac{\tau_0}{Ta}\frac{a^3}{R^3} + 1 + \frac{(13-20\nu)}{2(7-5\nu)}\frac{a^3}{R^3} - \frac{3}{2(7-5\nu)}\frac{a^5}{R^5}, \\
(\sigma_{\varphi\varphi}/T)_{\varphi=\pi/2} &= -\frac{\tau_0}{Ta}\frac{a^3}{R^3} + \frac{3}{2(7-5\nu)}\frac{a^3}{R^3} - \frac{9}{2(7-5\nu)}\frac{a^5}{R^5}.
\end{aligned}
\tag{35}
$$

Recall that both surface elasticity and the plane boundaries have been ignored in the above equations.

3.4. *Effects of void size.* Three cases of different void radii were examined, when both the strip half-thickness ($d = 20$ nm) and eccentricity ($c = 6$ nm) were fixed. This is a typical parametric study that
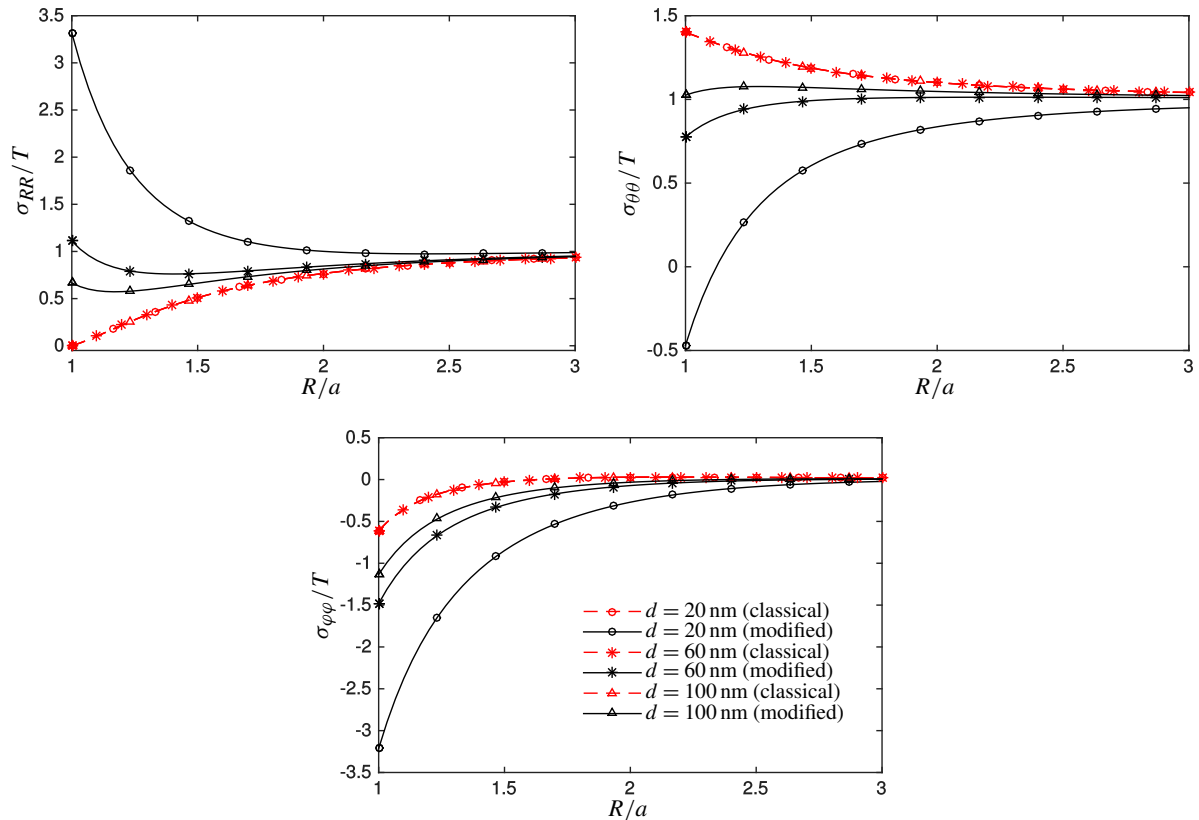
Figure 8. Variation of radial, left; hoop, right; and tangential stresses, bottom, as a function of nondimensionalized radial coordinate R/a. The polar coordinate is kept constant: $\varphi = 90°$. The remaining adjustable parameters are set to: $a = 0.3d$, $c = 0.6d$, and $\lambda_0 = \mu_0 = \tau_0 = 1$ for nonclassical cases.

was performed for a nanovoid embedded in an infinite domain [He and Li 2006; Mi and Kouris 2014]. Emphasis was given to the stress concentrations along the void surface. The hoop ($\sigma_{\theta\theta}$) and tangential ($\sigma_{\varphi\varphi}$) stresses for nanovoids of radius $a = 3$, 6, and 9 nm are shown in Figure 9. The three classical curves vary from one to another due to the presence of eccentricity. The stress distributions are almost symmetric about the x-y plane for the case of $a = 3$ nm. For larger voids, asymmetry in both stress components becomes obvious. The dependence of stress concentration factors on surface effects is quite clear and is as expected. The smaller the nanovoid, the more pronounced the surface effects become. Benefiting from the positive residual surface stress ($\tau_0 = 1$ nm) in the selected nominal model, improvements in stress concentrations were observed in all three cases.

3.5. *Effects of eccentricity.* The last numerical experiment we performed focuses on the influence of eccentricity. Figure 10 illustrates stress concentrations along the surface of a void of radius $a = 6$ nm. Three eccentricities, i.e., $c = 0$, 6, and 12 nm, were considered. For all cases, high tensile values of stress concentration factors were found at the two poles of the void. Low tensile/compressive values
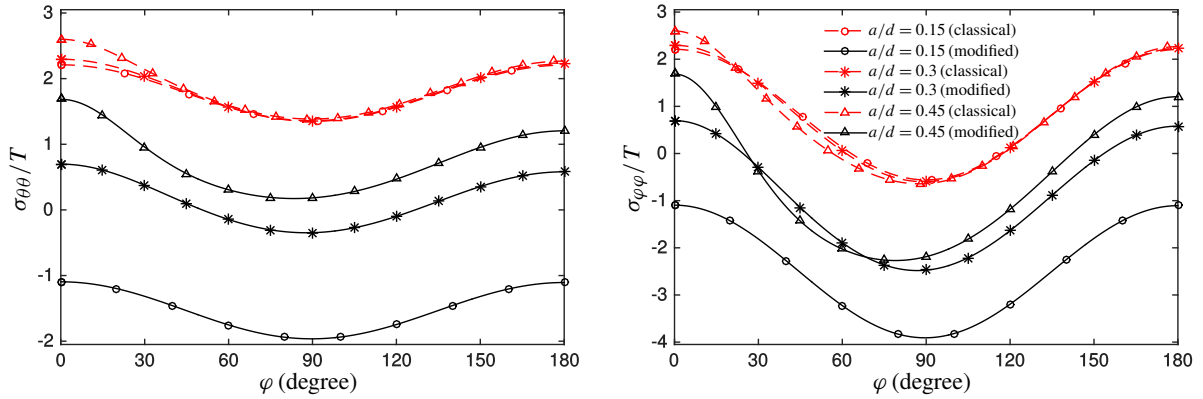
Figure 9. Distribution of hoop, left, and tangential stresses, right, along the void surface ($R = a$). The remaining adjustable parameters are taken to be: $d = 20\,\text{nm}$, $c = 0.3d$, and $\lambda_0 = \mu_0 = \tau_0 = 1$ for nonclassical cases.
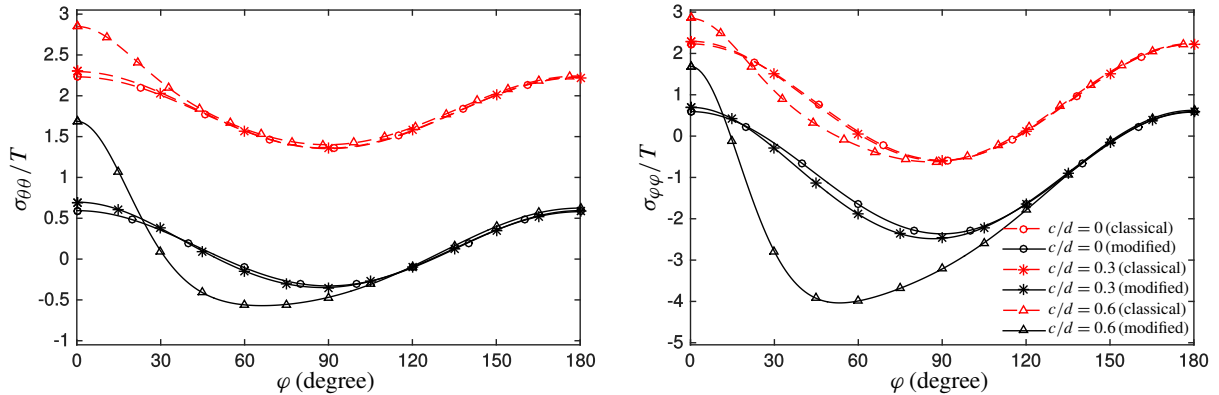

Figure 10. Distribution of hoop, left, and tangential, right, stresses along the void surface ($R = a$). The remaining adjustable parameters are assumed to be: $d = 20\,\text{nm}$, $a = 0.3d$, and $\lambda_0 = \mu_0 = \tau_0 = 1$ for nonclassical cases.

occur near (but not on) the equator of the void, approaching from the north hemisphere. The dependence of stress distributions on the degree of eccentricity is very clear.

As expected, complete symmetry in stress distributions was found for the case of $c = 0$. Due also to the small ratio of void radius to half-thickness ($a/d = 0.3$), both the classical and modified solutions for this case can be reasonably approximated by those due to an infinite substrate. For example, the stress concentration factors at the poles are very close to $\sigma_{\theta\theta/T} = \sigma_{\varphi\varphi}/T = -\tau_0/Ta + 12/(7 - 5\nu)$. Those on the equator of the void surface are well approximated by $\sigma_{\theta\theta}/T = -\tau_0/Ta + 3(4 - 5\nu)/(7 - 5\nu)$ and $\sigma_{\varphi\varphi}/T = -\tau_0/Ta - 3/(7 - 5\nu)$, respectively. For cases with nonzero eccentricities, however, stress distributions on the north hemisphere are significantly disturbed. The disturbance is much less pronounced on the south hemisphere, as can be seen from Figure 10.

4. Concluding remarks

Within the framework of Gurtin and Murdoch's continuum model of surface mechanics, we successfully developed a semianalytical solution, in the forms of infinite series and improper integrals, to the stress concentration problem of a nanosized void embedded in an infinite strip. All-around tensile loads applied at infinity were considered. The method of displacement functions was employed to explore displacements and stresses as functions of void surface material properties, model size, void radius, and eccentricity. The major challenge of the proposed method lies in the evaluation of a number of integrals of Howland type, particularly of those involving Bessel functions. Following extensive numerical experiments, a few observations and conclusions can be summarized:

- Stress distributions were found to depend strongly on the combination of surface material properties. Dimension analysis suggests that for a metallic system the residual surface stress τ_0 is far more crucial than the surface Lamé constants. Positive τ_0 helps to reduce the stress concentration whereas negative values worsen the situation.

- The effects of void surface mechanics are important only for those models whose characteristic lengths are less than 100 nm. Beyond this scale, the void radius to half-thickness ratio (a/d) and relative eccentricity (c/d) govern the strength of stress concentrations.

- Not surprisingly, the impact of void surface mechanics on stress concentrations is in inverse proportion to void radius. For reasonably small ratios a/d, stress distributions degenerate to those of a nanovoid embedded in an infinite medium.

- Eccentricity plays an indispensable role in the determination of stress distributions. As the void approaches the upper boundary, stress concentration factors at the north pole of the void become unbounded for both the classical and modified solutions.

Appendix A: Evaluation of integrals of Howland type

To perform numerical experiments, the integrals defined in (31) must be evaluated. The integrals $I_n^{\pm}$ and $L_n^{\pm}$ have previously been computed [Ling and Lin 1971; Ling 1978] to 25 significant figures. It is worth noticing that as n approaches infinity, I_n^+ and L_n^+ tend to 2 and $\frac{1}{2}^k$, respectively. On the other hand, both I_n^- and L_n^- tend to zero.

Now, let us expand $\sinh[2cx/d]$ into the power series of its argument; the integrals $J_n^{\pm}$ then become

$$J_n^{\pm} = \sum_{m=0}^{\infty} \left(\frac{c}{d}\right)^{2m+1} \frac{(n+2m+1)!}{n!(2m+1)!} I_{n+2m+1}^{\pm}.$$

Since I_n^+ tends to 2 as the integer n tends to infinity, J_n^+ is a slowly convergent series. In order to improve the convergence, a Kummer transformation may be enforced [Ling 1957]:

$$J_n^+ = \frac{\{(1+c/d)^{n+1} - (1-c/d)^{n+1}\}}{(1-c^2/d^2)^{n+1}} + \sum_{m=0}^{\infty} \left(\frac{c}{d}\right)^{2m+1} \frac{(n+2m+1)!}{n!(2m+1)!} (I_{n+2m+1}^+ - 2).$$

In contrast, the series J_n^- converges rapidly to zero with increasing n. Following the same strategy, the integrals $K_n^{\pm}$ can be evaluated as

$$K_n^+ = \frac{\{(1+c/d)^{n+1} + (1-c/d)^{n+1}\}}{(1-c^2/d^2)^{n+1}} + \sum_{m=0}^{\infty} \left(\frac{c}{d}\right)^{2m} \frac{(n+2m)!}{n!(2m)!} (I_{n+2m}^+ - 2),$$

$$K_n^- = \sum_{m=0}^{\infty} \left(\frac{c}{d}\right)^{2m} \frac{(n+2m)!}{n!(2m)!} I_{n+2m}^-.$$

Benefiting from the rapid convergence of both L_n^+ and L_n^-, series expansions of the hyperbolic sine and cosine functions are sufficient for evaluating the integrals $M_n^{\pm}$ and $N_n^{\pm}$:

$$M_n^{\pm} = \sum_{m=0}^{\infty} \left(\frac{c}{d}\right)^{2m+1} \frac{(n+2m+1)!}{n!(2m+1)!} L_{n+2m+1}^{\pm}, \qquad N_n^{\pm} = \sum_{m=0}^{\infty} \left(\frac{c}{d}\right)^{2m} \frac{(n+2m)!}{n!(2m)!} L_{n+2m}^{\pm}.$$

Appendix B: Expressions of dimensionless functions defined in (32)

$$i_{A1} = (n+1)(n+2), \quad i_{B1} = \frac{n(n^2+3n-2\nu)}{(2n-1)}, \quad i_{B2} = \frac{(n+1)(n+2)(n+5-4\nu)}{(2n+3)},$$

$$i_{SA1} = \frac{(n+1)(n+2)(2\lambda_0+2\mu_0+(n+1)\tau_0)}{2aG} \frac{d^{n+3}}{a^{n+3}},$$

$$i_{SB2} = \frac{(n+1)(n+2)(n+5-4\nu)(2\lambda_0+2\mu_0+(n+1)\tau_0)}{2aG(2n+3)} \frac{d^{n+3}}{a^{n+3}},$$

$$i_{SB1} = \frac{n\{(n^2-n(1-4\nu)+2-4\nu)(2\lambda_0+2\mu_0)+(n^3+n^2(6-4\nu)-n(1-4\nu)-2)\tau_0\}}{2aG(2n-1)} \frac{d^{n+1}}{a^{n+1}},$$

$$l_{A1} = (n+2), \quad l_{B1} = \frac{(n^2-2+2\nu)}{(2n-1)}, \quad l_{B2} = \frac{(n+2)(n+5-4\nu)}{(2n+3)},$$

$$l_{SA1} = \frac{(n+2)((n+1)\lambda_0+2n\mu_0+2\tau_0)}{2aG} \frac{d^{n+3}}{a^{n+3}},$$

$$l_{SB2} = \frac{(n+2)(n+5-4\nu)((n+1)\lambda_0+2n\mu_0+2\tau_0)}{2aG(2n+3)} \frac{d^{n+3}}{a^{n+3}},$$

$$l_{SB1} = \frac{\{n(n^2-n(1-4\nu)+2-4\nu)\lambda_0+2(n^3-n^2(2-4\nu)-2n+4-4\nu)\mu_0+2(n^2+4(n-1)(1-\nu))\tau_0\}}{2aG(2n-1)} \frac{d^{n+1}}{a^{n+1}},$$

$$i_{\alpha1} = n(n-1), \quad i_{\beta1} = \frac{n(n-1)(n-4+4\nu)}{(2n-1)}, \quad i_{\beta2} = \frac{(n+1)(n^2-n-2-2\nu)}{(2n+3)},$$

$$i_{S\alpha1} = \frac{n(n-1)(2\lambda_0+2\mu_0-n\tau_0)}{2aG} \frac{a^{n-2}}{d^{n-2}},$$

$$i_{S\beta1} = \frac{n(n-1)(n-4+4\nu)(2\lambda_0+2\mu_0-n\tau_0)}{2aG(2n-1)} \frac{a^{n-2}}{d^{n-2}},$$

$$i_{S\beta2} = \frac{(n+1)\{(n^2+n(3-4\nu)+4-8\nu)(2\lambda_0+2\mu_0)-(n^3-n^2(3-4\nu)-2n(5-6\nu)-4+8\nu)\tau_0\}}{2aG(2n+3)} \frac{a^n}{d^n},$$

$$l_{\alpha 1} = -(n-1), \quad l_{\beta 1} = -\frac{(n-1)(n-4+4\nu)}{(2n-1)}, \quad l_{\beta 2} = -\frac{(n^2+2n-1+2\nu)}{(2n+3)},$$

$$l_{S\alpha 1} = \frac{(n-1)(n\lambda_0 + 2(n+1)\mu_0 - 2\tau_0)}{2aG} \frac{a^{n-2}}{d^{n-2}},$$

$$l_{S\beta 1} = \frac{(n-1)(n-4+4\nu)(n\lambda_0 + 2(n+1)\mu_0 - 2\tau_0)}{2aG(2n-1)} \frac{a^{n-2}}{d^{n-2}},$$

$$l_{S\beta 2} = \frac{\begin{Bmatrix} (n+1)(n^2+n(3-4\nu)+4-8\nu)\lambda_0 + 2(n^3+n^2(5-4\nu)+n(5-8\nu)-3)\mu_0 \\ -2(n^2-n(2-4\nu)-7+8\nu)\tau_0 \end{Bmatrix}}{2aG(2n+3)} \frac{a^n}{d^n}.$$

Appendix C: Evaluation of integrals of Howland type involving a Bessel function

The 24 integrals that were encountered when evaluating stresses in cylindrical coordinates from (13) and (14) are as follows:

$$\begin{Bmatrix} IS_{m,n}^{\pm} \\ IC_{m,n}^{\pm} \end{Bmatrix} = \frac{1}{n!} \int_0^{\infty} \begin{Bmatrix} \sinh[zx/d] \\ \cosh[zx/d] \end{Bmatrix} I^{\pm} x^n J_m[rx/d] \, \mathrm{d}x,$$

$$\begin{Bmatrix} JS_{m,n}^{\pm} \\ JC_{m,n}^{\pm} \end{Bmatrix} = \frac{1}{n!} \int_0^{\infty} \begin{Bmatrix} \sinh[zx/d] \\ \cosh[zx/d] \end{Bmatrix} I^{\pm} x^n \sinh[2cx/d] J_m[rx/d] \, \mathrm{d}x,$$

$$\begin{Bmatrix} KS_{m,n}^{\pm} \\ KC_{m,n}^{\pm} \end{Bmatrix} = \frac{1}{n!} \int_0^{\infty} \begin{Bmatrix} \sinh[zx/d] \\ \cosh[zx/d] \end{Bmatrix} I^{\pm} x^n \cosh[2cx/d] J_m[rx/d] \, \mathrm{d}x,$$

$$\begin{Bmatrix} LS_{m,n}^{\pm} \\ LC_{m,n}^{\pm} \end{Bmatrix} = \frac{1}{n!} \int_0^{\infty} \begin{Bmatrix} \sinh[zx/d] \\ \cosh[zx/d] \end{Bmatrix} I^{\pm} e^{-2x} x^n J_m[rx/d] \, \mathrm{d}x,$$

$$\begin{Bmatrix} MS_{m,n}^{\pm} \\ MC_{m,n}^{\pm} \end{Bmatrix} = \frac{1}{n!} \int_0^{\infty} \begin{Bmatrix} \sinh[zx/d] \\ \cosh[zx/d] \end{Bmatrix} I^{\pm} e^{-2x} x^n \sinh[2cx/d] J_m[rx/d] \, \mathrm{d}x,$$

$$\begin{Bmatrix} NS_{m,n}^{\pm} \\ NC_{m,n}^{\pm} \end{Bmatrix} = \frac{1}{n!} \int_0^{\infty} \begin{Bmatrix} \sinh[zx/d] \\ \cosh[zx/d] \end{Bmatrix} I^{\pm} e^{-2x} x^n \cosh[2cx/d] J_m[rx/d] \, \mathrm{d}x.$$

Take the first group of the above integrals as an example. Consider the auxiliary integrals

$$\bar{I}_{m,n}^{\pm} = \frac{1}{n!} \int_0^{\infty} I^{\pm} x^n J_m[rx/d] \, \mathrm{d}x.$$

Following [Ling and Wu 1982], we replace the Bessel function by its usual series representation and integrate:

$$\bar{I}_{m,n}^{\pm} = \sum_{k=0}^{\infty} \frac{(-1)^k (n+m+2k)!}{n! k! (m+k)! 2^n} \left(\frac{r}{4d} \right)^{m+2k} I_{n+m+2k}^{\pm}.$$

Since the limit of I_n^+ is 2 as n tends to infinity, the convergence of $\bar{I}_{m,n}^+$ may again be improved by the use of a Kummer transformation. Finally, the first group of the 24 integrals can be evaluated in terms of

the auxiliary integrals

$$IS_{m,n}^{\pm} = \sum_{k=0}^{\infty} \frac{(n+2k+1)!}{n!(2k+1)!}\left(\frac{z}{d}\right)^{2k+1}\bar{I}_{m,n+2k+1}^{\pm}, \quad IC_{m,n}^{\pm} = \sum_{k=0}^{\infty} \frac{(n+2k)!}{n!(2k)!}\left(\frac{z}{d}\right)^{2k}\bar{I}_{m,n+2k}^{\pm}.$$

Although tedious, the remaining integrals can be evaluated in a procedure similar to the one described above.

Acknowledgements

References

[Arfken et al. 2013] G. B. Arfken, H. J. Weber, and F. E. Harris, *Mathematical methods for physicists: a comprehensive guide*, 7th ed., Elsevier, Amsterdam, 2013.

[Barber 2010] J. R. Barber, *Elasticity*, 3rd ed., Springer, New York, 2010.

[Benveniste 2006] Y. Benveniste, "A general interface model for a three-dimensional curved thin anisotropic interphase between two anisotropic media", *J. Mech. Phys. Solids* **54**:4 (2006), 708–734.

[Boccardo et al. 2015] V. Boccardo, E. Godoy, and M. Durán, "An efficient semi-analytical method to compute displacements and stresses in an elastic half-space with a hemispherical pit", *Adv. Appl. Math. Mech.* **7**:3 (2015), 295–322.

[Cammarata 1994] R. C. Cammarata, "Surface and interface stress effects in thin films", *Prog. Surf. Sci* **46**:1 (1994), 1–38.

[Chen and Yao 2014] S. Chen and Y. Yao, "Elastic theory of nanomaterials based on surface-energy density", *J. Appl. Mech.* (*ASME*) **81**:12 (2014), art. id. 121002, 12 pp.

[Duan et al. 2009] H. L. Duan, J. Wang, and B. Karihaloo, "Theory of elasticity at the nanoscale", *Adv. Appl. Mech.* **42** (2009), 1–68.

[Gradshteyn and Ryzhik 2014] I. S. Gradshteyn and I. M. Ryzhik, *Table of integrals, series, and products*, 8th ed., Elsevier, Boston, Massachusetts, 2014.

[Gumbsch and Daw 1991] P. Gumbsch and M. S. Daw, "Interface stresses and their effects on the elastic moduli of metallic multilayers", *Phys. Rev. B* **44** (1991), 3934–3938.

[Gurtin and Murdoch 1975] M. E. Gurtin and I. A. Murdoch, "A continuum theory of elastic material surfaces", *Arch. Ration. Mech. Anal.* **57**:4 (1975), 291–323. Correction in **59**:4 (1975), 389–390.

[Gurtin and Murdoch 1978] M. E. Gurtin and A. I. Murdoch, "Surface stress in solids", *Int. J. Solids Struct.* **14**:6 (1978), 431–440.

[He and Li 2006] L. H. He and Z. R. Li, "Impact of surface stress on stress concentration", *Int. J. Solids Struct.* **43**:20 (2006), 6208–6219.

[Huang and Wang 2013] Z. Huang and J. Wang, "Micromechanics of nanocomposites with interface energy effect", pp. 303–348 in *Handbook of micromechanics and nanomechanics*, edited by S. Li and X.-L. Gao, CRC Press, Boca Raton, FL, 2013.

[Li et al. 2006] Z. R. Li, C. W. Lim, and L. H. He, "Stress concentration around a nano-scale spherical cavity in elastic media: effect of surface stress", *Eur. J. Mech. A Solids* **25**:2 (2006), 260–270.

[Ling 1957] C.-B. Ling, "Tables of values of 16 integrals of algebraic-hyperbolic type", *Math. Tables Aids Comput.* **11** (1957), 160–166.

[Ling 1978] C.-B. Ling, "Further evaluation of Howland integrals", *Math. Comput.* **32** (1978), 900–904.

[Ling and Lin 1971] C.-B. Ling and J. Lin, "A new method of evaluation of Howland integrals", *Math. Comput.* **25** (1971), 331–337.

[Ling and Wu 1982] C.-B. Ling and M.-J. Wu, "Evaluation of integrals of Howland type involving a Bessel function", *Math. Comput.* **38** (1982), 215–222.

[Mi and Kouris 2006] C. Mi and D. Kouris, "Nanoparticles under the influence of surface/interface elasticity", *J. Mech. Mater. Struct.* **1**:4 (2006), 763–791.

[Mi and Kouris 2013] C. Mi and D. Kouris, "Stress concentration around a nanovoid near the surface of an elastic half-space", *Int. J. Solids Struct.* **50**:18 (2013), 2737–2748.

[Mi and Kouris 2014] C. Mi and D. Kouris, "On the significance of coherent interface effects for embedded nanoparticles", *Math. Mech. Solids* **19**:4 (2014), 350–368.

[Mi and Kouris 2015] C. Mi and D. Kouris, "Surface mechanics implications for a nanovoided metallic thin-plate under uniform boundary loading", *Math. Mech. Solids* (2015), art. id. 1081286515595262, 19 pp.

[Mi et al. 2008] C. Mi, S. Jun, D. A. Kouris, and S. Y. Kim, "Atomistic calculations of interface elastic properties in noncoherent metallic bilayers", *Phys. Rev. B* **77** (2008), art. id. 075425, 12 pp.

[Mi et al. 2016] C. Mi, Z. Sun, and D. Kouris, "The hemispherical nanopit at the plane boundary of an elastic half-space subjected to statically equivalent shear tractions", *J. Mech. Mater. Struct.* **11**:5 (2016), 595–614.

[Mura 1987] T. Mura, *Micromechanics of defects in solids*, Martinus Nijhoff, Boston, 1987.

[Sharma and Ganti 2004] P. Sharma and S. Ganti, "Size-dependent Eshelby's tensor for embedded nano-inclusions incorporating surface/interface energies", *J. Appl. Mech. (ASME)* **71**:5 (2004), 663–671.

[Shenoy 2005] V. B. Shenoy, "Atomistic calculations of elastic properties of metallic fcc crystal surfaces", *Phys. Rev. B* **71** (2005), art. id. 094104, 11 pp.

[Springholz et al. 1998] G. Springholz, V. Holy, M. Pinczolits, and G. Bauer, "Self-organized growth of three-dimensional quantum-dot crystals with fcc-like stacking and a tunable lattice constant", *Science* **282**:5389 (1998), 734–737.

[Tsuchida and Nakahara 1970] E. Tsuchida and I. Nakahara, "Three-dimentsional stress concentration around a spherical cavity in a semi-infinite elastic body", *Bull. Jpn. Soc. Mech. Eng.* **13**:58 (1970), 499–508.

[Tsuchida and Nakahara 1972] E. Tsuchida and I. Nakahara, "Stresses in a semi-infinite body subjected to uniform pressure on the surface of a cavity and the plane boundary", *Bull. Jpn. Soc. Mech. Eng.* **15**:79 (1972), 1–10.

[Tsuchida and Nakahara 1974] E. Tsuchida and I. Nakahara, "Stress concentration around a spherical cavity in a semi-infinite elastic body under uniaxial tension", *Bull. Jpn. Soc. Mech. Eng.* **17**:112 (1974), 1207–1217.

[Tsuchida and Nakahara 1976] E. Tsuchida and I. Nakahara, "Three-dimensional stress concentration around a spherical cavity in a thick plate under uniaxial tension", *Bull. Jpn. Soc. Mech. Eng.* **19**:136 (1976), 1107–1114.

[Tsuchida et al. 1976] E. Tsuchida, S. Togawa, I. Nakahara, and M. Kodama, "Stresses in a thick plate containing an eccentric spherical cavity under uniaxial tension", *Bull. Jpn. Soc. Mech. Eng.* **19**:134 (1976), 838–848.

[Wang et al. 2011] J. Wang, Z. Huang, H. Duan, S. Yu, X. Feng, G. Wang, W. Zhang, and T. Wang, "Surface stress effect in mechanics of nanostructured materials", *Acta Mech. Solida Sin.* **24**:1 (2011), 52–82.

CHANGWEN MI: mi@seu.edu.cn
Jiangsu Key Laboratory of Engineering Mechanics, School of Civil Engineering, Southeast University, 2 Sipailou Street, Nanjing, 210096, China

msp

SUBMISSION GUIDELINES

ORIGINALITY

Authors may submit manuscripts in PDF format online at the Submissions page. Submission of a manuscript acknowledges that the manuscript is original and has neither previously, nor simultaneously, in whole or in part, been submitted elsewhere. Information regarding the preparation of manuscripts is provided below. Correspondence by email is requested for convenience and speed. For further information, write to contact@msp.org.

LANGUAGE

Manuscripts must be in English. A brief abstract of about 150 words or less must be included. The abstract should be self-contained and not make any reference to the bibliography. Also required are keywords and subject classification for the article, and, for each author, postal address, affiliation (if appropriate), and email address if available. A home-page URL is optional.

FORMAT

Authors can use their preferred manuscript-preparation software, including for example Microsoft Word or any variant of TeX. The journal itself is produced in LaTeX, so accepted articles prepared using other software will be converted to LaTeX at production time. Authors wishing to prepare their document in LaTeX can follow the example file at www.jomms.net (but the use of other class files is acceptable). At submission time only a PDF file is required. After acceptance, authors must submit all source material (see especially Figures below).

REFERENCES

Bibliographical references should be complete, including article titles and page ranges. All references in the bibliography should be cited in the text. The use of BibTeX is preferred but not required. Tags will be converted to the house format (see a current issue for examples); however, for submission you may use the format of your choice. Links will be provided to all literature with known web locations; authors can supply their own links in addition to those provided by the editorial process.

FIGURES

Figures must be of publication quality. After acceptance, you will need to submit the original source files in vector format for all diagrams and graphs in your manuscript: vector EPS or vector PDF files are the most useful. (EPS stands for Encapsulated PostScript.)

Most drawing and graphing packages—Mathematica, Adobe Illustrator, Corel Draw, MATLAB, etc.—allow the user to save files in one of these formats. Make sure that what you're saving is vector graphics and not a bitmap. If you need help, please write to graphics@msp.org with as many details as you can about how your graphics were generated.

Please also include the original data for any plots. This is particularly important if you are unable to save Excel-generated plots in vector format. Saving them as bitmaps is not useful; please send the Excel (.xls) spreadsheets instead. Bundle your figure files into a single archive (using zip, tar, rar or other format of your choice) and upload on the link you been given at acceptance time.

Each figure should be captioned and numbered so that it can float. Small figures occupying no more than three lines of vertical space can be kept in the text ("the curve looks like this:"). It is acceptable to submit a manuscript with all figures at the end, if their placement is specified in the text by means of comments such as "Place Figure 1 here". The same considerations apply to tables.

WHITE SPACE

Forced line breaks or page breaks should not be inserted in the document. There is no point in your trying to optimize line and page breaks in the original manuscript. The manuscript will be reformatted to use the journal's preferred fonts and layout.

PROOFS

Page proofs will be made available to authors (or to the designated corresponding author) at a Web site in PDF format. Failure to acknowledge the receipt of proofs or to return corrections within the requested deadline may cause publication to be postponed.